Multiplicity dependence of two-particle correlation in $\sqrt{s} = 7$ TeV pp collisions at LHC-ALICE experiment

Jihyun Bhom

Doctoral Program in Physics

Submitted to the Graduate School of

Pure and Applied Sciences

in Partial Fulfillment of the Requirements

for the Degree of Doctor of Philosophy

in Science

at the

University of Tsukuba

Abstract

Early stage of universe or inside of neutron stars are supposed to be Quark Gluon Plasma (QGP) state. The QGP is a state of matter in quantum chromodynamics (QCD), which exists at extremely high temperature and/or high density. In high energy nuclear collisions experiment, hot dense matter or QGP has been studied, the collective flow of the system has been one of key issues to understand the state of matter.

Large Hadron Collider (LHC) has served pp collisions at a nucleon nucleon center-of-mass energy of 7 TeV in 2010, where the maximum charged particle multiplicity has been measured as large as 100∼200 charged particles in $|\eta|$ <2.5 in $dN/d\eta$ like Cu-Cu collisions $\sqrt{s_{NN}} = 200$ GeV at mid-peripheral at RHIC. A Large Ion Collider Experiment (ALICE) detector at the LHC is optimized for studying the high-temperature and high-density system called as QGP.

Angular correlations between two charged particles are measured with central and forward detectors in ALICE experiment. The correlations are measured over the combination of central- and forward pseudorapidity with the coverage of full azimuthal angle in different intervals of event multiplicity and transverse momentum.

In order to study the hot dense matter created in high multiplicity pp collisions, this analysis focuses on anisotropic expansion. The extension of the elongated structure along $\Delta\eta$ axis at $\Delta\varphi \approx 0$ in intermediate transverse momentum ranges, which is called "Ridge structure" is observated in high multiplicity. The multiplicity dependence of azimuthal angle correlation functions is quantified with the second Fourier coefficients such as the elliptic flow parameter v_2, that is about 7.4% in the transverse momentum of $1-4$ GeV/c. Jet-like correlation shapes are also enhanced with increasing multiplicity selections both experimental result and PYTHIA simulation. Moreover, the double ridges, which have similar magnitude between near side and away side enhancement in $\Delta\varphi \approx 0$ and π, are observed, when the associate particle yield per trigger in low multiplicity event is subtracted from the one in high multiplicity events. The multiplicity dependence of particle yields per trigger is summarized with the integrated yield in $|\Delta\varphi| < 0.8$ and the integrated yield increases with increasing multiplicity selections. The observed structure both ridge and double ridge have been found to increase continuously with the event multiplicity and cannot be explained by

the existing Monte-Carlo event generator such as PYTHIA.

Ridge structure had been observed in high multiplicity pp collisions, which imply the formation of hot dense matter like heavy ion collisions and p-Pb collisions. The extraction of elliptic parameter coefficients could serve as an estimate of the amount of collective flow in pp collisions. Since the observed ridge structure in high multiplicity pp collisions could come from collective phenomena like heavy ion collisions.

Acknowledgements

I would like to express my appreciation to Prof. Yasuo Miake for giving me a chance to be at Tsukuba University, Japan and QGP physics field. I am also grateful to Prof. ShiIchi Esumi for teaching logical though, English, computer programming and inspiring heavy ion experiment. I appreciate Prof. Tatsuya Chujo for supporting ALICE detector experiment. I thank Prof. Motoi Inaba for the instructions of detector constructions. I thank Prof. Hiroshi Masui for advices about the analysis-note. I also thank Mr. Sumio Kato for arranging computer system at our lab.

I respectfully express my thanks to all member of high energy nuclear physics group at Tsukuba University. Let me take this opportunity of thanking Dr. Yoshimasa Ikeda, Dr. Dr. Takahito Todoroki, Dr. Takafumi Niida, Mr.Masato Sano, Dr. Sanshiro Mizuno, Mr. Hiroshi Nakagomi, Mr. Daisuke Watanabe, Mr. Taiyou Kobayashi, Mr. Naoto Tanaka, Mr. Hiroki Yokoyama, Mr. Wataru Sato, Mr. Toshihiro Nonaka, Mr. Ritsuya Hosokawa, Mr. Ryo Aoyama, Mr. JooNIL LEE, Mr. Tomohiro Shioya, Mr. Tetsuro SUGIURA, Mr. Masahiro Hirano, Mr. Hiroki Yamamoto, Mr. Kyoichiro ITO, Mr. Byung Chul KIM, Ms. Sakiko KUDO, Ms. MaRi CHANG and Mr.Yusuke FUKUDA.

I would like to express many thanks to RHIC-PHENIX collaboration, LHC-ALICE collaboration and ALICE PAG-CF members.

At last, I want to thank my family for the support.

Contents

List of Figures

Chapter 1

Introduction

The Standard Model describes well the fundamental forces and all their carrier particles, and interprets how these forces act on all the matter particles. Theoretical descriptions of the event generator are discussed. PYTHIA is one of the standard models for p-p scattering. The results of PYTHIA are compared with experimental results (ALICE experimental data). EPOS is one of the global event generators that include hydro-dynamic collective effects in collisions depending on the local density of string tubes both pp and heavy ion collisions.

1.1 The Standard Model of Particle Physics

The Standard Model shown in Figure 1.1 is the basic concept of Quantum Chromo Dynamics (QCD) and the experimental concepts of high energy collisions. The Standard Model successfully describes the fundamental forces and the composition of matter, except for gravity. The Standard Model covers the electromagnetic, strong and weak forces and all their carrier particles, and interpret how these forces act on all the matter particles. QCD contains quark and gluon fields as fundamental degrees of freedom. A hadronic models such as Monte-Carlo (MC) able to reproduce the observed particle production in high energy physics (HEP) experiments.

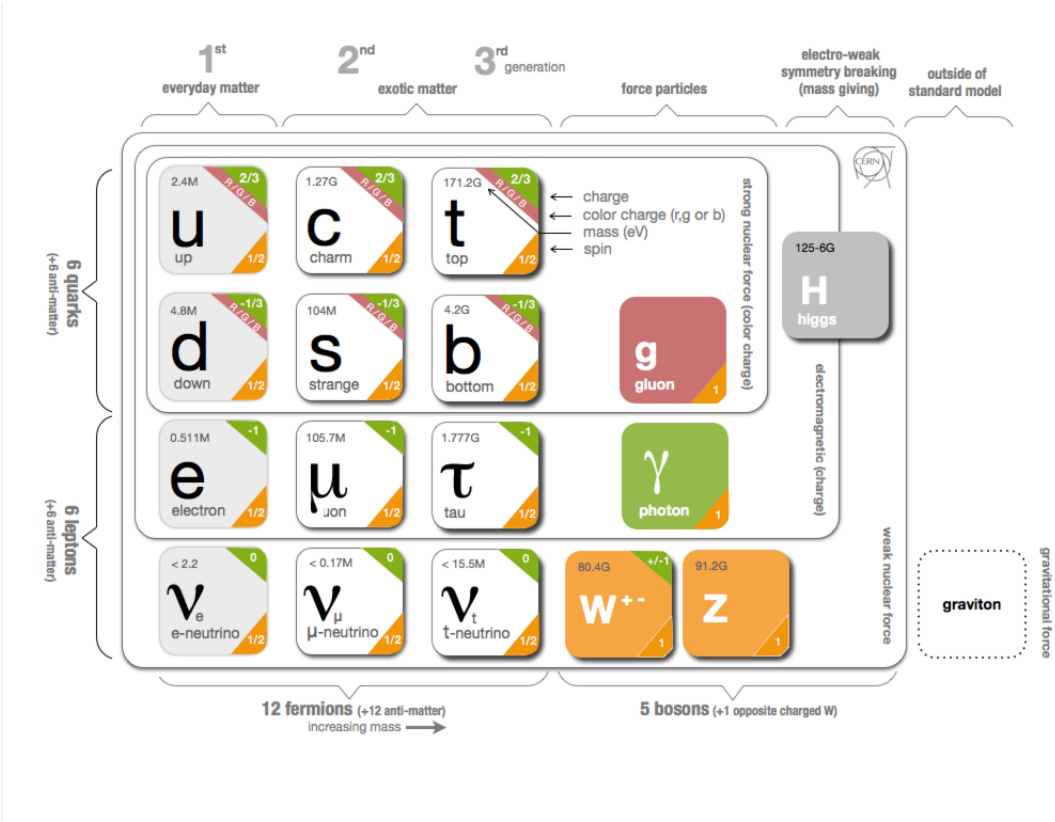

Figure 1.1: The Standard Model [38].

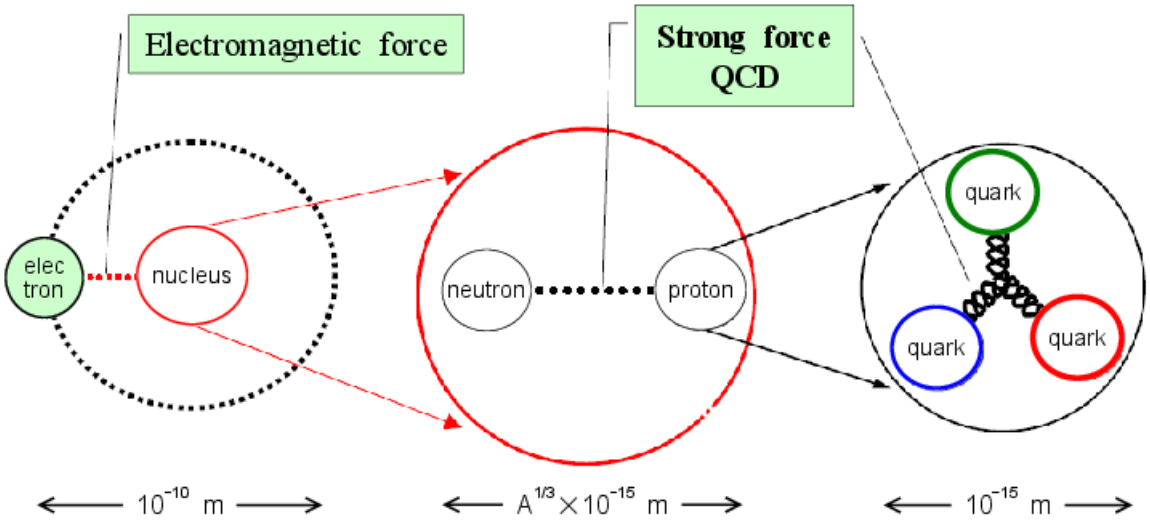

Figure 1.2: Atom, nucleus, neucleons and quarks. A is the mass number, number of protons+number of neutrons in a nucleus [39].

1.1.1 Quantum Chromodynamics

The hydrogen atom is familiar with us and is the simplest atom that is composed of an electron and a proton, as shown in Figure 1.2. Protons have positive charge and electrons have negative charge, they attract each other. Proton and electron are bound together, and this is how atoms are formed. The force between protons and electrons (charged particles) is electromagnetic force that is described by quantum electrodynamics (QED). Protons (unlike electrons) are made up of elementary particles, which are called quarks. Quarks are confined within hadrons (color-white composite object), where baryons are composed of three quarks and mesons are composed of a quark and an anti-quark. The quarks have 6 types: the up quark, the down quark, the charm quark, the strange quark, the top quark, and the bottom quark. A proton is two up quarks and a down quark (uud), and a neutron is an up quark and two down quarks (udd). The up quark has charge +2/3 and the down quark has charge -1/3. Therefore, a proton has charge +1 and a neutron has charge 0. QCD has three color charges, red, green, and blue. Gluons are the binding forces between quarks. QCD is a gauge field theory that describes the strong interaction between quarks and gluons.

The main difference between QCD and QED is the difference between photons and gluons shown in Figure 1.3. Photons interact with only charged particles. But photons have no charge. This means that photons do not interact with each other. On the other hand, gluons interact with color charged particles. And gluons have also color charge. Therefore, gluons are able to interact with other gluons. A gluon can split apart into two or more gluons. So, a quark will emit gluons, which will make more gluons.

For a quark with mass m, the classical Lagrangian density is given by [1];

$$\mathcal{L}_{cl} = q^{\alpha}(i\gamma^{\mu}(D_{\mu}) - m\delta_{\alpha\beta})q^{\beta} - \frac{1}{4}F^{a}_{\mu\nu}F^{\mu\nu}_{a} \tag{1.1}$$

α and β run from 1 to 3, a runs from 1 to 8, which corresponds to 8 gluons, q^{α} is the quark field with color index α, γ^{μ} are Dirac matrixes, and $F^{a}_{\mu\nu}$ is the gluon field strength tensor with color index a. The D_{μ} is the covariant derivative acting on the color-triples quark field

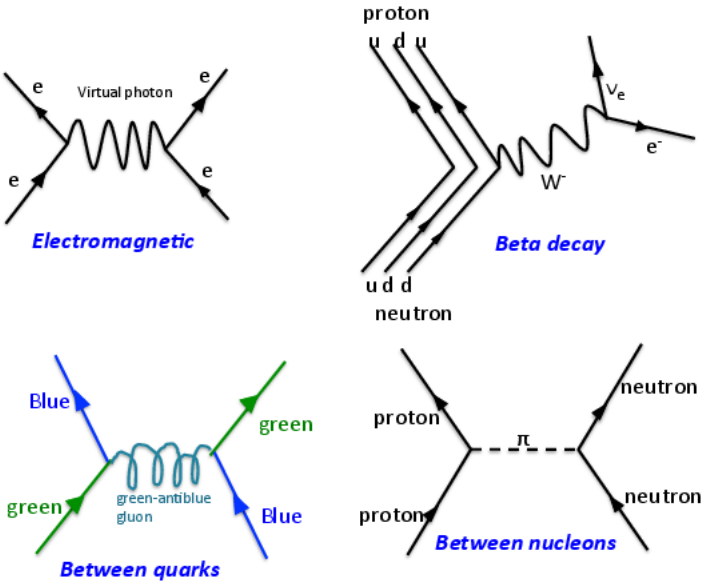

Figure 1.3: Examples of Feynman diagrams.

defined as:

$$D_\mu = \partial_\mu + igt^a A^a_\mu \tag{1.2}$$

g is the gauge coupling parameter in QCD, and t^a is the fundamental representation of the color $SU_c(3)$ Lie algebra and A^a_μ is the gluon field.

The field strength tensor of the gluon field $F^a_{\mu\nu}$ is defined as:

$$F^a_{\mu\nu} = \partial_\mu A^a_\nu - \partial_\nu A^a_\mu - g f_{abc} A^b_\mu A^c_\nu \tag{1.3}$$

The third term in Eq. 1.3 means gluons themselves carrying color charge that is related to non-commutativity as $AB \neq BA$. f_{abc} is the structure constants of color $SU_c(3)$. During the renormalized parameters (renormalized scale μ^2_R), the gauge coupling parameter g take into the fine structure constant $\alpha_s = g^2/4\pi$ in the strong (electromagnetic) interaction.

The coupling constant of the strong interaction is a useful tool to explain the asymptotic freedom at high energies and the confinement of color in low energy which are two important characteristics of quark-gluon dynamics in QCD.

The coupling constant can be calculated by perturbative QCD (pQCD) [3]:

$$\alpha_s(Q^2) = \frac{1}{\beta_0 ln(Q^2/\Lambda^2)} \tag{1.4}$$

$$\beta_0 = \frac{33 - 2N_f}{12\pi} \tag{1.5}$$

Λ is the QCD scale parameter ($\Lambda \approx$200 MeV). N_f is the number of active quark flavors. Figure 1.4 shows the energy dependence of the coupling constant α_s as a function of the momentum transfer Q. α_s means how much interacting to each quarks. At high energy, α_s is closer to 0. This means the quarks are very weakly interacting or free, which is called asymptotic freedom of the strong force. On the other hand, at low energy, α_s is going to become very large and the perturbative approach is not possible. An alternative approach is lattice QCD that is a non-perturbative QCD method.

Quarks can not be separated at large distances because the force between them grows linearly with the distance unlike Coulomb's force. Quarks are confined within a hadron to be white in color charge, that is color confinement. This is why we cannot observe quarks and gluons as free particle. However, in high density, we expect the a phase transition.

Figure 1.5 shows the phase transition in a lattice calculation (e/T^4) as a function of

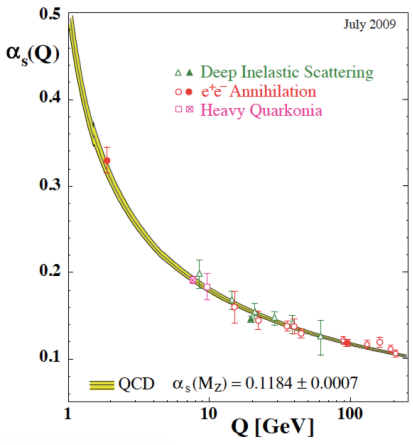

Figure 1.4: Summary of measurements of α_s as a function of the respective momentum transfer Q [3].

temperature, where hadronic states are seen at low temperature and the light quarks at high temperature in lattice QCD simulation. ϵ is the energy density, T is the temperature and T_c is the critical temperature. A sudden increase of e/T^4 for all three cases is seen at T_c. The

discrete transition points are expected to occur as a first or second order phase transition where the state above the transition temperature is called as quark-gluon plasma (QGP). After T_c, all three lattice cases show the Stefan-Boltzmann limit. The chiral limit (m_q=0) of T_c are found to be $T_c(N_f = 0) \approx 273\ MeV$, $T_c(N_f = 2) \approx 175\ MeV$, $T_c(N_f = 3) \approx 155$ MeV with $\pm 10\ MeV$ [1].

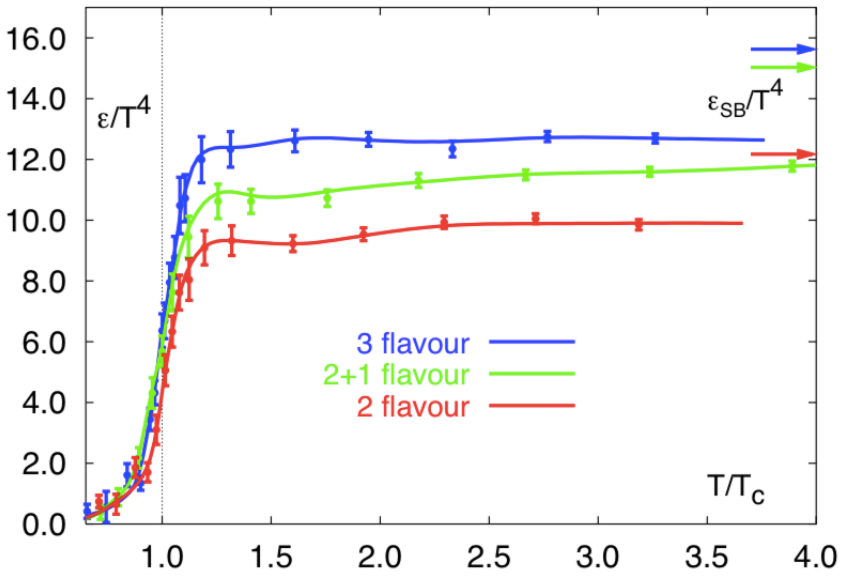

Figure 1.5: The hadrons and the deconfinements in temperature scale. [5].

1.1.2 High Energy Nuclear Collisions

The Large Hadron Collider (LHC) is the world largest and most powerful particle accelerator at CERN (the European Organization for Nuclear Research, Conseil Europeen pour la Recherche Nucleaire) in Switzerland. LHC is built to understand confinement and the Higgs discovery and beyond standard model physics and confirmation of QGP in QCD.

This section describes the schematic history of high energy hadron collision by the space-time evolution. Figure 1.6 shows a schematic figure indicating the time history in the space-time diagram. Figure 1.6(a) reproduces the classical description of a proton-proton (pp) scattering in HEP model. Figure 1.6(b) is commonly used for heavy ion (HI) collisions. "Projectile" and "Target" refer to two opposite directions along the beam axis (z, longitudinal direction). The horizontal axis (t) is "z : space, t: time". A hyperbola (line) represents particles with the same proper time. The two nuclei are Lorentz contracted in

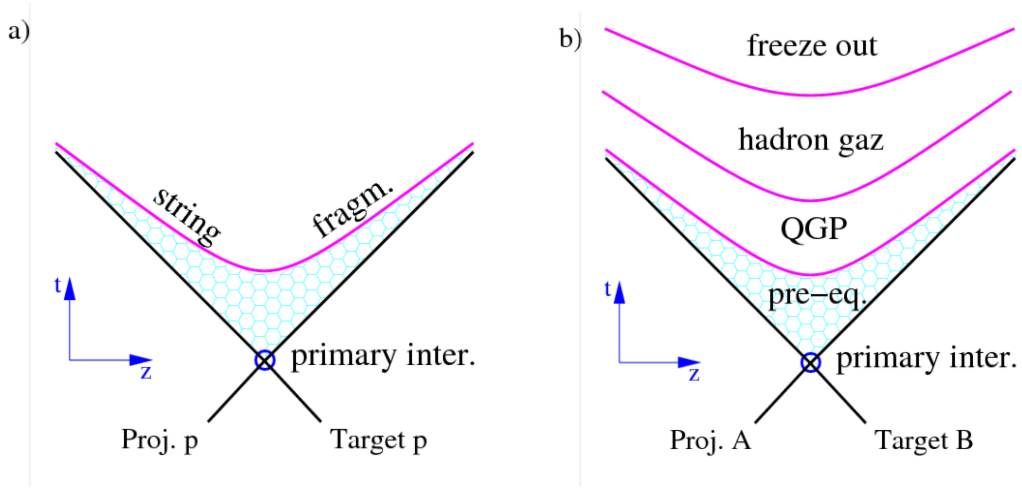

(a) The standard approach for p-p scattering

(b) HI collision

Figure 1.6: Space time evolution of the particle production in a hadronic interaction. (a) is the standard approach for p-p scattering while (b) is a more complete treatment used usually for HI collision [7].

the beam direction and collide at z=0 and t=0 in center of mass frame. After the collision, the space-time evolution of overlapped two nuclei is described by Bjorken scaling variable.

The collision of ultra-relativistic hadron is a process of huge entropy production. To understand this mechanism, two classes of model, which are incoherent models and the coherent model are proposed [1]. In incoherent models, the minijet (semi-hard partons) production had worked well in pQCD with the production of dijet at an infrared cutoff of order 1-2 GeV. The equilibration process is calculated by the relativistic Boltzmann equation with the parton distribution function (PDF).

One of the coherent models is the color strings and rope (the coherent color-electric fields), which subsequently decay into real partons by the Schwinger mechanism. The real partons move to thermal distribution by the relativistic Boltzmann equation with parton collisions and the color-electric field background. Another of the coherent models is the color glass condensate (CGC).

Above two classes models, we assume that the entropy production and subsequent local thermalization is reached before QGP. The entropy production and subsequent local thermalization produce condition of hydrodynamical evolution of the system.

By lattice QCD calculations, then, quarks and gluons are not confined in hadron at high temperature and density that is called QGP. A QGP is expected after the Big Bang in very

short time. And QGP may exist in the core of neutron stars. And we expect QGP in heavy ion collisions experiment such as at LHC or RHIC. Figure 1.7 shows expected history of heavy ion collisions with QGP phase.

We take the QGP to be a (locally) thermally equilibrated state of matter in which quarks and gluons are deconfined from hadrons, so that color degrees of freedom become manifest over nucleus, rather than merely nucleonic, volumes [2]. In the relativistic heavy ion collisions experiment, the strongest evidence of QGP at LHC or RHIC is the suppression of back-to-back peak [14] and elliptic flow (v_2) [12] [19].

In the heavy ion collisions, a high density matter with the size of nucleus volume is created. If the cross section of parton/particle is large, there are many interactions. A pressure gradient is generated with in the volume. Then, a collective expansion is generated.

Let's consider non-central collisions where the initial geometry is elliptic. When the mean-free-path (l) is longer than the size of system (R), the partons emission is isotropic in the transverse plane, same as an independent superposition of nucleon-nucleon collisions, as shown in Figure 1.8(a). On the other hand, when the mean-free-path is short enough ($l << R$), as shown in Figure 1.8(b), difference of pressure gradients between in-plane and out-of-plane are expected. Therefore the particle elliptic emission is affected by the initial geometric shape via a elliptic expansion. Most of particles at low p_T are shown to v_2 or vn (v1=$< cos\varphi >$ and $v_2 =< cos2\varphi >$, where φ is the azimuthal angle of the particle with respect to the reaction plane). On the other hand, the particles at high p_T passing through QGP show to v_2 or vn by path length dependence of energy loss as shown in Figure 1.7.

Because of similar multiplicity, centrality 0-15% Cu+Cu collisions at $\sqrt{s_{NN}}$ = 62.4 GeV, shown in Figure 1.9 can be compared with 0-5% pp collisions at $\sqrt{s}$ = 7 GeV, see Figure 3.20. The v_2 in $|\eta| \approx 2$ for Cu+Cu collisions at $\sqrt{s_{NN}}$ = 62.4 GeV, show in Figure 1.10 show about 0.02. It is comparable to $p2^{long}$ (v_2^2) for 0-1% multiplicity of pp collisions at $\sqrt{s}$ = 7 GeV, see Figure 5.10 ($\sqrt{0.005 \sim 0.07}$ in 1-4 GeV/c). Figure 1.11 show a general trend of two-particle correlation of pp, Cu+Cu and Au+Au collisions at $\sqrt{s}$ or $\sqrt{s_{NN}}$= 200 GeV. Cu+Cu and Au+Au collisions are shown the centrality 10%. Figure 1.11 (a) shows a ordinary shape for pp collisions, (b) shows a high multiplicity CuCu collisions in $\Delta\varphi \approx 0$ and (c) shows heavy ion collisions.

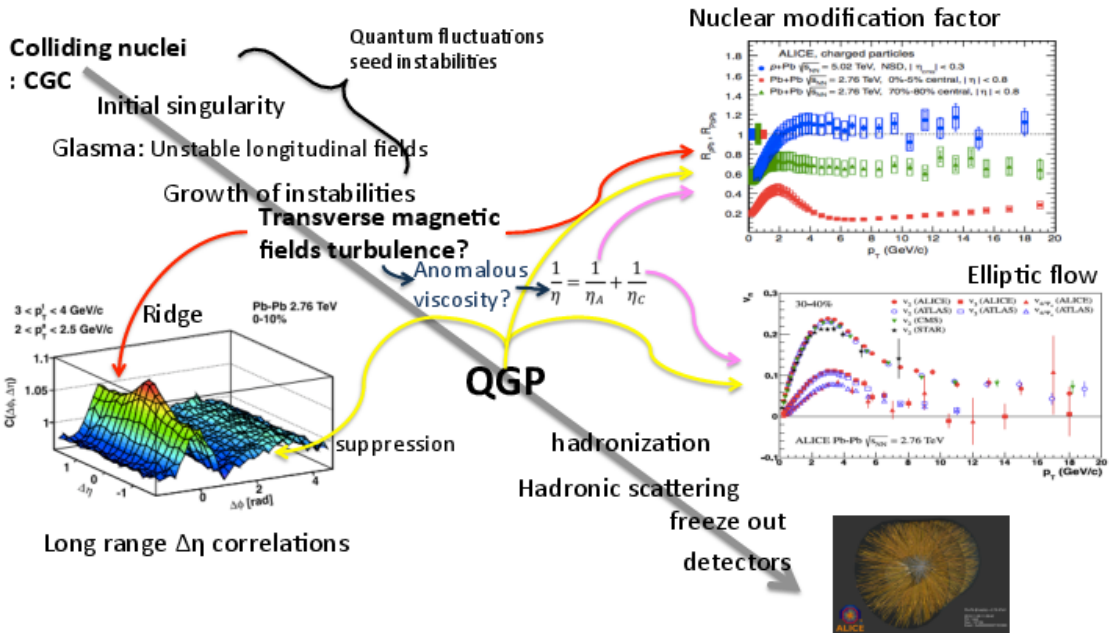

Figure 1.7: Expected history of heavy ion collisions with QGP [12] [14] [15].

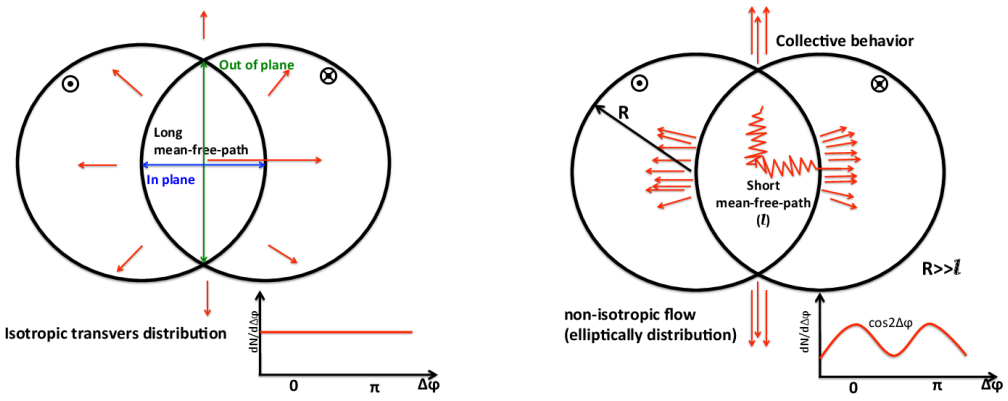

(a) Long mean-free-path

(b) Short mean-free-path

Figure 1.8: The difference between long- and short mean-free-path evolutions in transvers plane are shown.

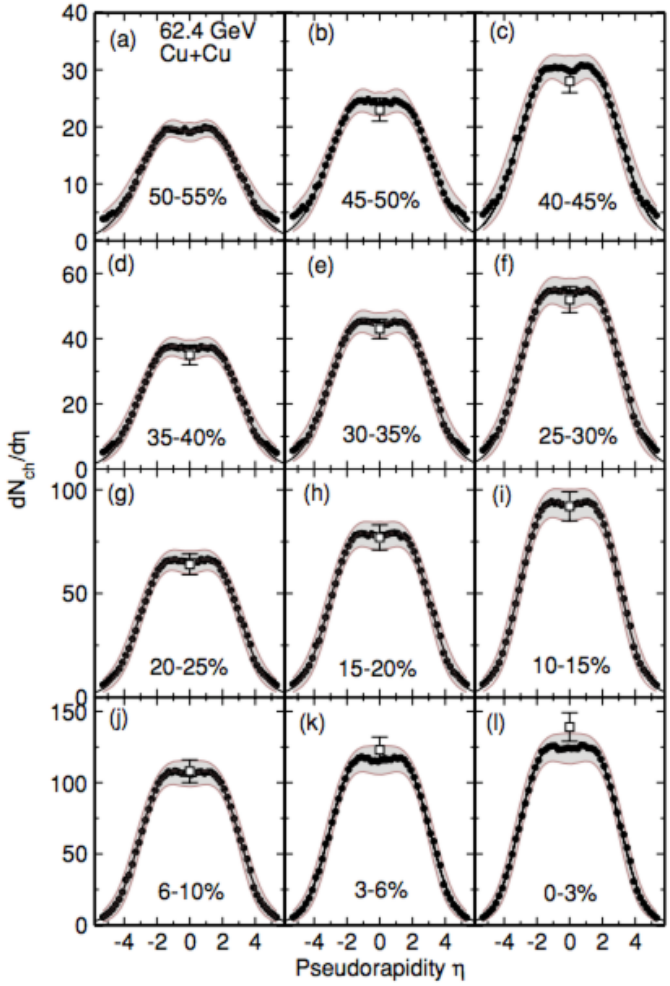

Figure 1.9: $dN_{ch}/d\eta$(Color online) as function of η acceptance are shown for twelve centrality bins representing 55% of the total cross section for Cu + Cu collisions at $\sqrt{s_{NN}} = 62.4$ GeV [16].

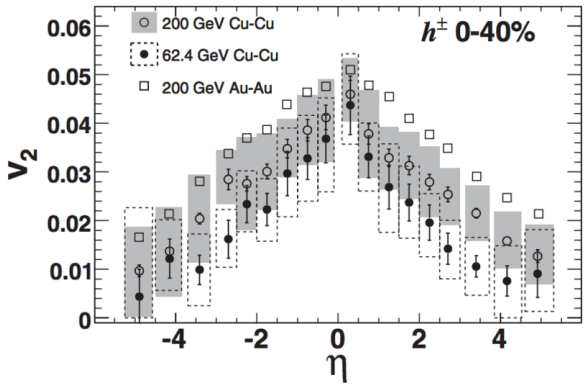

Figure 1.10: The elliptic flow signal (v_2) as function of η for Cu+Cu collisions at $\sqrt{s_{NN}} =$ 62.4 GeV and 200 GeV for the 40% most central collisions [19].

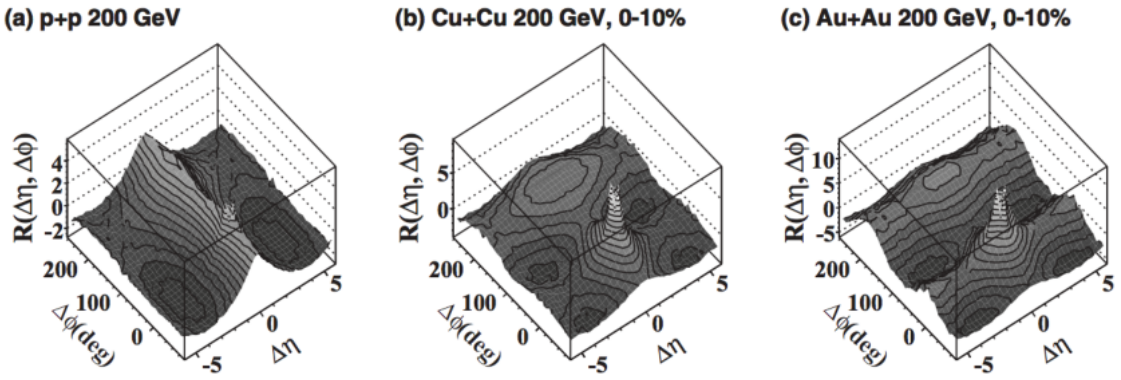

Figure 1.11: 2-D Two-particle angular correlation functions for (a) p + p, the central 10% (b) Cu + Cu and (c) Au + Au collisions at $\sqrt{s}$ or $\sqrt{s_{NN}}$= 200 GeV [20].

1.2 High multiplicity pp collisions

1.2.1 Multi Parton Interaction and PYTHIA

In order to probe hadrons, we made the hadron collider that the hadron beams are accelerated to about velocity of light and are collided each other. At the hadron collision, multiple parton hard scatterings can occur simultaneously to create two or more hard parton interactions in a hadron-hadron collision in one event. For example, the cross sections increase with collision beam energy as shown in Figure 1.12, which is given by Multiple Parton Interactions (MPI) [10]. In general, those are explained by 3 processes of collisions, "soft", "semi-hard" and "hard". Soft interactions are defined by having small momentum transfers by transverse momentum threshold. Hard interactions are defined by having high momentum transfers. And semi-hard interactions are defined by the intermediate region between soft and hard interactions. Multiple parton interactions in an event could also include soft interactions. Monte Carlo (MC) event generators may help to understand the pp collisions [10].

The PYTHIA generator is commonly used to describe proton proton collisions at LHC energies. PYTHIA is a Monte Carlo event generator that is modeled as parton distribution

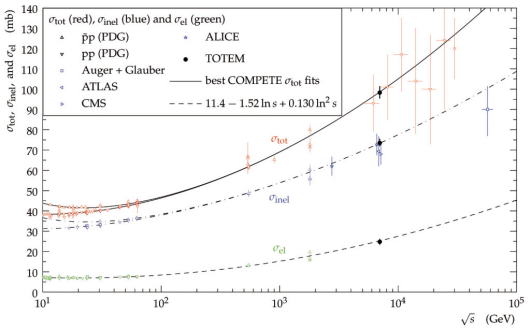

Figure 1.12: The increase with energy of the proton-proton total cross-section at $\sqrt{s} = 7$ TeV [4].

functions (PDFs) and cross sections. Those processes are sensitive to the range of momentum transfers. In this analyses, PYTHIA 6.4 event generator with the tune Perugia-0 with particle transport through the detector using Geant 3 is used for comparisons.

The charged particle multiplicity has been studied by many previous experiments at various energies. The distribution of the charged particle multiplicity depends on the beam energy [8]. Figure 1.13 shows the measured multiplicity distributions of PYTHIA versions in $|\eta| < 1$ for the INEL$> 0_{|\eta|<1}$ (inelastic) event class in ALICE pp 7 TeV. D6T (dashed line), ATLAS-CSC (dotted line) and Perugia-0 (dash-dotted line) are various version of PYTHIA. D6T and Perugia-0 cannot represent high multiplicity events. ATLAS-CSC is close to the data at high multiplicity selections ($N_{ch} > 25$). But it does not reproduce the data in $8 < N_{ch} < 25$. The results of PYTHIA cannot reproduce the experimental result.

1.2.2 Collective flow and EPOS

Due to large mass and large number of particle multiplicity in heavy ion collisions such as Pb-Pb collisions exhibit collective effects in high energy collisions. On the other hand, the collective effects were not expected in pp collisions. Therefore, traditionally we have been treating differently the pp and heavy ion collisions. This chapter describes a global model such as EPOS. The global model considers the pp and heavy ion collisions with a same physics that is a collective effect.

We expect the QGP in heavy ion collisions at LHC and RHIC. The produced matter expands as a perfect fluid, which has been studied by azimuthal anisotropies. The hydro-

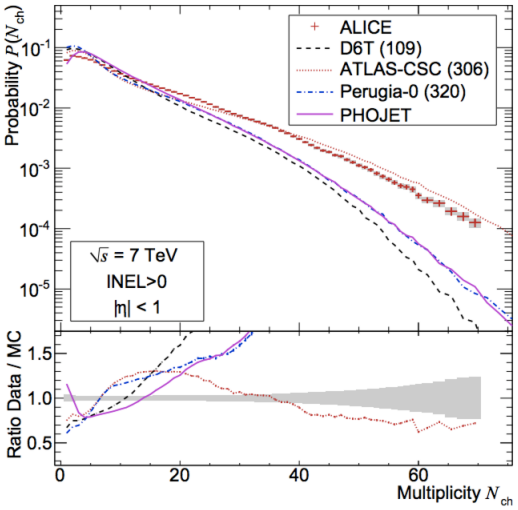

Figure 1.13: Measured multiplicity distributions for inelastic event class. The data at 7 TeV are compared to models: PHOJET (solid line), PYTHIA tunes D6T (dashed line), ATLAS-CSC (dotted line) and Perugia-0 (dash-dotted line). In the lower part, the ratio between the measured values and model calculations are shown with the same convention. The shaded area represents the combined statistical and systematic uncertainties [8].

dynamic model calculation has been recognized to explain the expanding matter during the heavy ion collisions at LHC and RHIC.

EPOS model suggests both pp and heavy ion collisions are treated using the same collective effect. Under the extreme hot and dense matter, in hydrodynamic model, the result of EPOS has described the experimental data well [9]. The hydrodynamic concept of the particle production is shown in Figure 1.14. A small volume with high density and thermalized matter is called as core, the low density surrounding areas is corona. A hyperbola (line) represents particles with the same proper time.

2-D dihadron correlation functions from the EPOS LHC model in $1 < p_T < 3$ GeV/c are shown in Figure 1.15. In EPOS LHC assumption, it is considered only for high multiplicity events in pp collisions. EPOS LHC expects more than 10 strings in high multiplicity events, about 30% of the particles coming from the core [7]. Without hydrodynamic assumption, as shown in Figure 1.15(a), two-particle correlation presents di-jet event shape in $\Delta\eta \approx 0$ without ridge structure at $|\Delta\varphi| \approx 0$ in long range $\Delta\eta$. With hydrodynamic assumption as shown in Figure 1.15(b), there is a ridge structure in long range $\Delta\eta$ [21]. The hydrodynamic assumption may explain the ridge structure in high multiplicity pp collisions, see Section 4 .

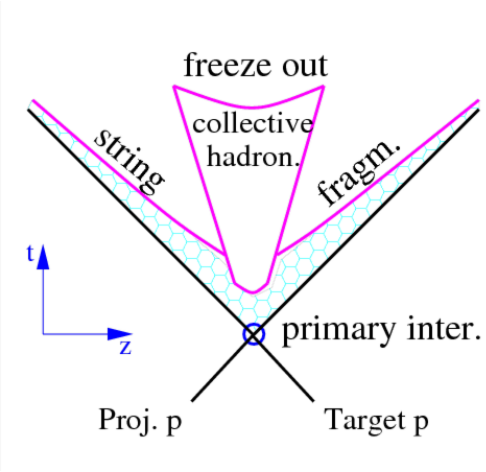

Figure 1.14: Schematic view of the space time evolution of the particle production in an hadronic interaction in EPOS LHC. The same treatment is used for p-p or A-B but the collective hadronization, which can be local, is simplified compared to the full HI picture shown in Figure 1.6 [7].

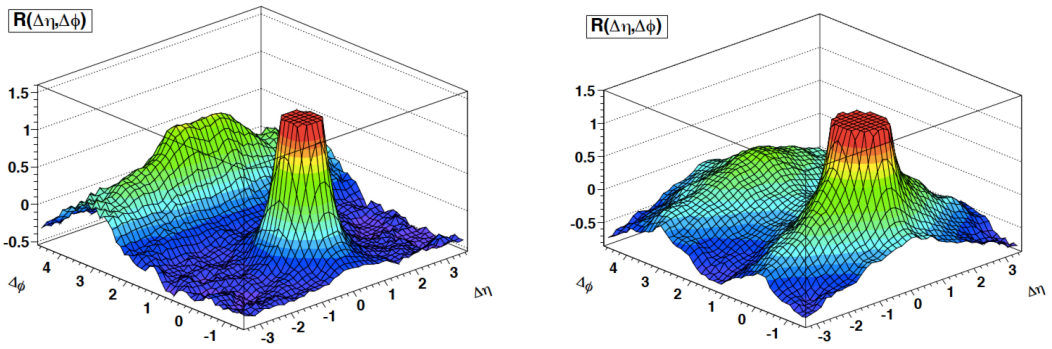

(a) without hydrodynamic evolution

(b) with hydrodynamic evolution

Figure 1.15: EPOS model for 2-D charged particle angular correlation functions for high multiplicity events in pp collisions at $\sqrt{s} = 7$ TeV with $1 < p_T < 3$ GeV/c are shown with (a) without hydrodynamic evolution and (b) with hydrodynamic evolution [21].

1.2.3 Motivation

The 2nd order Fourier coefficient such as v_2 have very important physics meaning. v_2 does not mean hot dense matter is created in hadron collisions. v_2 mean an elliptic event anisotropy of parton distribution. The Fourier coefficients are needed to constrain viscosity of QGP. This analysis discusses the ridge structure in long range $\Delta\eta$ and $\Delta\varphi \approx 0$ in ultra-high multiplicity events as shown in Figure 1.16 (d) and introduce a new method to extract v_2 (the second Fourier coefficients) in small system.

We suppose no volume in pp collisions (No impact parameter, b). However, the shapes of two-particle correlation are different for different multiplicities, as shown in Figure 1.16. What does the observed ridge mean in pp collisions? What happens to the high multiplicity pp collisions? The ridge structure can be considered as a manifestation of collective effect, such as elliptic shape (parameter v_2, the second Fourier coefficients), see Figure 1.8. We could imagine a hot and dense matter is created in high multiplicity pp collisions, which is called QGP.

Is the ridge observed in CMS confirmed in ALICE experiment? This analyses focus on the shape modification of two-particle correlation function with multiplicity, especially focusing on the long-range ridge-like correlation structure in intermediate p_T region with various event estimators. The differences between multiplicities are quantified with the second Fourier coefficients.

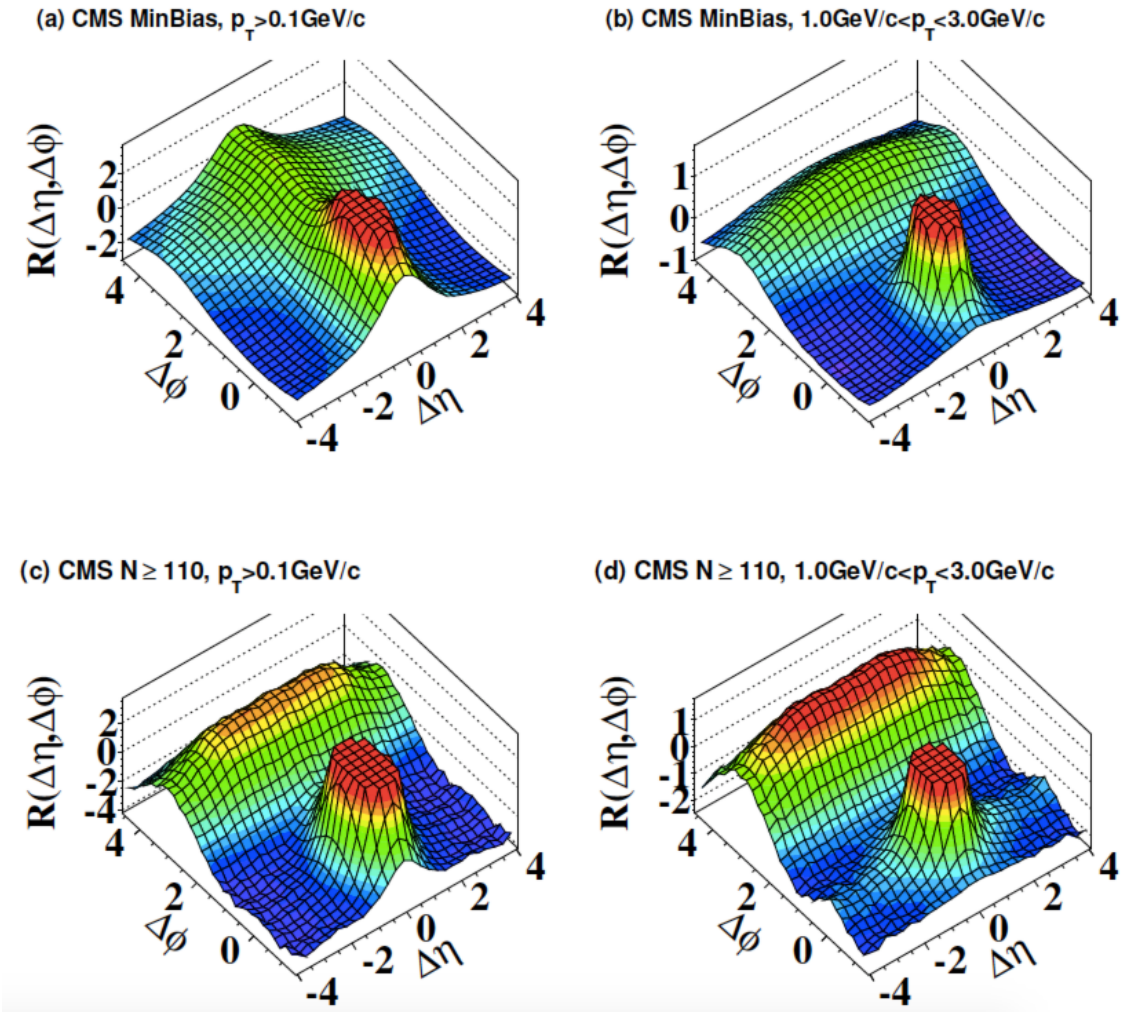

Figure 1.16: 2-D two-particle correlation functions for 7 TeV pp (a) minimum bias events with $p_T > 0.1$ GeV/c, (b) minimum bias events with $1 < p_T < 3$ GeV/c, (c) high multiplicity (Noffline ≥ 110) events with $p_T > 0.1$ GeV/c and (d) high multiplicity (Noffline ≥ 110) events with $1 < p_T < 3$ GeV/c. The sharp near-side peak from jet correlations is cut off in order to better illustrate the structure outside that region [22].

Chapter 2

Experiment

The Large Hadron Collider (LHC) is the world/s largest and most powerful particle accelerator. It first started up on 10 September 2008, and remains the latest addition to CERNs accelerator complex. The LHC consists of a 27-kilometre ring of superconducting magnets with a number of accelerating structures to boost the energy of the particles along the way [40]. The LHC is located in the Swiss-French border area close to Geneva.

2.1 Large Hadron Collider

The LHC have six experiments projects, ALICE (A Large Ion Collider Experiment), ATLAS (A Toroidal LHC ApparatuS), CMS (Compact Muon Solenoid), LHCb (The Large Hadron Collider beauty experiment), LHCf (Large Hadron Collider forward experiment), and TOTEM (TOTal Elastic and diffractive cross-section Measurement) as shown in Figure 2.1. The present analyses are performed at ALICE. The LHC serves a luminosity $10^{34} cm^{-2} s^{-1}$ for protons and $10^{27} cm^{-2} s^{-1}$ for Pb ions. However, the LHC delivers a lower luminosity to the ALICE experiment during proton collisions (about 3 $\times 10^{30} cm^{-2} s^{-1}$) by means of defocusing or displacing the beams.

2.2 ALICE Experiment

ALICE detectors are shown in Figure 2.2. ALICE detectors are the ITS (Inner Tracking System), TPC (Time-Projection Chamber), TRD (Transition-Radiation Detector), TOF

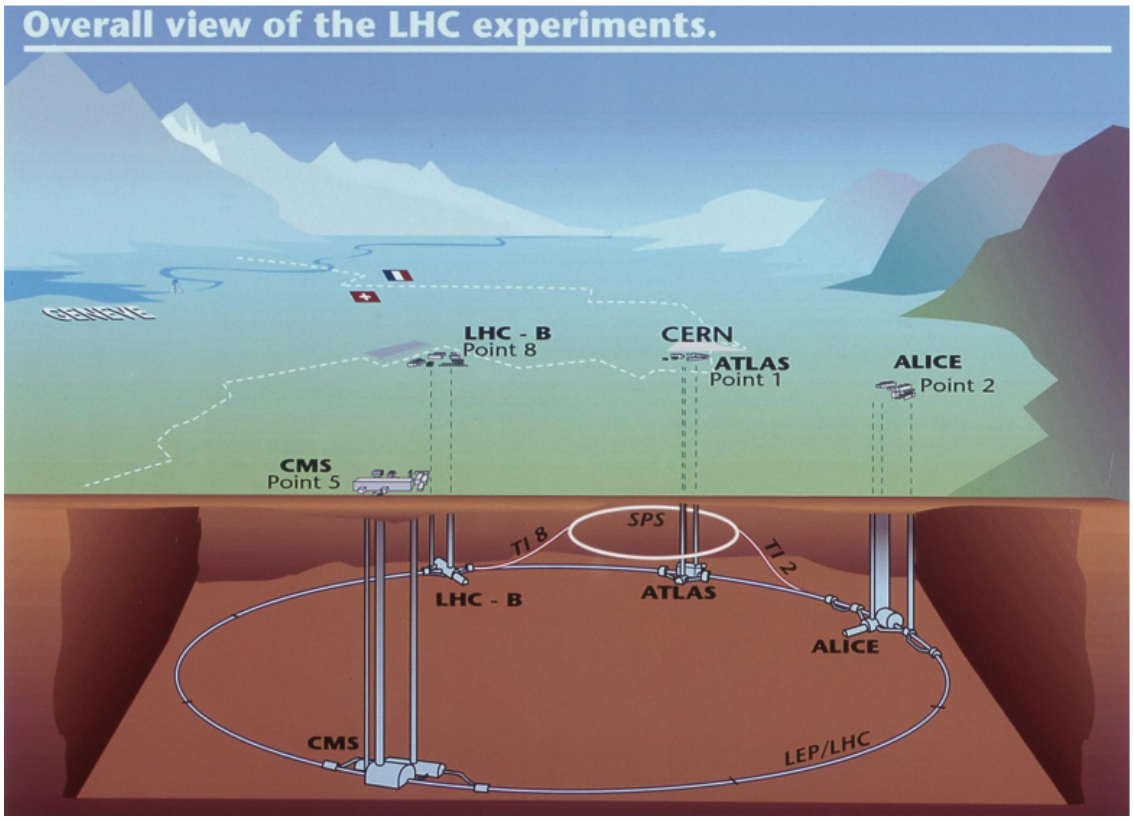

Figure 2.1: Overall view of the LHC experiments [41].

(Time-Of-Flight Detector), PHOS (Photon Spectrometer), EMCal (ElectroMagnetic Calorimeter), HMPID (High-Momentum Particle Identification Detector), ACORDE (ALICE Cosmic Ray Detector) in the central barrel. The ALICE forward detectors are the PMD (Photon Multiplicity Detector), FMD (Forward Multiplicity Detector), VZERO, T2, ZDC (Zero-Degree Calorimeter) and the muon spectrometer. This chapter explains ITS, TPC and VZERO.

2.2.1 Inner Tracking System

ITS is the inner tracking system or vertex detector in ALICE. The Inner Tracking System (ITS) consists of six cylindrical layers of silicon detectors with radii from 3.9 cm to 43 cm. ITS consists of each two layers of Silicon Pixel Detector (SPD), Silicon Drift Detector (SDD) and Silicon Strip Detector (SSD). Main task of ITS is identifying the short-living heavy particles, which have a very small distance before decaying such as B, D mesons and hyperons, by measuring the location of the decay. The particles are reconstructed

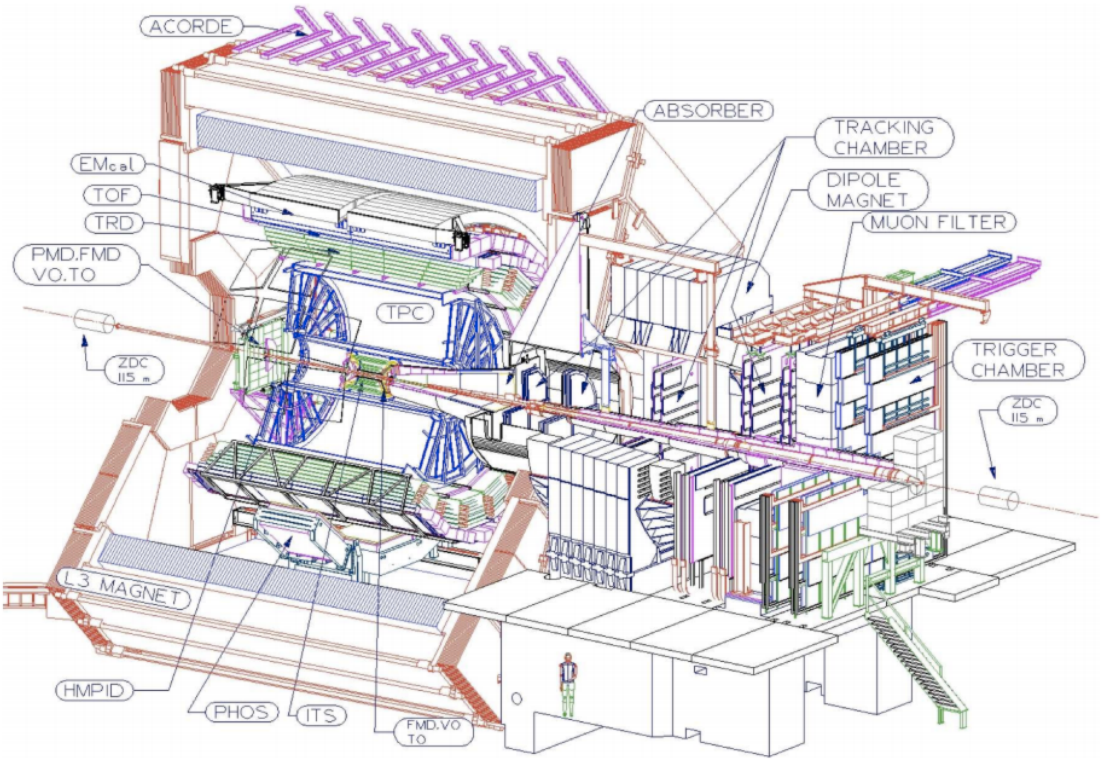

Figure 2.2: General layout of the ALICE experiment [24].

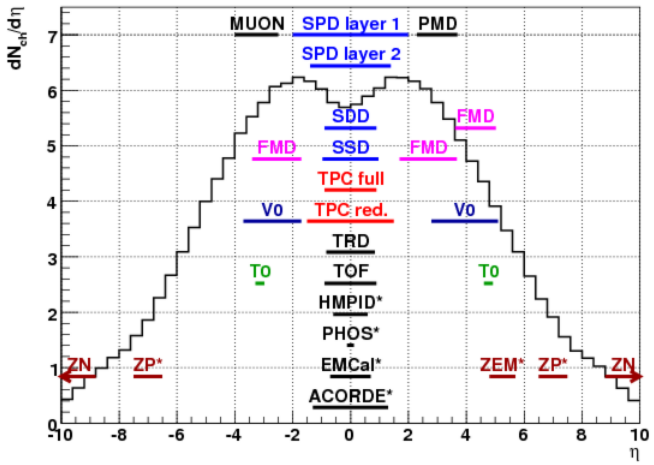

Figure 2.3: The acceptance in η of all ALICE subdetectors overlayed with a dNch/dη prediction by PYTHIA [42].

with the primary vertex of collisions. Because the ITS can measure the specific energy loss (dE/dx) and can track the charged particle. ITS is used to perform stand-alone tracking for low momentum particles which can not reach the TPC. The reconstruction of secondary particles have a resolution better than 100 μm in transverse direction.

The SPD (first and the second layer) have 3.9 cm and 7.6 cm with an acceptance of η <2.0

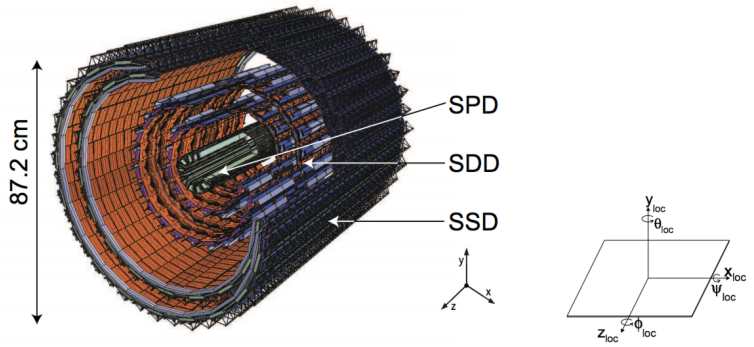

Figure 2.4: Layout of the ITS (left) and orientation of the ALICE global coordinate system (right) [24].

and η <1.4. The SPD provides a measurement of the charged particle multiplicity. The p_T cut of SPD is 35 MeV/c. SPD can measure to a very high rate of maximum 50 particles per 1 cm^2. The rate of SDD and SSD are below one particle per 1 cm^2. Total 9.8 million channels are read out in SPD. The silicon detector diodes in SPD are a thickness of 200 μm. Dut to no energy-loss information in SPD, the SPD does not contribute to particle identification. The information of the SPD is used as tracklets, CL1 multiplicity, L0 trigger, a fast OR signal for ALICE-FPGA and minimum bias trigger.

The SDD (third and fourth layer) have total 133,000 channels. The silicon detectors of SDD have a 300 μm thick homogeneous high-resistivity silicon. Due to analog type readout of SDD, the SDD can measure the energy-loss for particle identification. The detector employs a drift time measurement resulting in a similar granularity as the SPD and SSD.

The SSD (fifth and sixth layer) has about 2.6 million channels in 35 rad. The silicon micro-strips of SSD measure the position and energy-loss for particle identification.

2.2.2 Time Projection Chamber

The TPC is the main tracking detector in the central barrel of the ALICE. The TPC is located in a radius 0.85 m to 2.5 m with a length 5 m (volume 90 m^3) that is the biggest TPC in the world. The TPC officially tracks particles in $|\eta| < 0.9$. TPC provides p_T from 200 MeV/c up to 100 GeV/c and the charged particle momentum resolution of the tracks is about 2.5% (below 4 GeV/c). TPC provides information of the measured charged particles such a momentum, particle identification, and production vertex together with the other detectors such as ITS, TRD and TOF. [25]

TPC is a gas detector in cylindrical shape with filled with Ne/CO2/N2 gas. 100 kV drift field hold between z = 0 and z = ± 2.5 m in 160 clusters in TPC. 160 clusters in TPC are used to reconstruct a track and TPC can track up to 20,000 tracks in an event. The tracks are reconstructed and identified. The readout plane for TPC is consisting of multi-wire proportional chambers. Electrons must pass a gating grid by a L1 trigger for the drift time interval, about 90 μs. The readout of TPC consists of about 560,000 channels in 36 sectors.

The tracking efficiency is about 90%, because of the magnetic field and the insensitive region. Due to the long drift time interval of TPC, TPC is the lowest detector in ALICE. Because other detectors do not need the time interval of 90 μs. And there were the huge pile-up event in pp collisions, which are measured together within the triggered event.

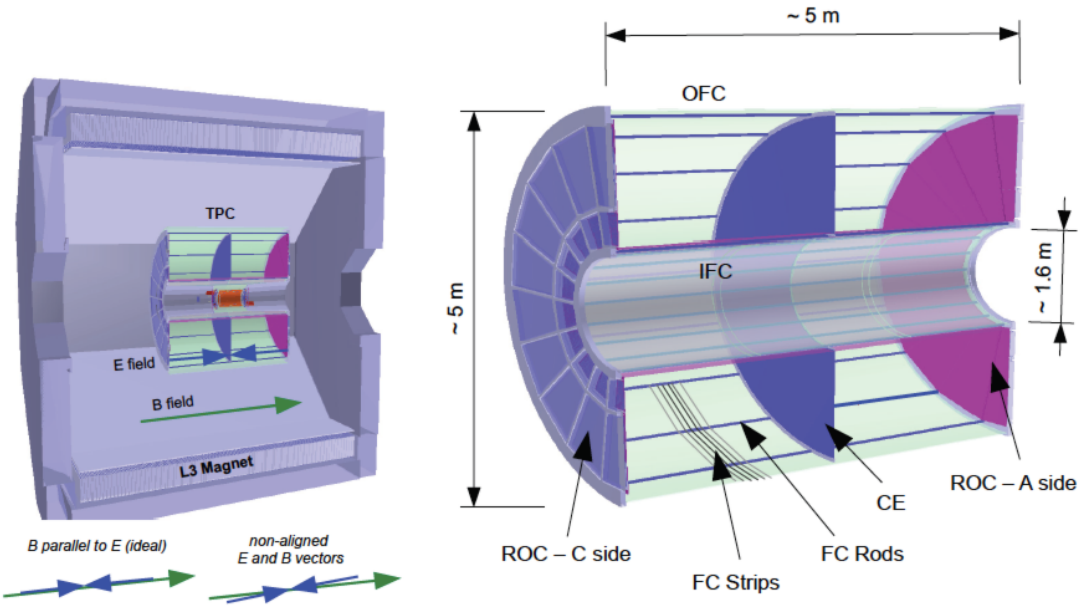

Figure 2.5: Schematic view of the TPC [43]

2.2.3 VZERO Detector

The VZERO system is one of the forward region detectors in ALICE. The VZERO

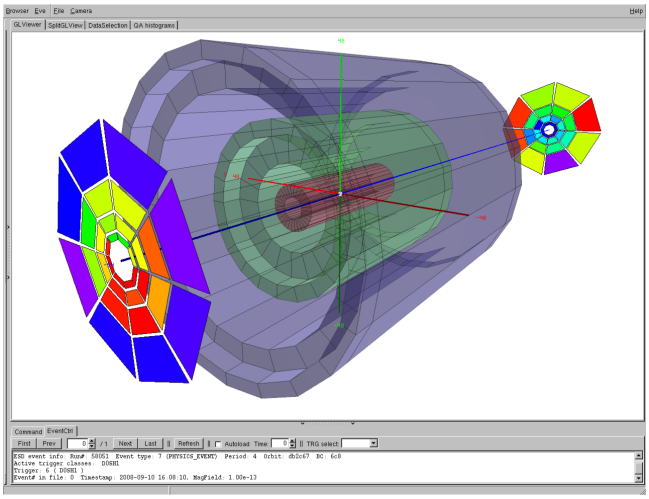

Figure 2.6: On-line event display showing the VZERO data taking [43].

provides trigger information such as minimum bias or centrality trigger. And the VZERO separates beam-beam interactions from background events such as beam-gas interactions, at trigger level or in off-line analyses. Also the VZERO used to measure beam luminosity, charged particle multiplicity and azimuthal distributions. The absolute cross-section value of reaction processes determine the controls of the luminosity. The multiplicity of charged particle is essential for the evaluation of the centrality of hadron-hadron collisions. The azimuthal distribution of particle is important for determining the HI collision (Pb-Pb) reaction plane [26].

V0 is composed of two arrays, V0A and V0C. V0A is covering the pseudorapidity range $2.8 < \eta < 5.1$ (z = 3.4 m). And V0C is covering $-3.7 < \eta < -1.7$ (z = -0.9 m), which are given in Table 2.1. Each channel of both arrays is made of a scintillator (BC404 plastic) with a thickness of 2.5 and 2.0 cm for V0A and V0C, respectively. The time resolution is about 1 ns. Each of the V0A and V0C is segmented in 4 rings in the radial direction, and each ring is divided in eight sections in the azimuthal direction.

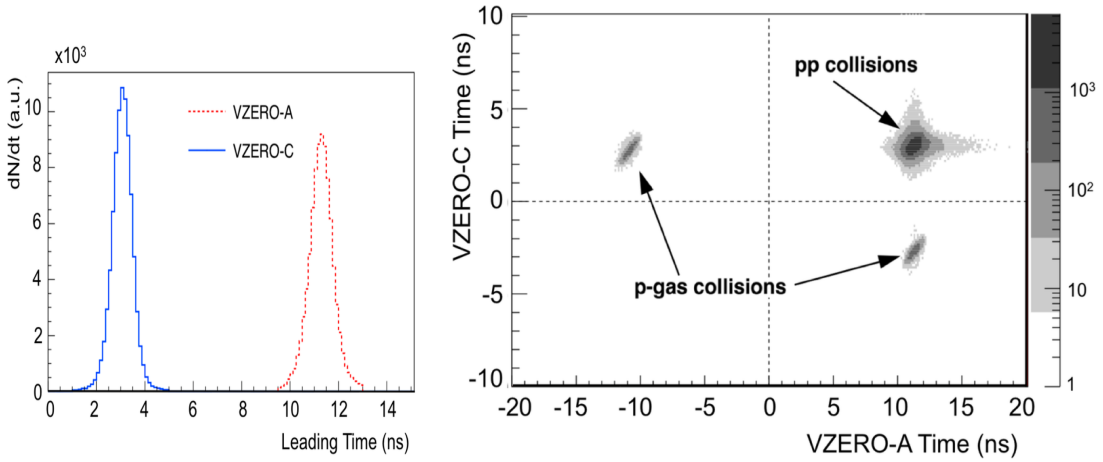

(a) V0A (red-dashed line) and V0C (blue-solid line).

(b) The dashed line intersection represents the time of the collisions at the interaction point, or the crossing time of the background tracks at the vertical plane z=0.

Figure 2.7: Weighted average time of flight of the particles detected in V0C versus V0A [43].

Table 2.1: Pseudorapidity and angular (deg.) acceptances, radius coverages (cm) and z (cm) positions along the beam axis of V0A and V0C median plane rings [26].

	V0A				V0C			
Ring	η_{max}/η_{min}	$\theta_{max}/\theta_{min}$	r_{max}/r_{min}	z	η_{max}/η_{min}	$\theta_{max}/\theta_{min}$	r_{max}/r_{min}	z
0	5.1/4.5	0.7/1.3	4.3/7.5	329	-3.7/-3.2	177.0/175.3	4.5/7.1	-86
1	4.5/3.9	1.3/2.3	7.7/13.7	329	-3.2/-2.7	175.3/172.3	7.3/11.7	-87
2	3.9/3.4	2.3/3.8	13.9/22.6	329	-2.7/-2.2	172.3/167.6	11.9/19.3	-88
3	3.4/2.8	3.8/6.9	22.8/41.2	329	-2.2/-1.7	167.6/160.0	19.5/32.0	-88

Chapter 3

Data Analysis

3.1 Event Selection

After reconstruction of raw data, ALICE experimental data are stored as two types of output data that are Event-Summary Data (ESD) and Analysis-Object Data (AOD) formats. ESD contains only high-level information that relates with ALICEs High Level Trigger (HLT) software, such as the vertex position of event, reconstructed charged particles parameters, PID. AOD formation is converted from ESD. AOD is smaller-sized objects that contains further compressed and selected information usually used for the analyses. This analysis choose AOD version 147. Monte-Carlo (MC) simulation data are created with PYTHIA 6.4 event generator including detector simulation based on Geant code (LHC10f6a saved in ALICE MonALISA).

Event selection of experimental data are applied in order to select the minimum bias trigger (kMB), event z-vertex position of $|V_z|$ <10 cm and pile up event rejection. Figure 3.1 shows the number of selected events after various event selection cuts. The minimum bias trigger is designed to select the inelastic events, such as pp collisions that has been determined by combination of V0 and SPD. V0 detector determines the events happening in different bunch crossings and the vertex detector (SPD) measures the simultaneous collisions within a bunch crossing. Pile up events rejection is designed to remove overlapping events for the different integration time of the SPD (100 ns) and the TPC (90μs). This is because

the rejected events increase with increasing multiplicity selections by pile up rejection. Multiplicity definitions are explained in section 3.2. Good quality events are selected in the following analyses.

Rec.MC Pythia (Rec.MC) events cuts are based with in the reconstructed information of PYTHIA generator including the detector simulation using Geant code. Similar event selection cuts are also applied for Rec.MC Pythia data as same as for ALICE experimental data, as shown in Figure 3.1.

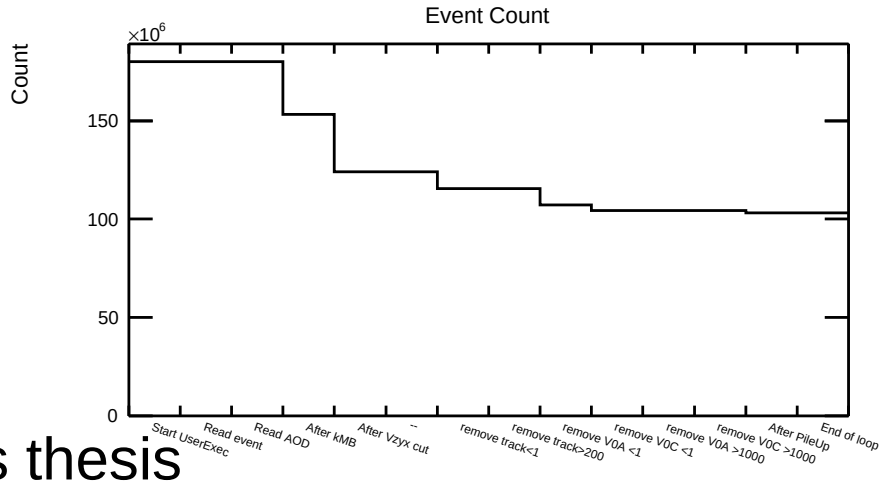

(a) ALICE experimental data, the selected events through event cuts.

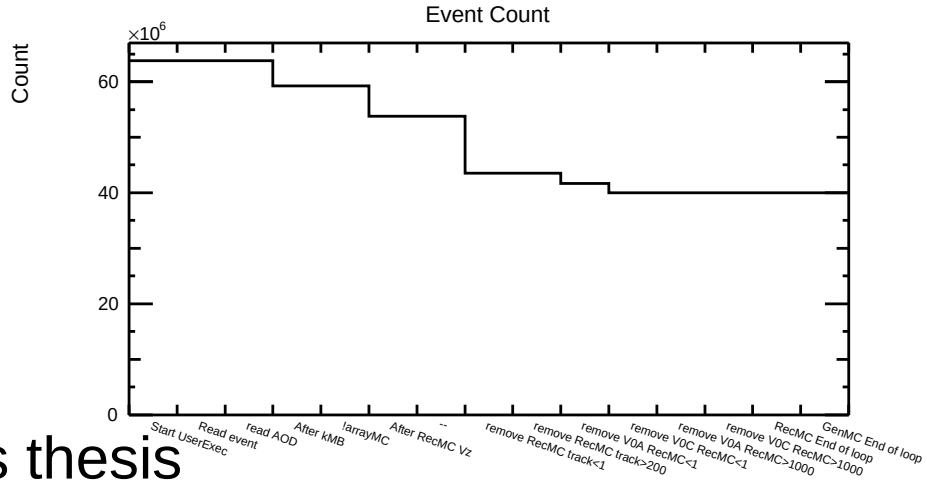

(b) PYTHIA simulation, the selected events through MC event cuts.

Figure 3.1: ALICE experimental data, Events counts.

3.2 Multiplicity Selection for event class

The 4 different event estimators are used to categorize the event class based on the charged particle multiplicity measured in TPC, V0A, V0C and V0E. The event selections are based on cuts on the total charge deposited in the V0 detector or the total number of tracks in the TPC. There are 5 multiplicity bins that are the lowest multiplicity class (about $100\% - 80\%$), the 2nd lowest multiplicity class (about $80\% - 50\%$), mid multiplicity class (about $50\% - 5\%$), the 2nd highest multiplicity class (about $5\% - 1\%$) and the highest multiplicity class (about $0\% - 1\%$).

Figure 3.2 shows various event estimators with 5 multiplicity classess. Due to the different η acceptance of different detectors, multiplicity distributions are different from each other. TPC event estimator uses the number of reconstructed tracks and measures about up to 100 tracks in $|\eta|$ <0.9 in *pp* collisions. V0A, V0C and V0E event estimators use the charged particle multiplicity in forward/backward rapidities, $2.8 < \eta <5.1$ for V0 A-side, and $-3.7 < \eta < -1.7$ for V0 C-side. V0E event estimator for hybrid event definition is the charged particle multiplicity in V0A side 2, 3 rings ($2.8 < \eta < 3.9$) and V0C side 0, 1 rings ($-3.7 < \eta < -2.7$) in order to have the symmetric η acceptance, as shown in Table 2.1.

When calculating the V0A or V0C multiplicity class, 4 rings are summed.

–V0A event estimator = total charge of V0A side of 0 ring, 1 ring, 2 ring, 3 ring.

–V0C event estimator = total charge of V0C side of 0 ring, 1 ring, 2 ring, 3 ring.

–V0E event estimator = total charge of V0A side 2, 3 ring and V0C side 0, 1 ring.

–TPC event estimator = total number of reconstructed tracks within $|\Delta\eta| < 0.9$.

3.3 Track and p_T selection

This section explains the track selection. Track cuts for AOD are bit options saved in *AliAODTrack.h*. Loose track selection is applied based on the Global hybrid track cuts ($AliAODTrack :: IsHybridGlobalConstrainedGlobal$, BIT(768)) with η cut of $|\eta|$ <0.9 and transverse momentum (p_T) cut of 0.2 - 10 GeV/c. Global tracking conditions are applied by combining the information of the different detectors, ITS, TPC, TRD and TOF.

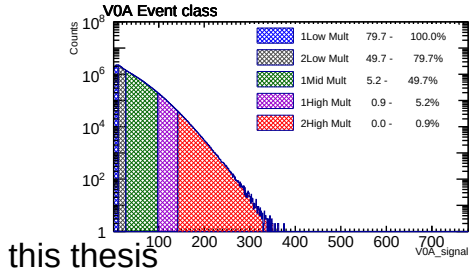

(a) ALICE experimental data, V0A event estimator.

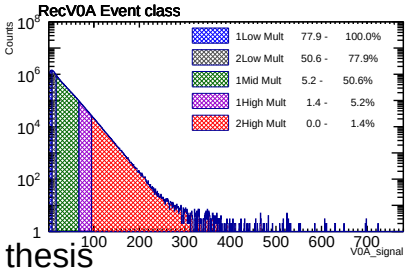

(b) Rec.MC, V0A event estimator.

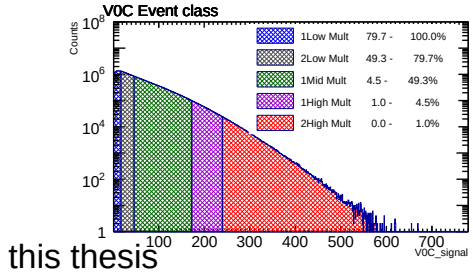

(c) ALICE experimental data, V0C event estimator.

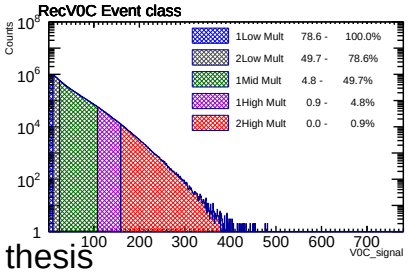

(d) Rec.MC, V0C event estimator.

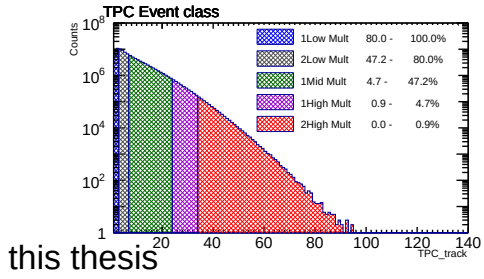

(e) ALICE experimental data, TPC event estimator.

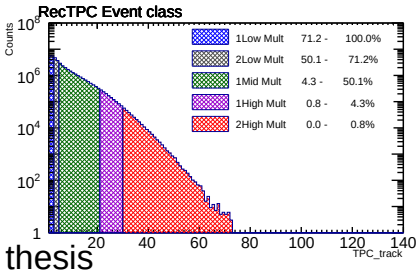

(f) Rec.MC, TPC event estimator.

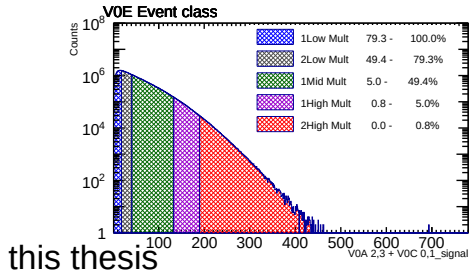

(g) ALICE experimental data, V0E event estimator.

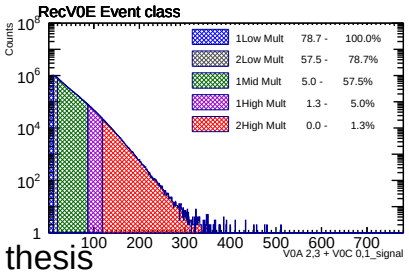

(h) Rec.MC, V0E event estimator.

Figure 3.2: The 5 multiplicity classess by various event estimators are measured by ALICE experiment.

The default track selection cuts are listed in the following:

–Minimum number of clusters in TPC is 70.

–Maximum χ^2 per cluster in TPC is 3.6 for high-p_T tracks.

–During the global tracking, reconstructed tracks in ITS and TPC are refitted.

–A distance of closest approach in z-direction to the primary vertex (DCA_z) cut is 2 cm.

–DCA_{xy} cut is 2.4 cm.

Track cuts are varied to determine the systematic uncertainty. The choices of the track cuts are based on Bit 4 and Bit 5 with respect to the hybrid track. Bit 4 track cut is $AliAODTrack :: kTrkGlobalNoDCA$. And Bit 5 track cut is $AliAODTrack :: kTrkGlobal$. Bit 4 and Bit 5 include more tight selections as a central quality assurance (QA) requiring hits on ITS by extrapolating the reconstructed tracks in TPC. Therefore, Bit 4 and Bit 5 have several missing track acceptance regions in $\varphi - \eta$ plane for the loss of efficiency caused by bad channels of ITS. In order to avoid the contamination of secondary particle, default track is applied based on Bit 5. p_T distributions of ALICE experimental data for the 5 multiplicity classes by various event estimators are shown in Figure 3.3(a), Figure 3.3(d), Figure 3.3(g) and Figure 3.3(j). p_T distributions of Pythia for the 5 multiplicity classes by various event estimators are shown in Figure 3.3(b), Figure 3.3(e), Figure 3.3(h) and Figure 3.3(k). The ratios of one of ALICE experimental data over Pythia are shown in Figure 3.3(c), Figure 3.3(f), Figure 3.3(i) and Figure 3.3(l). There are some weak multiplicity dependences in all the estimators. TPC event estimator shows some multiplicity dependence, which could be due to the self-correlation bias (high multiplicity selection should bias towards the hard events with jet production) from the multiplicity selection.

3.4 Tracking and Efficiency corrections

Efficiency of the reconstructed tracks in TPC is calculated as a function of p_T. There is no significant multiplicity dependence but TPC event estimator shows some multiplicity dependence, which could be due to the self-correlation bias from the multiplicity selection. The inverse of reconstruction efficiency is applied as efficiency correction for each associated particle. The tracking efficiency in TPC is about 0.8.

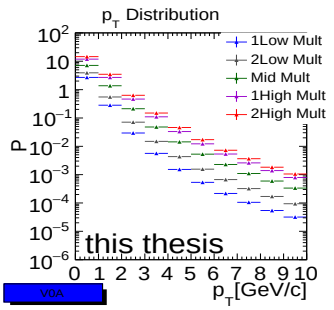

(a) ALICE experimental data, V0A event estimator.

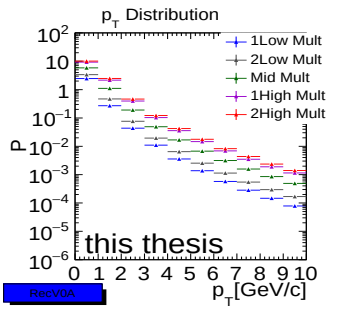

(b) Rec.MC, V0A event estimator.

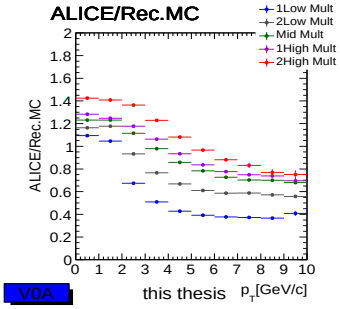

(c) V0A event estimator, Ratio of ALICE experimental data over Rec.MC.

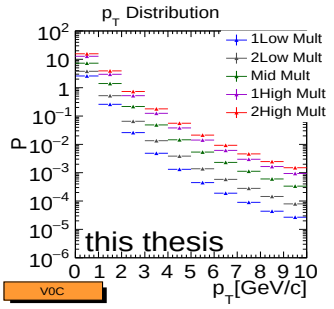

(d) ALICE experimental data, V0C event estimator.

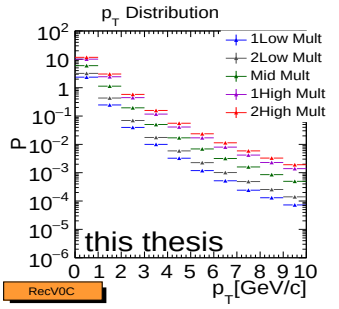

(e) Rec.MC, V0C event estimator.

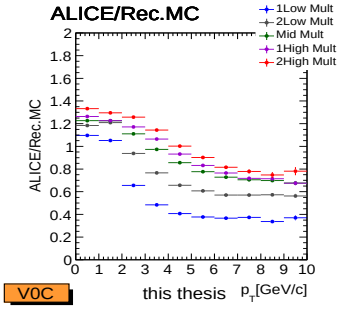

(f) V0C event estimator, Ratio of ALICE experimental data over Rec.MC.

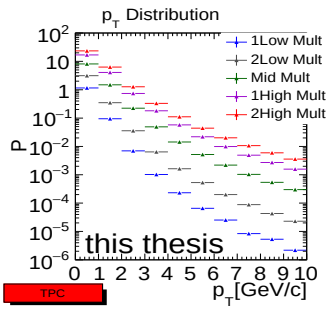

(g) ALICE experimental data, TPC event estimator.

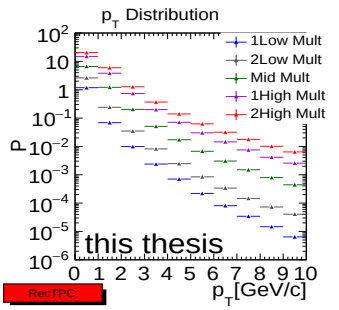

(h) Rec.MC, TPC event estimator.

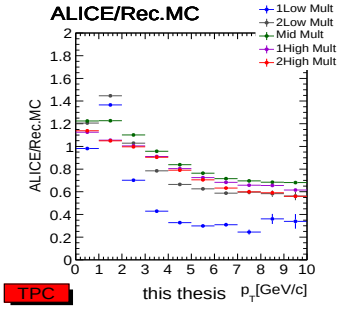

(i) TPC event estimator, Ratio of ALICE experimental data over Rec.MC.

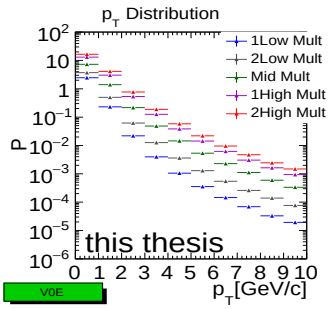

(j) ALICE experimental data, V0E event estimator.

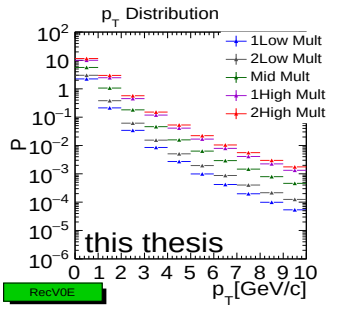

(k) Rec.MC, V0E event estimator.

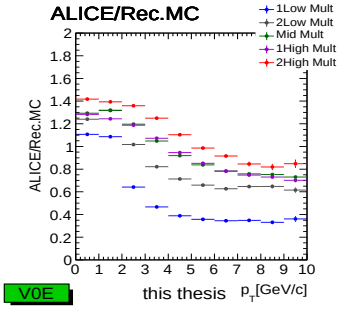

(l) V0E event estimator, Ratio of ALICE experimental data over Rec.MC.

Figure 3.3: p_T distributions by various event estimators are shown for the 5 multiplicity classes.

$$\epsilon_{TPC} = \frac{Number\ of\ reconstructed\ tracks\ in\ MC}{Number\ of\ generated\ tracks\ in\ MC} \tag{3.1}$$

The efficiency of V0 detector could become larger than 1 because this can include more secondary background as V0 detector measures the total number of charged particles traversing the scintillation detector cell. V0 efficiency depends on various event estimators. In case of V0A event estimator, V0A rings efficiency shows strong multiplicity dependence. On the other hand, there is no significant multiplicity dependence in V0C rings. In case of V0C event estimator, V0C rings efficiency shows strong multiplicity dependence. On the other hand, there is no significant multiplicity dependence in V0A rings. In case of TPC event estimator, V0 efficiency shows weak multiplicity dependence and the efficiency of V0C rings, which were closer to TPC in η acceptance, are higher than the dependence of V0A ring efficiency. And the efficiency of V0C 0_{th} ring, which are located behind the T-zero (T0) detector in ALICE experimental setup, shows higher value in all of event estimators. Efficiency is much larger than unity, which would mean there are more secondary particles in V0. Figure 3.5 presents the efficiency used in this analysis. V0C 0_{th} and 1_{st} rings, V0A 2_{nd} and 3_{rd} rings are combined to ensure the symmetry of η range for a determination of the event estimator. V0E efficiency also shows some multiplicity dependences of event estimators both V0A and V0C.

$$\epsilon_{V0} = \frac{Mean\ hit\ in\ reconstructed\ MC}{Mean\ hit\ in\ generated\ MC} \tag{3.2}$$

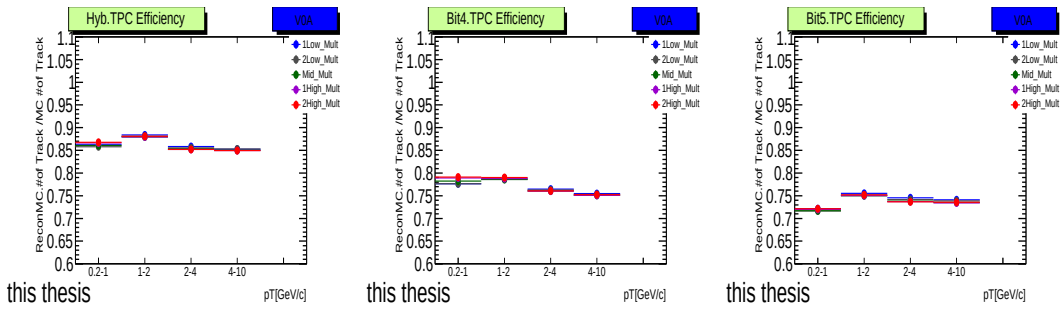

(a) Hyb., V0A event estimator. (b) Bit 4, V0A event estimator. (c) Bit 5, V0A event estimator.

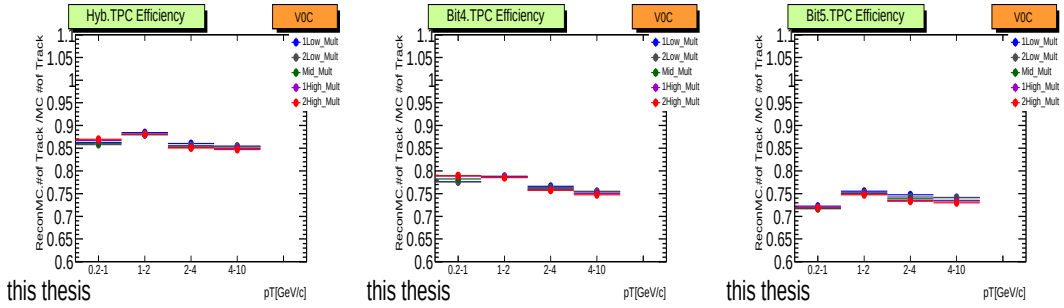

(d) Hyb., V0C event estimator. (e) Bit 4, V0C event estimator. (f) Bit 5, V0C event estimator.

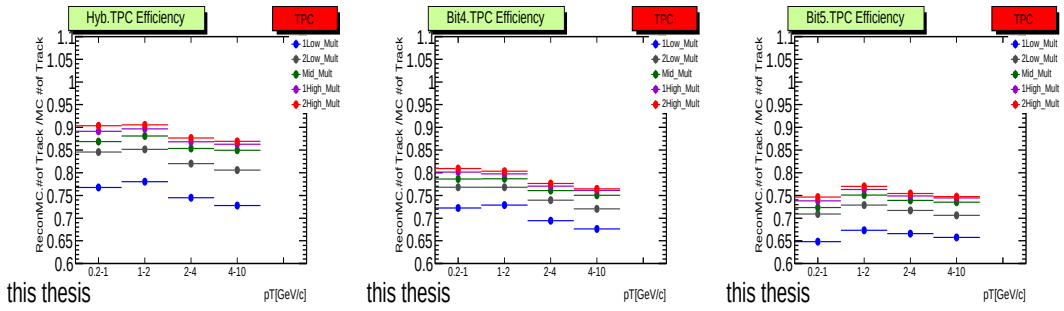

(g) Hyb., TPC event estimator. (h) Bit 4, TPC event estimator. (i) Bit 5, TPC event estimator.

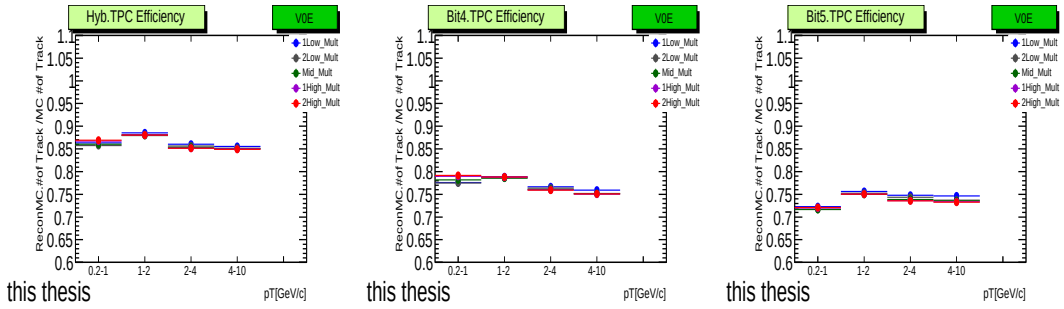

(j) Hyb., V0E event estimator. (k) Bit 4, V0E event estimator. (l) Bit 5, V0E event estimator.

Figure 3.4: TPC tracking efficiency of different 3 track cuts by various event estimators are shown for the 5 multiplicity classes.

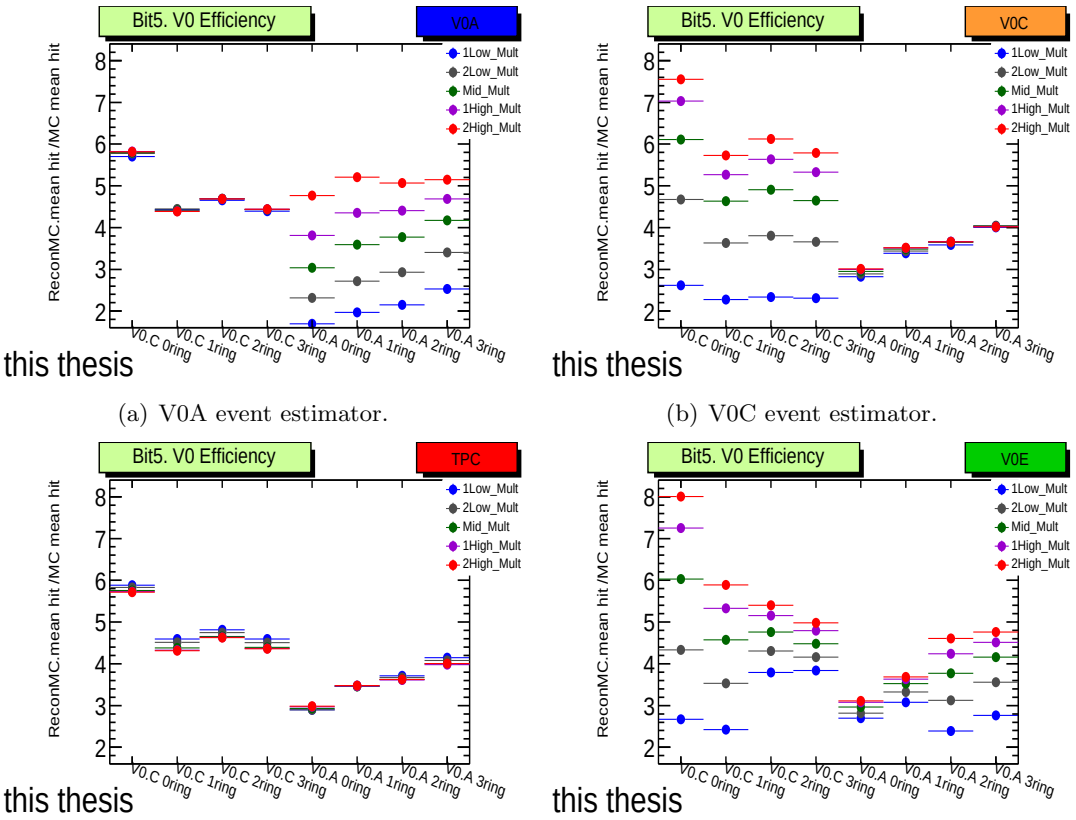

(a) V0A event estimator.

(b) V0C event estimator.

(c) TPC event estimator.

(d) V0E event estimator.

Figure 3.5: V0 efficiency by various event estimators are shown for the 5 multiplicity classes.

3.5 Definition and determination of p_T bin (window) for the analysis

In order to p_T selection, four p_T bins are defined as 0.2-1, 1-2, 2-4, 4-10 GeV/c with three multiplicities, 100-50%, 50-5% and 5%. Figure 3.6(a) show p_T dependence of 1-D renormalized correlation functions (see in section 3.6.3 about renormalized correlation functions), which are $C(\Delta\varphi)$ in $1.5 \leq |\Delta\eta| < 1.8$ and trigger particles are $2 \leq p_{T,Trig} < 4$ GeV/c. Intermediate p_T, which are $1 \leq p_{T,Assoc} < 4$ GeV/c, show the enhanced ridge structure in $\Delta\varphi \approx 0$. On the other hand, low p_T and high p_T, which are $0.2 \leq p_{T,Assoc} < 1$ GeV/c and $4 \leq p_{T,Assoc} < 10$ GeV/c, do not show a significant ridge structure. p_T dependence of $p2$ parameters (v_2^2) are shown in Figure A.5. $p2$ parameters are enhanced in $1 \leq p_T < 4$ GeV/c. MC Pythia (Rec.MC) do not reproduce the ridge structures, in Figure 3.6(b). To study the ridge structures, the optimum p_T range is selected in order to focus on the biggest signal around the middle p_T region ($1 \leq p_T < 4$ GeV/c) at around $\Delta\varphi \approx 0$ and in $1.5 \leq |\Delta\eta| < 1.8$ of two-particle correlation.

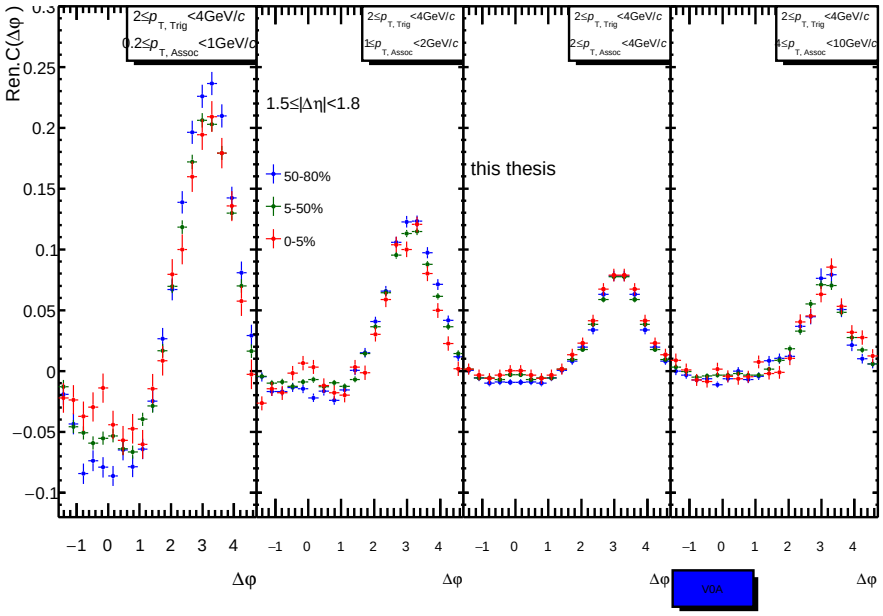

(a) ALICE experimental data, V0A event estimator.

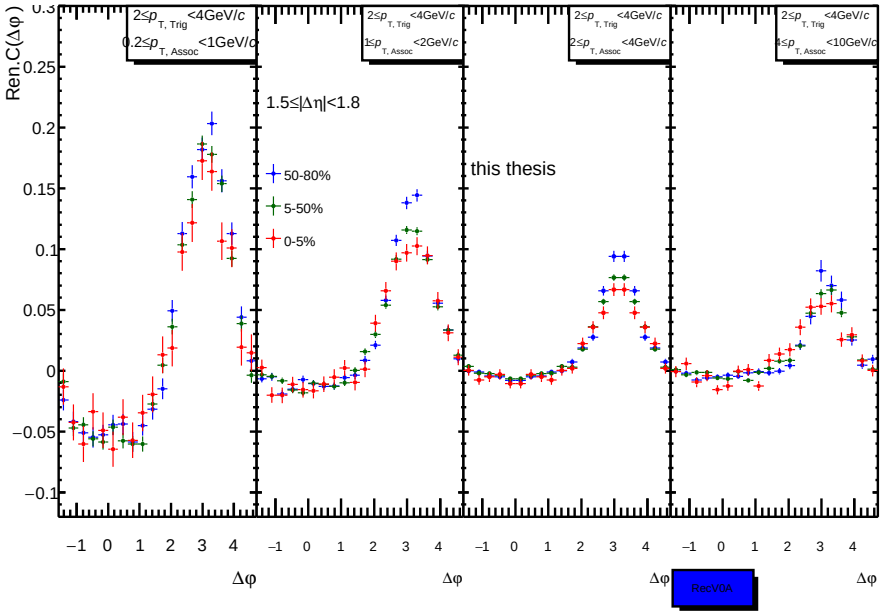

(b) Rec.MC, V0A event estimator.

Figure 3.6: 1-D renormalized correlation functions shown for $p_{T,Assoc}$ dependence in $1.5 \leq \Delta\eta < 1.8$ are shown for the 3 multiplicity classes.

Figure 3.7 shows 2-D single φ and η distributions for different multiplicity classes with different event estimators. The different panels in vertical direction correspond to event estimators and the same in horizontal direction corresponds to the multiplicity dependence. The distributions show jet-veto like effect at small multiplicity. That is because this enhances jets (or particle multiplicity) in a different (or far away) η region from various event estimators in case of the lowest and 2nd lowest multiplicity selections. One the other hand, there are more jets (or particle multiplicity) close to (or within) the η acceptance of various event estimators in case of the highest and 2nd highest multiplicity selections. Therefore, φ and η distributions are all different for the 5 multiplicity classes and various event estimators that is mostly given by the jet and multiplicity bias from the different η regions. In order to study the multiplicity dependence, the presented analyses in the following are performed with V0E because of the symmetric η acceptance. However all the other estimators are also used to study the systematic dependence of the results. The most of the features described above are rather well reproduced in MC calculation with PYTHIA as shown in Figure 3.8.

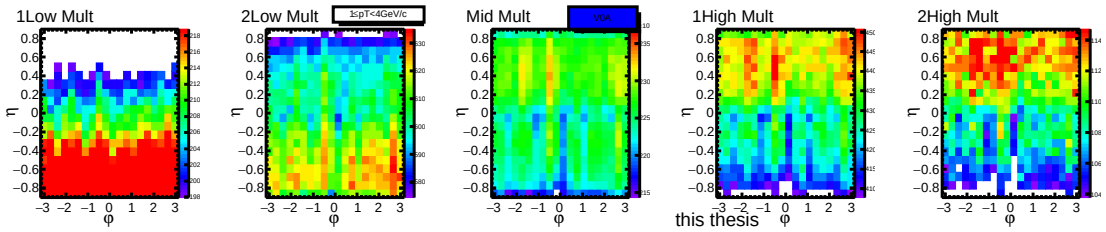

(a) ALICE experimental data, V0A event estimator, φ and η distributions for the 5 multiplicity classes.

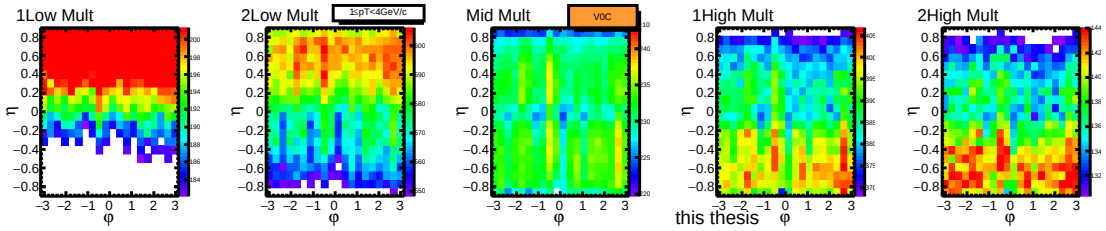

(b) ALICE experimental data, V0C event estimator, φ and η distributions for the 5 multiplicity classes.

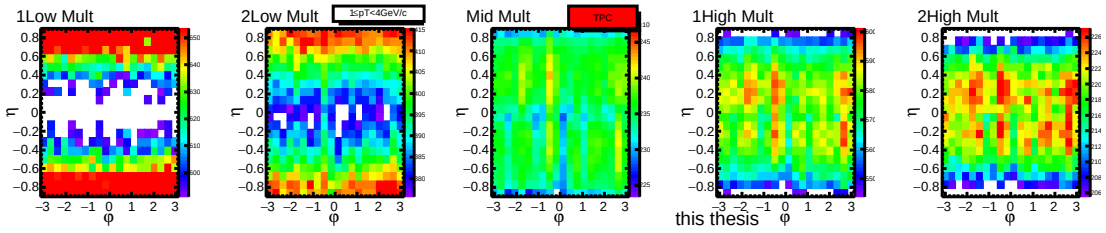

(c) ALICE experimental data, TPC event estimator, φ and η distributions for the 5 multiplicity classes.

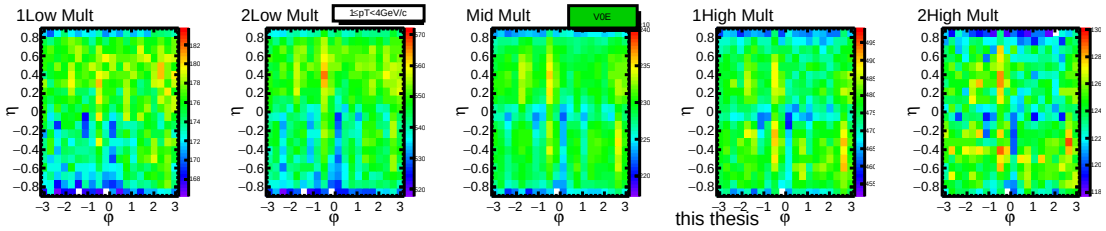

(d) ALICE experimental data, V0E event estimator, φ and η distributions for the 5 multiplicity classes.

Figure 3.7: ALICE experimental data, φ and η distributions by various event estimators for $1 \leq p_T < 4$ GeV/c are shown for the 5 multiplicity classes.

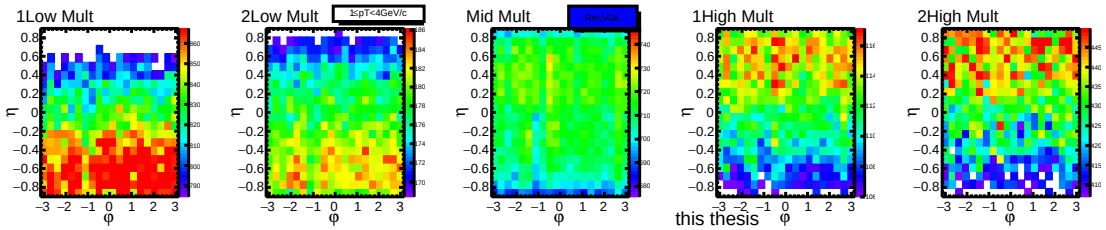

(a) Rec.MC, V0A event estimator, φ and η distributions for the 5 multiplicity classes.

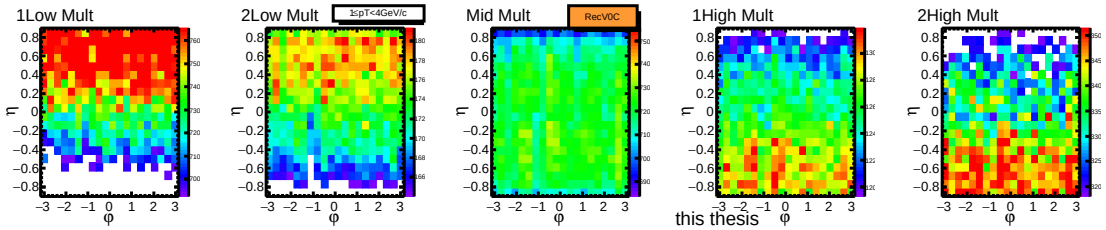

(b) Rec.MC, V0C event estimator, φ and η distributions for the 5 multiplicity classes.

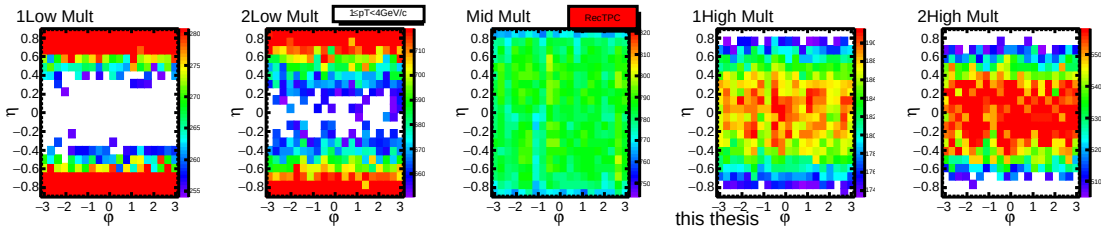

(c) Rec.MC, TPC event estimator, φ and η distributions for the 5 multiplicity classes.

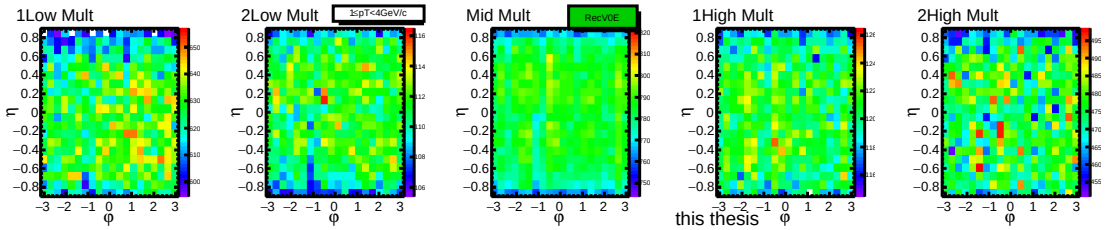

(d) Rec.MC, V0E event estimator, φ and η distributions for the 5 multiplicity classes.

Figure 3.8: Rec.MC, φ and η distributions by various event estimators for $1 \leq p_T < 4$ GeV/c are shown for the 5 multiplicity classes.

3.6 Two-particle correlation measurement

To study the jet shapes, two-particle correlation method is utilized. This section presents the definition of two-particle correlation function ($C(\Delta\varphi, \Delta\eta)$) in section 3.6.1, renormalized correlation function ($Ren.C((\Delta\varphi, \Delta\eta))$ in section 3.6.3, the 2-D flat background subtraction from associated particle yields per trigger ($Yield(\Delta\varphi, \Delta\eta)$) in section 3.6.4 a subtraction of low multiplicity from the high multiplicity associated particle yields per trigger in sec-

tion 3.6.5, trigger η dependence of correlation function ($Trig.EtaC(\Delta\varphi, \Delta\eta)$) in section 3.6.6 and ratio of correlation function ($C(\Delta\varphi)$) over the fitted function ($F(\Delta\varphi)$) in section 3.6.7.

3.6.1 Definition of correlation function

For a given event multiplicity class, the two-particle correlation between pairs of trigger and associated charged particles is measured as a function of relative azimuthal angle ($\Delta\varphi = \varphi^{Assoc} - \varphi^{Trig}$ defined within $-\pi/2 \sim 3\pi/2$) and relative pseudorapidity ($\Delta\eta = \eta^{Assoc} - \eta^{Trig}$). The same event pairs (signal pairs $S(\Delta\varphi, \Delta\eta)$) is evaluated within an event for a set of given p_T bins of trigger and associate particles. A mixed pairs (mixed background, $B(\Delta\varphi, \Delta\eta)$) is evaluated from 10 different events within the same z-vertex and multiplicity bin using the same p_T bin definition as the "same event pairs". Therefore, the mixing event pairs have no physics correlation with a same acceptance unlike same event pairs.

The correlations are expressed in terms of ratio of same event pairs over mixed pairs ($C(\Delta\varphi)$) and the associated yield per trigger particle ($Yield(\Delta\varphi, \Delta\eta)$) for a given transverse momentum bins of trigger (p_T^{Trig}) and associate (p_T^{Associ}) and for a given event multiplicity bin, as shown in Figure 3.9. In the signal, each associated particle is weighted with an inverse of efficiency that accounts for correcting the reconstruction efficiency and secondary particles. The detector acceptance is corrected by the event mixing. The tracking efficiency in the TPC and the total multiplicity reconstruction efficiency of the V0 detector are estimated with PYTHIA Monte-Carlo generator including detector simulation with Geant as described earlier. Signal pairs distribution is defined as

$$S(\Delta\varphi, \Delta\eta) = \sum_{i=0}^{9}\sum_{j=0}^{9} \frac{d^2N_{same}}{d\Delta\varphi_{ij}d\Delta\eta_{ij}} \tag{3.3}$$

where i runs over the number of V_z bins (10), j runs over the number of η bins (10).

$$B(\Delta\varphi, \Delta\eta) = \sum_{i=0}^{9}\sum_{j=0}^{9} \frac{d^2N_{mix}}{d\Delta\varphi_{ij}d\Delta\eta_{ij}} \tag{3.4}$$

A mixed background is evaluated in the same way as in the case of signal pairs distribution from the real/true event, where trigger and associated tracks stem from different events

for the mixed event. The correlation function $C(\Delta\varphi, \Delta\eta)$ and associate particle yield per trigger particle $Yield(\Delta\varphi, \Delta\eta)$ are defined as

$$C(\Delta\varphi, \Delta\eta) = \frac{N_{mix}}{N_{same}} \frac{S(\Delta\varphi, \Delta\eta)}{B(\Delta\varphi, \Delta\eta)} \tag{3.5}$$

$$Yield(\Delta\varphi, \Delta\eta) = \frac{N_{same}}{N_{trig}} C(\Delta\varphi, \Delta\eta) \frac{1}{efficiency} \tag{3.6}$$

where N_{same} is the total (integrated) number of particle pairs in the same events class, N_{mix} is the total (integrated) number of combinatorial mixed event pairs in the events class for trigger and associate particle p_T intervals. N_{trig} is the total number of trigger particles in the events class and p_T^{trig} interval.

The functions are defined with statistic errors, $S \pm \sqrt{S}$ where S is number of counts of same

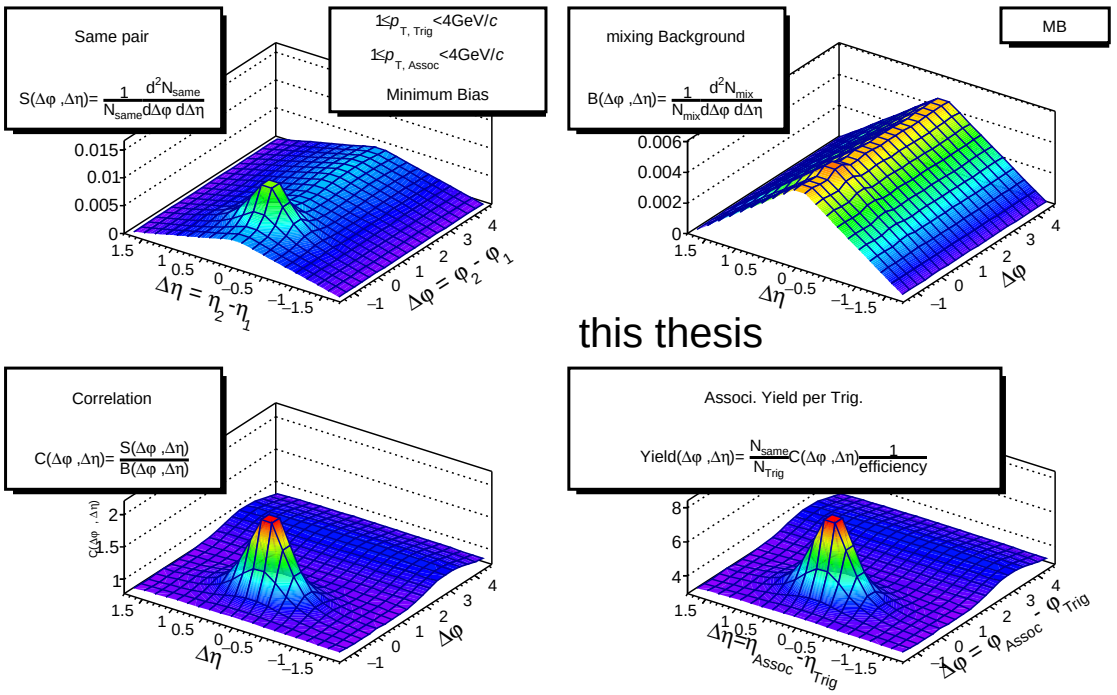

Figure 3.9: Correlation Function definition, example of MB (No event estimator).

event pairs and $\sqrt{S}$ become a statistic error and the same for the mixed pair as $B \pm \sqrt{B}$. TPC-TPC correlation function with statistic error is then defined;
$C(\Delta\varphi, \Delta\eta) \pm dC(\Delta\varphi, \Delta\eta) = C(\Delta\varphi, \Delta\eta) \pm C(\Delta\varphi, \Delta\eta)\sqrt{(\frac{dS(\Delta\varphi,\Delta\eta)}{S(\Delta\varphi,\Delta\eta)})^2 + (\frac{dB(\Delta\varphi,\Delta\eta)}{B(\Delta\varphi,\Delta\eta)})^2}$.
The same pair of V0-TPC correlation are defined as $S_W \pm < w > \sqrt{S} = S_W \pm \sqrt{S_W < w >}$ where S is the number of entries of the bin, S_W is the summation of weighting values of

the bin, $< w >= \frac{S_W}{S} = \frac{s_{sum}}{s_{entries}}$ is the average weighting value per V0 sector, s_{sum} is total integral of S_W and $s_{entries}$ is the total number of entries of S_W.

3.6.2 Long range $\Delta\eta$, TPC-V0 correlation

Charged particles in V0 detectors and in TPC are used to construct long range correlation function (V0-TPC correlations). Long range correlations are shown in the associated particles side in $|\eta| < 0.9$ of TPC from V0 (about $1.8< |\eta| <4.8$). For each combination for V0-TPC correlations between 8 V0 rings and TPC, $\Delta\eta$ axis are transferred:

$\Delta\eta$ of V0C 0_{th} -TPC = -3.7-0.9 to -3.2+0.9

$\Delta\eta$ of V0C 1_{st} -TPC = -3.2-0.9 to -2.7+0.9

$\Delta\eta$ of V0C 2_{nd} -TPC = -2.7-0.9 to -2.2+0.9

$\Delta\eta$ of V0C 3_{rd} -TPC = -2.2-0.9 to -1.7+0.9

$\Delta\eta$ of V0A 0_{th} -TPC = 4.5-0.9 to 5.1+0.9

$\Delta\eta$ of V0A 1_{st} -TPC = 3.9-0.9 to 4.5+0.9

$\Delta\eta$ of V0A 2_{nd} -TPC = 3.4-0.9 to 3.9+0.9

$\Delta\eta$ of V0A 3_{rd} -TPC = 2.8-0.9 to 3.4+0.9

For example, V0C 0, 1 rings and TPC correlations are shown within the $\Delta\eta$ range of $-4.6 < \Delta\eta < -1.8$ and V0A 2, 3 rings and TPC correlations are shown within the range of $1.9 < \Delta\eta < 4.8$.

3.6.3 Correlation shape measurement by renormalization

In order to visualize and to observe how the shapes of the correlation functions $C(\Delta\varphi, \Delta\eta)$ change from the lowest to the highest multiplicity events classes, the correlation functions $C(\Delta\varphi, \Delta\eta)$ are renormalized between 0 and 1 ($Ren.C(\Delta\varphi, \Delta\eta)$). This process first subtracts the base line around minimum of correlation function, and then expand the correlation scale such that the near-side peak at $(\Delta\varphi, \Delta\eta) = (0, 0)$ to be unity. The re-normalization factor is defined by the difference between average minimum of 4 minimum areas (red area, avg.ZYAM) around $1.0 < |\Delta\eta| < 1.5$, $1.0 < |\Delta\varphi| < 1.5$ and the near-side maximum (blue area) as shown in Figure 3.10(a). The correlation functions $C(\Delta\varphi, \Delta\eta)$ are rescaled between 0 and 1 by the re-normalization factor from the left panel (before the re-nomalization,

original correlation function $C(\Delta\varphi, \Delta\eta)$) to the right panel (after the re-normalization, renormalized correlation function $Ren.C(\Delta\varphi, \Delta\eta)$), as shown in Figure 3.10(b). And those renormalized correlation functions $Ren.C(\Delta\varphi, \Delta\eta)$ are projected to $\Delta\varphi$ and $\Delta\eta$ for a given $\Delta\eta$ and $\Delta\varphi$ slice.

The average minimum value defined by these 4 regions will also be used later for a flat subtraction of background in section 3.6.4.

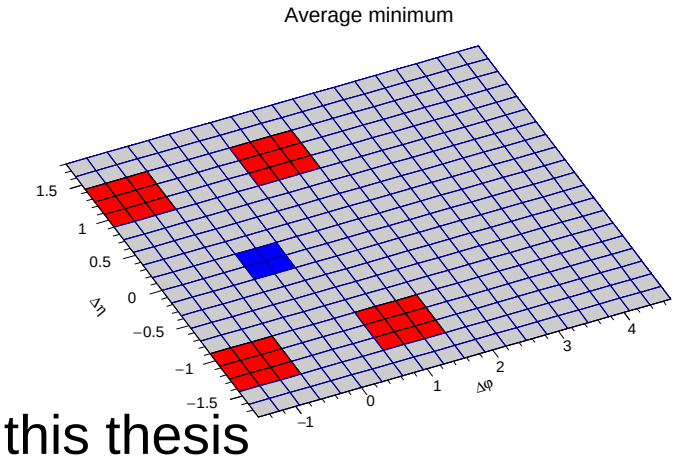

(a) The minimum area(Red) and the maximum area(Blue).

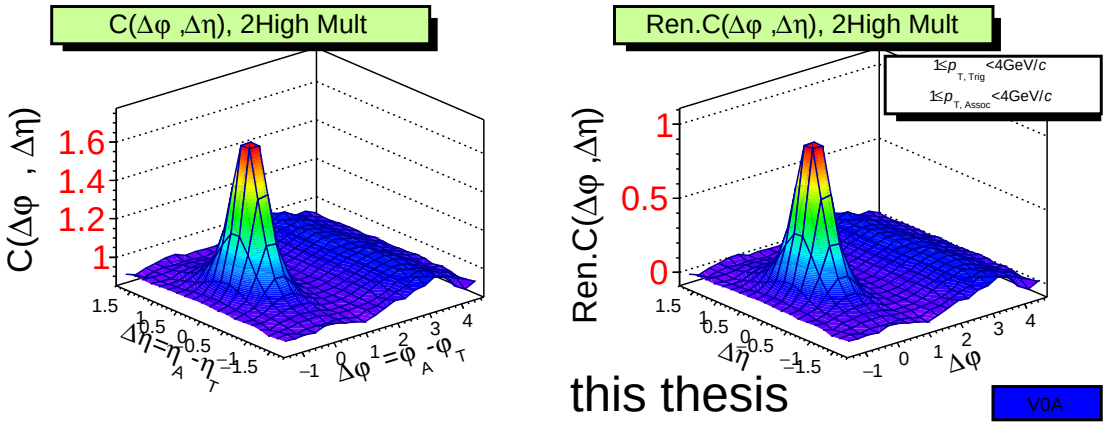

(b) Correlation function and renormalized correlation function by renormalizing factor.

Figure 3.10: 2-D Correlation function and renormalized correlation function.

$$F_{\text{renormalization-factor}} = Max - < Min > \tag{3.7}$$

$$Ren.C(\Delta\varphi, \Delta\eta) = \frac{C(\Delta\varphi, \Delta\eta) - < Min >}{F_{\text{renormalization-factor}}} \tag{3.8}$$

3.6.4 Associate yield per trigger particle normalization with flat background subtraction

The flat backgrounds ($Sub.Y(\Delta\varphi, \Delta\eta)$) are determined according to Figure 3.10(a). Then, the associate particles yield in the near side jets and away side jets regions are integrated in $-0.8 < \Delta\varphi < 0.8$ and $2.3 < \Delta\varphi < 3.9$ (or $\pi - 0.8 < \Delta\varphi < \pi + 0.8$) for a given $\Delta\eta$ slice after subtracting the defined background level in order to quantify the distributions.

3.6.5 Extraction of double ridges by subtraction of low multiplicity yield from high multiplicity yield

This analyses utilize the subtraction of particles yield per trigger between high and low multiplicity selections. This method is a similar process as described in an earlier ALICE publication on pPb correlation analysis [27].

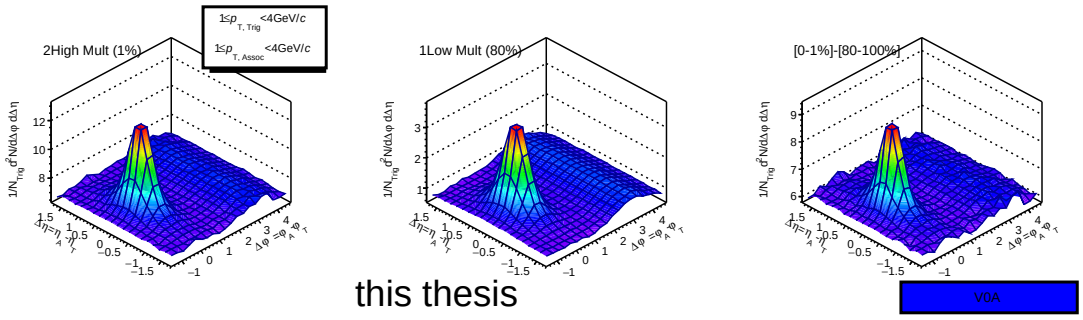

Figure 3.11: Example of subtraction of correlation between events with lower multiplicity from higher multiplicity ($[0\% - 1\%] - [80\% - 100\%]$).

3.6.6 Forward/Backward asymmetry in $\Delta\eta$ correlation with trigger eta selection

In this process, the $C(\Delta\varphi, \Delta\eta)$ are measured by η selecting trigger particle directions. The trigger particles are divided into 10 η bins from -0.9 to 0.9, that are -0.9< η_{trig} ≤-0.72, -0.72< η_{trig} ≤-0.54, -0.54< η_{trig} ≤-0.36, -0.36< η_{trig} ≤-0.18, -0.18< η_{trig} ≤0, 0< η_{trig} ≤0.18, 0.18< η_{trig} ≤0.36, 0.36< η_{trig} ≤0.54, 0.54< η_{trig} ≤0.72, 0.72< η_{trig} <0.9. The correlation functions $C(\Delta\varphi, \Delta\eta)$ defined in the previous section 3.6.1 are an average shape over the different η triggered correlation functions $C(\Delta\varphi, \Delta\eta)$. η triggered $Trig.EtaC(\Delta\varphi, \Delta\eta)$ might be expected to show some dependences as a function of trigger eta, in case of any jet

interaction or correlation with longitudinal distribution (or density profile) or longitudinal expansion of high temperature and/or density matter created in heavy-ion collisions as well as in high multiplicity pp collisions.

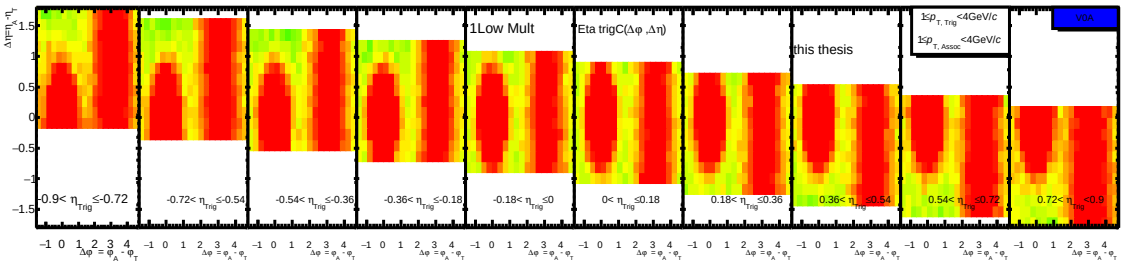

Figure 3.12: Example of 2-D η trigger $C(\Delta\varphi, \Delta\eta)$, the lowest multiplicity.

3.6.7 Systematic measurement of correlation shape by fitting with the average or the lowest multiplicity correlation shape

In order to investigate how the shapes of correlation functions $C(\Delta\varphi)$ change with the multiplicity selection in large $\Delta\eta$, $C(\Delta\varphi)$ are fitted with a newly defined fitting function $F(\Delta\varphi)$ which will be described later in this section. Then, the result $R(\Delta\varphi)$ are presented as the ratio of $C(\Delta\varphi)$ over $F(\Delta\varphi)$ as in Eq. 3.10. For this analyses, $F(\Delta\varphi)$ are defined by the data points of scaled $C(\Delta\varphi)_{1Low}$. The choice of event estimator is found to be not sensitive to the result of $R(\Delta\varphi)$. This method to extract the ratio $R(\Delta\varphi)$ is useful for studying any small changes of $C(\Delta\varphi)$ even if the change is very small. The Fourier 2nd coefficients can be extracted from $R(\Delta\varphi)$, which is called p2 $(=v_2^2)$ in this analysis, shown in Figure 3.14. However, $R(\Delta\varphi)$ would have bigger statistic errors than $C(\Delta\varphi)$ because of the addtional statistical errors from the newly defined functions $F(\Delta\varphi)$, which are basically defined by the reference correlation data points that should also include statistical errors.

For V0-TPC correlation functions, in order to see the $\Delta\eta$ dependence $F(\Delta\varphi)$ of V0-TPC correlation functions are separated in three $\Delta\eta$ regions, near, middle and away from V0C as shown in Figure 3.13.

$$F(\Delta\varphi) = a + bf(\Delta\varphi) \tag{3.9}$$

$$R(\Delta\varphi) = \frac{C(\Delta\varphi)}{F(\Delta\varphi)} \tag{3.10}$$

$f(\Delta\varphi)_{thelowest}$: Re-normalized correlation function $C(\Delta\varphi, \Delta\eta)$ of the lowest multiplicity class.

a,b : free parameter for baseline (a) and amplitude (b).

$C(\Delta\varphi)$: Correlation functions for 5 different multiplicity selections, the lowest, the 2nd lowest, Mid, the 2nd highest and the highest multiplicities.

After getting p_2 of V0A-TPC, V0C-TPC and V0-V0 correlation, the p_2^{long} parameter

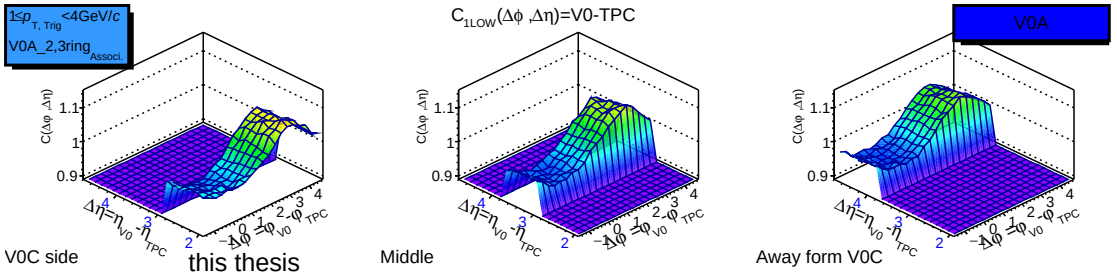

(a) V0A-TPC correlation function of the lowest multiplicity in close to V0C, middle and away from V0C.

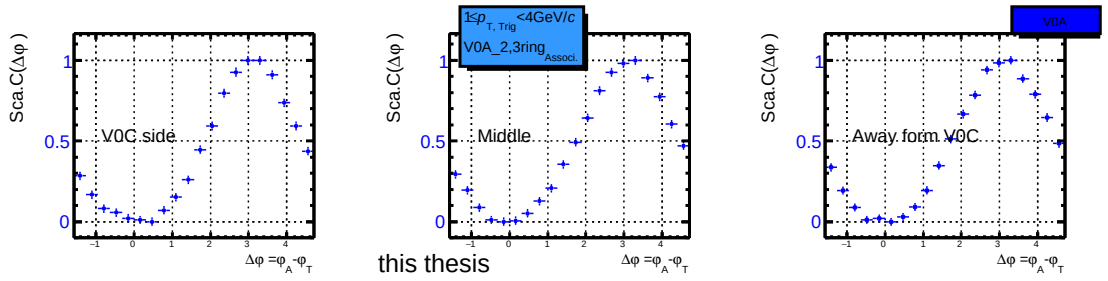

(b) Rescaled V0A-TPC correlation function of the lowest multiplicity ($f(\Delta\varphi)$)

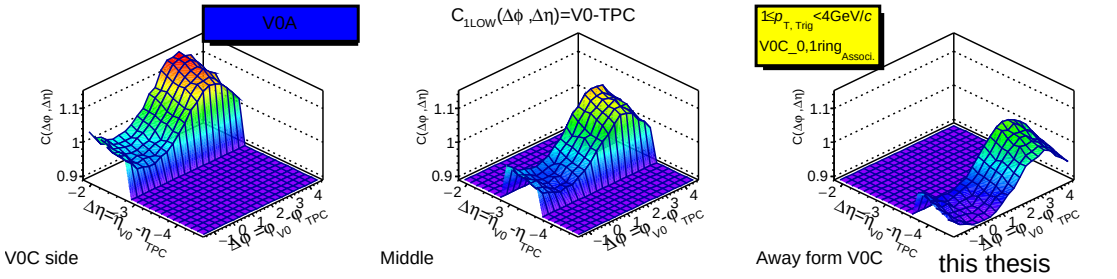

(c) V0C-TPC correlation function of the lowest multiplicity in close to V0C, middle and away from V0C.

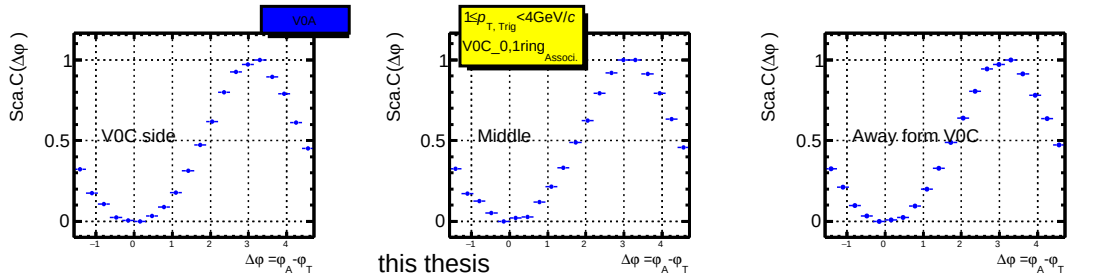

(d) Rescaled V0C-TPC correlation function of the lowest multiplicity ($f(\Delta\varphi)$)

Figure 3.13: $f(\Delta\varphi)$ with respect to the lowest multiplicity.

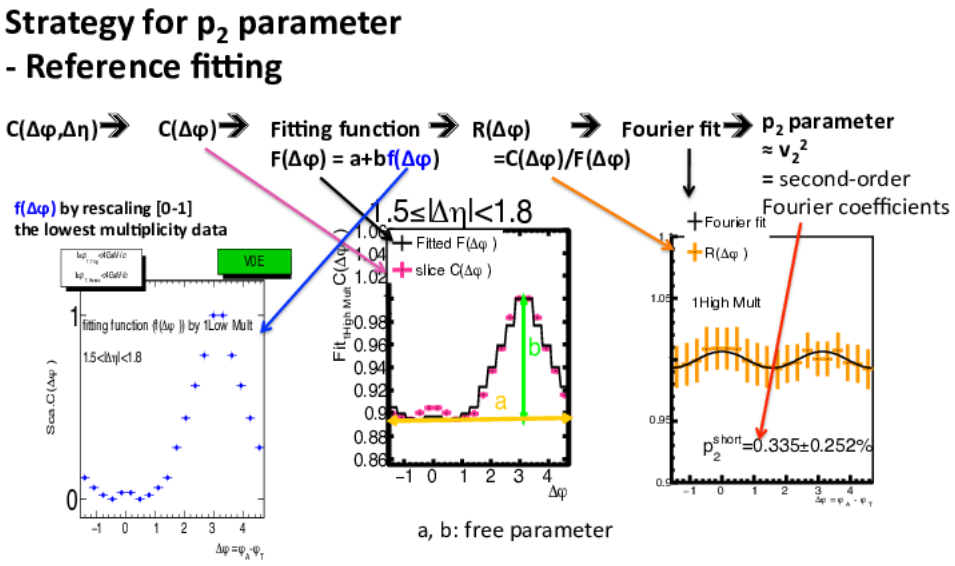

Figure 3.14: Strategy for p_2 parameter.

(v_2^2) in TPC, which contamination and/or background in V0A, V0C are canceled in the Equetion 3.11, shown in Figure 3.15. Equetion 3.11 shows how to extract v_2^2 in TPC with long range correlation.

$$p_2^{long} = \frac{p_{TA} \times p_{TC}}{p_{AC}} \tag{3.11}$$

where p_{TA} is p_2 of V0A-TPC correlation, p_{TC} is p_2 of V0C-TPC correlation and p_{AC} is p_2 of V0-V0 correlation. The $p2^{long}$ correspond to p_2 (v_2^2) based on TPC long range $\Delta\eta$ correlation measurements. $p2^{long}$ shown in Figure 4.32 and $p2^{short}$ shown in Figure 4.17.

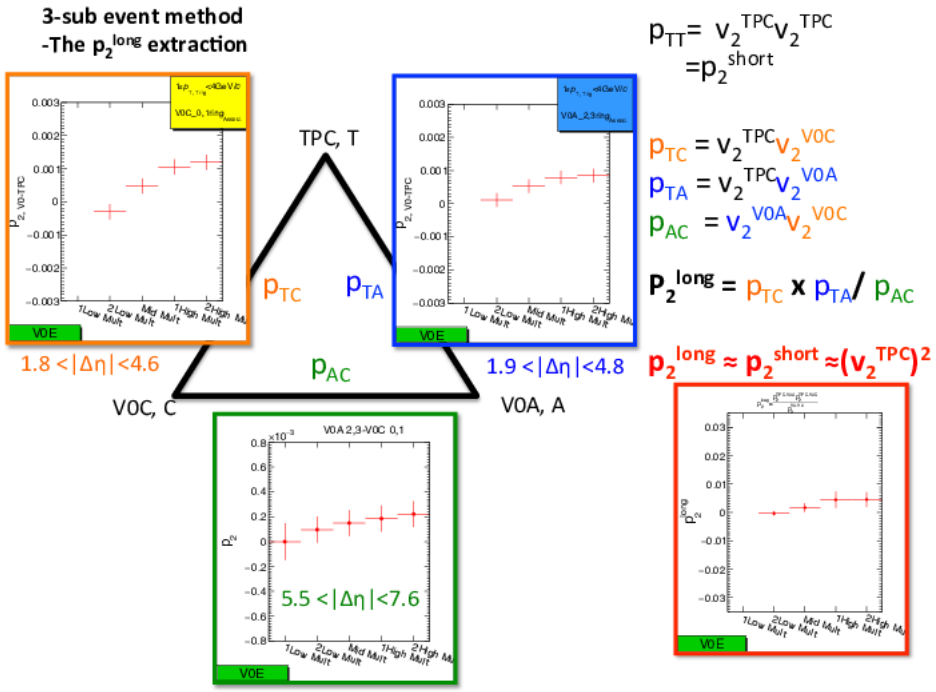

Figure 3.15: p_2^{long} extraction in long range $\Delta\eta$.

3.7 Systematic uncertainties

The analyses are done with three different sets of the track cuts as described in section 3.3. That are Hybrid track cuts (Bit 768, Hyb), Bit 4 and Bit 5, which are the ALICE official track filter. Due to the tight hit-track association matching requirement ITS and TPC, the acceptance with Bit 4 and Bit 5 shows the dead area of ITS, shown in Figure 3.16 and Figure 3.17. And hybrid track show flat single η distributions and φ distributions. The acceptance within Monte-Carlo simulation is found to be similar to the experimental acceptance, as shown in Figure 3.18 and Figure 3.19. Hybrid track has the secondary particle issue, which are reconstructed at the similar η directions. Therefore, Bit 4 and Bit 5 are used to determine the systematic error.

Figure 3.20 show distribution of number of tracks for the 5 multiplicity classes with three different track cuts. Rec.MC Pythia results shown in Figure 3.21 indicate narrower distributions than ALICE experimental data. The mean number of tracks are show in

Table 3.1. The mean numbers increase with increasing multiplicity selections by event definition.

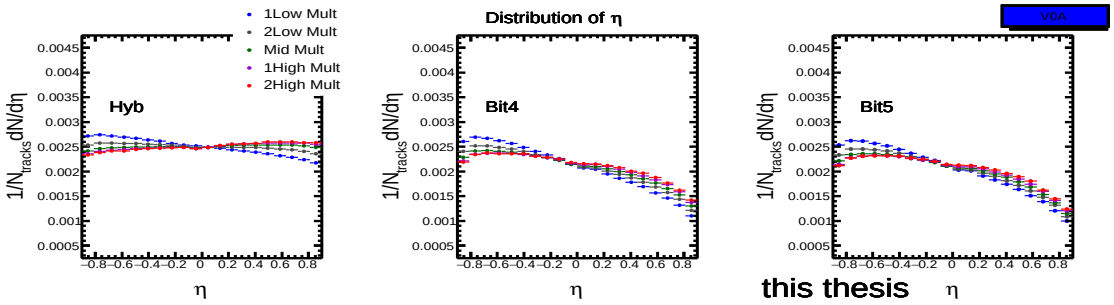

(a) ALICE experimental data, V0A event estimator.

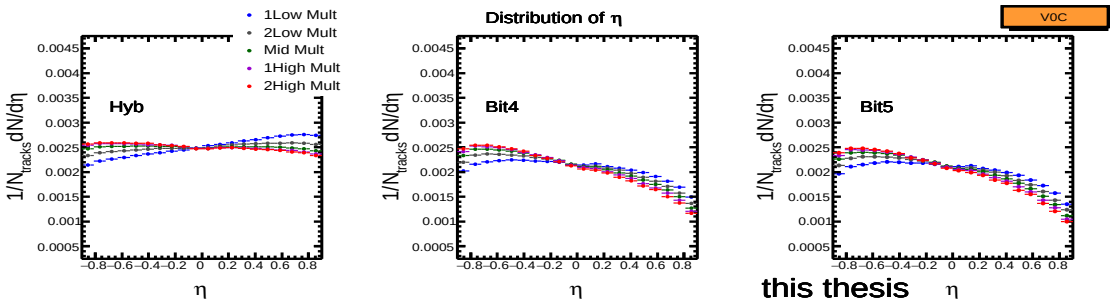

(b) ALICE experimental data, V0C event estimator.

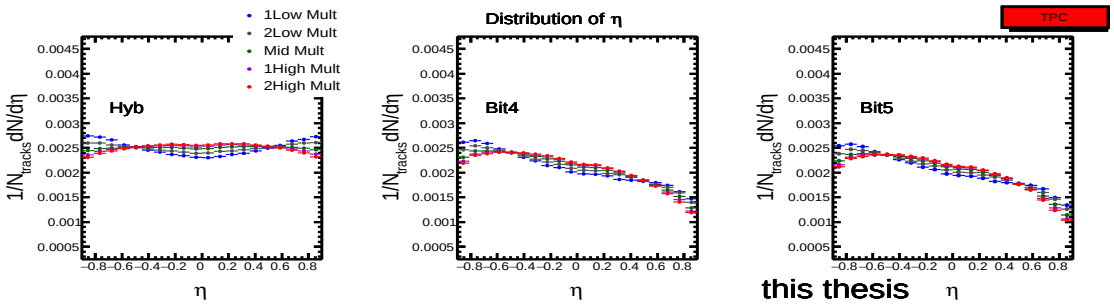

(c) ALICE experimental data, TPC event estimator.

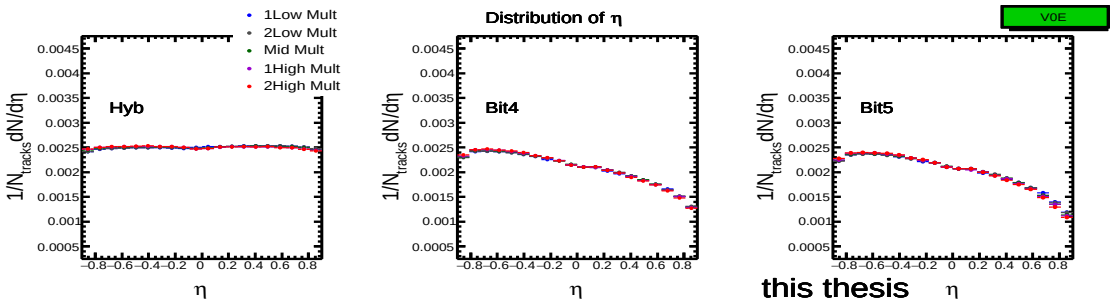

(d) ALICE experimental data, V0E event estimator.

Figure 3.16: ALICE experimental data, distributions of η with three different track cuts by various event estimators in pp collisions at $\sqrt{s} = 7$ TeV with $1 \leq p_T^{Trig} < 4$ GeV/c and $1 \leq p_T^{Assoc} < 4$ GeV/c are shown for the 5 multiplicity classes.

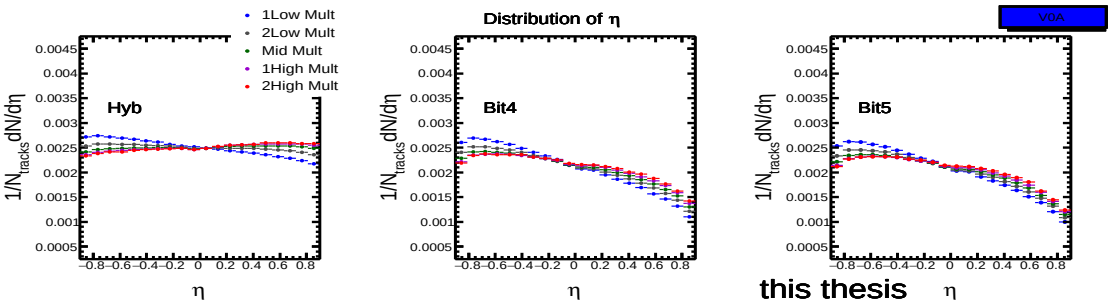

(a) ALICE experimental data, V0A event estimator.

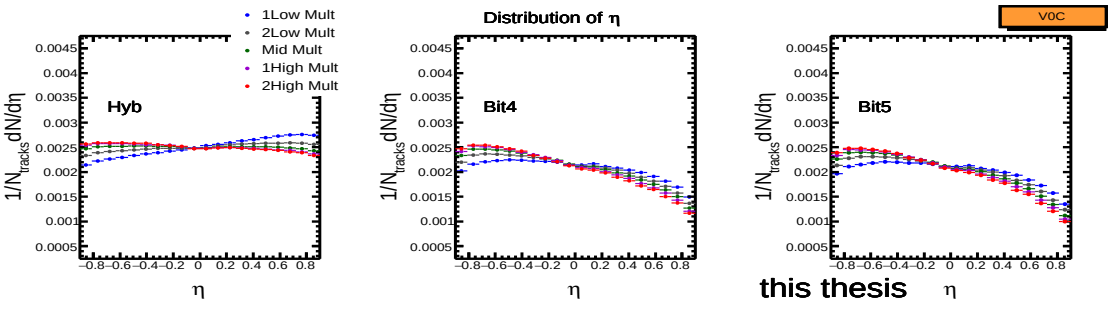

(b) ALICE experimental data, V0C event estimator.

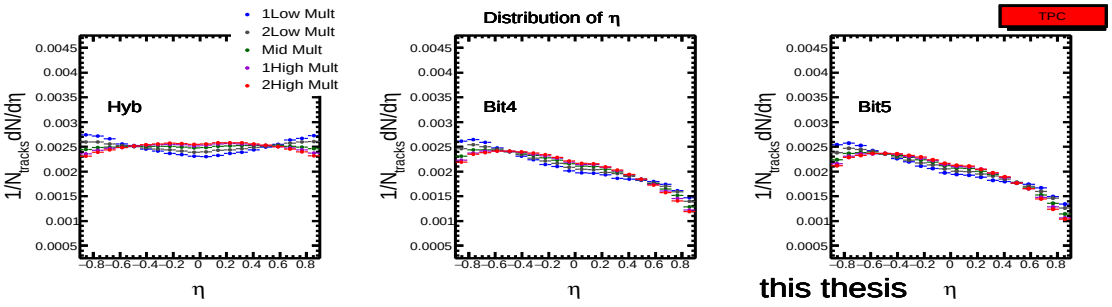

(c) ALICE experimental data, TPC event estimator.

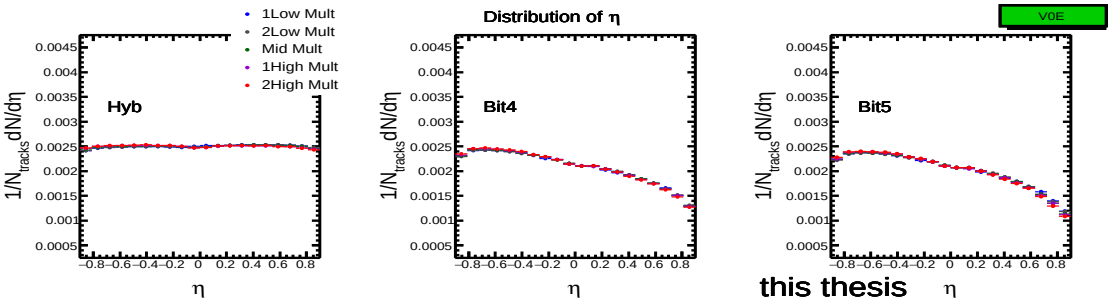

(d) ALICE experimental data, V0E event estimator.

Figure 3.17: ALICE experimental data, distributions of φ with three different track cuts by various event estimators in pp collisions at $\sqrt{s} = 7$ TeV with $1 \leq p_T^{Trig} < 4$ GeV/c and $1 \leq p_T^{Assoc} < 4$ GeV/c are shown for the 5 multiplicity classes.

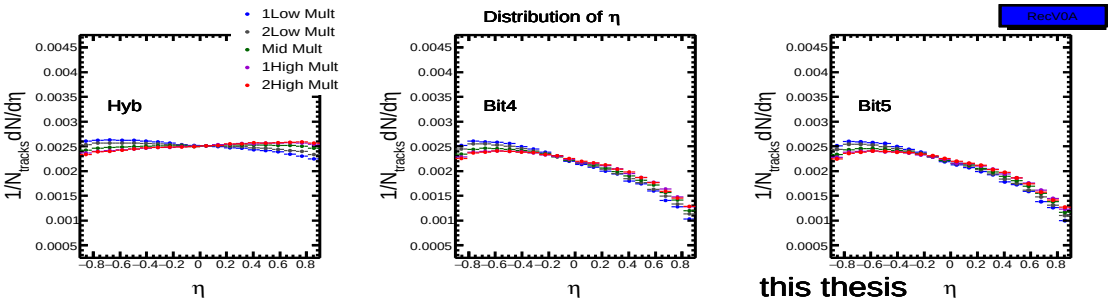

(a) Rec.MC, V0A event estimator.

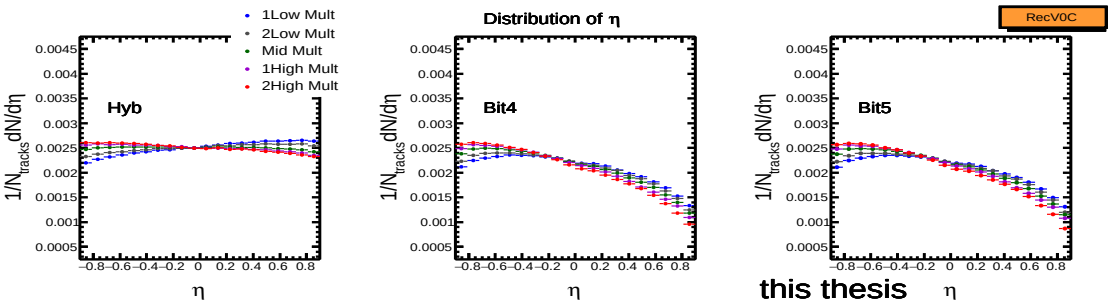

(b) Rec.MC, V0C event estimator.

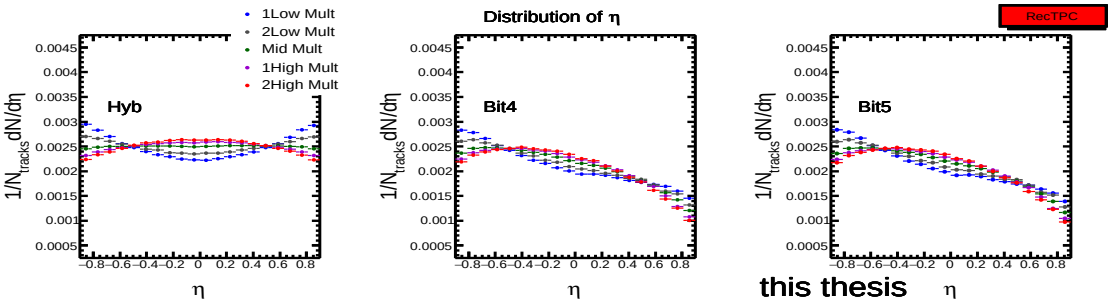

(c) Rec.MC, TPC event estimator.

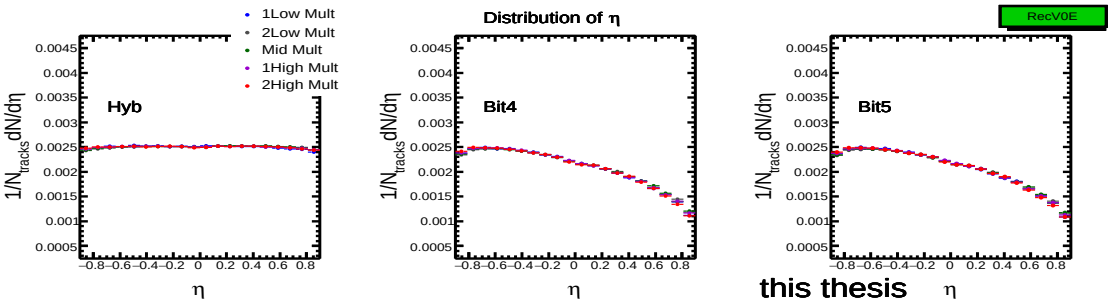

(d) Rec.MC, V0E event estimator.

Figure 3.18: Rec.MC, distributions of η with three different track cuts by various event estimators in pp collisions at $\sqrt{s}$ = 7 TeV with 1≤ p_T^{Trig} <4 GeV/c and 1≤ p_T^{Assoc} <4 GeV/c are shown for the 5 multiplicity classes.

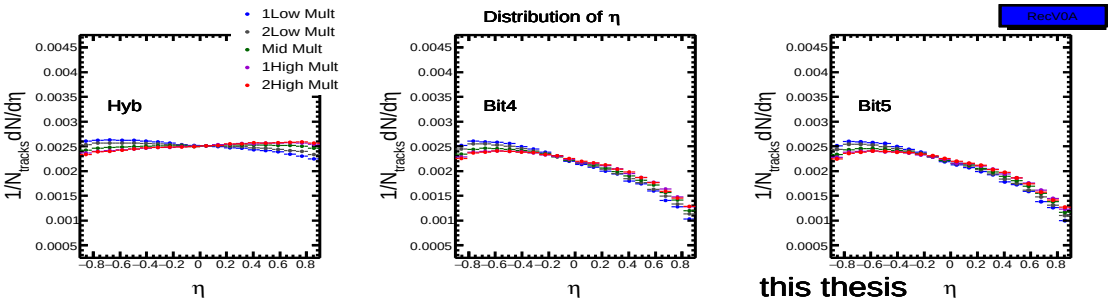

(a) Rec.MC, V0A event estimator.

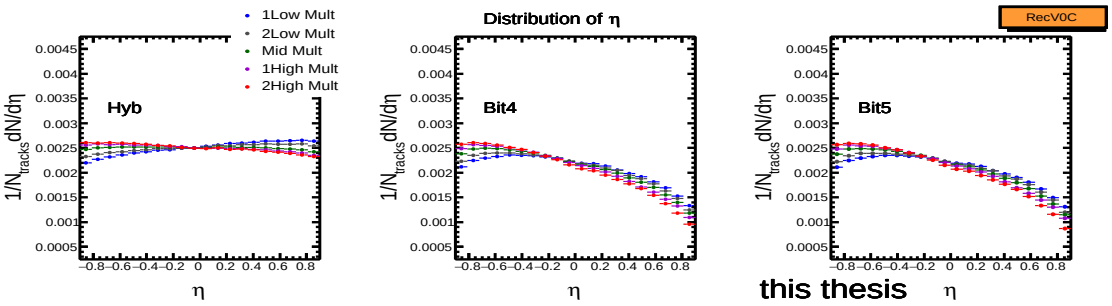

(b) Rec.MC, V0C event estimator.

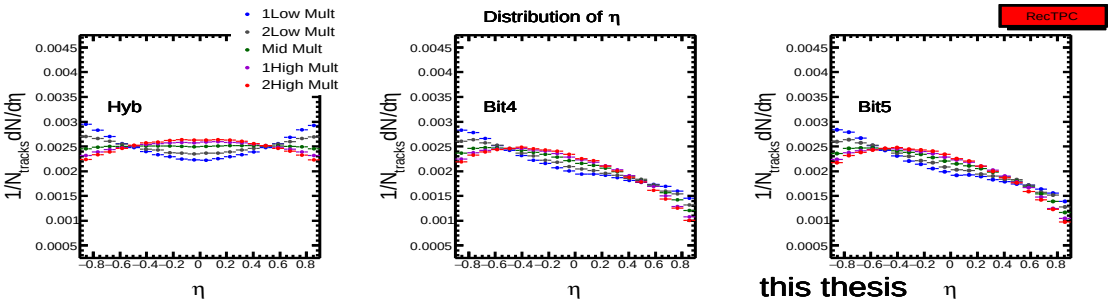

(c) Rec.MC, TPC event estimator.

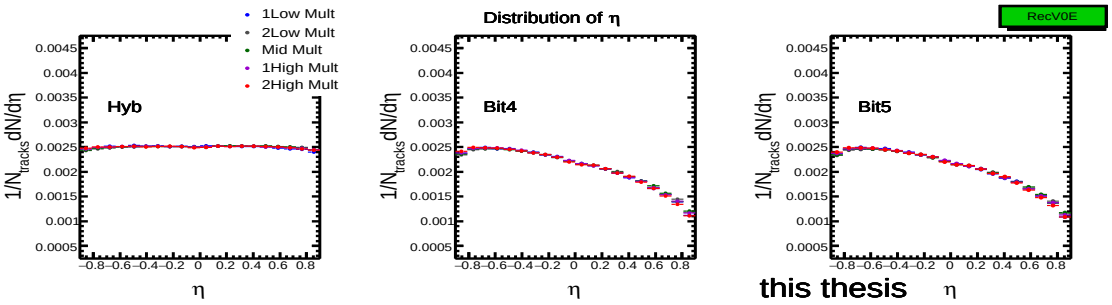

(d) Rec.MC, V0E event estimator.

Figure 3.19: Rec.MC, distributions of φ with three different track cuts by various event estimators in pp collisions at $\sqrt{s} = 7$ TeV with $1 \leq p_T^{Trig} < 4$ GeV/c and $1 \leq p_T^{Assoc} < 4$ GeV/c are shown for the 5 multiplicity classes.

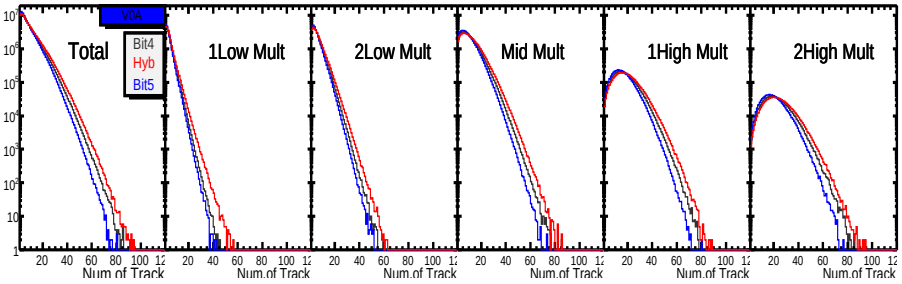

(a) ALICE experimental data, V0A event estimator, distributions of number of tracks.

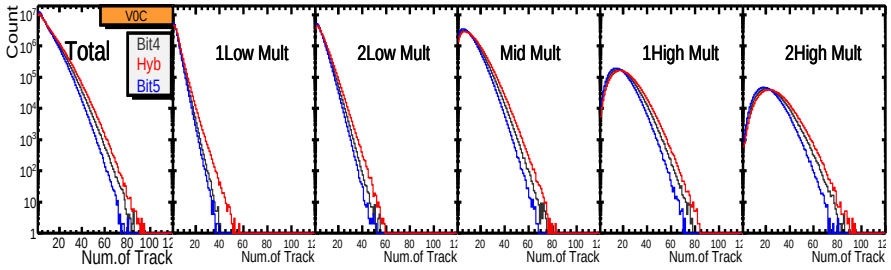

(b) ALICE experimental data, V0C event estimator, distributions of number of tracks.

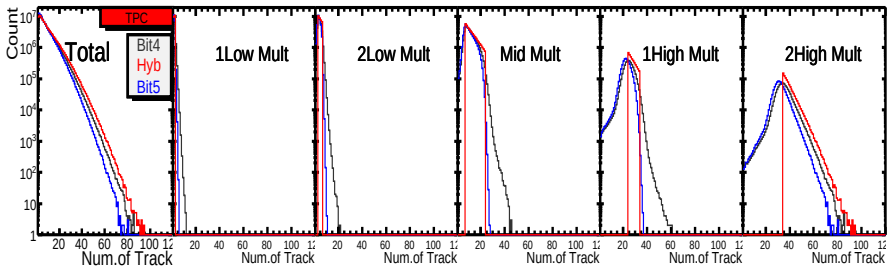

(c) ALICE experimental data, TPC event estimator, distributions of number of tracks.

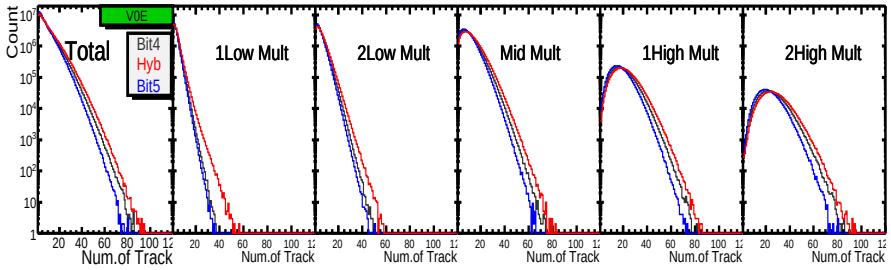

(d) ALICE experimental data, V0E event estimator, distributions of number of tracks.

Figure 3.20: ALICE experimental data, distributions of number of tracks with three different track cuts by various event estimators in pp collisions at $\sqrt{s} = 7$ TeV are shown for the 5 multiplicity classes.

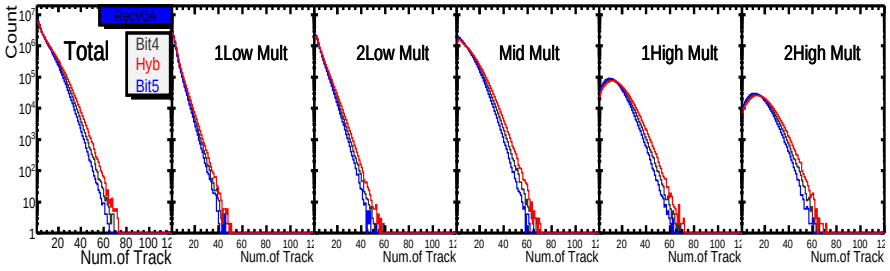

(a) Rec.MC, V0A event estimator, distributions of number of tracks.

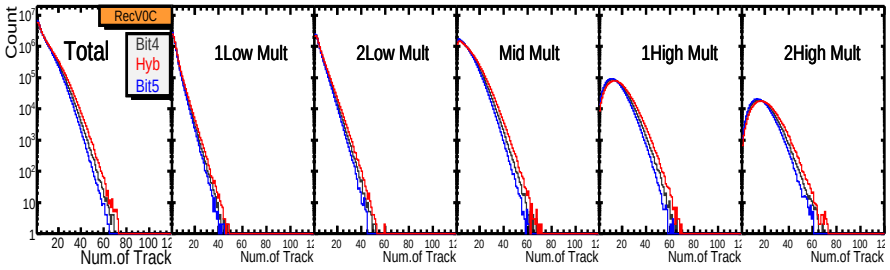

(b) Rec.MC, V0C event estimator, distributions of number of tracks.

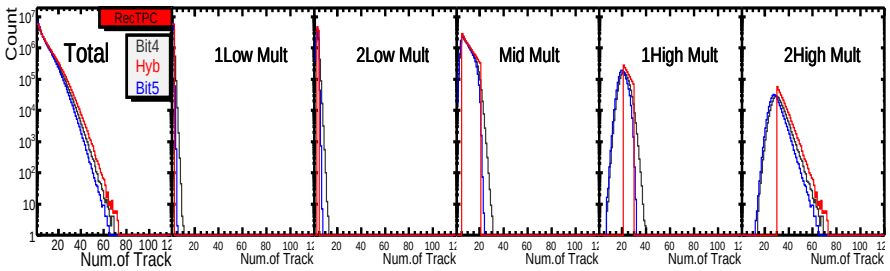

(c) Rec.MC, TPC event estimator, distributions of number of tracks.

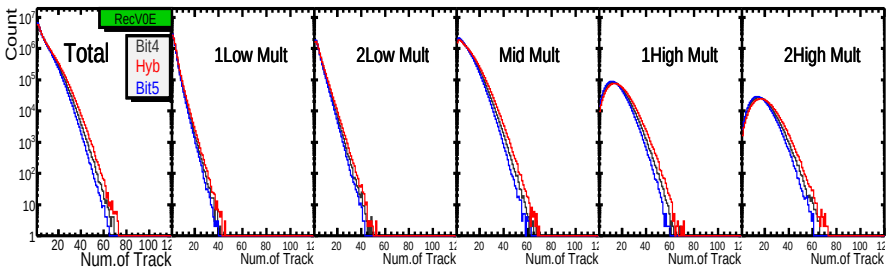

(d) Rec.MC, V0E event estimator, distributions of number of tracks.

Figure 3.21: Rec.MC, distributions of number of tracks with three different track cuts by various event estimators in pp collisions at $\sqrt{s} = 7$ TeV are shown for the 5 multiplicity classes.

Distributions of number of reconstructed tracks for the 5 multiplicity classes and with three different track cuts are shown in Figure 3.20. Number of track reconstruction by three different tracking methods for the 5 multiplicity classes are different for the most of

the results shown in Table 3.1. However, numbers of reconstructed tracks of MC results show narrower distributions than ALICE experimental data, that the mean multiplicity is less in the Monte-Carlo than in experimental data. The systematic uncertainties are defined as:

$$\Delta A = |A_{Bit5} - A_{Bit4}| \tag{3.12}$$

$$\Delta B = \frac{|B_{V0E} - B_{V0A}| + |B_{V0E} - B_{V0C}|}{2} \tag{3.13}$$

$$\Delta S = \sqrt{A^2 + B^2} \tag{3.14}$$

where is A_{Bit5} is a default track, B_{V0E} is a default event estimator. ΔA is the difference between different track cuts, as shown Equation. 3.12 and ΔB is the difference between different event estimators, as shown Equation. 3.13. ΔS are using both ΔA and ΔB, as shown Equation. 3.14. The systematic uncertainties are applied to ΔA and ΔS. ΔA are applying for all of in section. 5, except for the section. 5.4 (Figure 5.9 and Figure 5.10). ΔS are applying for the section. 5.4.

Table 3.1: ALICE experimental data, mean number of tracks with three different track cuts.

Exp.V0A.Event, Mean Track	Hyb	Bit4	Bit5
1Low Mult	3.78	3.27	3.00
2Low Mult	5.66	5.00	4.55
Mid Mult	10.87	9.80	8.83
1High Mult	18.69	17.03	15.27
2High Mult	23.04	21.14	18.87
Exp.V0C.Event, Mean Track	Hyb	Bit4	Bit5
1Low Mult	3.63	3.13	2.87
2Low Mult	5.48	4.84	4.41
Mid Mult	11.06	9.97	8.99
1High Mult	20.19	18.35	16.45
2High Mult	25.35	23.11	20.65
Exp.TPC.Event, Mean Track	Hyb	Bit4	Bit5
1Low Mult	1.53	1.45	1.26
2Low Mult	4.32	3.91	3.53
Mid Mult	12.24	10.93	9.89
1High Mult	27.32	24.23	21.99
2High Mult	39.13	34.55	31.42
Exp.V0E.Event, Mean Track	Hyb	Bit4	Bit5
1Low Mult	3.44	2.95	2.72
2Low Mult	5.35	4.72	4.30
Mid Mult	11.07	9.98	9.00
1High Mult	20.63	18.78	16.84
2High Mult	26.53	24.29	21.68

Table 3.2: Rec.MC, mean number of tracks with three different track cuts.

Rec.V0A.Event, Mean Track	Hyb	Bit4	Bit5
1Low Mult	3.32	2.98	2.78
2Low Mult	4.69	4.24	3.93
Mid Mult	8.62	7.81	7.21
1High Mult	14.37	13.04	12.03
2High Mult	15.92	14.46	13.33
Rec.V0C.Event, Mean Track	Hyb	Bit4	Bit5
1Low Mult	3.16	2.84	2.66
2Low Mult	4.46	4.02	3.74
Mid Mult	8.80	7.97	7.37
1High Mult	15.77	14.29	13.17
2High Mult	18.81	17.00	15.66
Rec.TPC.Event, Mean Track	Hyb	Bit4	Bit5
1Low Mult	1.50	1.41	1.26
2Low Mult	3.44	3.12	2.89
Mid Mult	9.70	8.76	8.12
1High Mult	23.90	21.43	19.94
2High Mult	34.10	30.46	28.42
Rec.V0E.Event, Mean Track	Hyb	Bit4	Bit5
1Low Mult	2.95	2.65	2.48
2Low Mult	4.13	3.72	3.46
Mid Mult	8.33	7.54	6.97
1High Mult	15.87	14.40	13.27
2High Mult	18.44	16.72	15.40

Chapter 4

Results

4.1 Small $\Delta\eta$ correlation in TPC-TPC correlation

This section shows the result of correlation functions and the subtraction of uncorrelated parts from the correlations function. TPC-TPC correlation functions are shown in $|\Delta\eta|$ <1.8 with $1 \leq p_T^{Trig} < 4$ GeV/c and $1 \leq p_T^{Assoc} < 4$ GeV/c.

4.1.1 Two-particle correlation shape comparison

This section shows the results of two-particle correlations within $|\Delta\eta| < 1.8$ with $1 \leq p_T^{Trig} < 4$ GeV/c and $1 \leq p_T^{Assoc} < 4$ GeV/c with 5 multiplicity selections using various event estimators. Figure 4.1 shows the minimum bias (MB) correlation functions with the 3 different event estimators. The left panels show the MB with TPC event estimator, the middle panels show the MB with V0E event estimator and the right panels show the MB without multiplicity event class in the event mixing. Upper panels show ALICE experimental results and lower panels show Rec.MC Ptythia results. The shapes of MB with various event estimators agree with Rec.MC Ptythia results. In order to study the multiplicity dependence, angular correlation functions with 5 multiplicity classes are shown for comparison among various event estimators, which are V0A, V0C, TPC and V0E (Hybrid) event estimators.

The two-dimensional (2-D) structure shows a variety of features of particle produc-

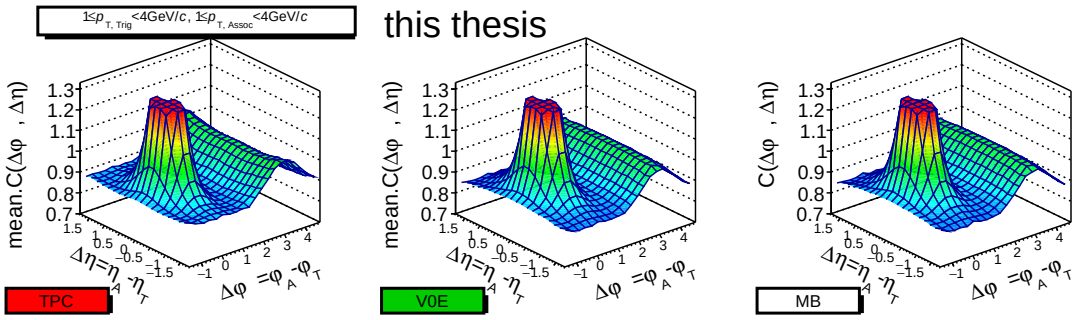

(a) ALICE experimental data, the mean of MB by various event estimators.

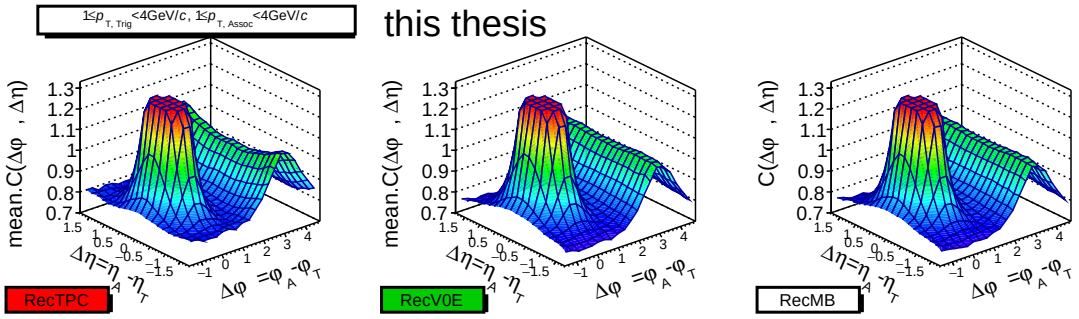

(b) Rec.MC, the mean of MB by various event estimators.

Figure 4.1: TPC-TPC correlation, 2-D dihadron correlation functions for mean of minimum bias (MB) in pp collisions at $\sqrt{s} = 7$ TeV with $1 \leq p_T^{Trig} < 4$ GeV/c and $1 \leq p_T^{Assoc} < 4$ GeV/c are shown for various event estimators.

tions for 5 multiplicity classes by various event estimators, as shown in Figure 4.2. In the horizontal direction, due to the combinatorial mixed background, the uncorrelated mixed backgrounds increase, therefore near side jets ($(\Delta\varphi, \Delta\eta) \approx (0, 0)$) decrease with increasing the multiplicity. In vertical direction, the 2-D shapes of correlation functions are different for various event estimators. The near side jet cones are originated from high p_T hard processes. The elongated structure along $\Delta\eta$ axis at $\Delta\varphi \sim \pi$ can be interpreted as momentum conservation or back-to-back jets. Ridge structures are shown in $0\% - 1\%$ and $1\% - 5\%$ at $\Delta\varphi \approx 0$ and $|\Delta\eta| > 1.0$. On the other hand, Rec.MC Pythia does not reproduce the ridge structure, as shown in Figure 4.3.

The strong variation of correlation shapes (wing-like structure) in $\Delta\eta$ of TPC event estimator can be understood by an auto-/self- correlation where both the correlation and event estimator are defined and calculated within the same detector acceptance. The various event estimators has jet-biased event selection in ALICE experiment. Above all various event estimators, auto correlation shows the strongest jet-bias in event selections. Especially, the away side jet shapes with TPC event estimator are different from the other event

estimators because of the auto-correlation from the jet-biased event selection. Most of the auto-correlation and jet-biased event selection are well reproduced in MC calculation with PYTHIA.

In order to study the multiplicity dependence in detail, 2-D correlation functions are projected to one-dimensional (1-D) $\Delta\varphi$ and $\Delta\eta$ with given ranges, as shown in Figure 4.4. They are two different projections in $\Delta\varphi$ with small and large $\Delta\eta$ cuts of $|\Delta\eta| \leq 0.2$ and $1.5 \leq |\Delta\eta| < 1.8$ and two different $\Delta\eta$ projections with small and large $\Delta\varphi$ cuts of $|\Delta\varphi| < 0.1$ and $2.3 < \Delta\varphi < 3.9$.

1-D angular correlation functions for a given p_T slice with 5 multiplicity classes by various event estimators are shown in Figure 4.5. $C(\Delta\varphi, \Delta\eta)$ is a trivial Signal/mixed background effect, as shown in Equation. 3.5. In the most left panels of Figure 4.5, one dimensional projected correlation functions 1-D $C(\Delta\varphi)$ for a given slice $|\Delta\eta| \leq 0.2$ show near side ($\Delta\varphi \approx 0$) and away side ($\Delta\varphi \approx \pi$) jet peaks for 5 multiplicity classes. The enhancement at $\Delta\varphi \approx \pi$ in $\Delta\varphi$ distribution is mostly because of the di-jet. 1-D $C(\Delta\eta)$ for a given slice $|\Delta\varphi| < 0.1$ (second column) show near side jet peaks for 5 multiplicity classes. 1-D $C(\Delta\varphi)$ for a given slice $1.5 \leq |\Delta\eta| < 1.8$ (third column) shows long rang $|\Delta\eta|$ correlation for 5 multiplicity classes (a widen graph is shown in Appendix A.1). There are very layered with multiplicity in $|\Delta\varphi| \approx 0$, while away side jets peaks in $|\Delta\varphi| \approx \pi$ are all similar with multiplicity (a counter balancing effect of near-side jet peak). 1-D $C(\Delta\eta)$ for a given slice $2.3 < \Delta\varphi < 3.9$ (fourth column) show away side jets (in $|\Delta\varphi| \approx \pi$) for 5 multiplicity classes. As shown $|\Delta\varphi| \approx \pi$ in the third column of it, away side jets (in $|\Delta\varphi| \approx \pi$) are all similar with multiplicities, except for TPC auto correlation with the strong jet-biased event selection.

The same decomposition procedure had been applied to the pythia simulation (Rec.MC Pythia), shown in Figure 4.3. And the shapes of MC pythia simulation are agreed with experimental results.

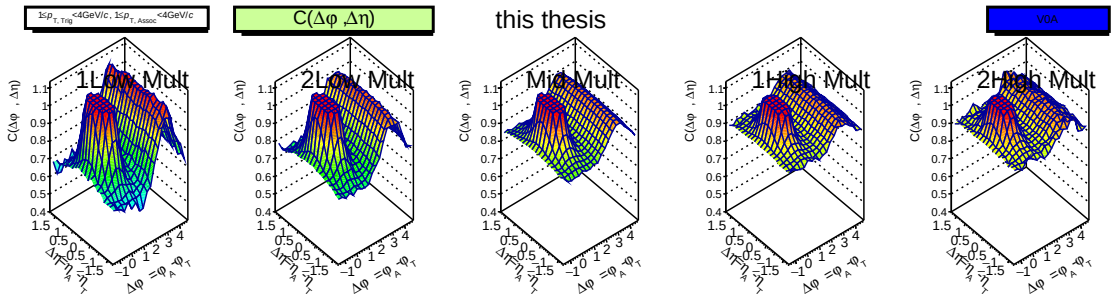

(a) ALICE experimental data, V0A event estimator.

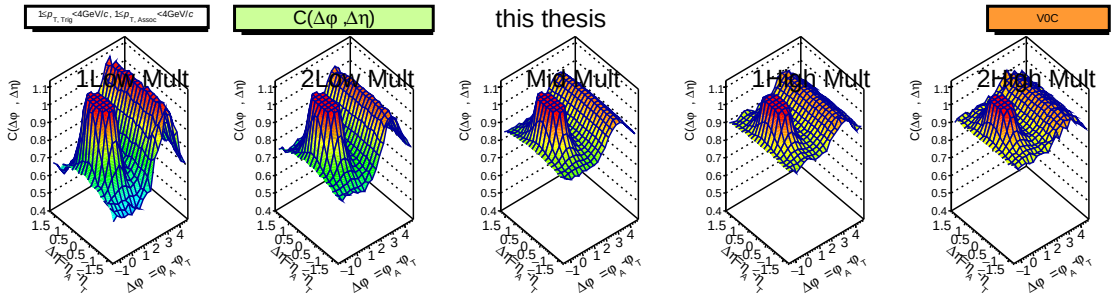

(b) ALICE experimental data, V0C event estimator.

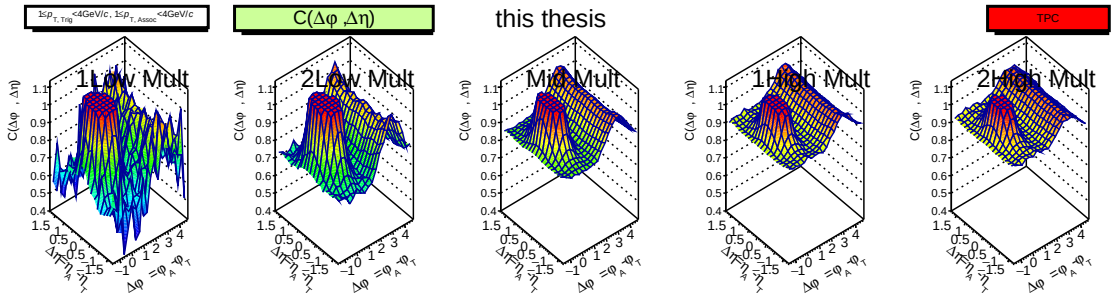

(c) ALICE experimental data, TPC event estimator.

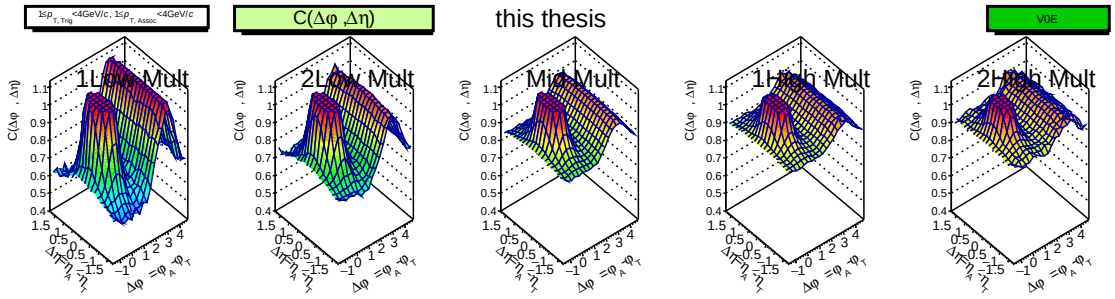

(d) ALICE experimental data, V0E event estimator.

Figure 4.2: ALICE experimental data, TPC-TPC correlation, 2-D dihadron correlation functions by various event estimators in pp collisions at $\sqrt{s}$ = 7 TeV with 1≤ p_T^{Trig} <4 GeV/c and 1≤ p_T^{Assoc} <4 GeV/c are shown for the 5 multiplicity classes.

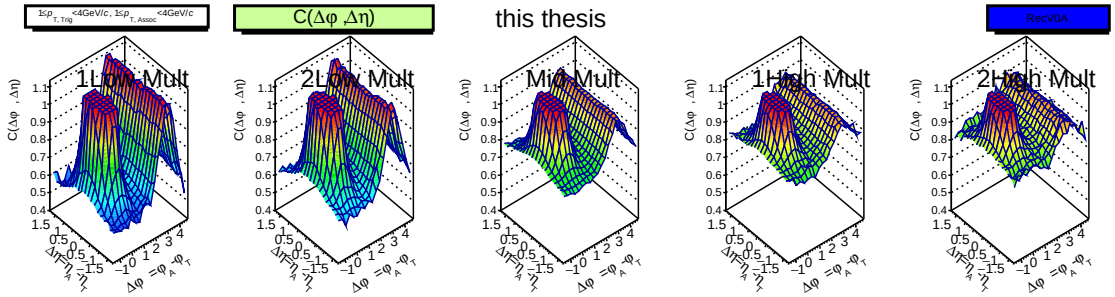

(a) Rec.MC, V0A event estimator.

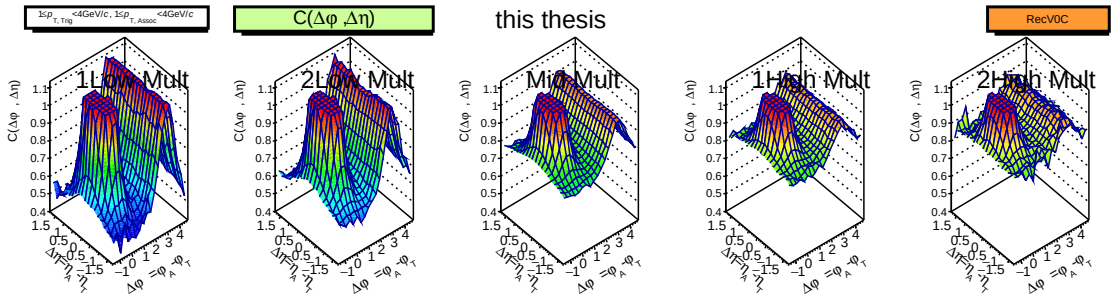

(b) Rec.MC, V0C event estimator.

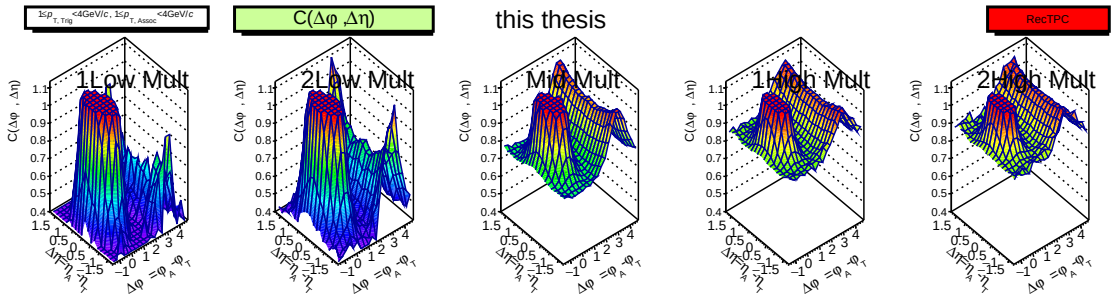

(c) Rec.MC, TPC event estimator.

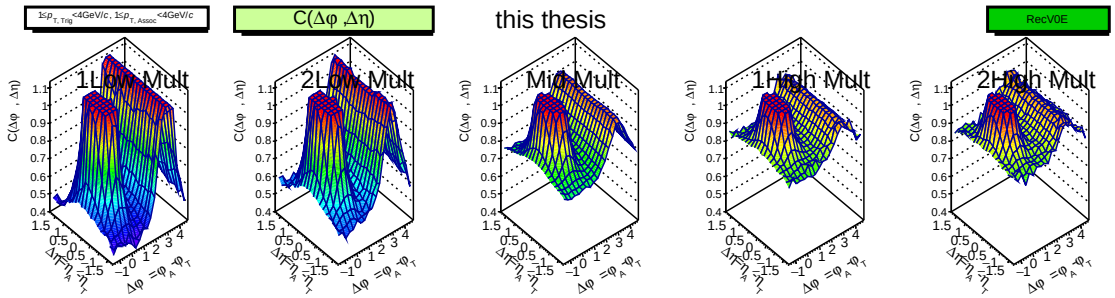

(d) Rec.MC, V0E event estimator.

Figure 4.3: Rec.MC, TPC-TPC correlation, 2-D dihadron correlation functions by various event estimators in pp collisions at $\sqrt{s} = 7$ TeV with $1 \leq p_T^{Trig} < 4$ GeV/c and $1 \leq p_T^{Assoc} < 4$ GeV/c are shown for the 5 multiplicity classes.

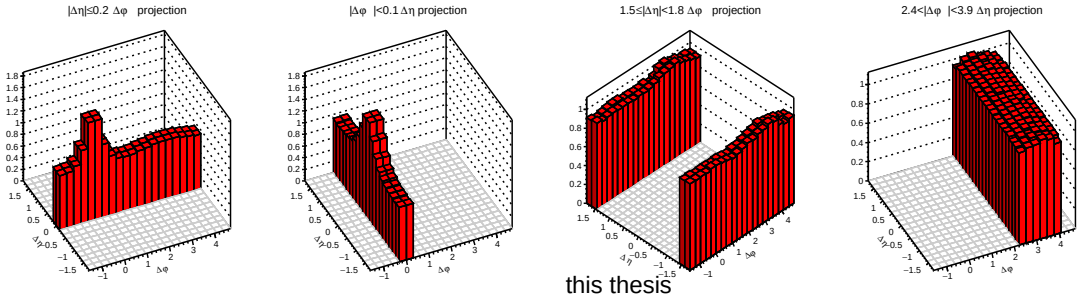

Figure 4.4: Example of 2-D short- and long- correlations function are shown for the highest multiplicity by V0A event estimator.

4.1.2 Renormalized correlation shape comparison

In order to compare the shapes of correlation functions among different multiplicity selections, the correlation functions $C(\Delta\varphi, \Delta\eta)$ are renormalized from minimum of 0 to maximum of 1 ($Ren.C(\Delta\varphi, \Delta\eta)$). And 2-D $Ren.C(\Delta\varphi, \Delta\eta)$ are projected to long- and short range $\Delta\varphi$ and $\Delta\eta$ 1-D angular correlation functions, as shown in Figure 4.7. In the most left panels and second panels, near side jets in $\Delta\varphi \approx 0$ are slightly narrower with increasing multiplicity selections, which could tell us more jet-like event shapes for both $|\Delta\eta| \leq 0.2$ and $|\Delta\varphi| < 0.1$ projections in high multiplicity selections, especially in the TPC event class. The most important results of this analysis are shown in the third column that in the $Ren.C(\Delta\varphi)$ in long range $|\Delta\eta|$ is observed the enhanced peak in $\Delta\varphi \approx 0$ in the highest and 2nd highest multiplicity selections in all of event estimators which are called the ridge structure. The away side jet shapes of $Ren.C(\Delta\eta)$ for 5 multiplicity classes are shown in the fourth column. Although, Rec.MC Pythia reproduce the multiplicity dependence of the near side jets effects, the ridge structures can not be reproduced in Rec.MC Pythia, as shown in Figure 4.8.

The near side jets are fitted with Gaussian function (shown in Appendix. B.1) and the σ values of near side jets are shown in Figure 4.9 and Figure 4.10. The σ values are reduced with increasing multiplicities.

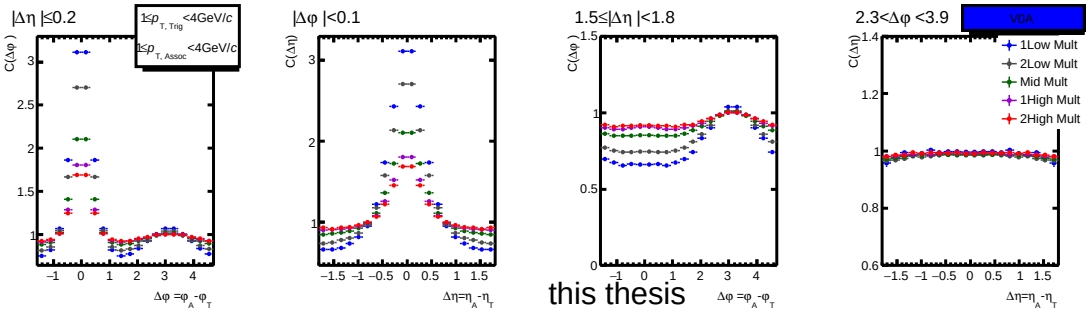

(a) ALICE experimental data, V0A event estimator.

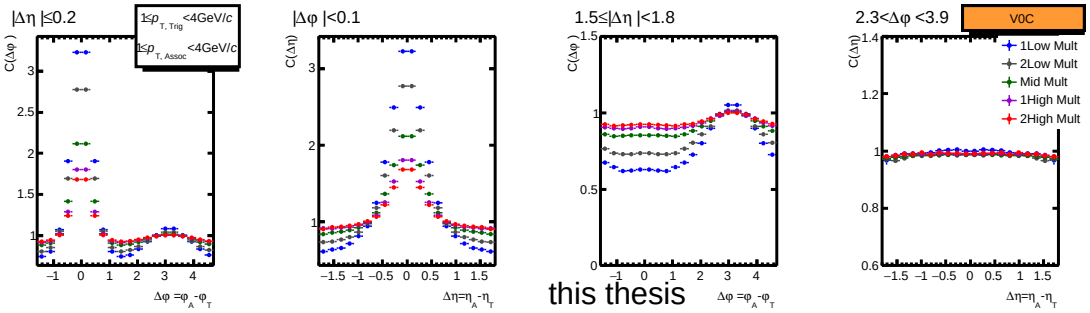

(b) ALICE experimental data, V0C event estimator.

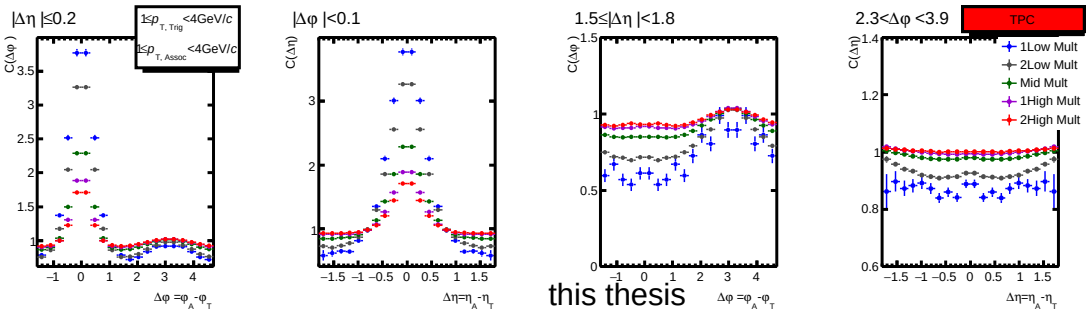

(c) ALICE experimental data, TPC event estimator.

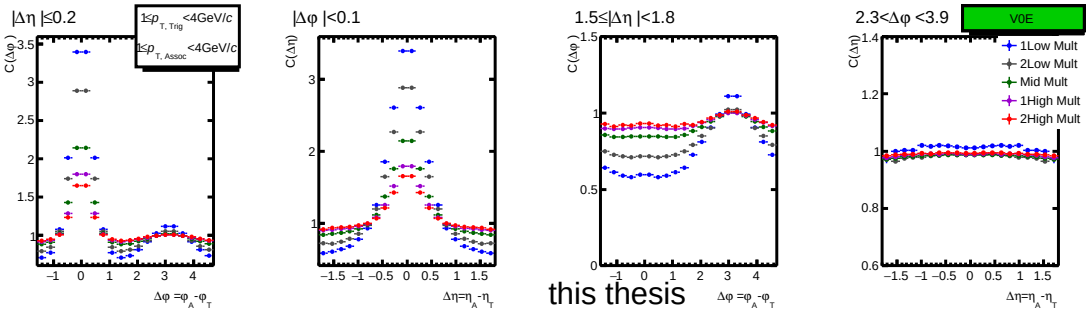

(d) ALICE experimental data, V0E event estimator.

Figure 4.5: ALICE experimental data, TPC-TPC correlation, short- and long- ranges 1-D correlation functions with $1 \leq p_T^{Trig} < 4$ GeV/c and $1 \leq p_T^{Assoc} < 4$ GeV/c in $|\Delta\eta| \leq 0.2$, $|\Delta\varphi| < 0.1$, $1.5 \leq |\Delta\eta| < 1.8$ and $2.3 < \Delta\varphi < 3.9$ by various event estimators are shown for the 5 multiplicity classes.

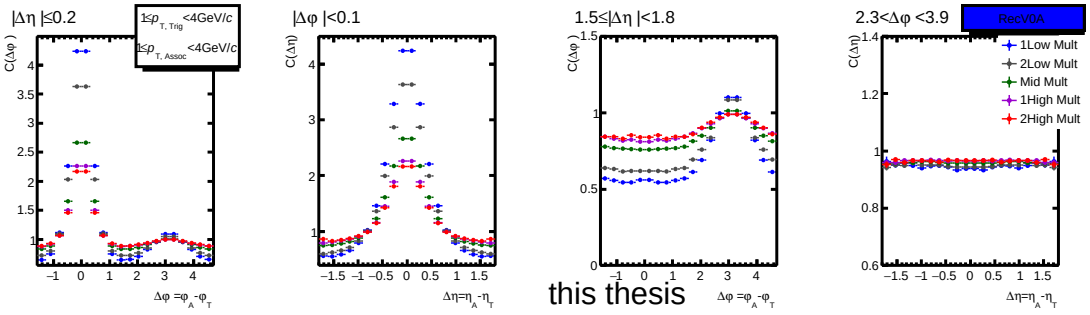

(a) Rec.MC, V0A event estimator.

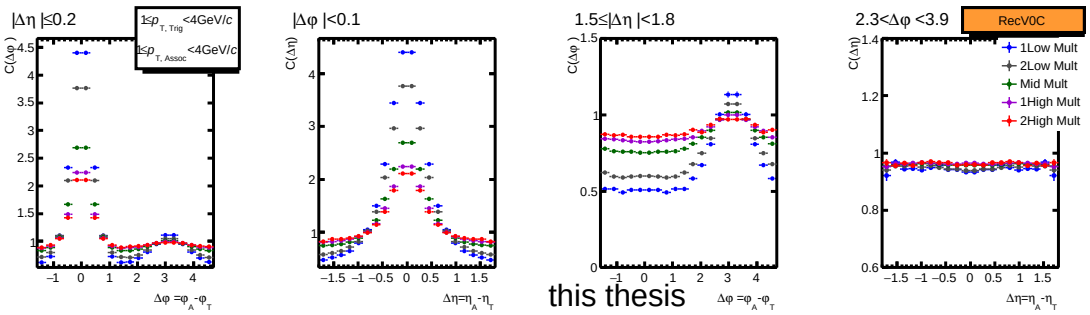

(b) Rec.MC, V0C event estimator.

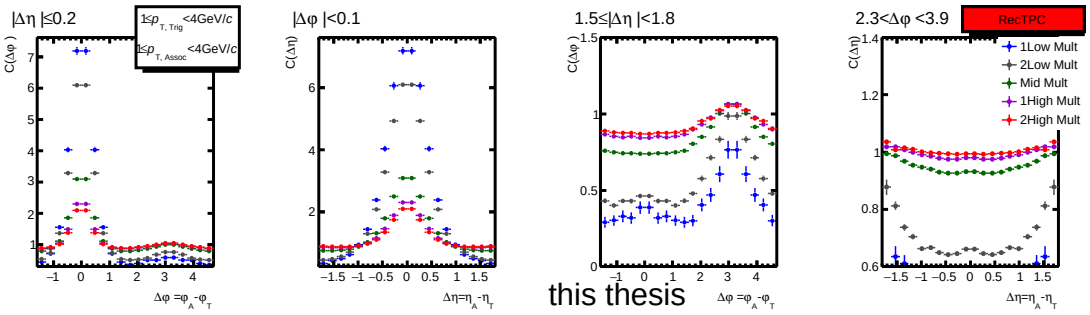

(c) Rec.MC, TPC event estimator.

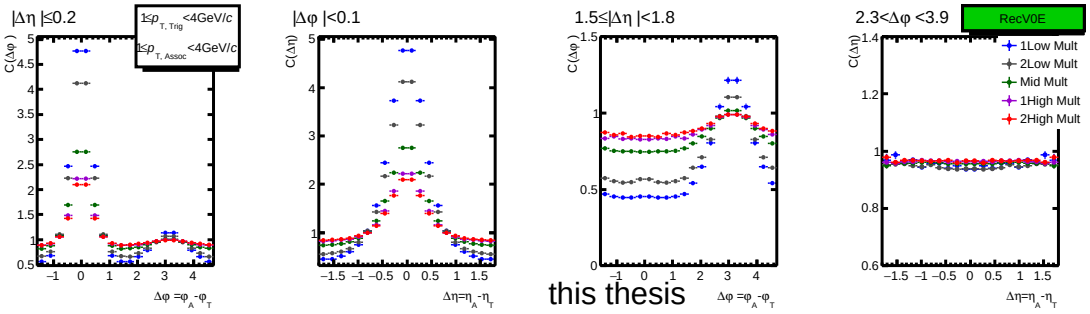

(d) Rec.MC, V0E event estimator.

Figure 4.6: Rec.MC, TPC-TPC correlation, short- and long- ranges 1-D correlation functions with $1 \leq p_T^{Trig} < 4$ GeV/c and $1 \leq p_T^{Assoc} < 4$ GeV/c in $|\Delta\eta| \leq 0.2$, $|\Delta\varphi| < 0.1$, $1.5 \leq |\Delta\eta| < 1.8$ and $2.3 < \Delta\varphi < 3.9$ by various event estimators are shown for the 5 multiplicity classes.

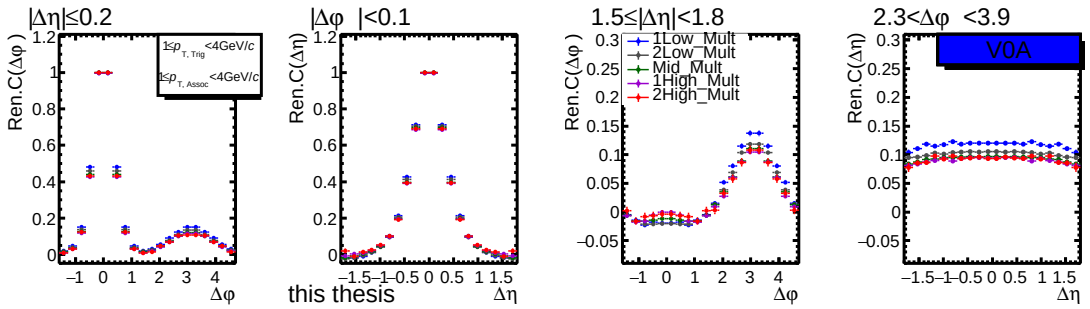

(a) ALICE experimental data, V0A event estimator.

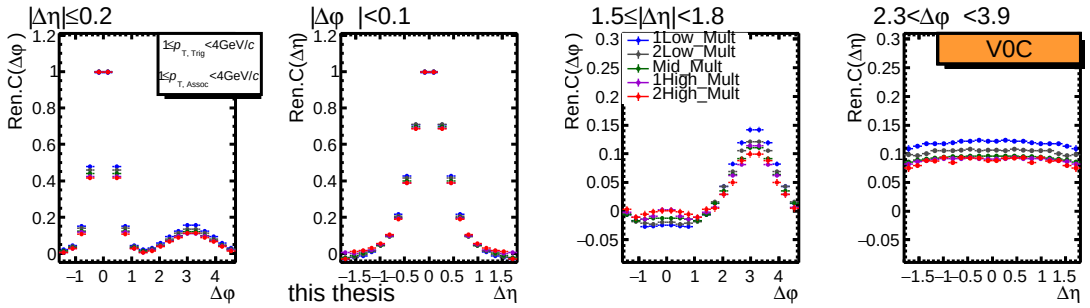

(b) ALICE experimental data, V0C event estimator.

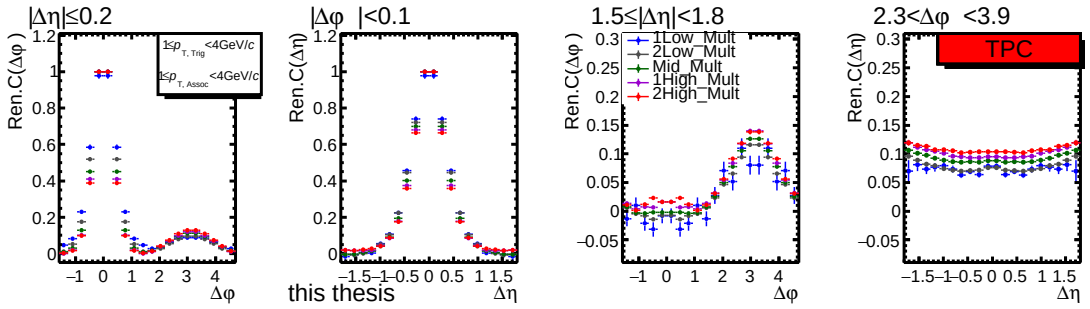

(c) ALICE experimental data, TPC event estimator.

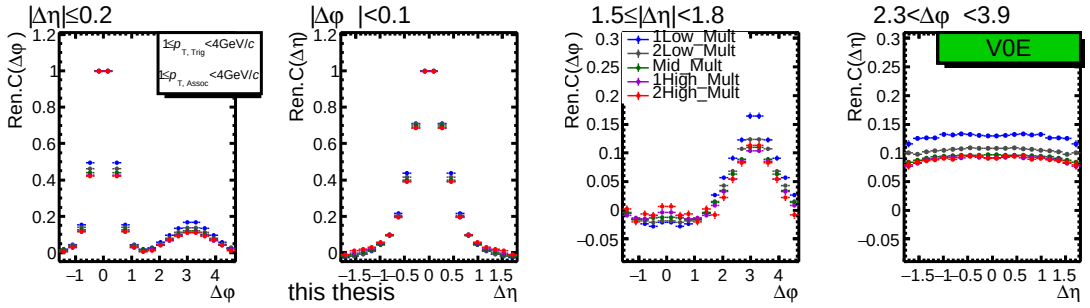

(d) ALICE experimental data, V0E event estimator.

Figure 4.7: ALICE experimental data, 1-D renormalized correlation functions in pp collisions at $\sqrt{s}$ = 7 TeV with 1≤ p_T^{Trig} <4 GeV/c and 1≤ p_T^{Asso} <4 GeV/c in $|\Delta\eta|$ ≤0.2, $|\Delta\varphi|$ <0.1, 1.5≤ $|\Delta\eta|$ <1.8 and 2.3 < $\Delta\varphi$ < 3.9 by various event estimators are shown for the 5 multiplicity classes.

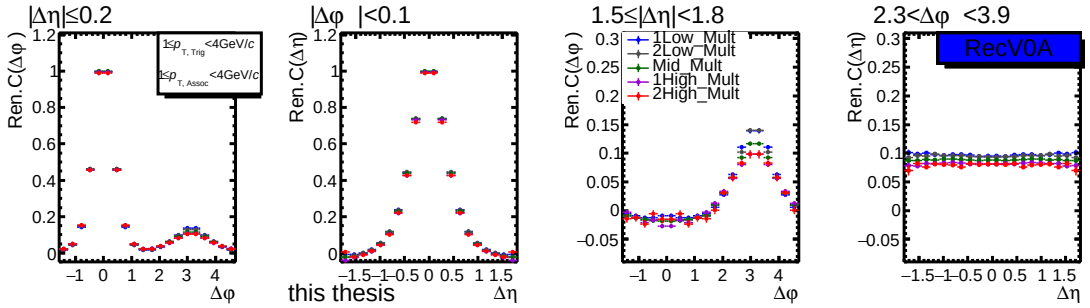

(a) Rec.MC, V0A event estimator.

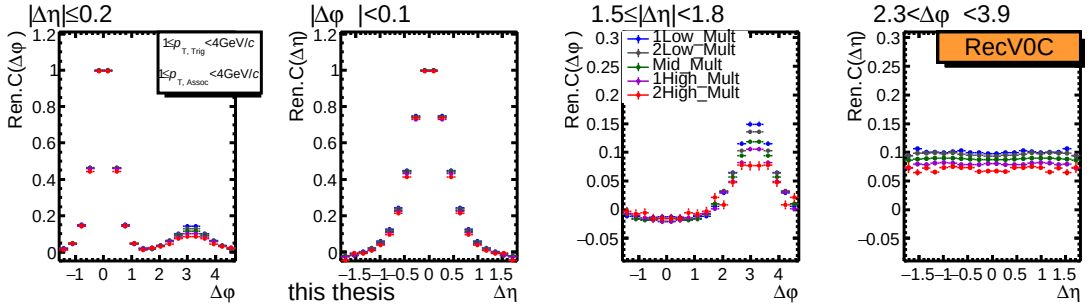

(b) Rec.MC, V0C event estimator.

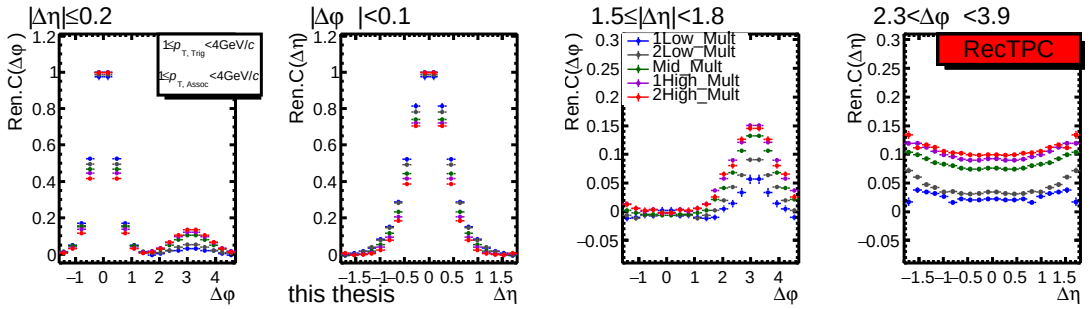

(c) Rec.MC, TPC event estimator.

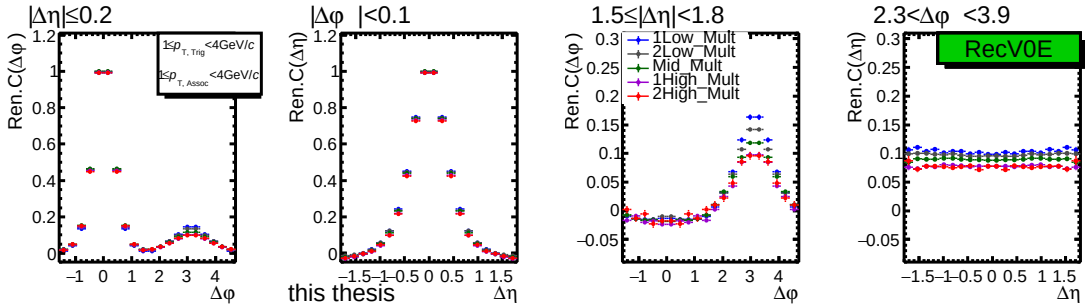

(d) Rec.MC, V0E event estimator.

Figure 4.8: Rec.MC, 1-D renormalized correlation functions in pp collisions at $\sqrt{s} = 7$ TeV with $1 \leq p_T^{Trig} < 4$ GeV/c and $1 \leq p_T^{Asso} < 4$ GeV/c in $|\Delta\eta| \leq 0.2$, $|\Delta\varphi| < 0.1$, $1.5 \leq |\Delta\eta| < 1.8$ and $2.3 < \Delta\varphi < 3.9$ by various event estimators are shown for the 5 multiplicity classes.

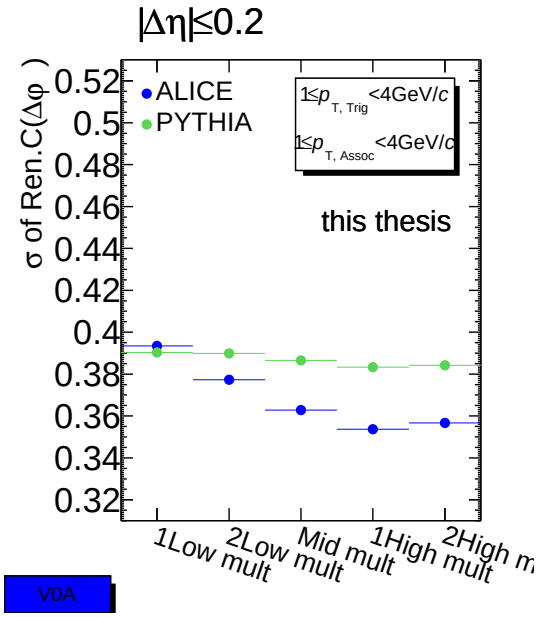

(a) ALICE experimental data, V0A event estimator.

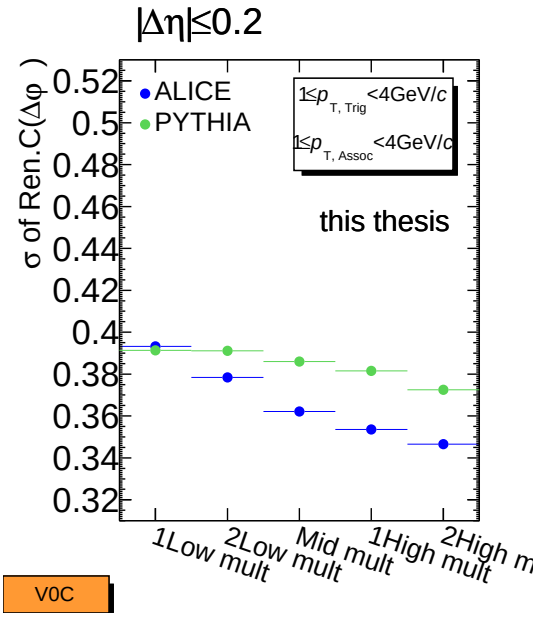

(b) ALICE experimental data, V0C event estimator.

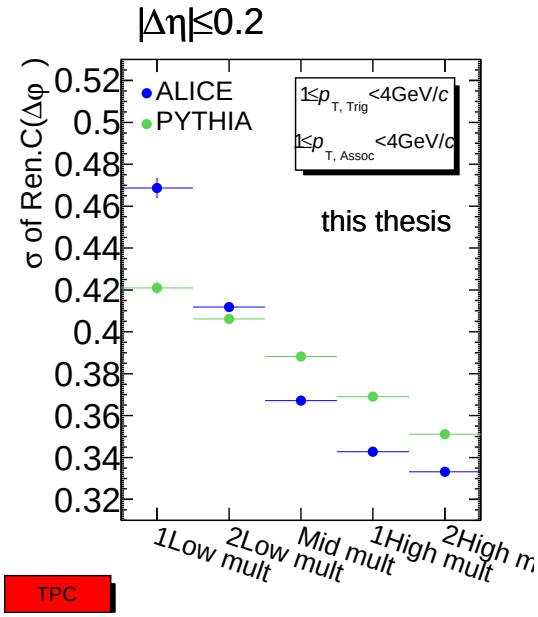

(c) ALICE experimental data, TPC event estimator.

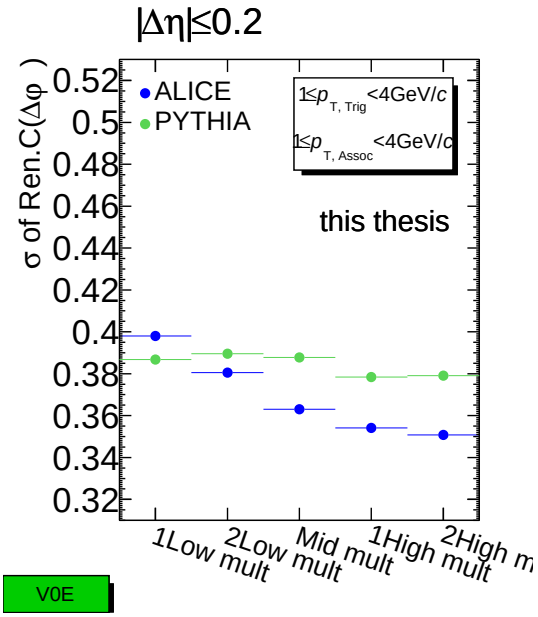

(d) ALICE experimental data, V0E event estimator.

Figure 4.9: σ values by Gaussian fitting ($dN/d\Delta\varphi$ in $|\Delta\eta| \leq 0.2$) in pp collisions at $\sqrt{s} =$ 7 TeV with $1 \leq p_T^{Trig} < 4$ GeV/c and $1 \leq p_T^{Asso} < 4$ GeV/c by various event estimators are shown for the 5 multiplicity classes.

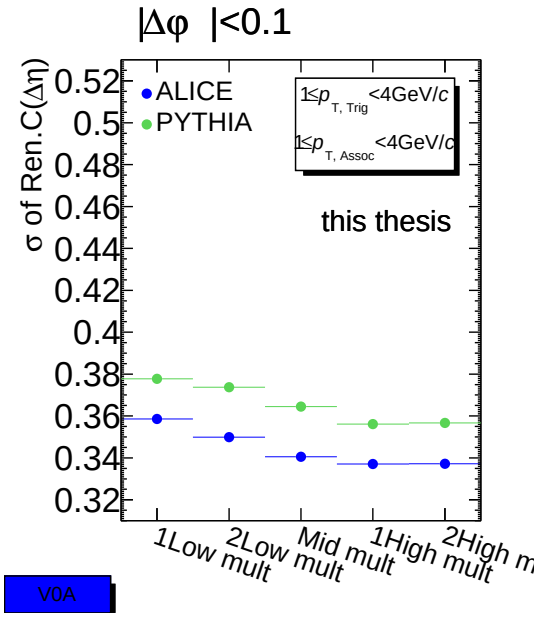

(a) ALICE experimental data, V0A event estimator.

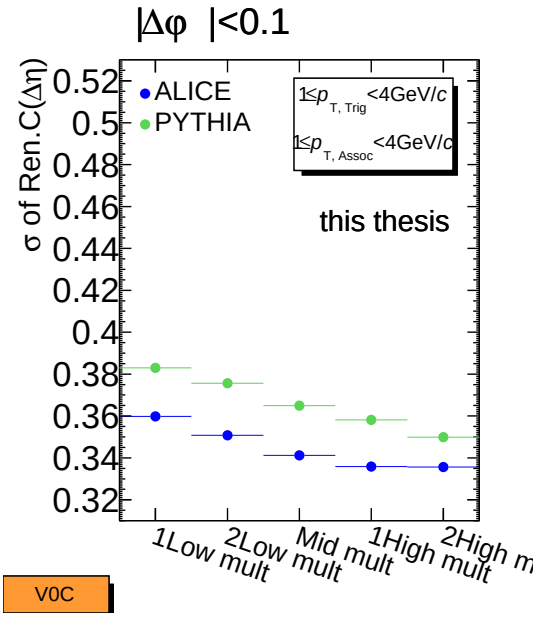

(b) ALICE experimental data, V0C event estimator.

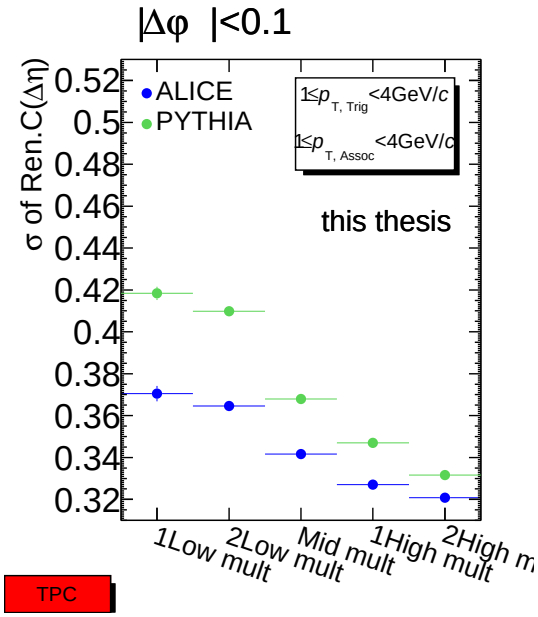

(c) ALICE experimental data, TPC event estimator.

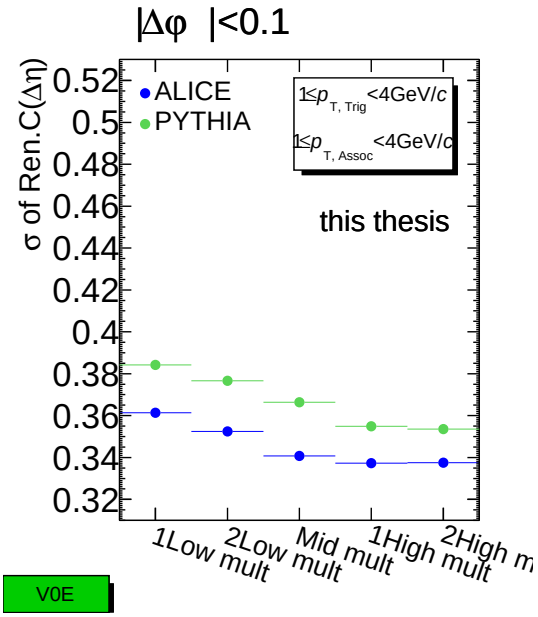

(d) ALICE experimental data, V0E event estimator.

Figure 4.10: σ values by Gaussian fitting ($dN/d\Delta\eta$ in $|\Delta\varphi| < 0.1$) in pp collisions at $\sqrt{s} =$ 7 TeV with $1 \leq p_T^{Trig}$ <4 GeV/c and $1 \leq p_T^{Asso}$ <4 GeV/c by various event estimators are shown for the 5 multiplicity classes.

4.1.3 $\Delta\eta$ correlation to test forward/backward asymmetry with trigger η selection

In this section, the η trigger dependences of correlation functions are presented for 5 different multiplicity selections and with various event estimators. The shapes of $C(\Delta\eta)$ are observed to vary with the η trigger selections, as explain in section. 3.6.6.

Figure 4.11 shows minimum bias (MB) of η trigger $C(\Delta\eta)$ which are mirror symmetric shapes with respect to negative/positive η trigger selections in both near and away sides $\Delta\eta$ correlation functions.

Figure 4.12 shows near side jet shapes of η trigger $C(\Delta\eta)$ in $|\Delta\varphi| < 0.1$ and Figure 4.13 shows away side jet shapes of η trigger $C(\Delta\eta)$ in $2.3 < \Delta\varphi < 3.9$. In case of V0A event estimator, the near side correlation magnitude is more enhanced for the trigger selection close to the V0A side (positive η side) ,on the other hand the away side correlation slope as a function of $C(\Delta\eta)$ is larger for the opposite side of V0A (negative η side). While in the case of V0C estimator, both effects for near and away sides mentioned above are naturally reversed between V0A (positive η) and V0C (negative η) sides. TPC event estimator shows a wing-like structure for each trigger η selection in both near and away sides $\Delta\eta$ correlation functions, that is caused by auto-/self- correlation and jet-biased event selection as discussed in section. 4.1.1. Most of the features described above are rather well reproduced in MC calculation with PYTHIA, as shown in Figure 4.14 and Figure 4.15. The shapes of two particle correlation function are changing with η trigger selection as well as the event estimators.

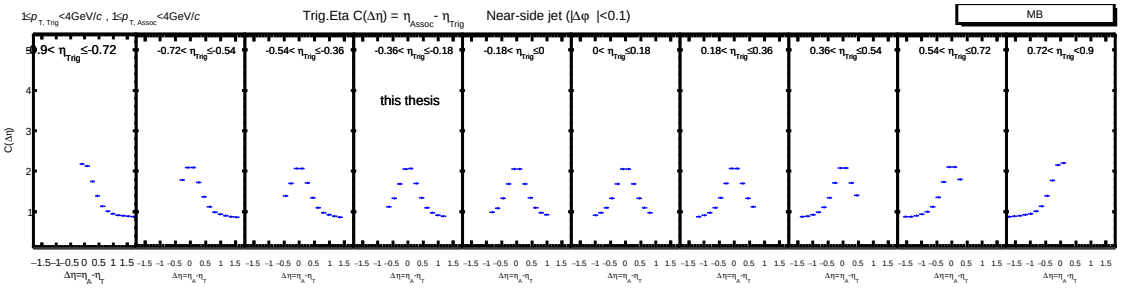

(a) ALICE experimental data, no event estimator, near side jets.

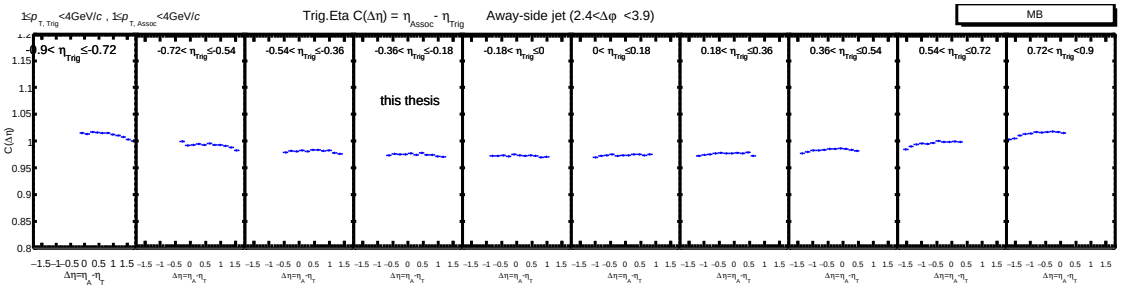

(b) ALICE experimental data, no event estimator, away side jets.

Figure 4.11: ALICE experimental data, the trigger dependence of 1-D correlation functions in pp collisions at $\sqrt{s} = 7$ TeV with $1 \leq p_T^{Trig} < 4$ GeV/c and $1 \leq p_T^{Assoc} < 4$ GeV/c in (a) $|\Delta\varphi| < 0.1$ and (b) $2.3 < \Delta\varphi < 3.9$ are shown for minimum bias.

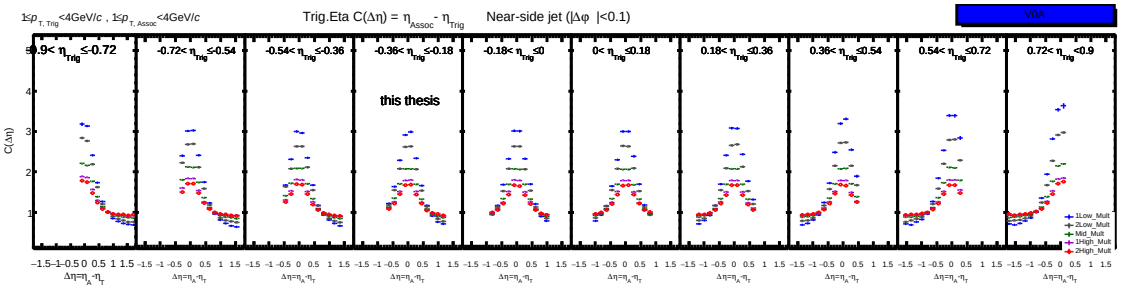

(a) ALICE experimental data, V0A event estimator.

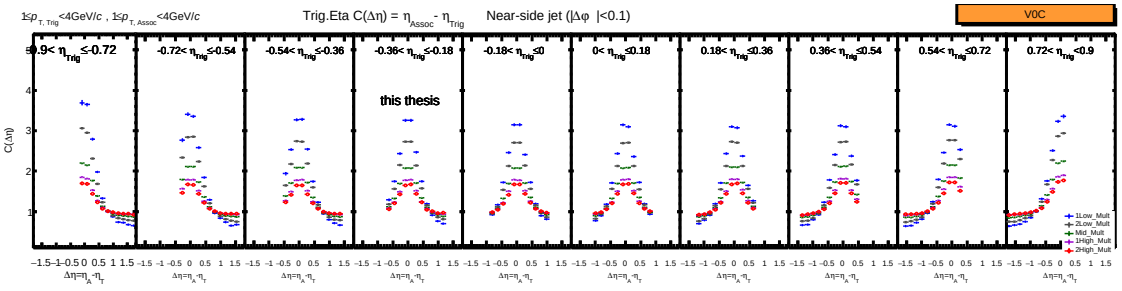

(b) ALICE experimental data, V0C event estimator.

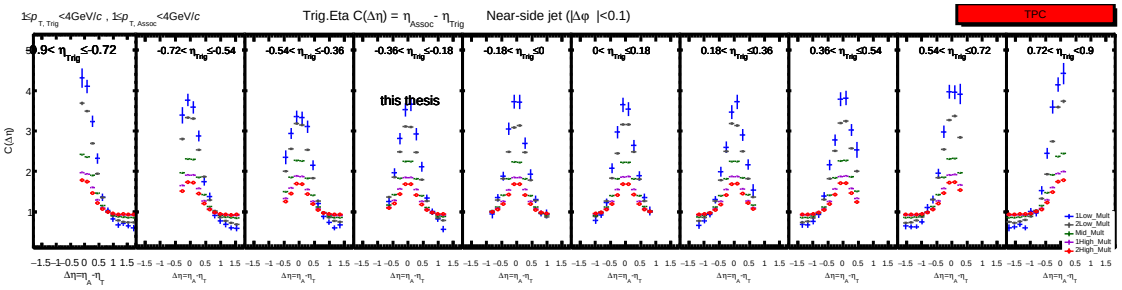

(c) ALICE experimental data, TPC event estimator.

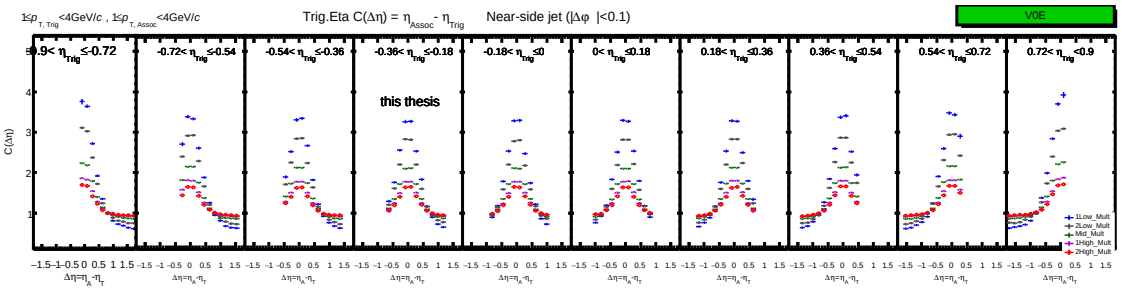

(d) ALICE experimental data, V0E event estimator.

Figure 4.12: ALICE experimental data, the trigger dependence of 1-D correlation functions by various event estimators in pp collisions at $\sqrt{s} = 7$ TeV with $1 \leq p_T^{Trig} < 4$ GeV/c and $1 \leq p_T^{Assoc} < 4$ GeV/c in $|\Delta\varphi| < 0.1$ are shown for the 5 multiplicity classes.

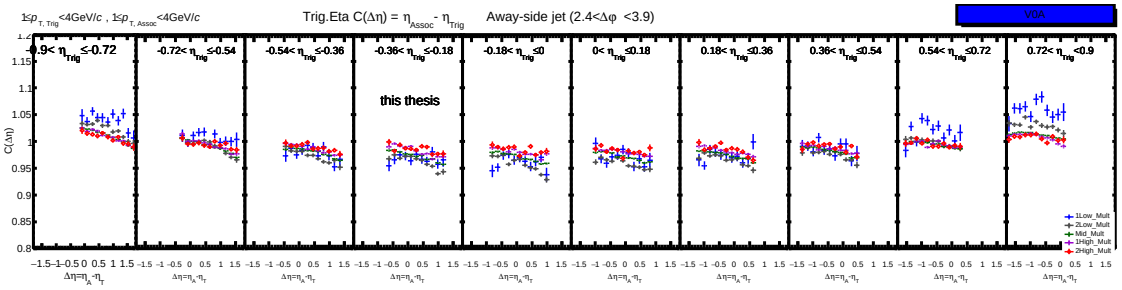

(a) ALICE experimental data, V0A event estimator.

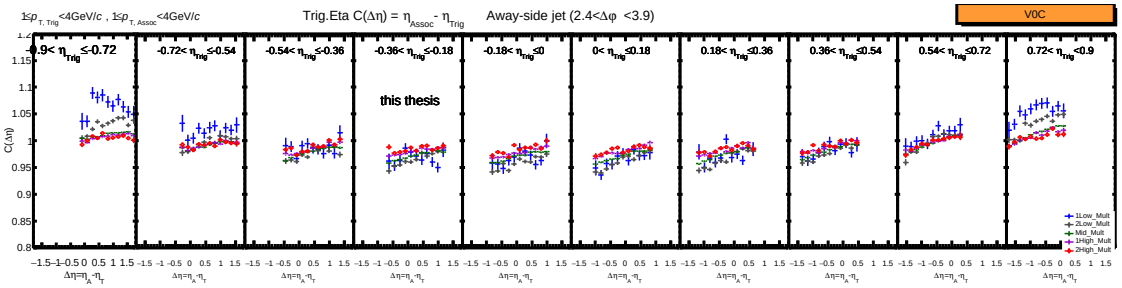

(b) ALICE experimental data, V0C event estimator.

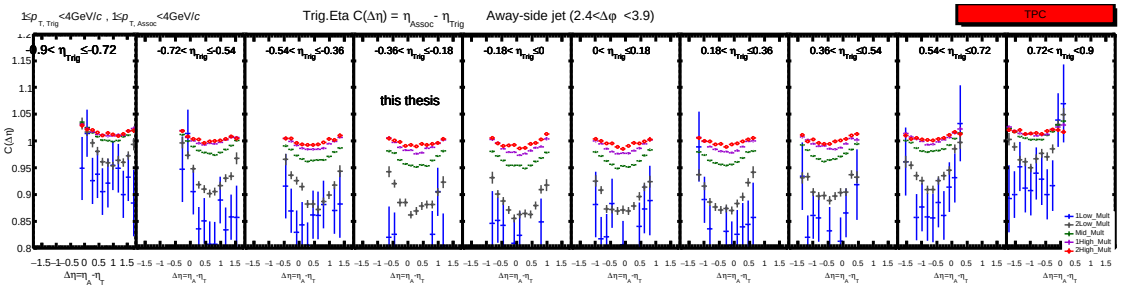

(c) ALICE experimental data, TPC event estimator.

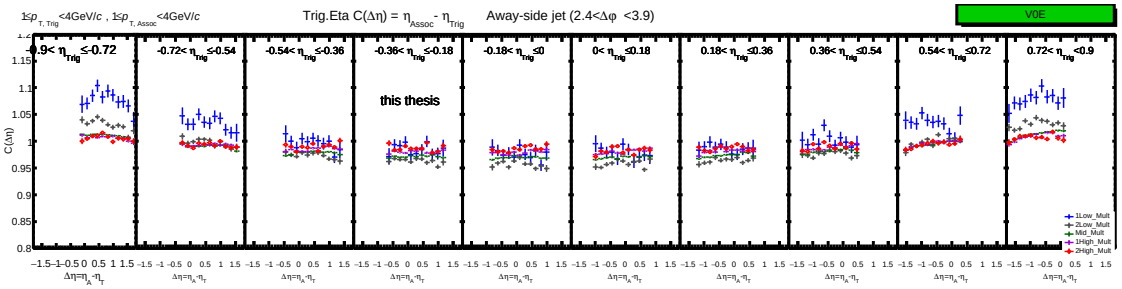

(d) ALICE experimental data, V0E event estimator.

Figure 4.13: ALICE experimental data, the trigger dependence of 1-D correlation functions by various event estimators in pp collisions at $\sqrt{s} = 7$ TeV with $1 \leq p_T^{Trig} < 4$ GeV/c and $1 \leq p_T^{Assoc} < 4$ GeV/c in $2.3 < \Delta\varphi < 3.9$ are shown for the 5 multiplicity classes.

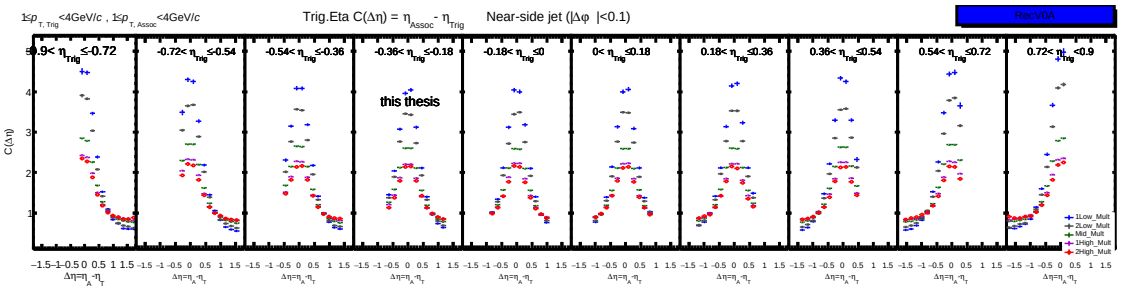

(a) Rec.MC, V0A event estimator.

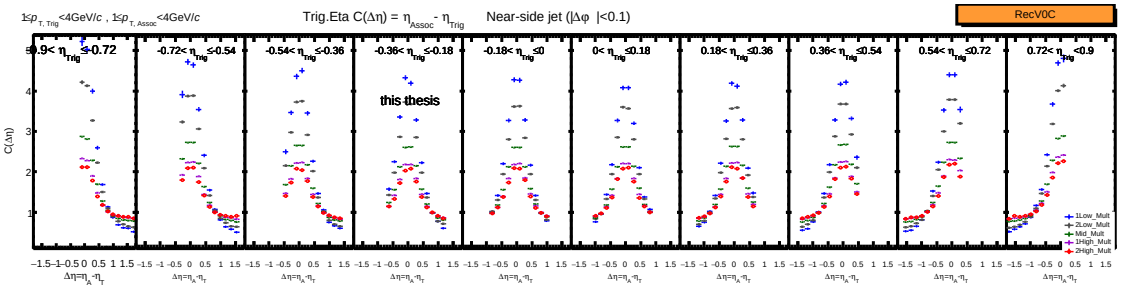

(b) Rec.MC, V0C event estimator.

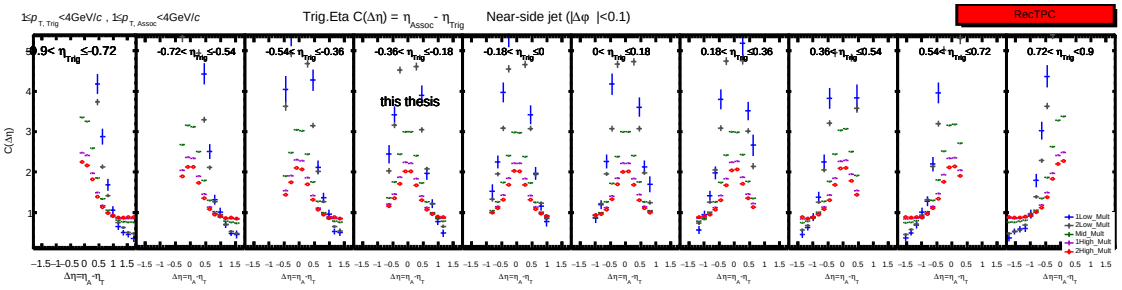

(c) Rec.MC, TPC event estimator.

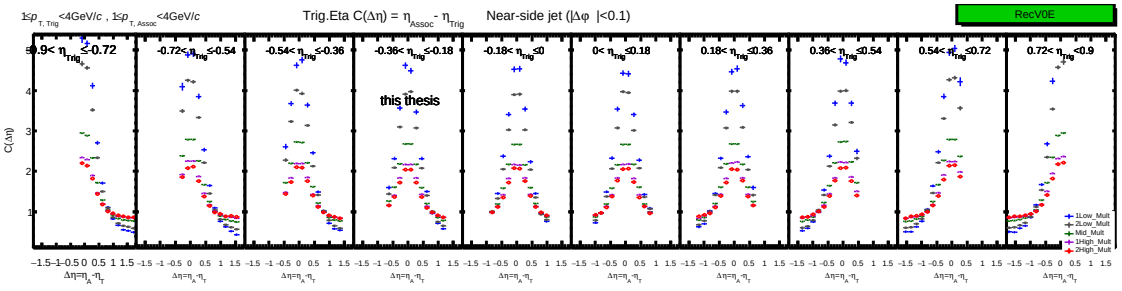

(d) Rec.MC, V0E event estimator.

Figure 4.14: Rec.MC, the trigger dependence of 1-D correlation functions by various event estimators in pp collisions at $\sqrt{s} = 7$ TeV with $1 \leq p_T^{Trig} < 4$ GeV/c and $1 \leq p_T^{Assoc} < 4$ GeV/c in $|\Delta\varphi| < 0.1$ are shown for the 5 multiplicity classes.

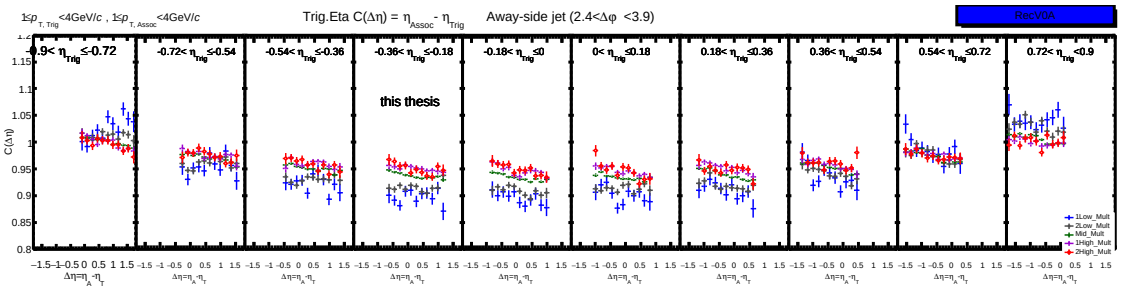

(a) Rec.MC, V0A event estimator.

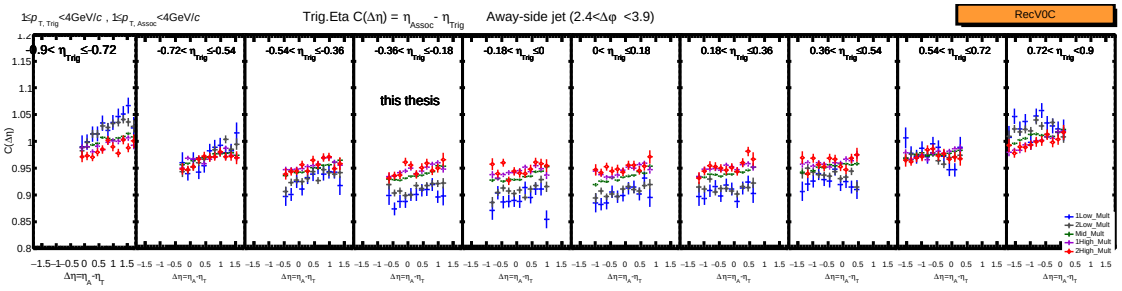

(b) Rec.MC, V0C event estimator.

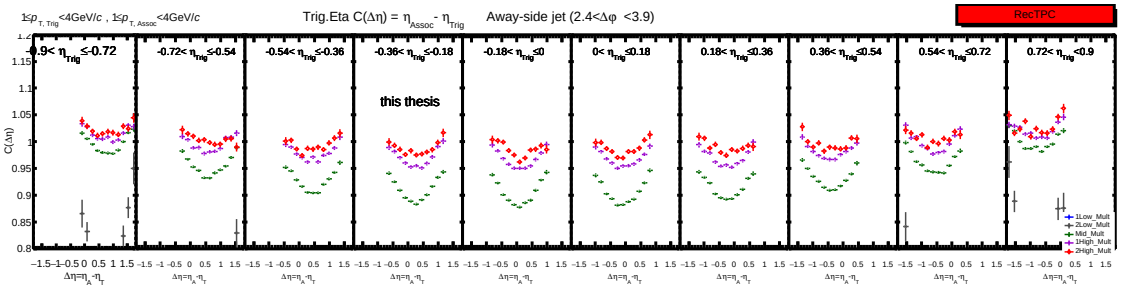

(c) Rec.MC, TPC event estimator.

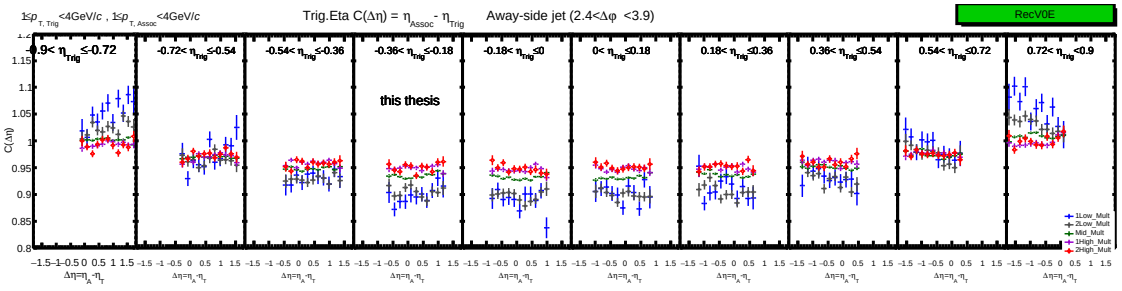

(d) Rec.MC, V0E event estimator.

Figure 4.15: Rec.MC, the trigger dependence of 1-D correlation functions by various event estimators in pp collisions at $\sqrt{s} = 7$ TeV with $1 \leq p_T^{Trig} < 4$ GeV/c and $1 \leq p_T^{Assoc} < 4$ GeV/c in $2.3 < \Delta\varphi < 3.9$ are shown for the 5 multiplicity classes.

4.1.4 $\Delta\varphi$ correlation shape variation as a function of multiplicity

In order to extract a small change in the correlation function shape as a function of event multiplicity, the one dimensional (1-D) $C(\Delta\varphi)$ are fitted by a newly defined function $F(x) = a + bf(x)$, which is given by the renormalized correlation function shape f(x) from the lowest multiplicity. The correlation functions are then divided by the fitted function in order to extract the small deviation between the measured correlation and fitted function. The experimental data ($C(\Delta\varphi)$) with fitted correlation functions ($F(\Delta\varphi)$) for 5 multiplicity classes for $1.5 \leq |\Delta\eta| < 1.8$ are shown in the upper panels in Figure 4.16(a). The ratios $R(\Delta\varphi)$ of correlation data over the fitted functions are shown in lower panels in the same Figure 4.16(a). The ratio $R(\Delta\varphi)$ shows a double peak-like structure in $1.5 \leq |\Delta\eta| < 1.8$ at $\Delta\varphi \approx 0$ and π, that is consistent with elliptic flow-like event shape. The elliptic shapes are becoming more enhanced with increasing multiplicities. On the other hand, Rec.MC Pythia results show negative double peak-like shape at $\Delta\varphi \approx 0$ and π, as shown in Figure 4.16(b). Rec.MC Pythia show an opposite shapes with ALICE experimental data.

v_2^2 parameters (p_2) are extracted by fitting the ratio $R(\Delta\varphi)$ with Fourier function $F(x) = N(1 + 2p_2 cos(2x))$ for 5 multiplicity classes by various event estimators, as shown in Figure 4.17. The elliptic p_2 parameters increase with increasing multiplicities. The elliptic p_2 parameters have no significant $\Delta\eta$ dependence between $1.2 \leq |\Delta\eta| < 1.5$ and $1.5 \leq |\Delta\eta| < 1.8$, except for TPC event estimators.

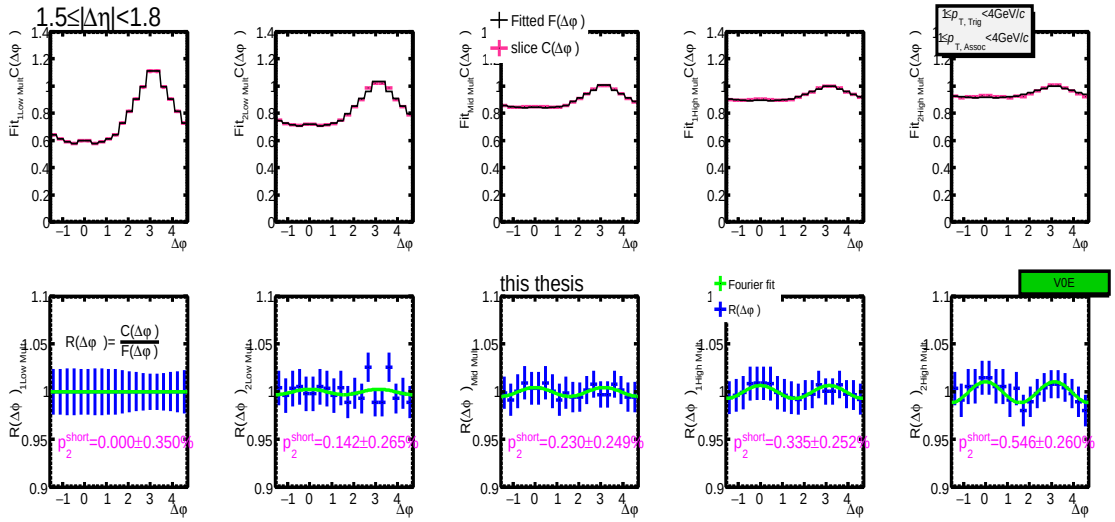

(a) ALICE experimental data, V0E event estimator. Up: $C(\Delta\varphi)$ and the fitted $F(\Delta\varphi)$, Down: $R(\Delta\varphi)$ in $1.5\leq |\Delta\eta| <1.8$ are shown for the 5 multiplicity classes.

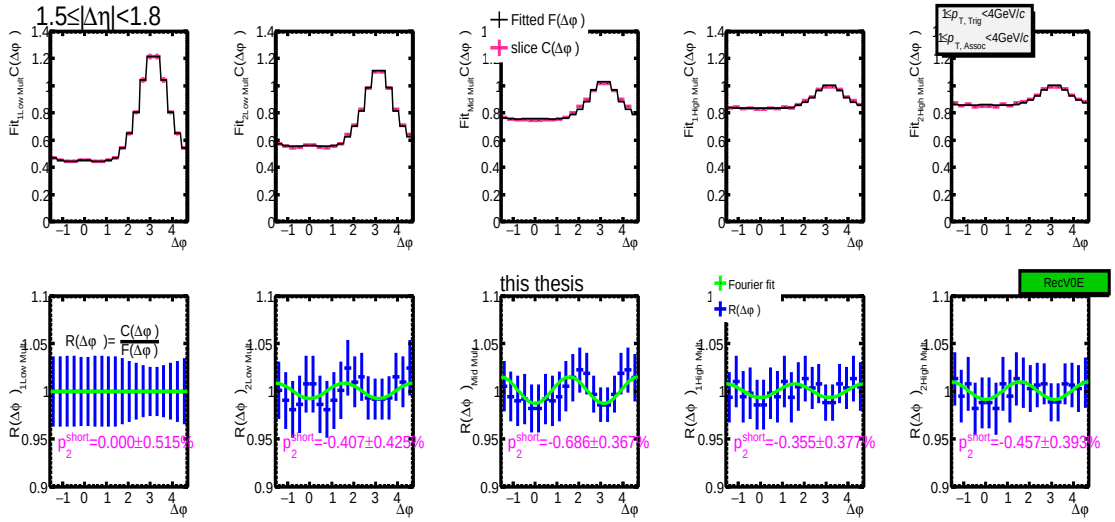

(b) Rec.MC, V0E event estimator. Up: $C(\Delta\varphi)$ and the fitted $F(\Delta\varphi)$, Down: $R(\Delta\varphi)$ in $1.5\leq |\Delta\eta| <1.8$ are shown for the 5 multiplicity classes.

Figure 4.16: The ratio of $C(\Delta\varphi)$ over fitted $F(\Delta\varphi)$ ($R(\Delta\varphi)$) in pp collisions at $\sqrt{s} = 7$ TeV with $1\leq p_T^{Trig} <4$ GeV/c and $1\leq p_T^{Assoc} <4$ GeV/c in slices of $|\Delta\eta|$ are shown for the 5 multiplicity classes.

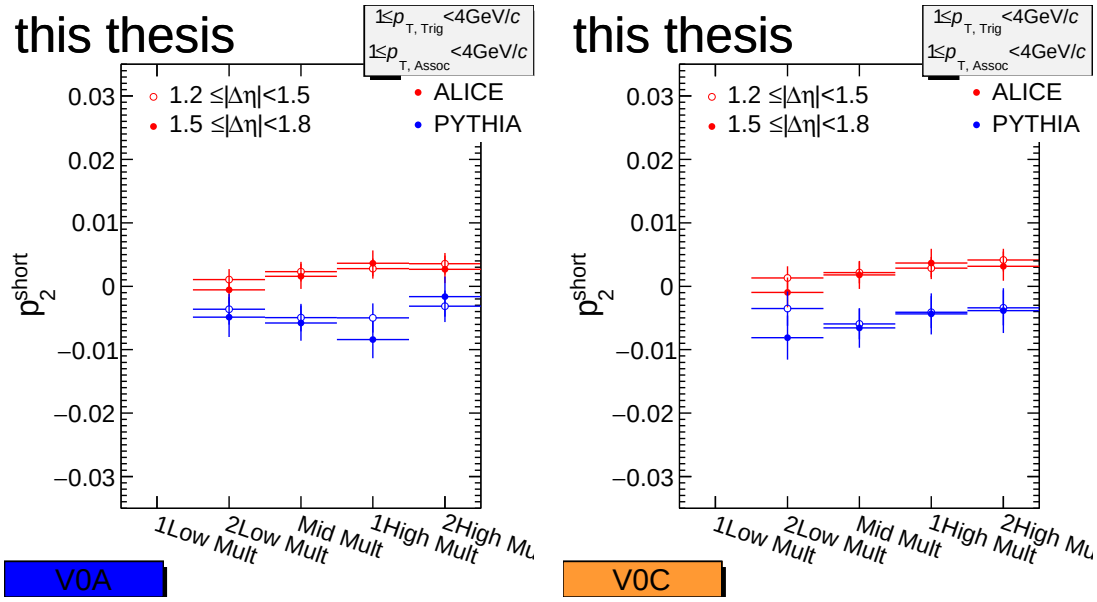

(a) V0A event estimator.

(b) V0C event estimator.

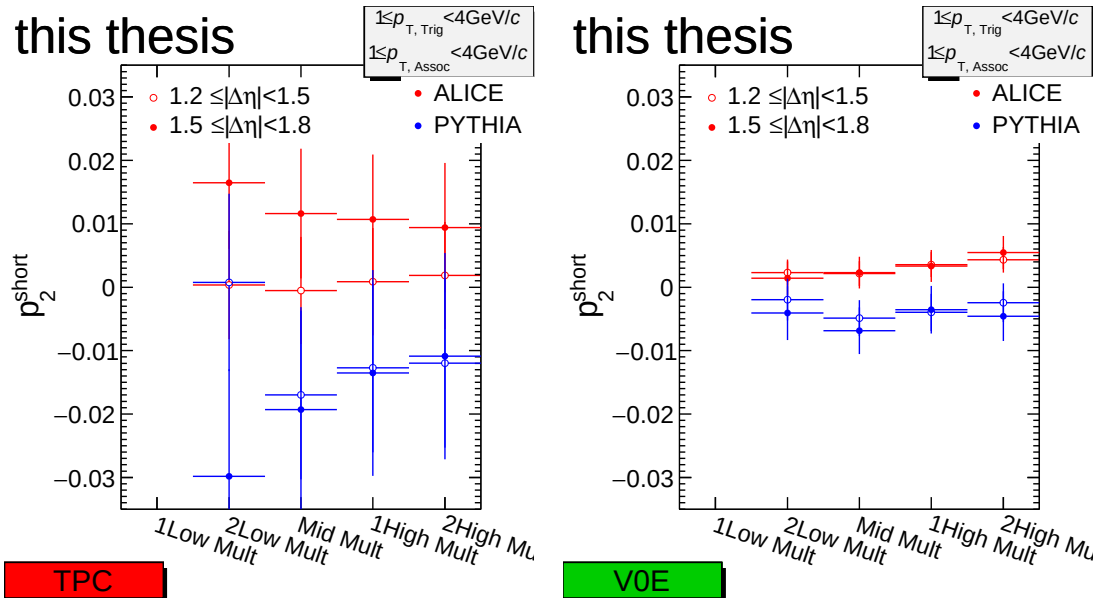

(c) TPC event estimator.

(d) V0E event estimator.

Figure 4.17: Product of two p_2^{short} parameters (for trigger and associate particles) of two-particle correlation with respect to the lowest multiplicity are shown for the 5 multiplicity classes.

4.1.5 Associate particle yield per trigger

In this section, the associated particle yields per trigger are shown as a function of multiplicity by various event estimators. The tracking efficiency is corrected for associated particles as shown in Figure 3.4 and Equation. 3.6. The associated particle yield per trigger are normalized by number of trigger particle from $C(\Delta\varphi)$ in section. 4.1. Figure 4.18 show the associated particle yield per trigger with various event estimators. Table 4.1 show the number of same pair per number of events, the number of mix pair per number of events and the number of trigger particles per number of events. The associated particle yield per trigger particle (background) increases with increasing multiplicities. The enhanced number of one mean event activity is higher for high multiplicity events, such as more enhanced jet or harder event. And there are the ridge structures at $\Delta\varphi \approx 0$ in the highest multiplicity and 2nd highest multiplicity in all various event estimators. TPC event estimator has a very strong effect from auto-correlation between event estimator and number of associated particles per trigger particle. The results of Rec.MC Pythia agree with the increasing background with increasing multiplicities, as shown in Figure 4.19 and Table 4.2. However, Rec.MC Pythia does not reproduce the ridge structure.

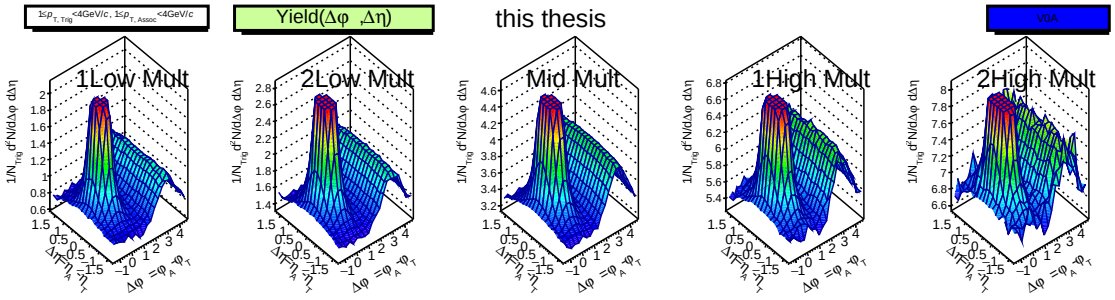

(a) ALICE experimental data, V0A event estimator.

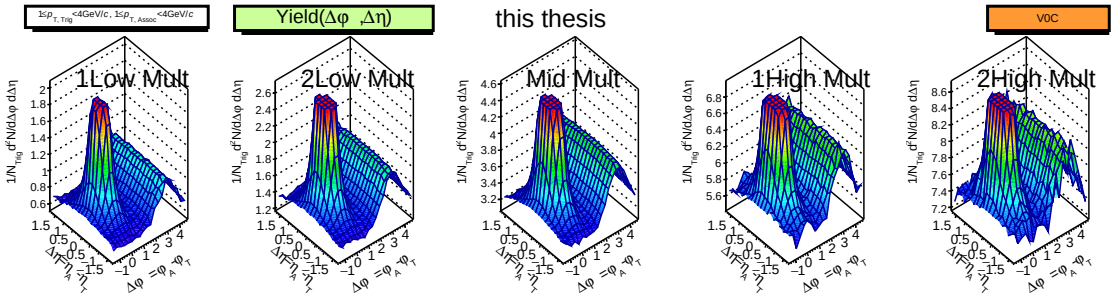

(b) ALICE experimental data, V0C event estimator.

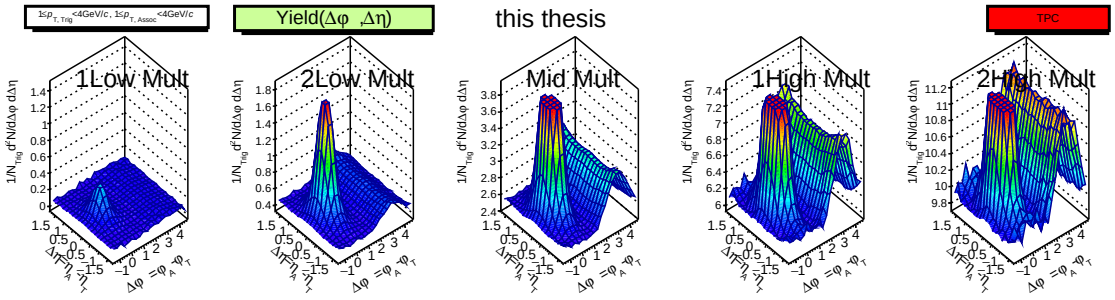

(c) ALICE experimental data, TPC event estimator.

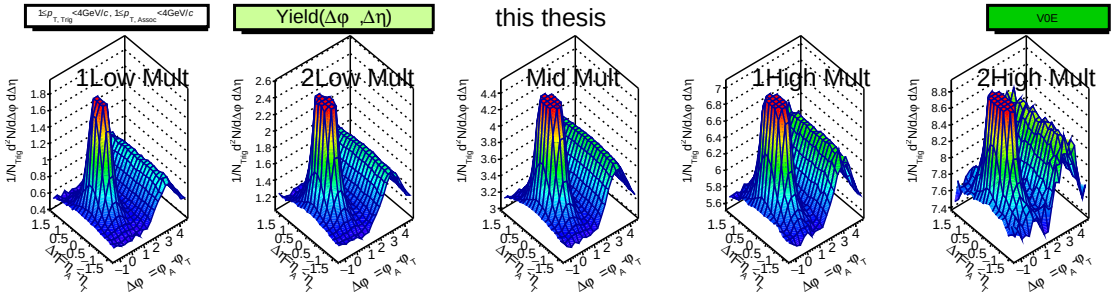

(d) ALICE experimental data, V0E event estimator.

Figure 4.18: ALICE experimental data, TPC-TPC correlations, associated particle yields per trigger by various event estimators in pp collisions at $\sqrt{s} = 7$ TeV with $1 \leq p_T^{Trig} < 4$ GeV/c and $1 \leq p_T^{Assoc} < 4$ GeV/c are shown for the 5 multiplicity classes. Full scale of z axis are fixed to 0.025.

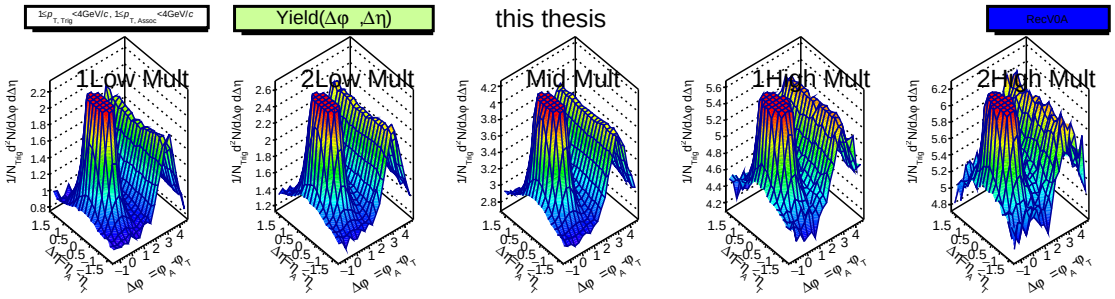

(a) Rec.MC, V0A event estimator.

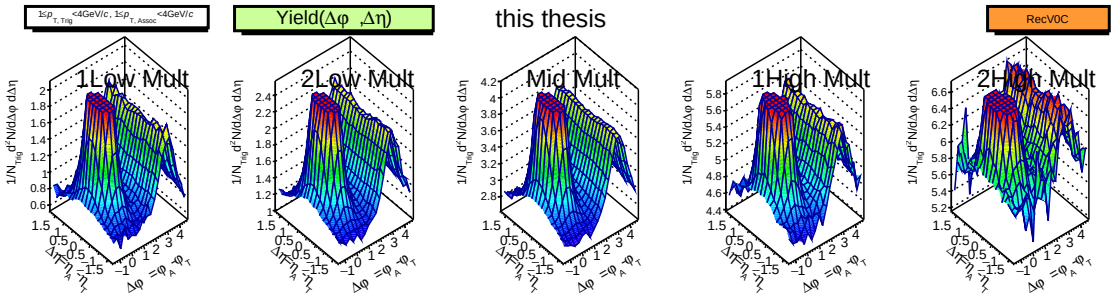

(b) Rec.MC, V0C event estimator.

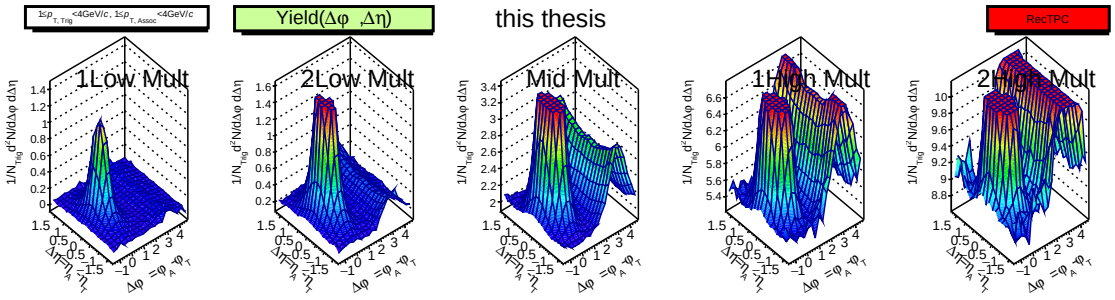

(c) Rec.MC, TPC event estimator.

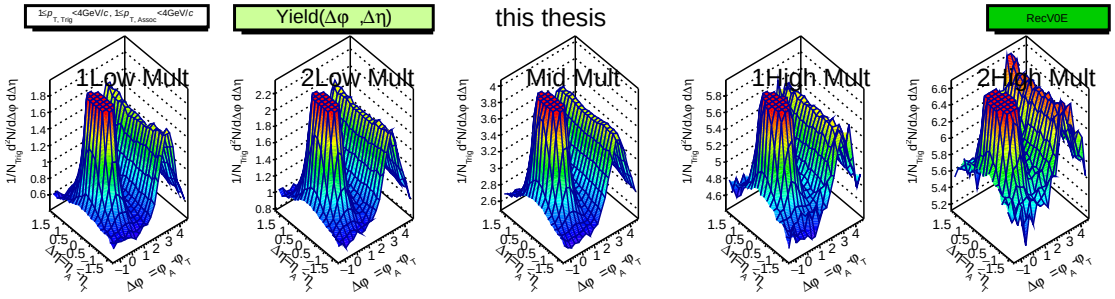

(d) Rec.MC, V0E event estimator.

Figure 4.19: Rec.MC, TPC-TPC correlations, associated particle yields per trigger by various event estimators in pp collisions at $\sqrt{s}$ = 7 TeV with 1$\leq p_T^{Trig}$ <4 GeV/c and 1$\leq p_T^{Assoc}$ <4 GeV/c are shown for the 5 multiplicity classes. Full scale of z axis are fixed to 0.025.

Table 4.1: ALICE experimental data, Number of Same/Event, Number of Mix/Event and Number of Trig/Event, with $1.0 \leq p_{T,Trig} < 4.0$ GeV/c, $1.0 \leq p_{T,Associ} < 4.0$ GeV/c

V0A Event	Num.of Same/Event	Num.of Mix/Event	Num.of Trig/Event
	Exp.	Bit5.	
1Low Mult , 20911702	0.27	0.90	0.32
2Low Mult , 30985612	0.93	3.65	0.64
Mid Mult , 45875940	4.72	23.82	1.62
1High Mult , 4426129	14.69	95.14	3.22
2High Mult , 911894	22.41	154.05	3.99
V0C Event	Num.of Same/Event	Num.of Mix/Event	Num.of Trig/Event
	Exp.	Bit5.	
1Low Mult , 20898842	0.22	0.75	0.29
2Low Mult , 31390292	0.81	3.24	0.60
Mid Mult , 46195596	4.72	24.81	1.65
1High Mult , 3626366	16.72	115.70	3.54
2High Mult , 1000182	27.32	198.66	4.54
TPC Event	Num.of Same/Event	Num.of Mix/Event	Num.of Trig/Event
	Exp.	Bit5.	
1Low Mult , 20671352	0.01	0.09	0.10
2Low Mult , 33773456	0.18	1.37	0.39
Mid Mult , 43868288	3.93	28.07	1.76
1High Mult , 3837517	25.12	219.87	4.89
2High Mult , 960668	60.72	523.85	7.37
V0E Event	Num.of Same/Event	Num.of Mix/Event	Num.of Trig/Event
	Exp.	Bit5.	
1Low Mult , 21367722	0.17	0.59	0.26
2Low Mult , 30817194	0.71	2.98	0.57
Mid Mult , 45723284	4.59	24.71	1.65
1High Mult , 4336193	17.26	121.55	3.64
2High Mult , 866886	29.55	218.83	4.75

Table 4.2: Rec.MC, Number of Same/Event, Number of Mix/Event and Number of Trig/Event, with $1.0 \leq p_{T,Trig} < 4.0$ GeV/c, $1.0 \leq p_{T,Associ} < 4.0$ GeV/c

V0A Event	Num.of Same/Event	Num.of Mix/Event	Num.of Trig/Event
	Rec.	Bit5.	
1Low Mult , 8847576	0.39	0.96	0.32
2Low Mult , 10889476	0.90	2.87	0.56
Mid Mult , 18132472	3.78	16.36	1.34
1High Mult , 1536537	9.97	59.66	2.48
2High Mult , 558219	11.77	72.74	2.63
V0C Event	Num.of Same/Event	Num.of Mix/Event	Num.of Trig/Event
	Rec.	Bit5.	
1Low Mult , 8566373	0.33	0.82	0.29
2Low Mult , 11535947	0.77	2.51	0.51
Mid Mult , 17950728	3.79	17.23	1.37
1High Mult , 1540461	11.59	74.98	2.78
2High Mult , 370772	15.16	104.60	3.07
TPC Event	Num.of Same/Event	Num.of Mix/Event	Num.of Trig/Event
	Rec.	Bit5.	
1Low Mult , 11522325	0.01	0.06	0.08
2Low Mult , 8416531	0.10	0.71	0.28
Mid Mult , 18320258	2.96	19.40	1.46
1High Mult , 1402751	21.71	191.38	4.44
2High Mult , 302416	47.24	412.21	6.00
V0E Event	Num.of Same/Event	Num.of Mix/Event	Num.of Trig/Event
	Rec.	Bit5.	
1Low Mult , 8530249	0.24	0.61	0.25
2Low Mult , 8446374	0.59	1.93	0.45
Mid Mult , 21003516	3.38	14.84	1.27
1High Mult , 1468465	11.72	76.25	2.80
2High Mult , 515678	15.40	104.82	3.15

4.1.6 Subtraction of flat background (average zyam: zero-yield at minimum)

This section shows the results after subtraction of a flat background (zyam: zero-yield at minimum) from associated particle yields per trigger ($Sub.Y(\Delta\varphi, \Delta\eta)$) for 5 multiplicity classes by various event estimators. Two dimensional associate yield per trigger ($\Delta\varphi$, $\Delta\eta$) is projected to one dimensional yield ($\Delta\varphi$) for several $|\Delta\eta|$ slices ,$0.6 < |\Delta\eta| \leq 1.0$, $1 < |\Delta\eta| \leq 1.4$ and $1.4 < |\Delta\eta| \leq 1.8$, as shown in Figure 4.20 and Figure 4.21. $|\Delta\eta| \leq$0.2

and 0.2< $|\Delta\eta\|leq0.6$ of one are shown in Appendix D.1. After the subtraction of flat background, ALICE experimental results, as shown in Figure 4.20, show the difference of the particle yield per trigger particle in $\Delta\varphi \approx 0$ and π between 5 events multiplicity classes. The near side yield decreases with increasing the $\Delta\eta$ gap, which is given by the η width of jet cone, and the near side yield generally increases with multiplicity because of the ridge structure in the highest multiplicity and 2nd highest multiplicity. Especially the yield at large $\Delta\eta$ shows almost flat distribution at $\Delta\varphi \approx 0$ in low multiplicity events, which means there is almost no near-side jet contribution, however the distribution at $\Delta\varphi \approx 0$ shows more peak-like structure (the ridge structure) in the highest multiplicity and 2nd highest multiplicity. Rec.MC Pythia results, as shown in Figure 4.21, do not show the difference of the particle yield per trigger particle in $\Delta\varphi \approx 0$ and π between 5 events multiplicity classes, except for TPC event estimator. The comparison between 5 multiplicity classes enhances the ridge yield in $\Delta\varphi \approx 0$ in the highest multiplicity and 2nd highest multiplicity. And the comparison between ALICE experimental results and Rec.MC Pythia tells us information of ridge yield at $\Delta\varphi \approx 0$ and away side jet yield $\Delta\varphi \approx \pi$.

In order to quantify the multiplicity dependence of per-trigger-particle associated yield, the associated yields are integrated in -0.8$\leq \Delta\varphi \leq$0.8 (near side) and 2.3$< \Delta\varphi <$3.9 (away side). The integrated yields of near side jets and away side jets are found to rise with increasing multiplicity selections with various event estimators, shown in Figure 4.22. For a given slice $|\Delta\eta|$, the integrated yields of near side (-0.8$\leq \Delta\varphi \leq$0.8) increase with increasing multiplicity especially for small $|\Delta\eta|$ range by various event estimators. And the integrated yields of away side (2.3$< \Delta\varphi <$3.9) for 5 multiplicity classes by various event estimators show similar multiplicity trends for different $|\Delta\eta|$ slices as expected from the relatively large η swing of di-jet production compared to the ALICE TPC acceptance ($|\eta| < 0.9$). This tells us that jet is responsible for this increase. In case of TPC event estimator, the integrated yields show strong multiplicity dependence caused by the trivial auto-correlation from the multiplicity definition in the same acceptance. Rec.MC Pythia shows a different multiplicity trend from ALICE experimental data. Because Rec.MC Pythia cannot describe jet at low p_T region.

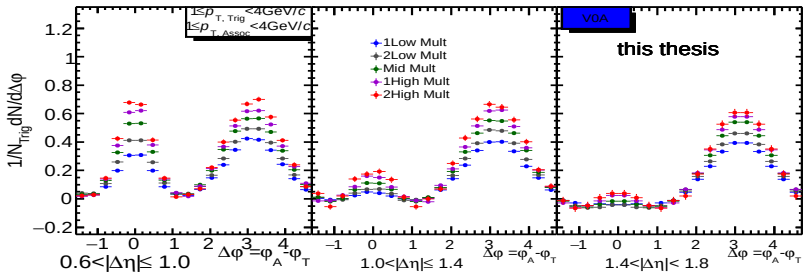

(a) ALICE experimental data, V0A event estimator.

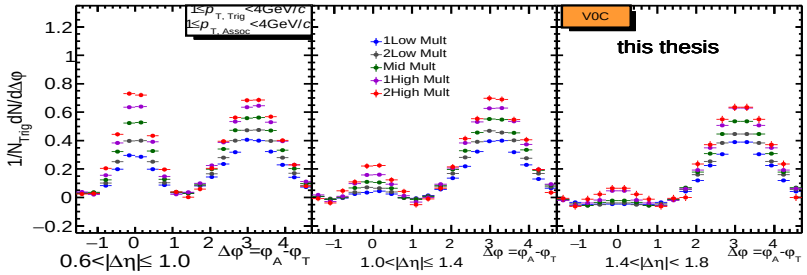

(b) ALICE experimental data, V0C event estimator.

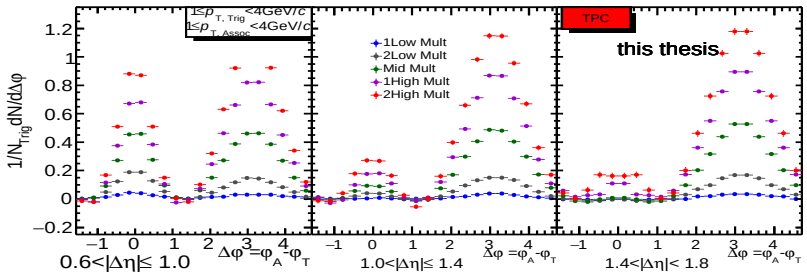

(c) ALICE experimental data, TPC event estimator.

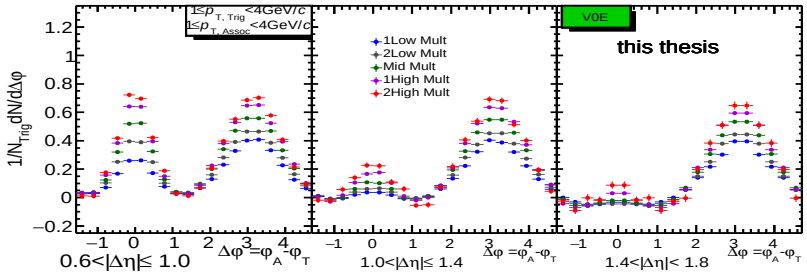

(d) ALICE experimental data, V0E event estimator.

Figure 4.20: ALICE experimental data, the subtracted flat background of associated particle yields per trigger in pp collisions at $\sqrt{s} = 7$ TeV with $1 \leq p_T^{Trig} < 4$ GeV/c and $1 \leq p_T^{Assoc} < 4$ GeV/c in $0.6 < |\Delta\eta| \leq 1.0$, $1.0 < |\Delta\eta||leq1.4$ and $1.4 < |\Delta\eta| \leq 1.8$ are shown for the 5 multiplicity classes.

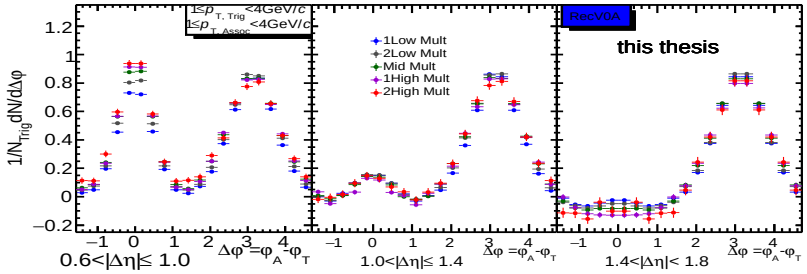

(a) Rec.MC, V0A event estimator.

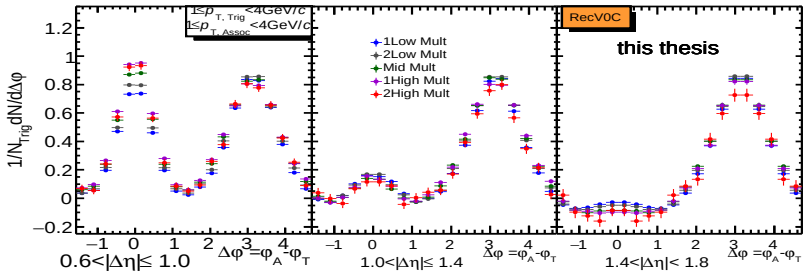

(b) Rec.MC, V0C event estimator.

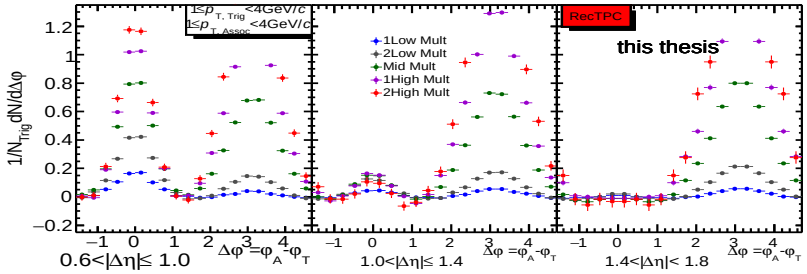

(c) Rec.MC, TPC event estimator.

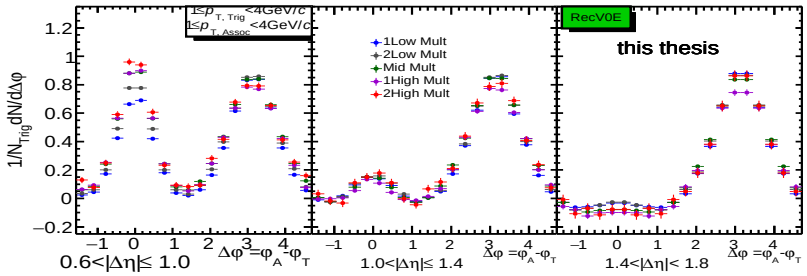

(d) Rec.MC, V0E event estimator.

Figure 4.21: Rec.MC, the subtracted flat background of associated particle yields per trigger in pp collisions at $\sqrt{s}$ = 7 TeV with 1≤ p_T^{Trig} <4 GeV/c and 1≤ p_T^{Assoc} <4 GeV/c in $0.6 < |\Delta\eta| \leq 1.0$, $1.0 < |\Delta\eta| \leq 1.4$ and $1.4 < |\Delta\eta| \leq 1.8$ are shown for the 5 multiplicity classes.

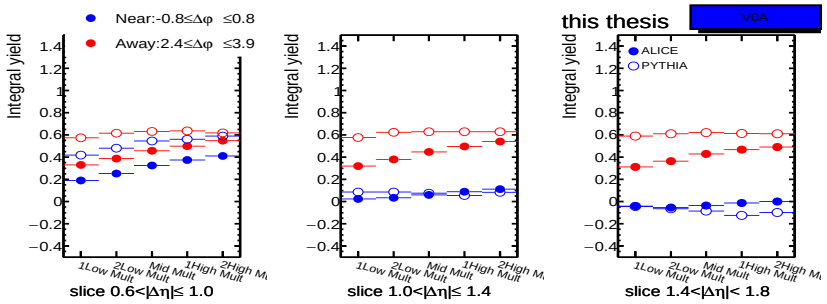

(a) V0A event estimator.

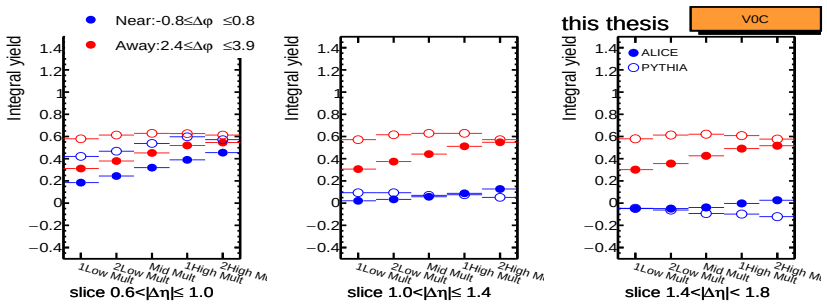

(b) V0C event estimator.

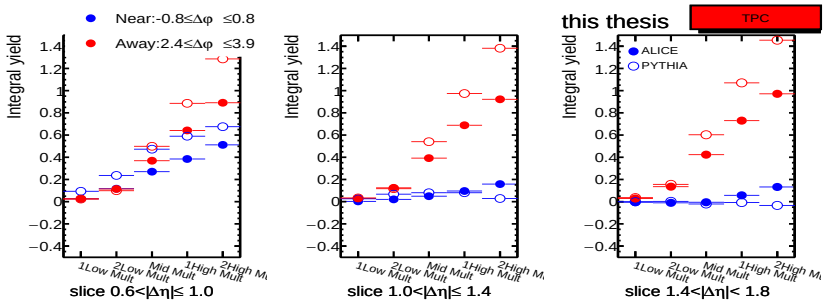

(c) TPC event estimator.

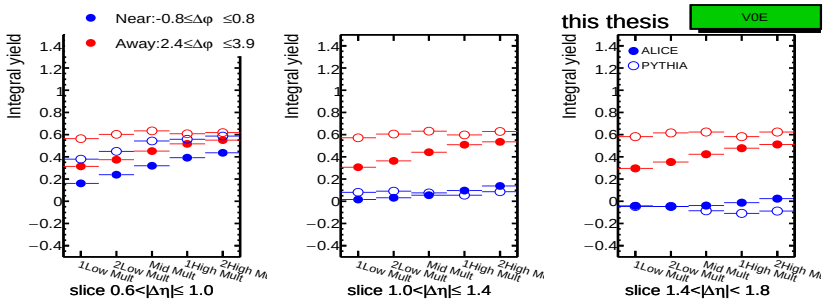

(d) V0E event estimator.

Figure 4.22: The integration yield of $-0.8 \leq \Delta\varphi \leq 0.8$ (near side jets) and $2.3 < \Delta\varphi < 3.9$ (away side jets) in pp collisions at $\sqrt{s} = 7$ TeV with $1 \leq p_T^{Trig} < 4$ GeV/c and $1 \leq p_T^{Assoc} < 4$ GeV/c are shown for the 5 multiplicity classes.

4.1.7 Extraction of double ridges (high mult. - low mult. yield)

This section shows the results of per-trigger-particle associate yield subtraction of lower multiplicity from higher multiplicity with various event estimators. Two dimensional $(\Delta\varphi, \Delta\eta)$ associate yield per trigger particle shows three features. The near side jets at $(\Delta\varphi, \Delta\eta) \approx (0, 0)$ are different with multiplicity selections. There are the enhanced peaks in $\Delta\varphi \approx 0$ and π in long range $\Delta\eta$ with similar magnitude, which is called a double ridge. In case of Rec.MC Pythia (PYTHIA Monte Carlo simulation), there are negative-correlation at $\Delta\varphi \approx 0$ and π instead of double ridges, as shown in Figure 4.23.

The projected one dimensional per-trigger associate yields for various event estimators are shown in Figure 4.24. The comparisons between ALICE experimental data and Rec.MC clearly show double ridge in experimental data and an opposite effect or very small effect (negaitve/double ridge or almost flat distribution) in PYTHIA simulation. Double ridge structures show slightly higher magnitude in away side ($\Delta\varphi \approx \pi$) than near side ($\Delta\varphi \approx 0$). However, PYTHIA simulation shows that the associate yield per trigger is larger (or jet-like correlation is stronger) in lower multiplicity than higher multiplicity.

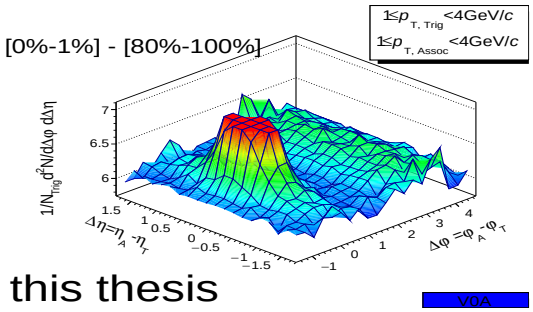

(a) ALICE experimental data, V0A event estimator.

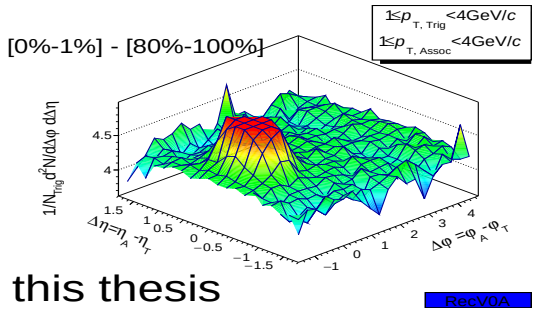

(b) Rec.MC, V0A event estimator.

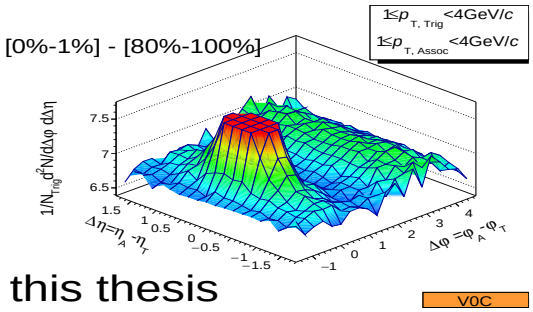

(c) ALICE experimental data, V0C event estimator.

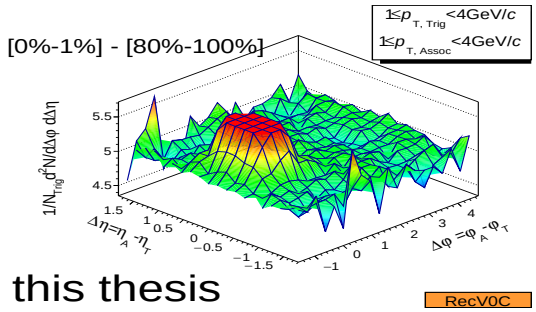

(d) Rec.MC, V0C event estimator.

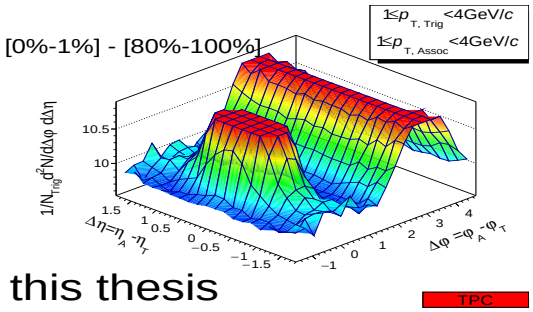

(e) ALICE experimental data, TPC event estimator.

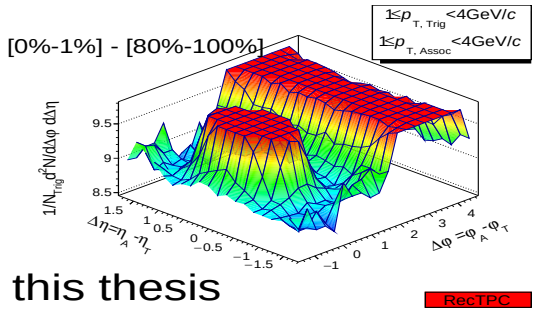

(f) Rec.MC, TPC event estimator.

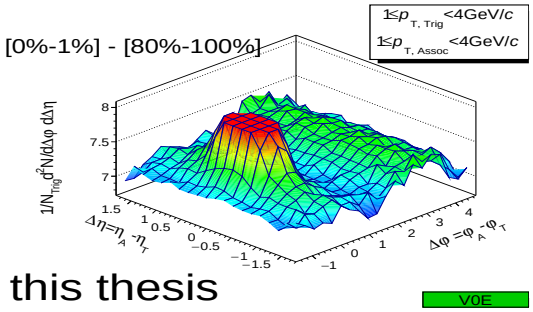

(g) ALICE experimental data, V0E event estimator.

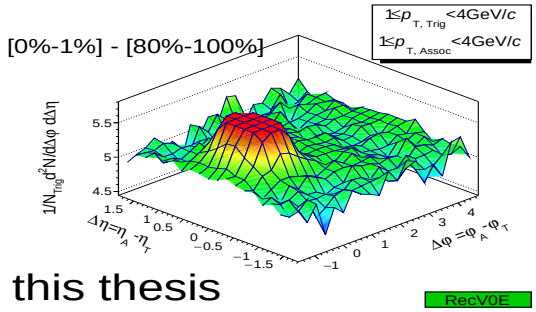

(h) Rec.MC, V0E event estimator.

Figure 4.23: The subtraction of lower multiplicity from higher multiplicity of 2-D particle yield per trigger particle that are $[0\% - 1\%] - [80\% - 100\%]$ with $1 \leq p_T^{Trig} < 4$ GeV/c and $1 \leq p_T^{Assoc} < 4$ GeV/c are shown for various event estimators. (a), (c), (e), (g) show ALICE experimental data and (b), (d), (f), (h) show Rec.MC. Full scale of z axis are fixed to 1.3.

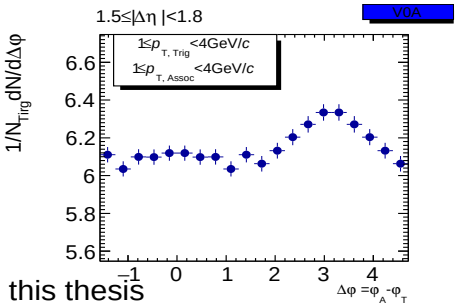

(a) ALICE experimental data, V0A event estimator.

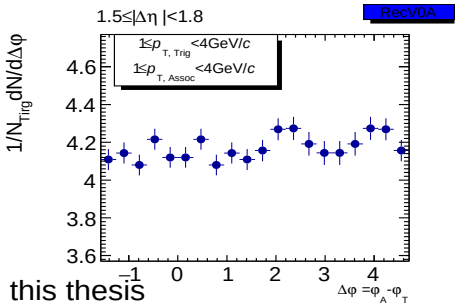

(b) Rec.MC, V0A event estimator.

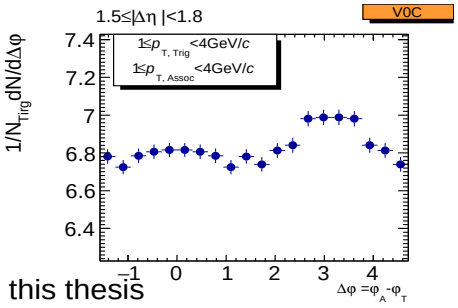

(c) ALICE experimental data, V0C event estimator.

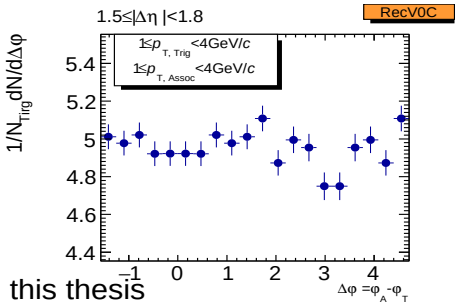

(d) Rec.MC, V0C event estimator.

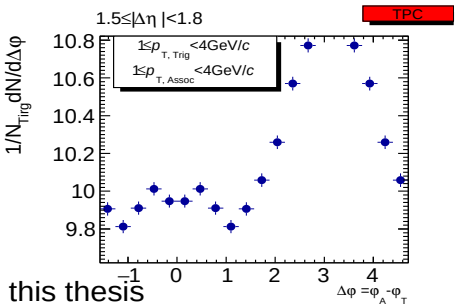

(e) ALICE experimental data, TPC event estimator.

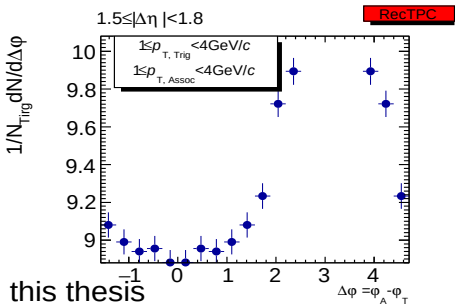

(f) Rec.MC, TPC event estimator.

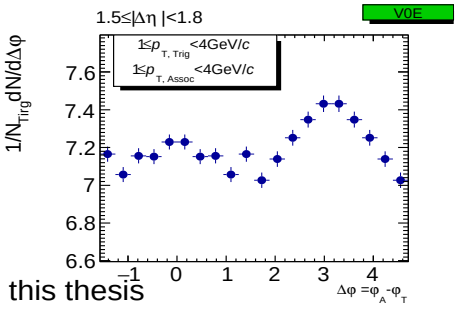

(g) ALICE experimental data, V0E event estimator.

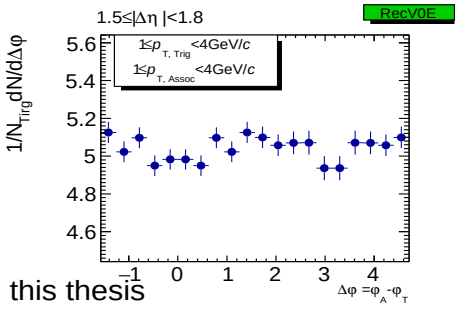

(h) Rec.MC, V0E event estimator.

Figure 4.24: The subtraction of lower multiplicity from higher multiplicity of 1-D particle yield per trigger particle that are $[0\% - 1\%] - [80\% - 100\%]$ with $1 \leq p_T^{Trig} < 4$ GeV/c and $1 \leq p_T^{Assoc} < 4$ GeV/c in $1.5 \leq |\Delta\eta| < 1.8$ are shown for various event estimators. (a), (c), (e), (g) show ALICE experimental data and (b), (d), (f), (h) show Rec.MC. Full scale of y axis are fixed to 1.2.

4.2 Large $\Delta\eta$ correlation with V0-TPC correlation

This section shows the result of long range $|\Delta\eta|$ correlation functions. V0-TPC correlation function is defined by trigger particle in TPC at $1 \leq p_T^{Trig} < 4$ GeV/c and associate particle in V0 rings with $|\Delta\eta|$ of about 2∼5. In order to have similar η acceptance between forward and backward η acceptances of V0 rings, V0C 0, 1 rings ($p^{Assoc}_{V0C0,1Rings}$, $-3.7 < \Delta\eta < -2.7$) and V0A 2, 3 rings ($p^{Assoc}_{V0A2,3Rings}$, $2.8 < \Delta\eta < 3.9$) are selected. Because V0 detector only measures the total number of charged particles in the detector segments, low p_T particles dominate the V0 signal. In order to comparer with small $|\Delta\eta|$ correlation, the results of TPC-TPC correlation with $1 \leq p_T^{Trig} < 4$ GeV/c and $0.2 \leq p_T^{Assoc} < 10$ GeV/c are additionally calculated.

4.2.1 Two-particle correlation shape comparison

This section shows the multiplicity dependence of the long range $\Delta\eta$ correlation functions obtained by various event estimators. The different η gap of event estimators with 5 multiplicity classes cause the strong slopes in correlation magnitude along $\Delta\eta$ axis, shown in Appendix E.1. However, the shapes of minimum bias without event estimator (no event mixing in multiplicity class) show the symmetric slopes both V0A-TPC and V0C-TPC correlations, as shown in Figure 4.25 and Figure 4.26 for 1-D projection $C(\Delta\varphi)$. 1-D projected correlation functions for 5 multiplicity classes with various event estimators are shown in Figure 4.27, Figure 4.28 for experimental $\Delta\varphi$ and pythia simulation, respectively.

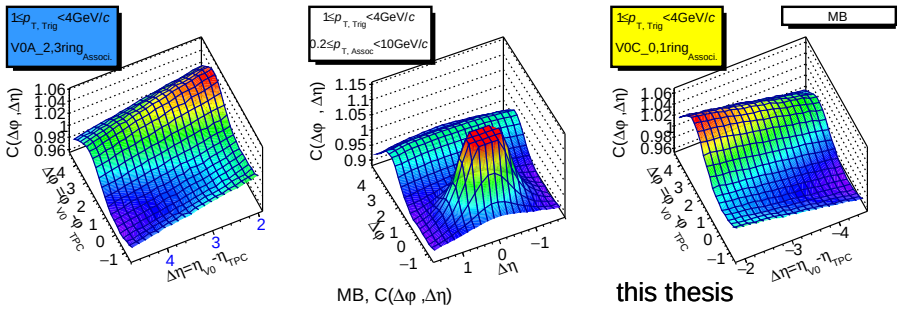

(a) ALICE experimental data, MB.

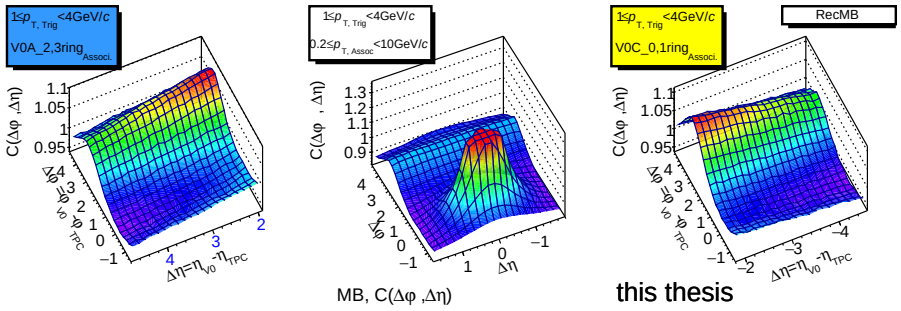

(b) Rec.MC, MB.

Figure 4.25: 2-D dihadron correlation functions of V0A-TPC, TPC-TPC and V0C-TPC in pp collisions at $\sqrt{s} = 7$ TeV are shown for the minimum bias (MB).

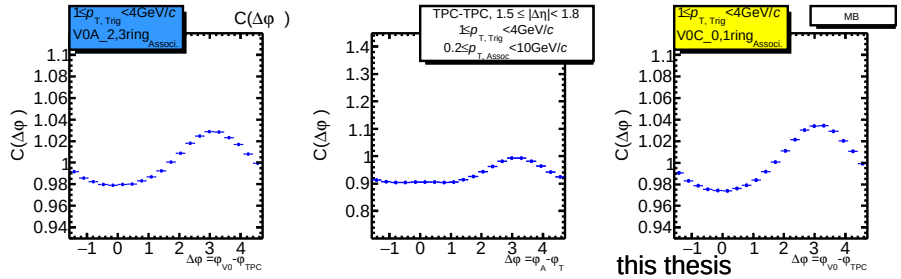

(a) ALICE experimental data, MB.

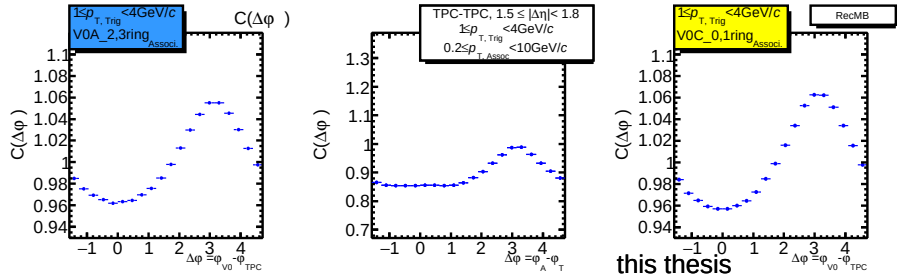

(b) Rec.MC, MB.

Figure 4.26: 1-D dihadron correlation functions of V0A-TPC, TPC-TPC and V0C-TPC in pp collisions at $\sqrt{s} = 7$ TeV in long range approximate 1.9< $\Delta\eta$ <4.8, 1.5≤ $|\Delta\eta|$ <1.8 and -1.8< $\Delta\eta$ <-4.6 are shown for the minimum bias (MB).

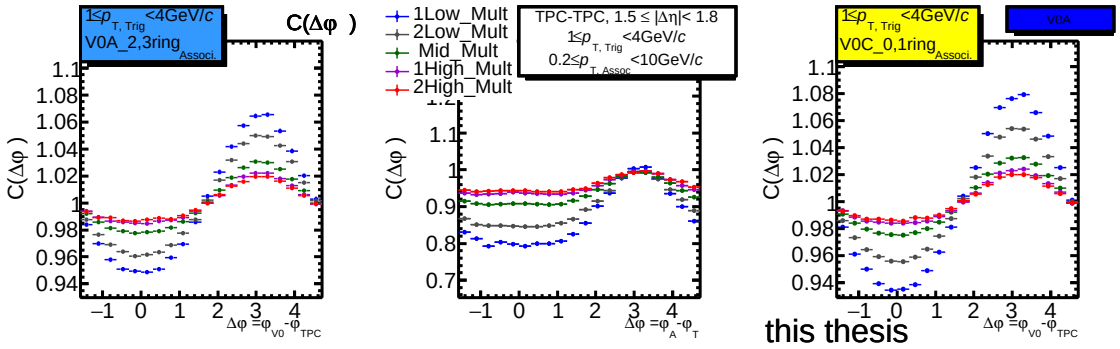

(a) ALICE experimental data, V0A event estimator.

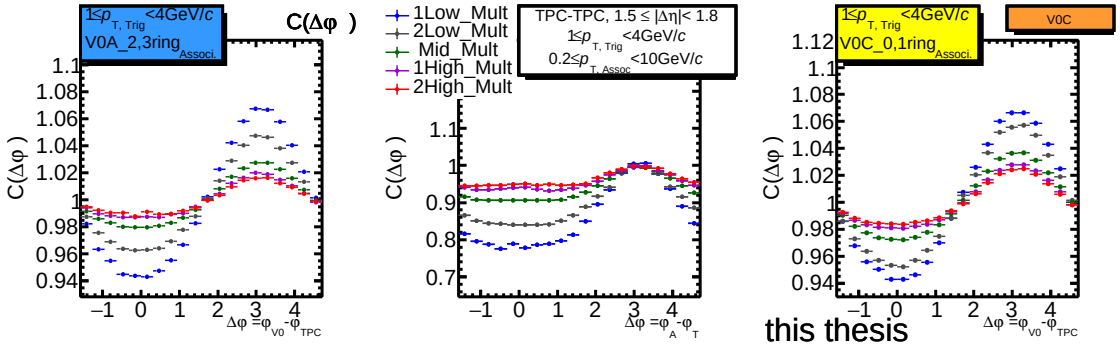

(b) ALICE experimental data, V0C event estimator.

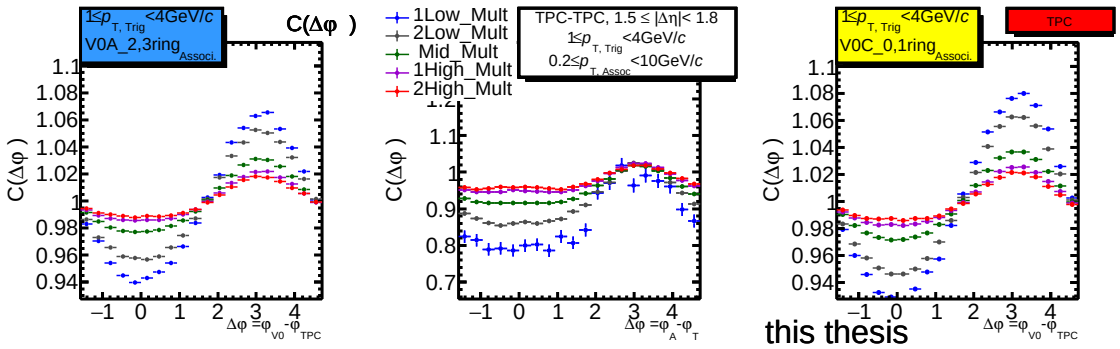

(c) ALICE experimental data, TPC event estimator.

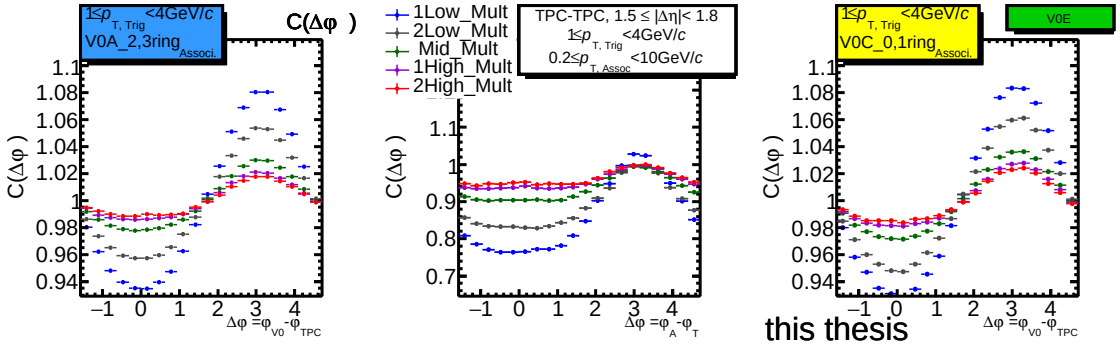

(d) ALICE experimental data, V0E event estimator.

Figure 4.27: ALICE experimental data, 1-D dihadron correlation functions of V0A-TPC, TPC-TPC and V0C-TPC by various event estimators in pp collisions at $\sqrt{s} = 7$ TeV in long range approximate 1.9< $\Delta\eta$ <4.8, 1.5≤ $|\Delta\eta|$ <1.8 and -1.8< $\Delta\eta$ <-4.6 are shown for the 5 multiplicity classes.

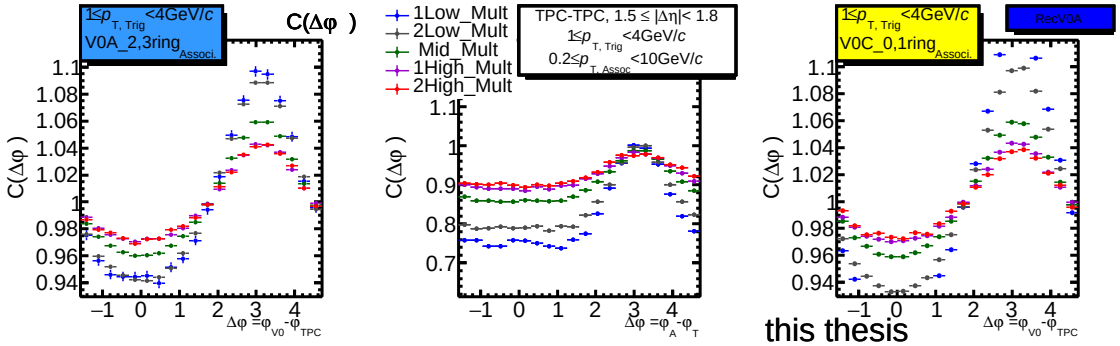

(a) Rec.MC, V0A event estimator.

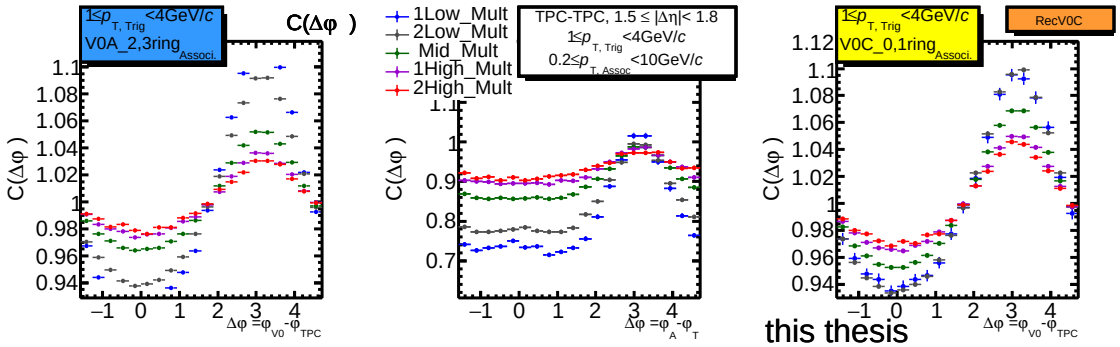

(b) Rec.MC, V0C event estimator.

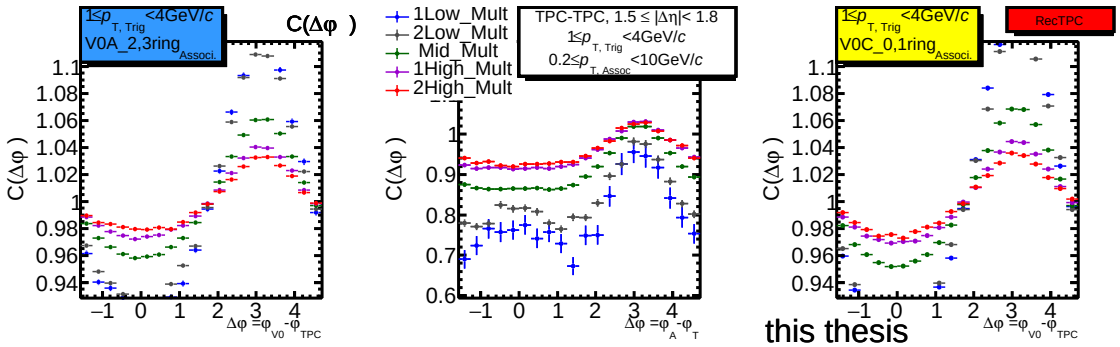

(c) Rec.MC, TPC event estimator.

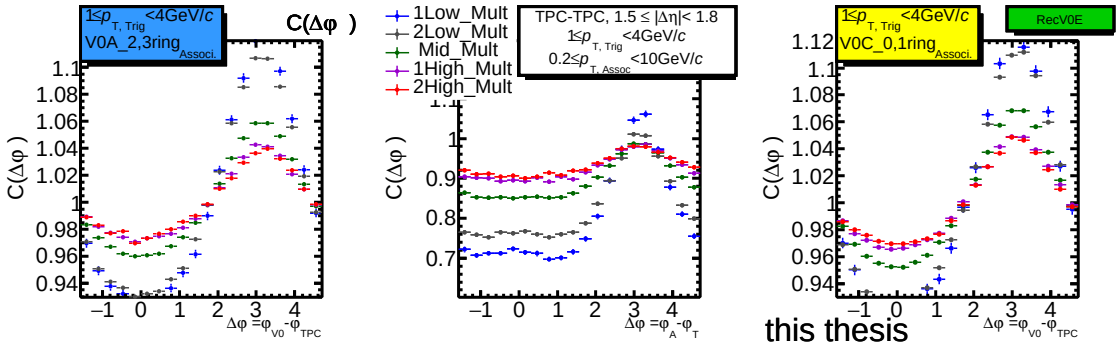

(d) Rec.MC, V0E event estimator.

Figure 4.28: Rec.MC, 1-D dihadron correlation functions of V0A-TPC, TPC-TPC and V0C-TPC by various event estimators in pp collisions at $\sqrt{s} = 7$ TeV in long range approximate 1.9< $\Delta\eta$ <4.8, 1.5≤ $|\Delta\eta|$ <1.8 and -1.8< $\Delta\eta$ <-4.6 are shown for the 5 multiplicity classes.

4.2.2 $\Delta\varphi$ correlation shape variation as a function of multiplicity

In order to extract a small change in V0-TPC correlation function shape as a function of event multiplicity, the one dimensional (1-D) $\Delta\varphi$ correlation functions are fitted by a newly defined function $F(x) = a + bf(x)$, which is given by the renormalized correlation function shape f(x) from the lowest multiplicity, as discussed in section 4.1.4. $R(\Delta\varphi)$ (=$C(\Delta\varphi)/F(\Delta\varphi)$) of V0-TPC correlation show up to 1.8< $|\Delta\eta|$ <4.8 for 5 multiplicity classes by various event estimators. Figure 4.29 shows the part of Figure 3.13 which is "Away from V0C" side with V0A event estimator in $-4.8 < \Delta\eta < -3.8$. Upper panels show $F(\Delta\varphi)$ and $C(\Delta\varphi)$. Lower panels show the ratio $R(\Delta\varphi)$. The ratio $R(\Delta\varphi)$ shows a double peak-like structure at $\Delta\varphi \approx 0$ and π, which is consistent with elliptic flow-like event shape, The elliptic shapes are becoming more enhanced with increasing multiplicities, as shown in Figure 4.2.2. On the other hand, Rec.MC Pythia results show negative double peak-like shape at $\Delta\varphi \approx 0$ and π, as shown in Figure 4.2.2. Rec.MC Pythia show opposite shapes with ALICE experimental data.

Figure 4.30 and Figure 4.31 show the combined $R(\Delta\varphi)$ in 1.8< $|\Delta\eta|$ <4.8, which are V0C 0, 1 rings ($p^{Assoc}_{V0C0,1Rings}$) and V0A 2, 3 rings ($p^{Assoc}_{V0A2,3Rings}$). The extracted elliptic p_2 parameters of the combined $R(\Delta\varphi)$, as shown in Figure 4.32. The p_2 parameters are increasing with increasing multiplicity in 1.8< $|\Delta\eta|$ <4.8. However, Rec.MC Pythia shows negative p_2 parameters in all multiplicity ranges.

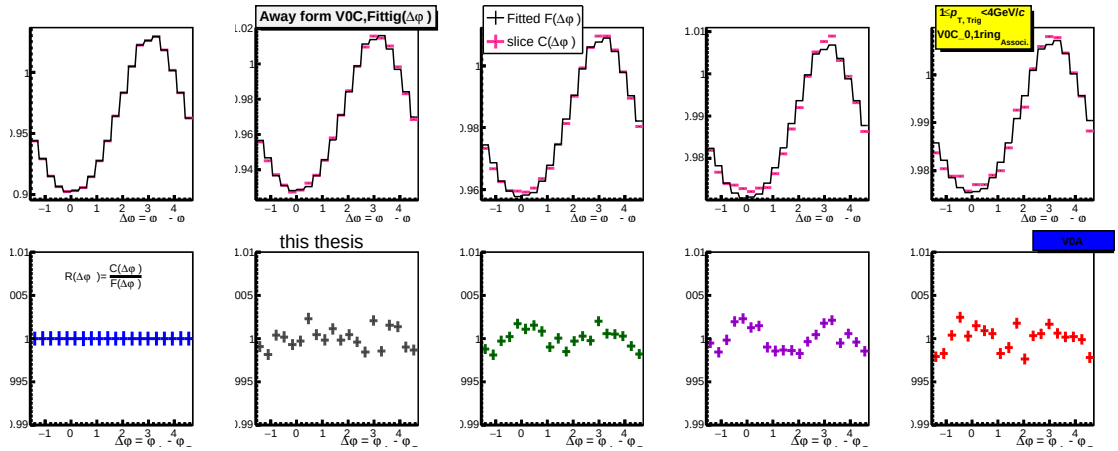

(a) ALICE experimental dat, Up: $C(\Delta\varphi)$ with fitted $F(\Delta\varphi)$, Down: $R(\Delta\varphi)$ of V0C-TPC correlation in away from V0C of $\Delta\eta$ region are measured by ALICE experiment.

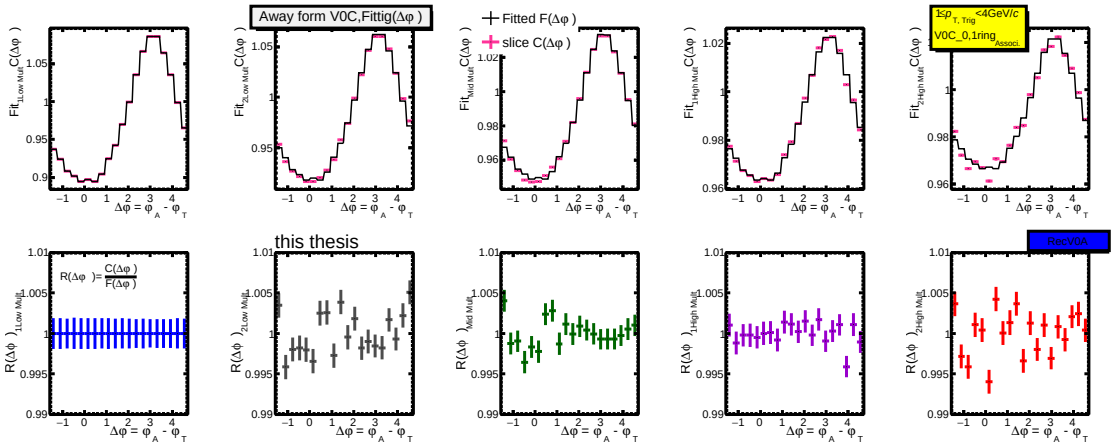

(b) Rec.MC, Up: $C(\Delta\varphi)$ with fitted $F(\Delta\varphi)$, Down: $R(\Delta\varphi)$ of V0C-TPC correlation in away from V0C of $\Delta\eta$ region are measured by ALICE experiment.

Figure 4.29: V0A event estimator, V0C-TPC correlation functions ($1 \leq p_T^{Trig} < 4$ and $V0C_{0,1Ring}^{Assoc}$), the fitted $F(\Delta\varphi)$ and $R(\Delta\varphi)$ in $-4.8 < \Delta\eta < -3.8$ (one of 3 regions) are shown for the 5 multiplicity classes, see in Figure 3.13.

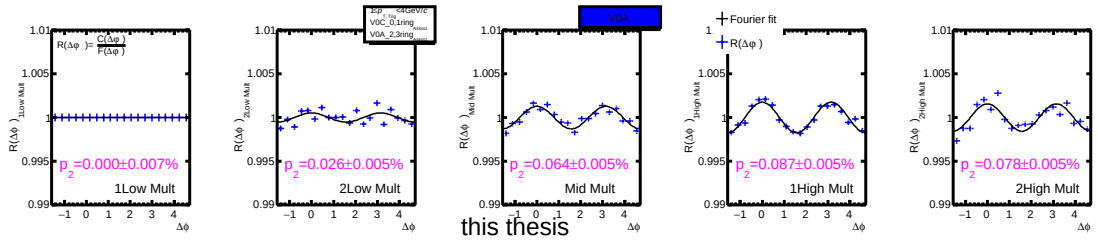

(a) V0A event estimator.

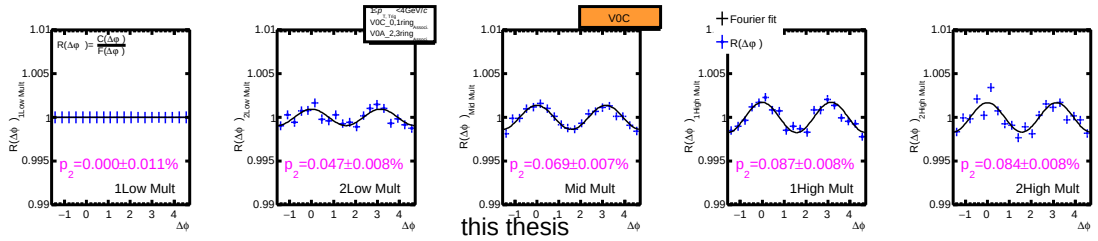

(b) V0C event estimator.

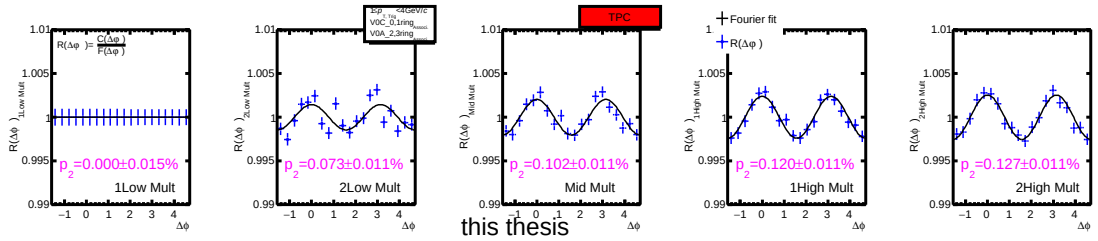

(c) TPC event estimator.

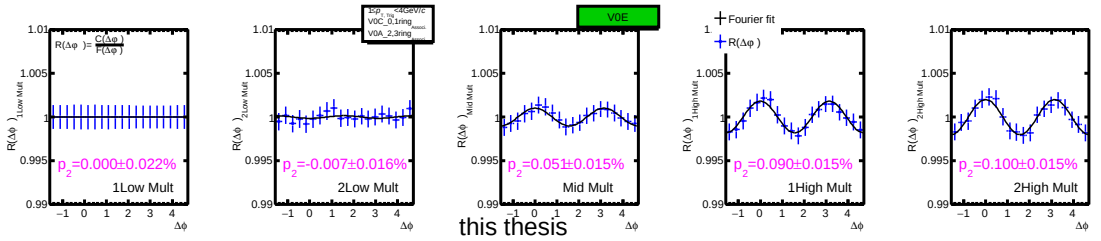

(d) V0E event estimator.

Figure 4.30: ALICE experimental data, $R(\Delta\varphi)$ of V0-TPC correlation in 1.8< $|\Delta\eta|$ <4.8 with $1 \leq p_T^(Trig) < 4GeV/c$ and $V0^{Assoc}$ are shown for the 5 multiplicity classes.

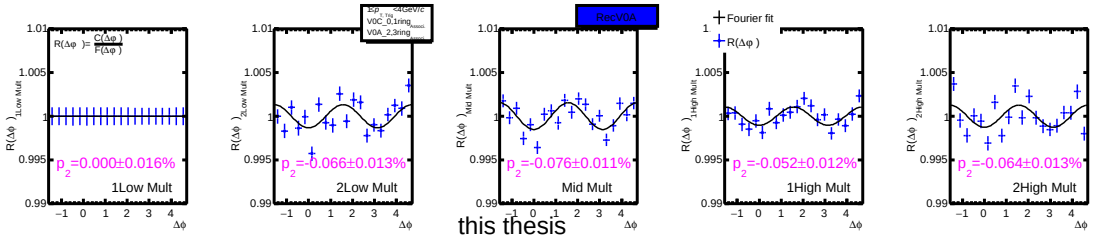

(a) V0A event estimator.

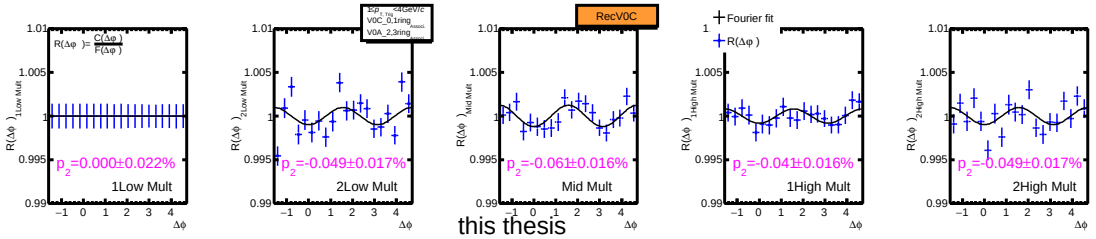

(b) V0C event estimator.

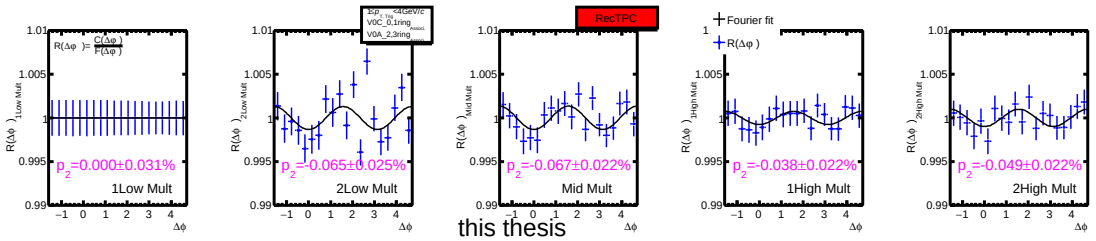

(c) TPC event estimator.

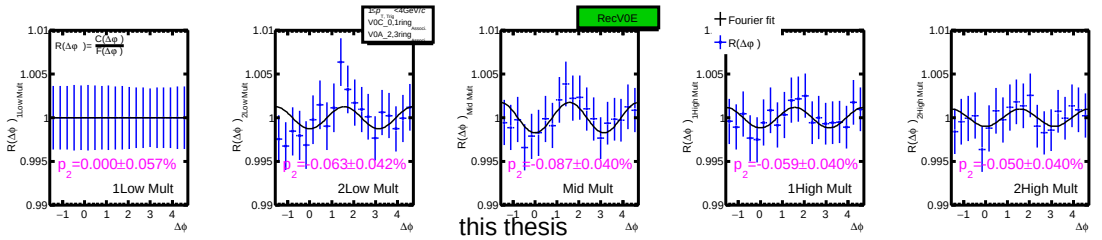

(d) V0E event estimator.

Figure 4.31: Rec.MC, $R(\Delta\varphi)$ of V0-TPC correlation in 1.8< $|\Delta\eta|$ <4.8 with $1 \leq p_T^{(}Trig) < 4GeV/c$ and $V0^{Assoc}$ by various event estimators are shown for the 5 multiplicity classes.

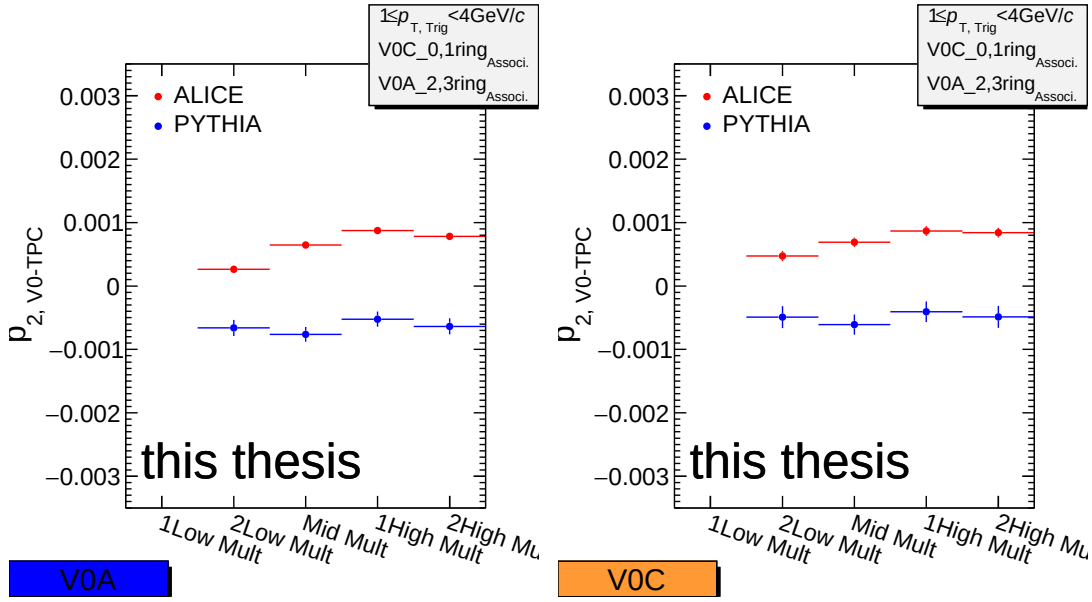

(a) V0A event estimator.

(b) V0C event estimator.

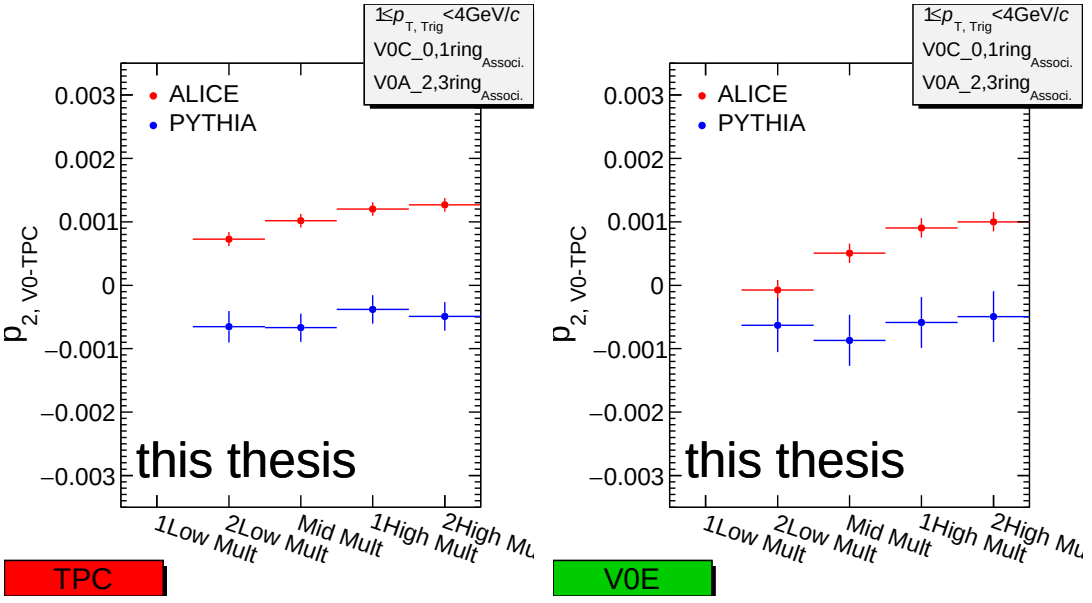

(c) TPC event estimator.

(d) V0E event estimator.

Figure 4.32: Product of two p_2 parameters (for trigger and associate particles) of TPC-V0 $C(\Delta\varphi)$ correlation with respect to the lowest multiplicity are shown for the 5 multiplicity classes.

4.2.3 Extraction of double ridges (high mult. - low mult. yield)

This section shows the results of per-trigger-particle associate yield subtraction of lower multiplicity from higher multiplicity with various event estimators up to $|\Delta\eta| \sim 5$. The same process under for TPC-TPC correlation as described in section. 4.1.7 had been applied for TPC-V0 correlation.

Figure 4.33 show TPC-V0A correlation (1.9< $\Delta\eta$ <4.8), TPC-TPC correlation ($|\Delta\eta|$ <1.8) and TPC-V0C correlation (-1.8< $\Delta\eta$ <-4.6) of the subtraction of the lowest multiplicity from the highest multiplicity (Before the subtraction, per-trigger-particle associate yield are shown in Appendix F.1). In the middle panels in Figure 4.33, TPC-TPC correlation has trigger $1 < p_T^{Trig} \leq 4GeV/c$ and associate $0.2 < p_T^{Assoc} \leq 10GeV/c$ (all p_T bin) to compare with TPC-V0 correlations. TPC-TPC correlation is $1 < p_T^{Trig} \leq 4GeV/c$ and $0.2 < p_T^{Assoc} \leq 10GeV/c$ (all p_T bin) to compare with TPC-V0 correlations. The near side jet size at $(\Delta\varphi, \Delta\eta) \approx (0, 0)$ in TPC-TPC correlation are different with multiplicity selections. There are double ridges in $\Delta\varphi \approx 0$ and π in $|\Delta\eta|$ >1.5 as discussed in Figure 4.23. The TPC-TPC correlation with TPC event estimator, as seen in Figure 4.33(c), shows the wing structure as discussed with auto-/self- correlation and jet-biased event selection. In case of Rec.MC Pythia (PYTHIA Monte Carlo simulation), there are negative-/anti- correlation at $\Delta\varphi \approx 0$ and π instead of double ridges, as shown in Figure 4.34. In the left panels in Figure 4.33, TPC-V0A correlation show in 1.9< $\Delta\eta$ <4.8 with various event estimators. There are all double ridge structure or flat in $\Delta\varphi \approx 0$ and π. TPC-V0A correlation with V0A event estimator in Figrure. 4.33(a) show the auto-/self- correlation in long range $\Delta\eta$ correlation. TPC-V0A correlation with V0C event estimator in Figrure. 4.33(b) show the least jet-biased event selection in long range $\Delta\eta$ correlation. TPC-V0A correlation with TPC event estimator in Figrure. 4.33(c) show double ridge and slightly jet-biased event selection as the extension of wing structure. TPC-V0A correlation with V0E event estimator in Figrure. 4.33(d) show double ridge and only half of jet-biased event selection. The most important part of this results is the ridge structure at $\Delta\varphi \approx 0$ up to $|\Delta\eta| \sim 5$ with various event estimators. However, Rec.MC Pythia results in Figure 4.34, do not show the ridge

structure at $\Delta\varphi \approx 0$ in all $\Delta\eta$. In the right panels in Figure 4.33, TPC-V0C correlations in -1.8< $\Delta\eta$ <-4.6 with various event estimators agree with the TPC-V0A correlation results.

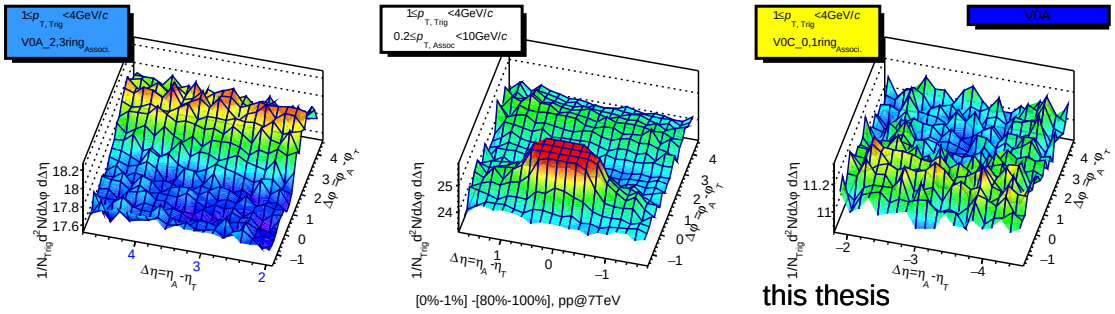

(a) ALICE experimental data, V0A event estimator.

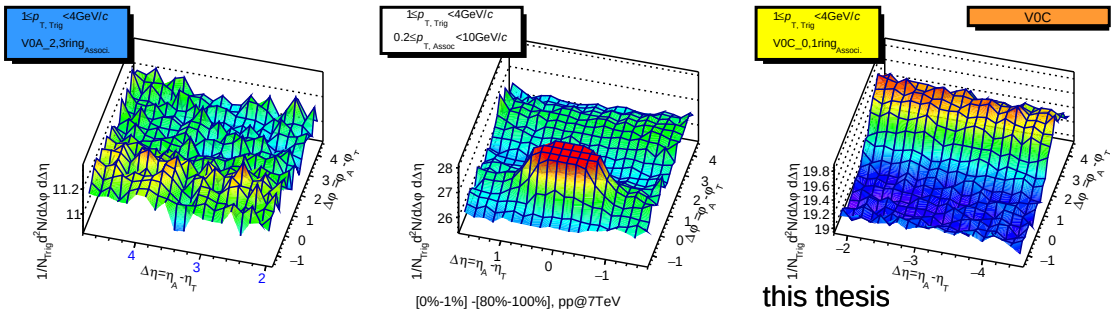

(b) ALICE experimental data, V0C event estimator.

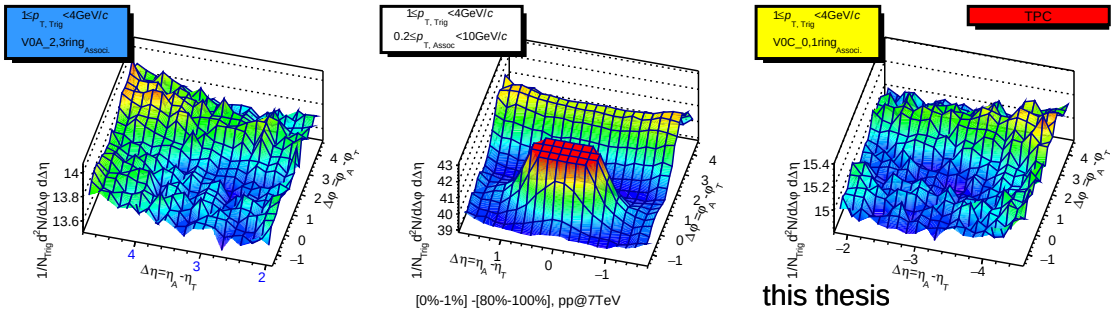

(c) ALICE experimental data, TPC event estimator.

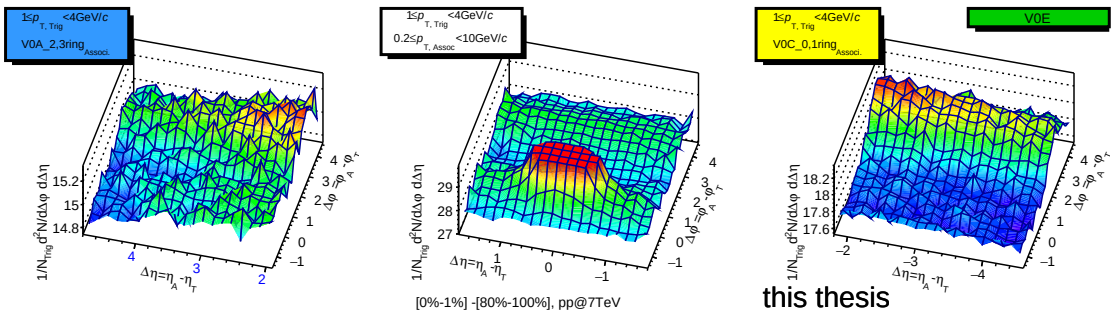

(d) ALICE experimental data, TPC event estimator.

Figure 4.33: ALICE experimental data, 2-D particle yield per trigger particle of V0A-TPC, TPC-TPC and V0C-TPC ($[0\%-1\%]-[80\%-100\%]$) are shown for various event estimators.

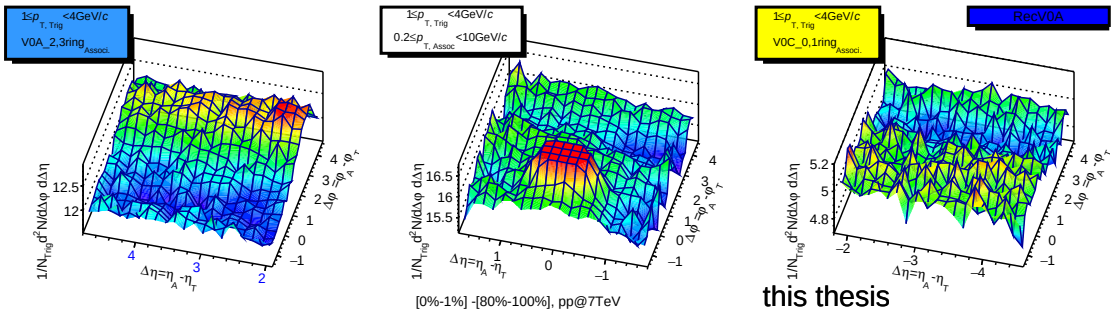

(a) Rec.MC, V0A event estimator.

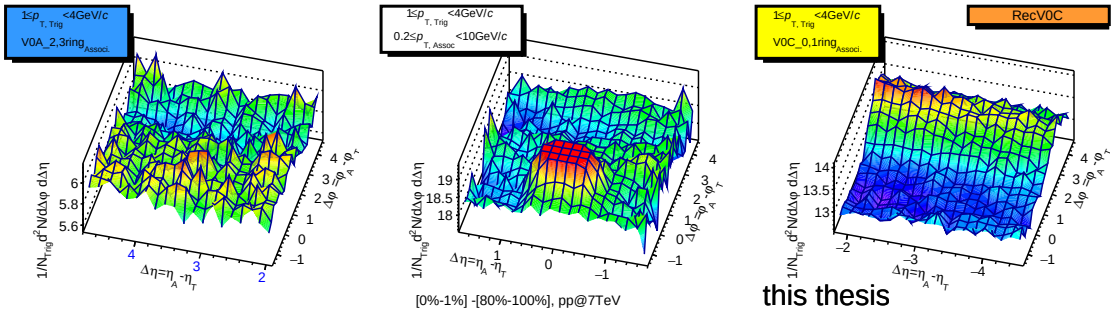

(b) Rec.MC, V0C event estimator.

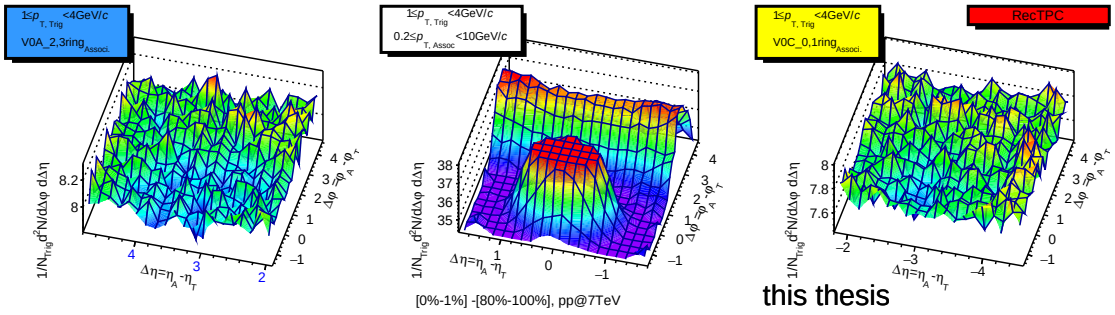

(c) Rec.MC, TPC event estimator.

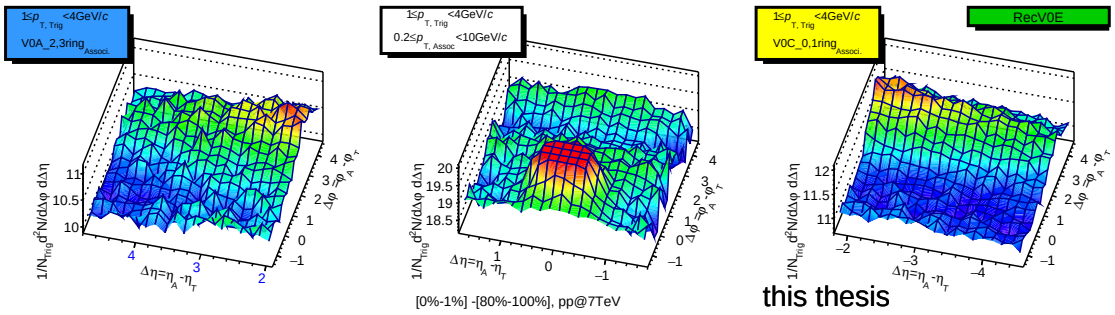

(d) Rec.MC, TPC event estimator.

Figure 4.34: Rec.MC, 2-D particle yield per trigger particle of V0A-TPC, TPC-TPC and V0C-TPC ($[0\% - 1\%] - [80\% - 100\%]$) are shown for various event estimators.

Figure 4.35 show one dimensional (1-D) $\Delta\varphi$ projection of Figure 4.33 and Figure 4.34. In order to compare between ALICE experimental data and Rec.MC, the mean value, which is at $\Delta\varphi = \pi/2$, is subtracted from 1-D particle yields per trigger. In the middle panels in Figure 4.35, TPC-TPC particle yields per trigger ($\Delta\varphi$) in $1.5 \leq |\Delta\eta| < 1.8$ show double ridge in $\Delta\varphi \approx 0$ and π in $1 < p_T^{Trig} \leq 4GeV/c$ and $0.2 < p_T^{Assoc} \leq 10GeV/c$ (all p_T bin) like Figure 4.24. However, Rec.MC Pythia shows negative-/anti- correlation instead of double ridges. In TPC event estimator, TPC-TPC particle yields per trigger ($\Delta\varphi$) show the strongest auto-/self- correlation and jet-biased event selection. In the left panels in Figure 4.35 show TPC-V0A particle yields per trigger ($\Delta\varphi$) with various event estimators in 1.9< $\Delta\eta$ <4.8. Due to strong auto-/self- correlation and jet-biased event selection, TPC-V0A particle yields per trigger ($\Delta\varphi$) with V0A event estimator in Figrure. 4.35(a) show the flat shape at $\Delta\varphi \approx 0$ and the enhanced away-side jet at $\Delta\varphi \approx \pi$. On the other hand, Rec.MC Pythia shows the hollow shape at $\Delta\varphi \approx 0$ and more enhanced away side jet at $\Delta\varphi \approx \pi$ than the experimental results. TPC-V0A particle yields per trigger ($\Delta\varphi$) with V0C event estimator in Figrure. 4.35(b) show slightly enhanced ridge at $\Delta\varphi \approx 0$ and the flat away side jet at $\Delta\varphi \approx \pi$. However, Rec.MC Pythia shows the flat shape at $\Delta\varphi \approx 0$ and the hollow shape at $\Delta\varphi \approx \pi$. TPC-V0A particle yields per trigger ($\Delta\varphi$) with TPC event estimator in Figrure. 4.35(c) show slightly enhanced double ridge at $\Delta\varphi \approx 0$ and π. On the other side, Rec.MC Pythia shows the flat shape in all $\Delta\varphi$. TPC-V0A particle yields per trigger ($\Delta\varphi$) with V0E event estimator in Figrure. 4.35(d) show double ridge at $\Delta\varphi \approx 0$ and π. On the contrary, Rec.MC Pythia shows the hollow shape at $\Delta\varphi \approx 0$ and more enhanced away side jet at $\Delta\varphi \approx \pi$ than the experimental results. In the right panels in Figure 4.35, TPC-V0C correlations in -1.8< $\Delta\eta$ <-4.6 with various event estimators agree with the TPC-V0A correlation results. As the results, the difference particles yields per trigger between ALICE experimental results and Rec.MC Pythia are small, but the correlation shapes are different. The the difference between ALICE experiment and Rec.MC Pythia enhance double ridge structure in $\Delta\varphi \approx 0$ and π in ALICE experimental results.

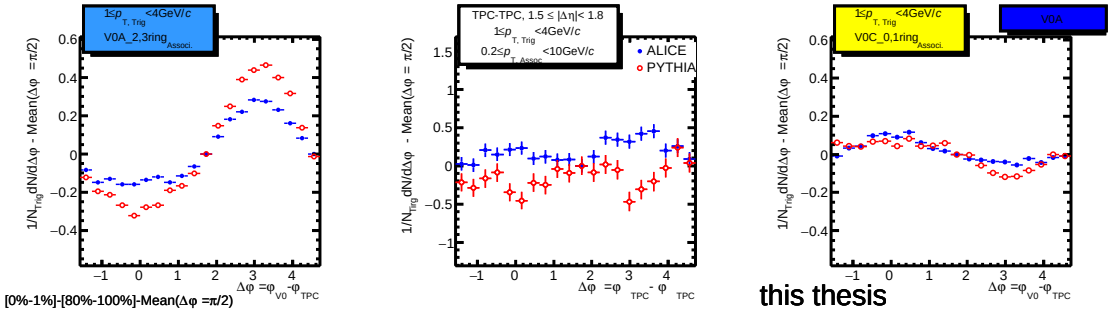

(a) V0A event estimator.

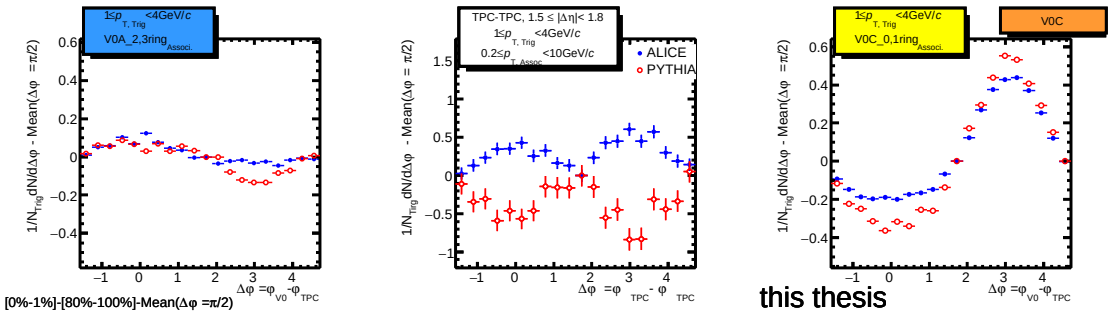

(b) V0C event estimator.

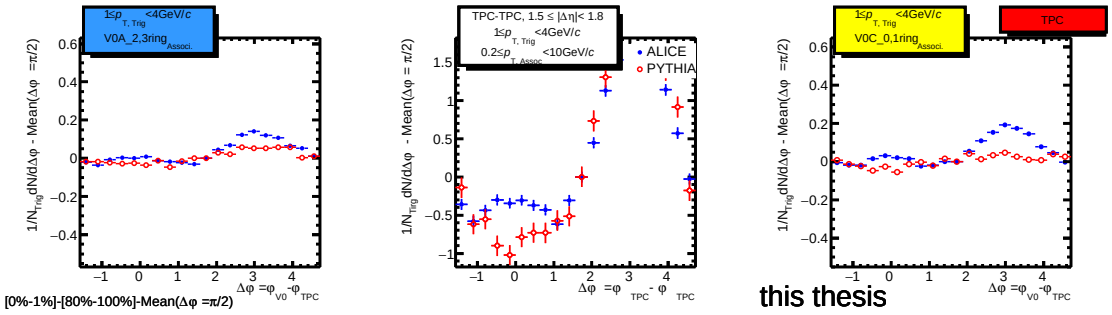

(c) TPC event estimator.

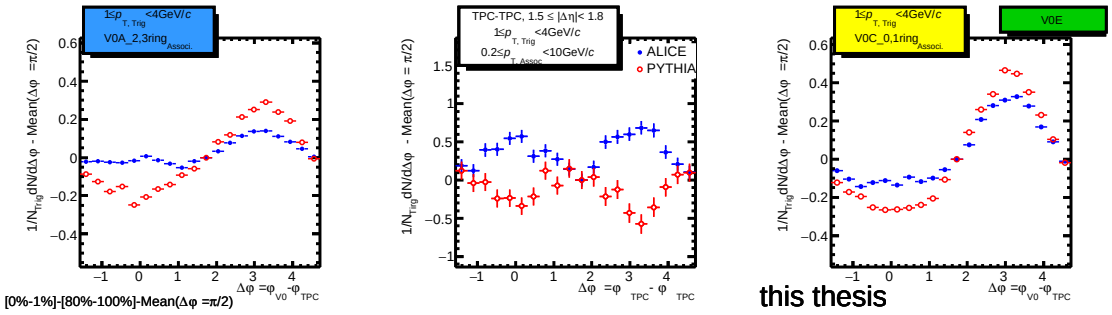

(d) V0E event estimator.

Figure 4.35: 1-D particle yield per trigger particle ($1/N_{Trig}dN/d\Delta\varphi$) of V0A-TPC, TPC-TPC and V0C-TPC ($[[0\% - 1\%] - [80\% - 100\%]] - Mean_{\Delta\varphi=\pi/2}$) in 1.9< $\Delta\eta$ <4.8, 1.5≤ $|\Delta\eta|$ <1.8 and -1.8< $\Delta\eta$ <-4.6 are shown for various event estimators.

4.3 The largest $\Delta\eta$ correlation with V0-V0 correlation

This section shows the result of the longest range $\Delta\eta$ (5.5< $|\Delta\eta|$ <7.6) V0-V0 correlation functions. In order to have similar η acceptance, between forward and backward η acceptances of V0 rings, V0C 0, 1 rings (($p^{Assoc}_{V0C0,1Rings}$)) and V0A 2, 3 rings ($p^{Assoc}_{V0A2,3Rings}$) are selected. Low p_T particles dominate the V0 signal like the case of TPC-V0 correlation, because V0 detector only measures the total number of charged particles in the detector segments.

4.3.1 Two-particle correlation shape comparison

This section shows the multiplicity dependence of the longest range $\Delta\eta$ V0-V0 correlation functions by various event estimators. Figure 4.36 show 1-D $C(\Delta\varphi)$ of V0-V0 in 5.5< $|\Delta\eta|$ <7.6. The $C(\Delta\varphi)$ of V0-V0 show multiplicity dependence in the largest η acceptance.

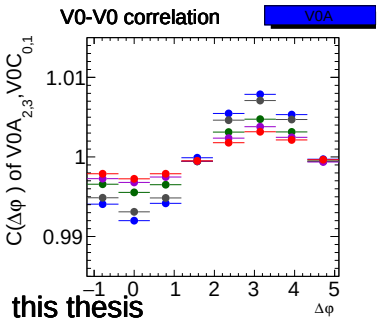

(a) ALICE experimental data, V0A event estimator.

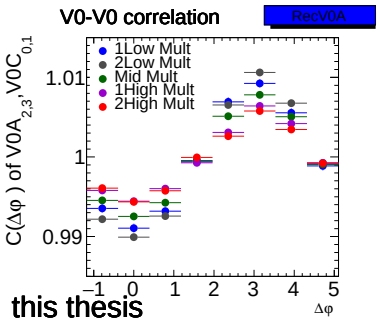

(b) Rec.MC, V0A event estimator.

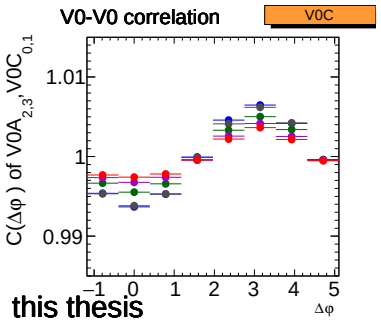

(c) ALICE experimental data, V0C event estimator.

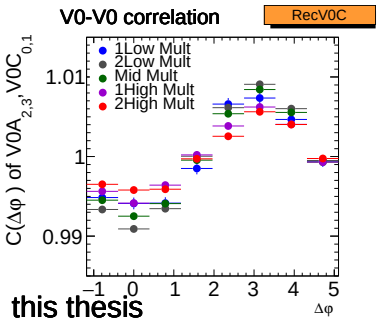

(d) Rec.MC, V0C event estimator.

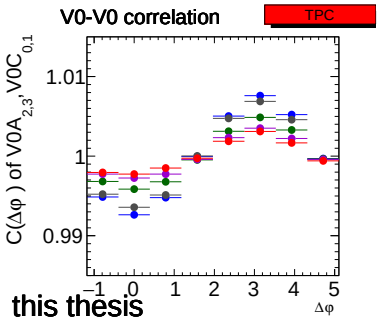

(e) ALICE experimental data, TPC event estimator.

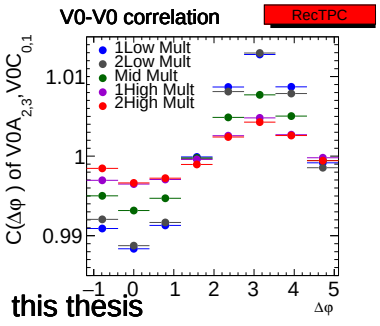

(f) Rec.MC, TPC event estimator.

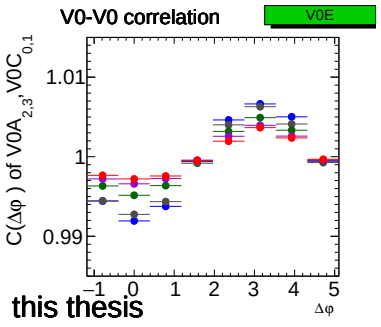

(g) ALICE experimental data, V0E event estimator.

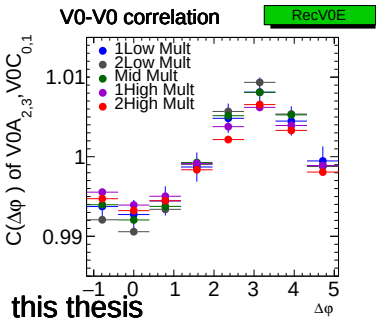

(h) Rec.MC, V0E event estimator.

Figure 4.36: 1-D $C(\Delta\varphi)$ of V0-V0 correlation in 5.5< $|\Delta\eta|$ <7.6 by various event estimators are shown for the 5 multiplicity classes.

4.3.2 $\Delta\varphi$ correlation shape variation as a function of multiplicity

In order to study the multiplicity dependence of correlation function shape in the longest range $\Delta\eta$ (5.5< $|\Delta\eta|$ <7.6), the one dimensional (1-D) V0-V0 $C(\Delta\varphi)$ functions are fitted by $F(x) = a + bf(x)$, which is given by the renormalized correlation function shape f(x) from the lowest multiplicity, as discussed in section. 4.1.4 and section. 4.2.2. The correlation functions are then divided by the fitted function ($R(\Delta\varphi) = C(\Delta\varphi)/F(x)$) in order to extract the small deviation between the measured correlation, $C(\Delta\varphi)$, and fitted function, $F(x)$. The ratio $R(\Delta\varphi)$, which is $C(\Delta\varphi)/F(\Delta\varphi)$, of V0-V0 are shown in Figure 4.37 and Figure 4.38. $R(\Delta\varphi)$ show double peak-like structure at $\Delta\varphi \approx 0$ and π that is consistent with elliptic flow-like event shape in $5.5 < |\Delta\eta| < 7.6$. The elliptic shapes are becoming more enhanced with increasing multiplicities. However, Rec.MC Pythia results show slightly negative double peaks at $\Delta\varphi \approx 0$ and π.

v_2^2 parameters (p_2) are extracted by fitting the ratio $R(\Delta\varphi)$ with Fourier function $F(x) = N(1 + 2p_2 cos(2x))$ for 5 multiplicity classes by various event estimators, as shown in Figure 4.39 and Figure 4.40. p_2 parameters are increasing with increasing multiplicity. However, p_2 parameters of Rec.MC Pythia show negative values in most of the results.

Now, this analysis ready for the condition of Equation. 3.11 that is $p_2^{long} = TA \times TC \div AC$, see in Figure 3.15. The function of TC and TA are shown in Figure G.1 and Figure G.2 ($\sim$ Figure 4.32), the function of AC is shown in Figure 4.39, and p_2^{long} is shown in Figure 4.40. p_2^{long} are increasing with increasing multiplicity. The results of $p2^{long}$ (Figure 4.40) are comparable with the results of $p2^{short}$ (Figure 4.17), shown in Figure 5.10.

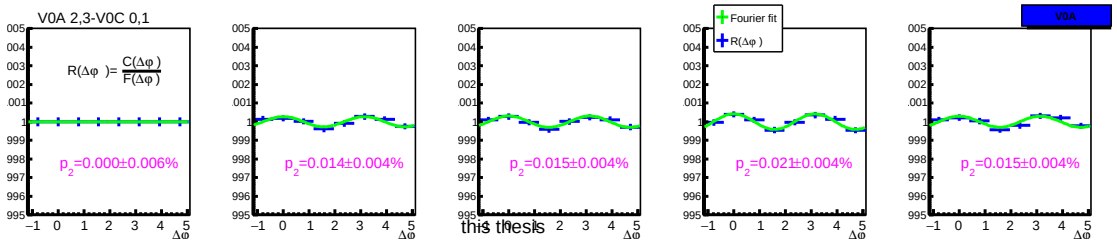

(a) ALICE experimental data, V0A event estimator.

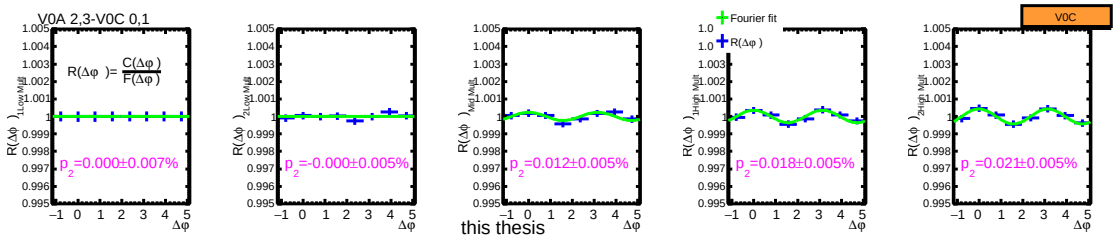

(b) ALICE experimental data, V0C event estimator.

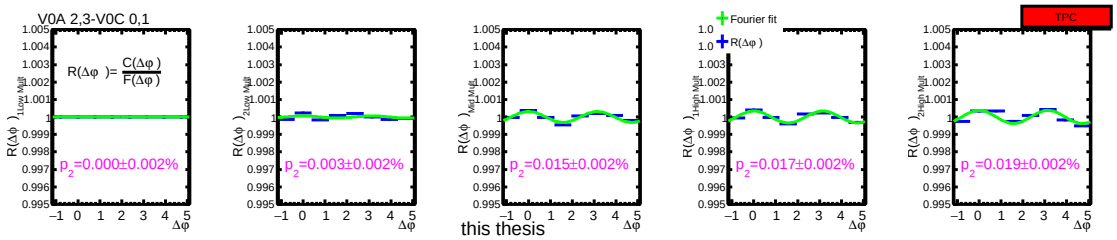

(c) ALICE experimental data, TPC event estimator.

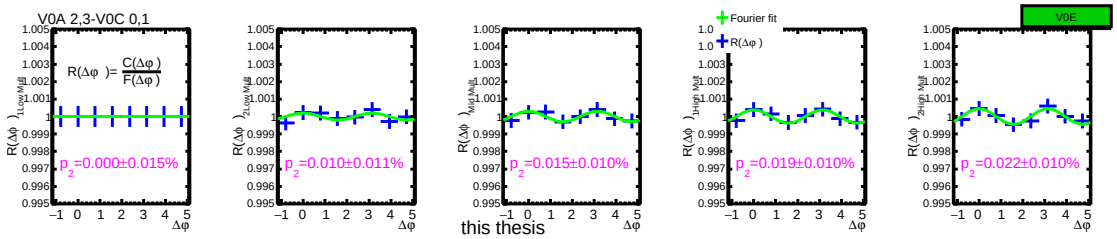

(d) ALICE experimental data, V0E event estimator.

Figure 4.37: ALICE experimental data, 1-D $C(\Delta\varphi)$ of V0-V0 correlation in 5.5< $|\Delta\eta|$ <7.6 by various event estimators are shown for the 5 multiplicity classes.

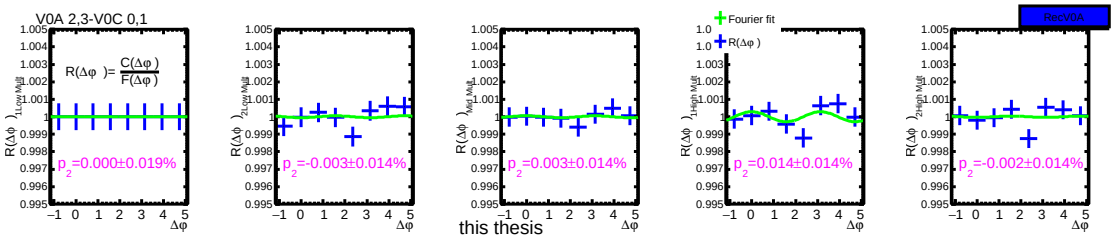

(a) Rec.MC, V0A event estimator.

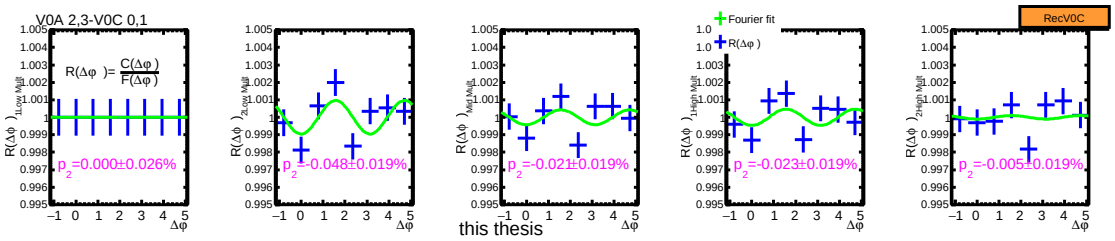

(b) Rec.MC, V0C event estimator.

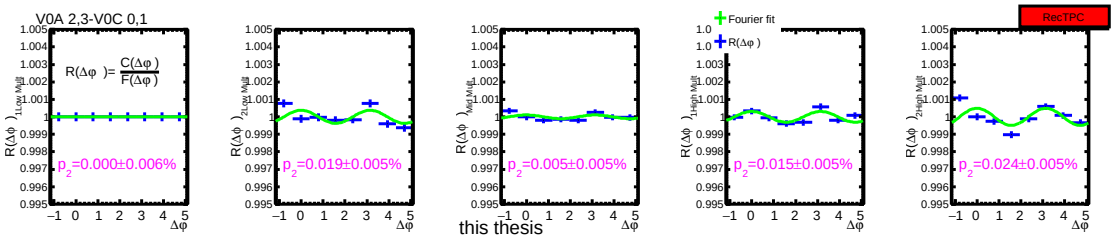

(c) Rec.MC, TPC event estimator.

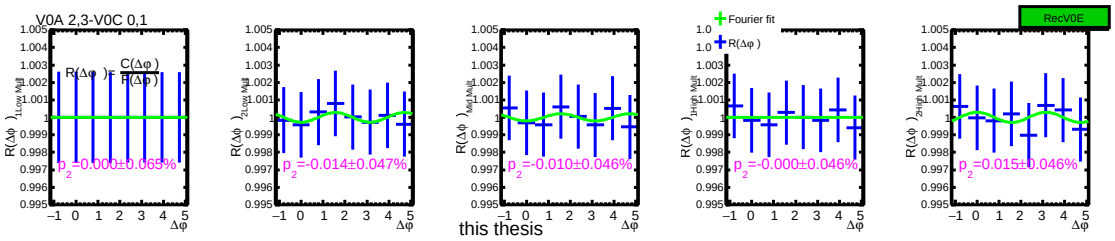

(d) Rec.MC, V0E event estimator.

Figure 4.38: Rec.MC, 1-D $C(\Delta\varphi)$ of V0-V0 correlation in 5.5< $|\Delta\eta|$ <7.6 by various event estimators are shown for the 5 multiplicity classes.

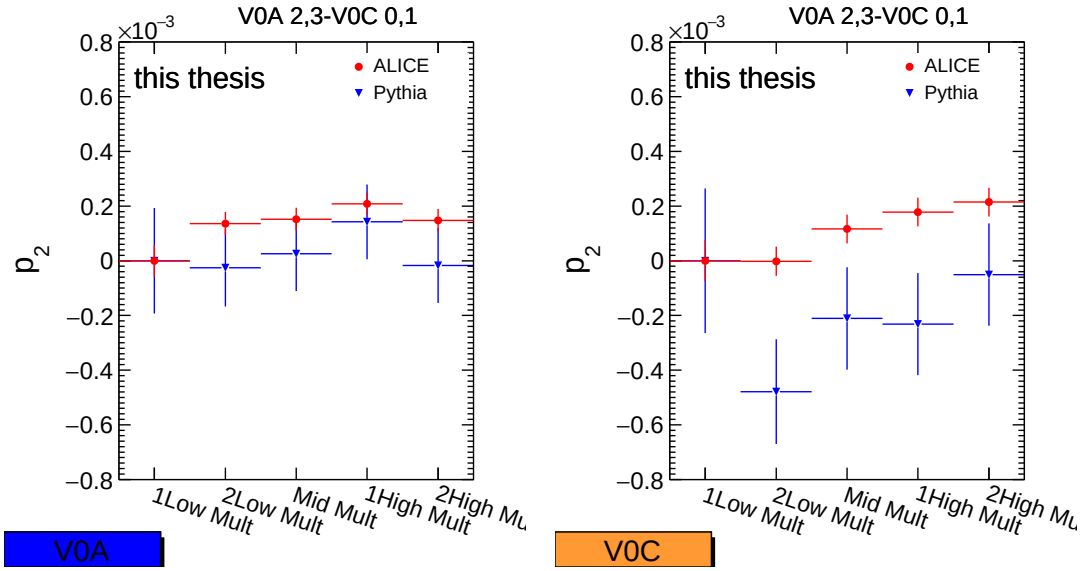

(a) V0A event estimator.

(b) V0C event estimator.

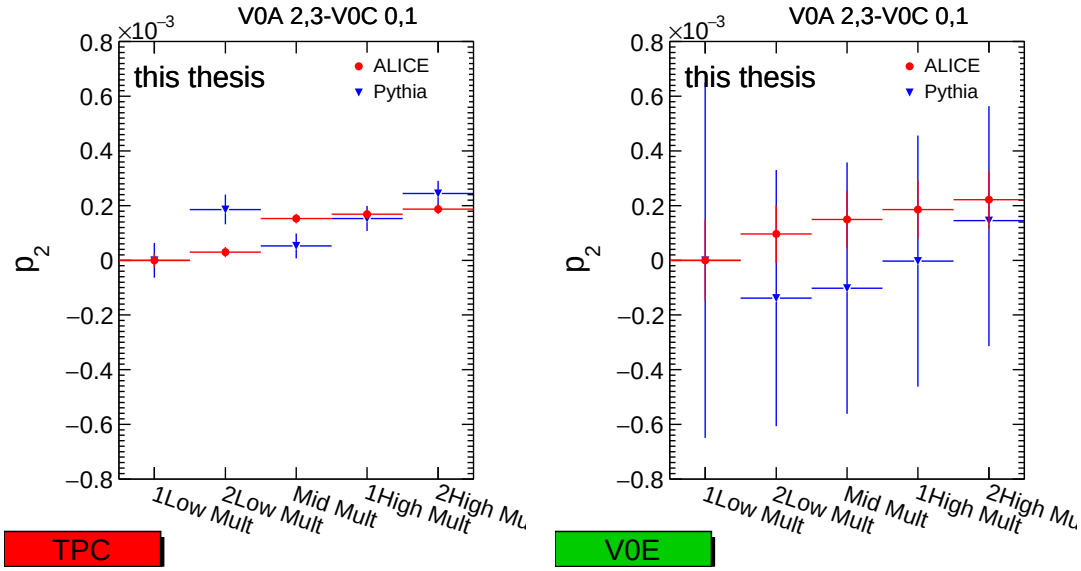

(c) TPC event estimator.

(d) V0E event estimator.

Figure 4.39: p_2 parameter of V0-V0 correlation in 5.5< $|\Delta\eta|$ <7.6 by various event estimators are shown for the 5 multiplicity classes.

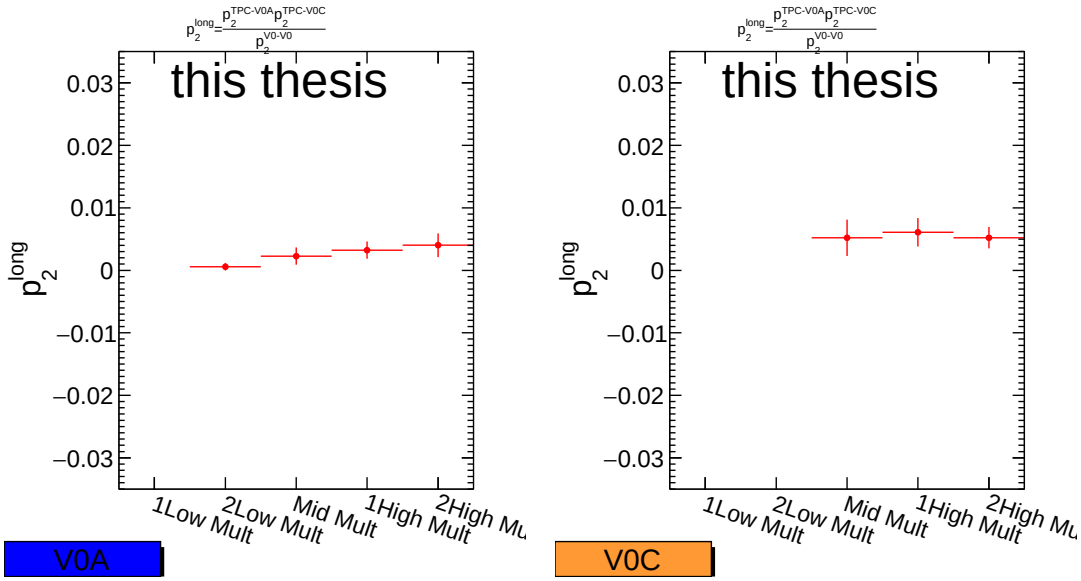

(a) V0A event estimator.

(b) V0C event estimator.

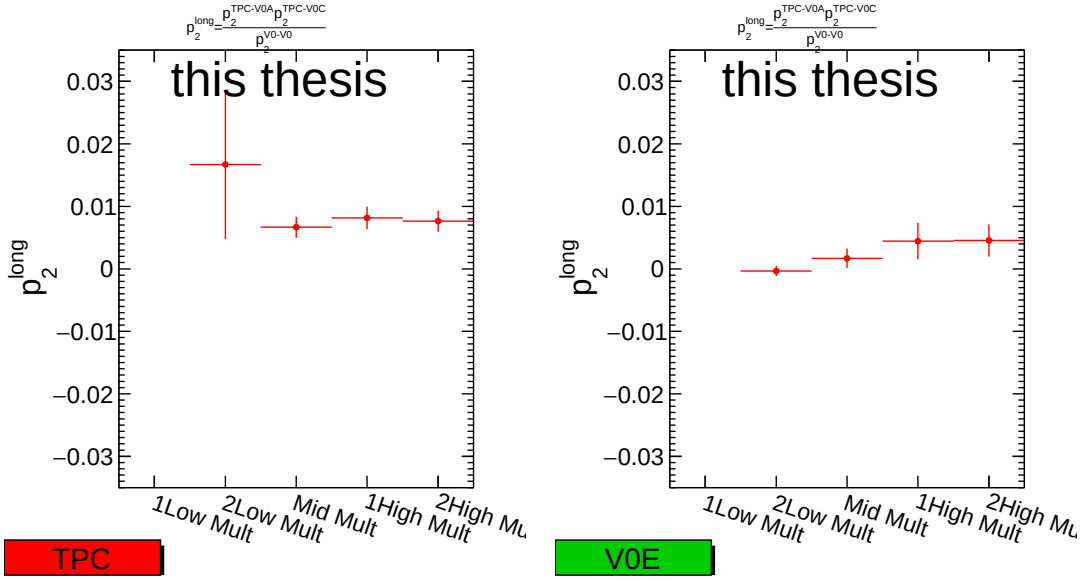

(c) TPC event estimator.

(d) V0E event estimator.

Figure 4.40: The extracted $p2^{long}$ parameter by various event estimators are measured by ALICE experiment.

Chapter 5

Discussions

5.1 Multiplicity dependence of jet shapes of two-particle correlation

Shape studies of two-particle correlations provide detailed information on the properties of particle production in pp collisions. Figure 5.1 shows the angular correlation function as a function of pseudorapidity ($\Delta\eta$) and measured azimuthal angle ($\Delta\varphi$) for all charged particles with $1 \leq p_T < 4$ GeV/c for categorized in 5 multiplicity classes, is described. The analysis procedure is described in section 3.6.1. The two-dimensional (2-D) structure in Figure 5.1 shows a variety of features of particle productions for 5 multiplicity classes. The near side jets at $(\Delta\eta, \Delta\varphi) \approx (0, 0)$ are originated from high p_T hard processes. The structure elongated along $\Delta\eta$ axis can be interpreted as the result of momentum conservation and the peaks at $\Delta\varphi \approx 0$ and π can be interpreted as back-to-back jets. There is the extension of the elongated structure along $\Delta\eta$ axis at $\Delta\varphi \approx 0$ and $|\Delta\eta| > 1.0$ in $0\% - 1\%$ and $1\% - 5\%$, which is called "Ridge structure". On the other hand, Rec.MC Pythia does not reproduce ridge structures, as shown in Figure 5.1(b). Near side jets become narrower with increasing multiplicity selections, shown in Figure 5.2 and Figure 5.3.

After projecting to one-dimensional (1-D) $\Delta\eta$ correlation functions for $|\Delta\varphi| < 0.1$ (near side jets) for the 5 multiplicity classes, the 1-D renormalized correlation functions as a

function of $\Delta\eta$ are shown in Figure 5.2. ALICE experimental data show near side jets become narrower with increasing the multiplicity and the effects of ridge structures are observed in $\Delta\varphi \approx 0$ and $|\Delta\eta| > 1.0$ in $0\% - 1\%$ and $1\% - 5\%$, as shown in Figure 5.1(a). Although, Rec.MC Pythia calculation reproduces near side jets effects for the 5 multiplicity classes, the effect of ridge structures can not be reproduced.

In Figure 5.3 calculated for 5 multiplicity classes, the extracted σ parameter,which is the width parameter of Gaussian function, decreases with increasing multiplicity selections which could tell us more jet-like particle productions in high multiplicity events. The general trend of near side Gaussian width parameters that reduce with increasing the multiplicity are reproduced in PYTHIA model, however the magnitude of the width is somewhat wider in the model.

1-D $\Delta\eta$ correlation functions for $2.3 < \Delta\varphi < 3.9$ (away side jets) for the 5 multiplicity classes, the renormalized correlation functions are shown in Figure 5.4. The away side jets shapes show a wide convexity in ALICE experimental data, as shown in Figure 5.4(a). On the contrary, the away side jets in Rec.MC Pythia show a flat or hollow, as shown in Figure 5.4(b).

Error bars indicate statistical uncertainties and small marks in brackets show systematic uncertainties, as Equation 3.12.

5.2 Ridge structures with 2-D flat back-ground (Avg.ZYAM) subtraction

The most significant feature of correlation functions is ridge structures in long rang $\Delta\eta$ in $\Delta\varphi \approx 0$ in high multiplicity at intermediate p_T, where the ridge effect appears to be strongest. The ridge effect is observed experimentally at large $\Delta\eta$ region, which is supposed to be originated from particle correlations formed in early stage of collisions. One of the possible scenario could be elliptic expansion (v_2) originated from the elliptic density distribution in the initial stage, which implys the created QGP in high multiplicity pp collisions. The normalized correlation functions by number of triggers ($1/N^{Trig}dN/d\Delta\varphi$) including 2-dimensional (2-D) flat background (average ZYAM) subtraction for the 5 mul-

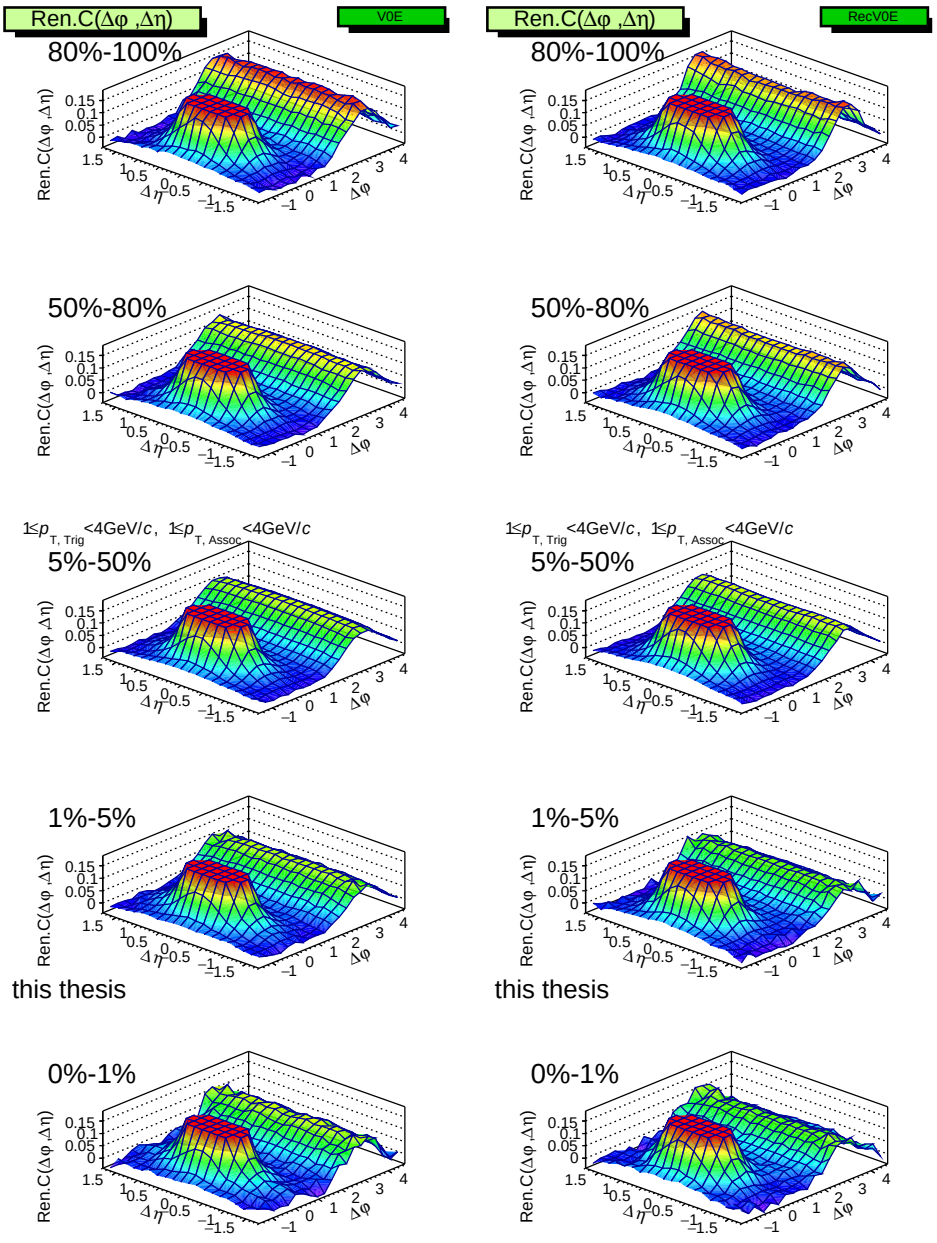

(a) ALICE experimental data, $Ren.C(\Delta\varphi, \Delta\eta)$.

(b) Rec.MC, $Ren.C(\Delta\varphi, \Delta\eta)$.

Figure 5.1: 2-D renormalized dihadron correlation functions in pp collisions at $\sqrt{s} = 7$ TeV with $1 \leq p_T^{Trig} < 4$ GeV/c and $1 \leq p_T^{Asso} < 4$ GeV/c for (a) ALICE experimental data and (b) Rec.MC Pythia are shown for the 5 multiplicity classes.

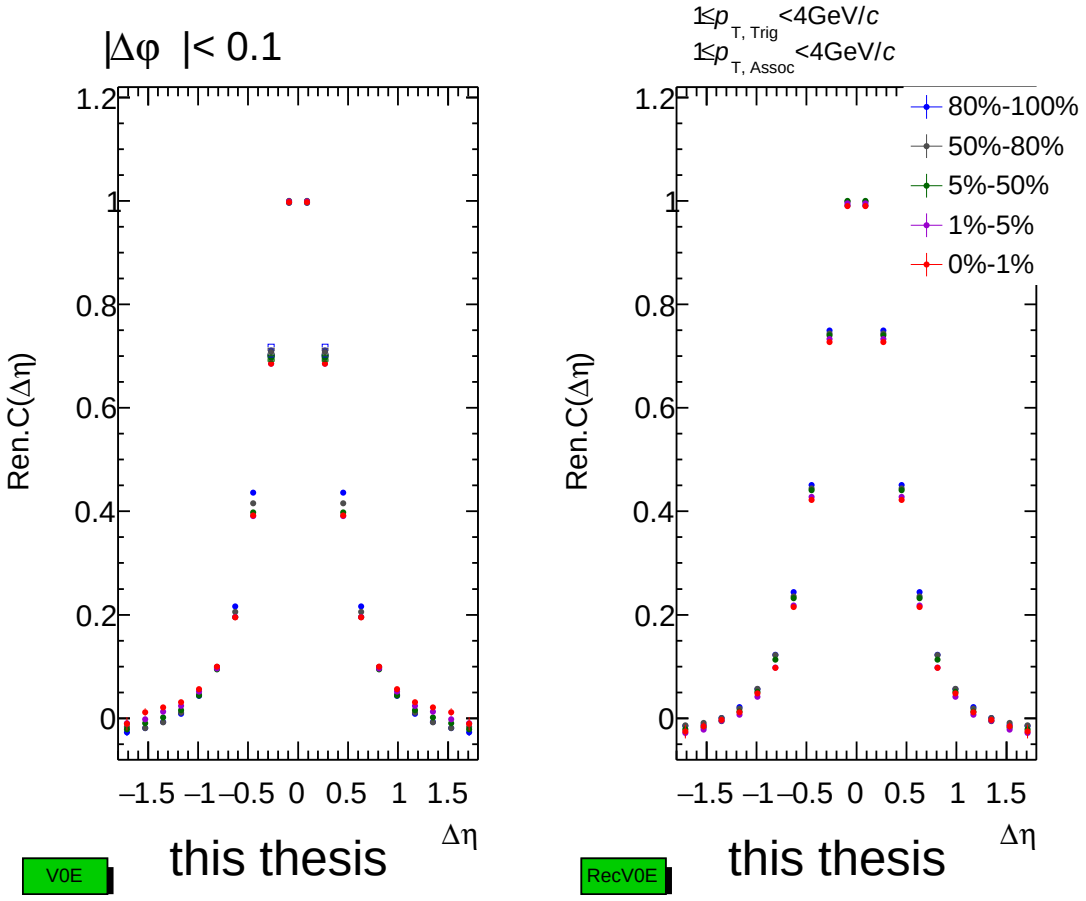

(a) ALICE experimental data, Near side jets.

(b) Rec.MC, Near side jets.

Figure 5.2: 1-D $\Delta\eta$ renormalized correlation functions for $|\Delta\varphi| < 0.1$ (near side jets) for (a) ALICE experimental data and (b) Rec.MC Pythia are shown for the 5 multiplicity classes.

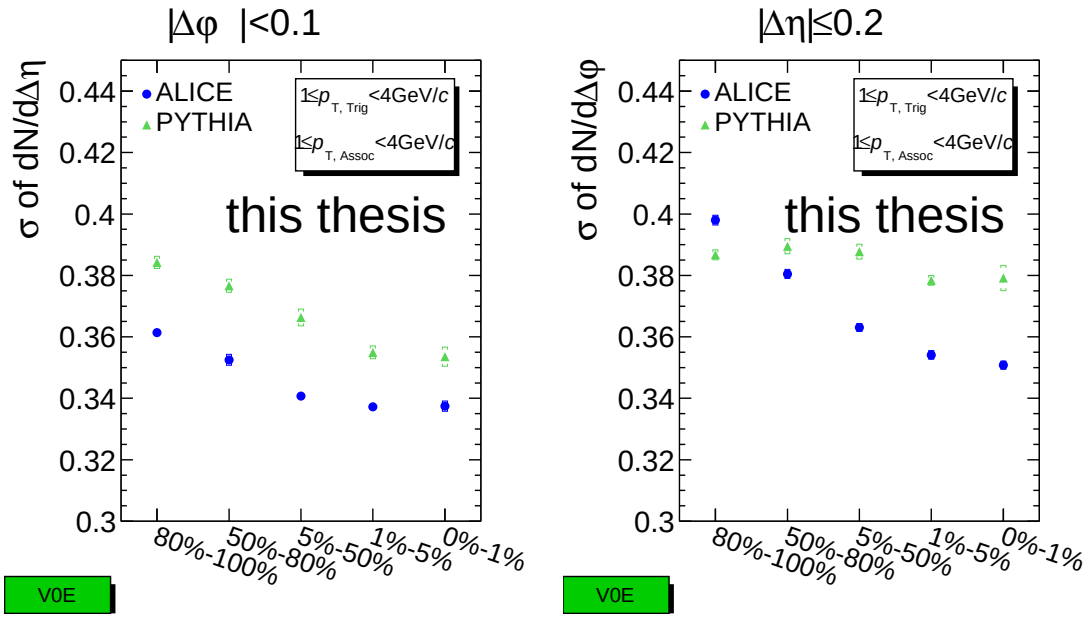

(a) σ values of $dN/d\Delta\eta$ in $|\Delta\varphi| < 0.1$.

(b) σ values of $dN/d\Delta\varphi$ in $|\Delta\eta| \leq 0.2$.

Figure 5.3: σ values by Gaussian fitting of near side jets in (a) $dN/d\Delta\eta$ ($|\Delta\varphi| < 0.1$) and (b) $dN/d\Delta\varphi$ ($|\Delta\eta| \leq 0.2$) are shown for the 5 multiplicity classes.

tiplicity classes are shown in Figure 5.5. ALICE experimental data show ridge structures in 1.4< $|\Delta\eta|$ <1.8 with 1≤ p_T <4 GeV/c at $\Delta\varphi \approx 0$ in $0\% - 1\%$ and $1\% - 5\%$. And away side jets in $\Delta\varphi \approx \pi$ are enhanced with increasing multiplicity selections. However, Rec.MC Pythia does not reproduce ridge structures and away side jets show little difference among the 5 multiplicity classes.

The integrated associated yield is calculated on the near side for the ridge ($-0.8 \leq \Delta\varphi \leq 0.8$) for the 5 multiplicity classes in the large $|\Delta\eta|$ region 1.4< $|\Delta\eta|$ <1.8, as shown in Figure 5.6. The integrated associated yield rises with increasing multiplicity selections. On the contrary, Rec.MC Pythia shows the reducing integrated yield in near side for the 5 multiplicity classes.

5.3 Double Ridge structure

To quantify the change from low to high multiplicity event classes, the per-trigger yield of the lower multiplicity class is subtracted from the higher multiplicity classes ($High - Low$). Figure 5.7 shows per-trigger-particle associated yield in $\Delta\varphi$ and $\Delta\eta$ for charged particles with 1≤ p_T <4 GeV/c for the $0\% - 1\%$ multiplicity class, after subtraction of the associated

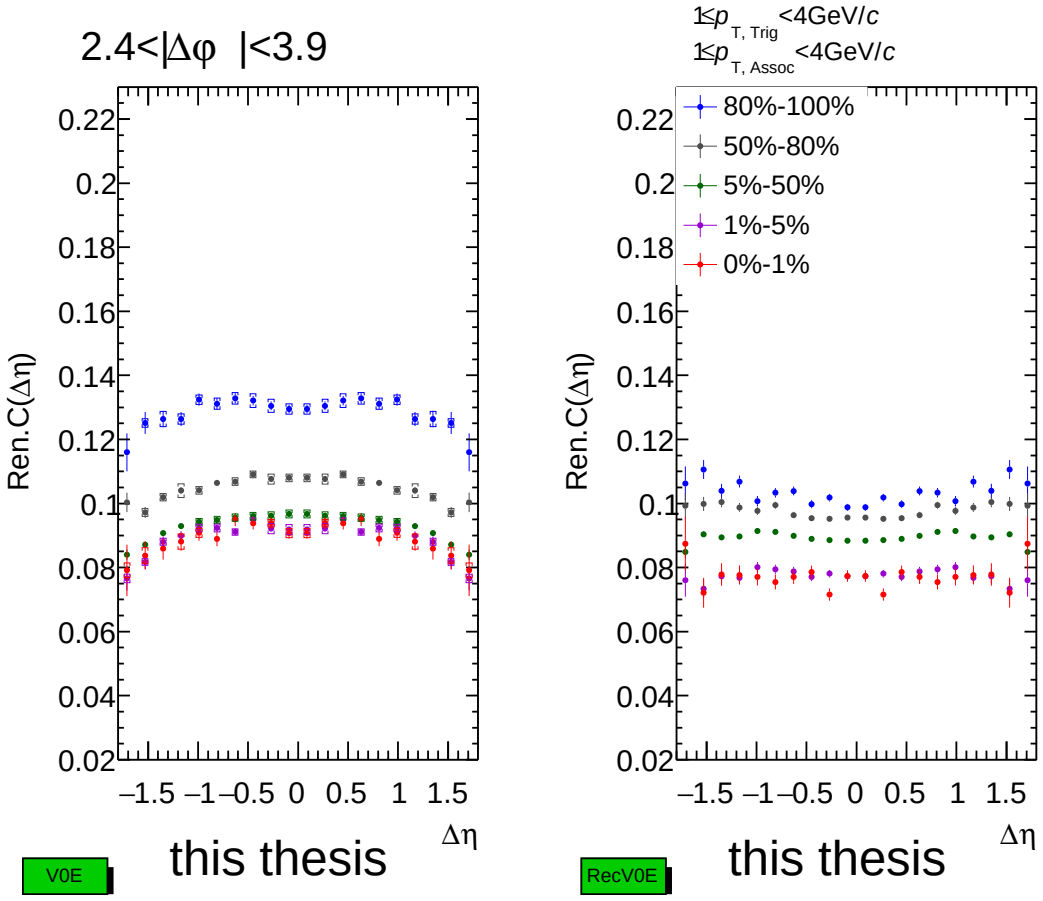

(a) ALICE experimental data, φ ridge.

(b) Rec.MC, No φ ridge.

Figure 5.4: 1-D $\Delta\eta$ renormalized correlation functions for $2.3 < \Delta\varphi < 3.9$ (away side jets) for (a) ALICE experimental data and (b) Rec.MC Pythia are shown for the 5 multiplicity classes.

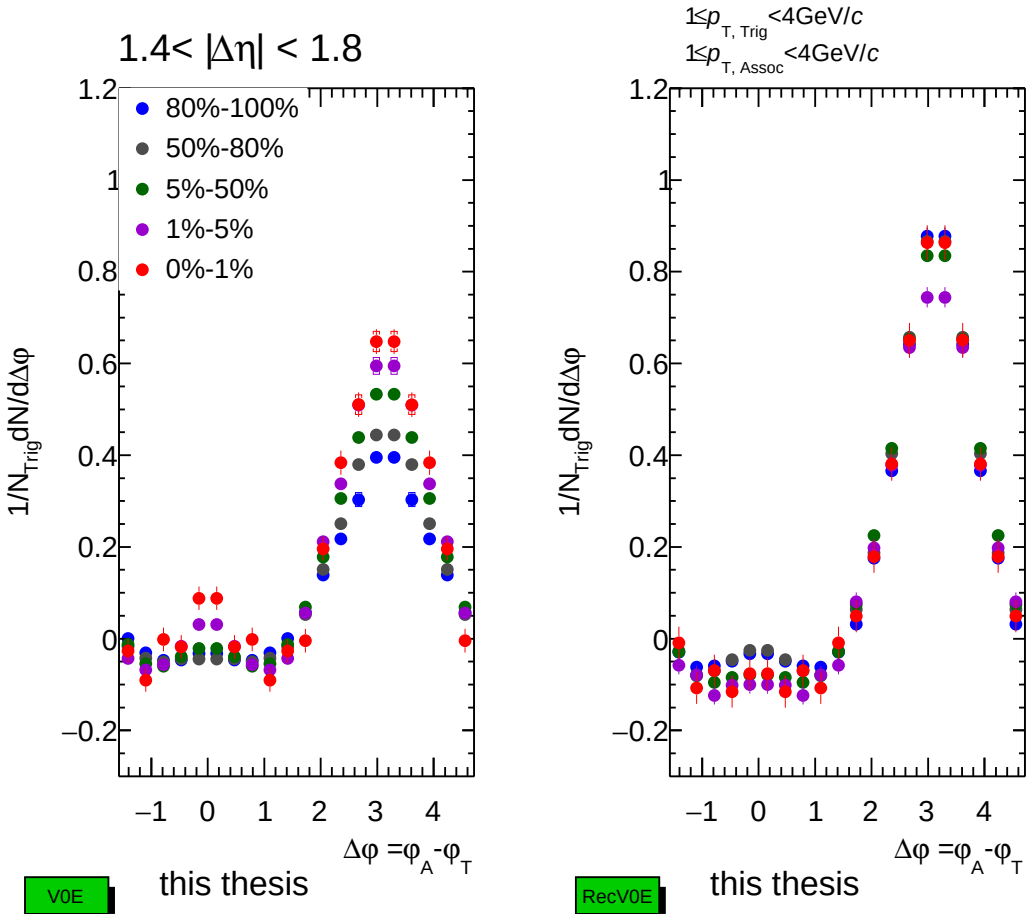

(a) ALICE experimental data, V0E event estimator.

(b) Rec.MC, V0E event estimator.

Figure 5.5: 1-D per-trigger-particle associated yield with subtracted by flat background for charged hadrons as function of $\Delta\varphi$ in $1\leq p_T <4$ GeV/c in $1.4< |\Delta\eta| <1.8$ in pp collisions at $\sqrt{s} = 7$ TeV, for (a) ALICE experimental data and (b) Rec.MC Pythia are shown for the 5 multiplicity classes.

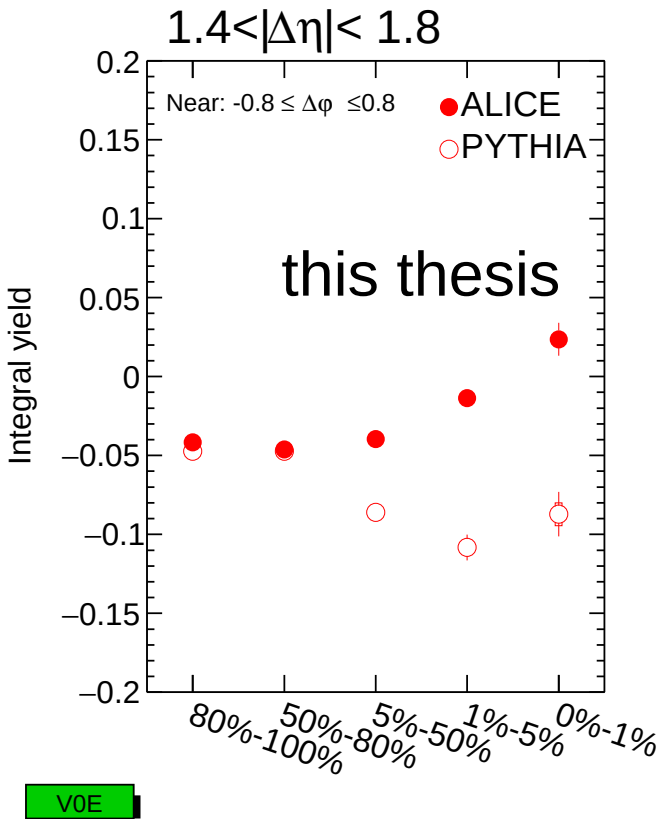

Figure 5.6: Integrated associated yield after the flat background subtraction in near side ridge ($-0.8 \leq \Delta\varphi \leq 0.8$) and away side jets ($2.3 < \Delta\varphi < 3.9$), for particles with $1 \leq p_T < 4$ GeV/c, as function of the 5 multiplicity classes from pp collisions at $\sqrt{s} = 7$ TeV, for ALICE experimental data are measured by the ALICE experiment.

yield obtained in the $80\% - 100\%$ event class ($[0-5\%] - [80-100\%]$). ALICE experimental data show double ridges (the long range $|\Delta\eta|$ >1 near side correlation enhancement together with similar long range $|\Delta\eta|$ enhancement in away side) in 1.5≤ $|\Delta\eta|$ <1.8 and different magnitude of near side jets $(\Delta\varphi, \Delta\eta) \approx (0, 0)$ between $[0\% - 1\%]$ and $[80\% - 100\%]$ event class. However, Rec.MC Pythia reproduces the near side jet only qualitatively with different magnitude and away side jets show opposite shape in $\Delta\varphi \approx \pi$.

In order to study longer range $\Delta\eta$ correlation functions, centeral- (TPC) and forward- (V0) rapidity correlation functions are performed up to $|\Delta\eta| \sim 5$. The subtraction of yield of associate particle in V0 per trigger particle in TPC between $[0\% - 1\%]$ and $[80\% - 100\%]$ shown in Figure 5.8. V0A-TPC correlation functions with $1 \leq p_T^{Trig} < 4GeV/c$ and charged particles of $V0A^{Assoc}_{Rings2,3}$, TPC-TPC correlation functions with $1 \leq p_T^{Trig} < 4GeV/c$ and $0.2 \leq p_T^{Assoc} < 10$ GeV/c and V0C-TPC correlation functions with $1 \leq p_T^{Trig} < 4GeV/c$ and charged particles of $V0C^{Assoc}_{Rings0,1}$ are compared. The correlation functions show reversed pattern between V0C-TPC and V0A-TPC correlation for two different event estimators with V0C and V0A by an auto-correlation and in the event selections. In case of V0A event estimator, V0A-TPC correlations show more enhanced di-jet signal in away side, that can be considered as an auto-(self-) correlation from various event estimators, which is rather well reproduced in Monte Carlo simulation with PYTHIA. Results of Rec.MC Pythia show not only an auto-correlation in V0A-TPC correlations but also anti-correlation in V0C-TPC correlations, which shows a slight reduction (dip) of di-jet signal in the away side. On the other hand, in case of V0C event estimator, V0C-TPC correlations show an enhanced di-jet correlation from the auto-correlation, similarly. Results of Rec.MC Pythia also show a similar effect but in opposite in η region, which is exactly same as in the experimental data. The TPC-TPC correlation functions with both V0A and V0C event estimators have similar results for the double ridges. On the other hand, the Monte Carlo simulation shows almost flat distribution as a function of $\Delta\varphi$, which means there is no change as a function of multiplicity or slightly opposite shape, as negative double ridge-like shape.

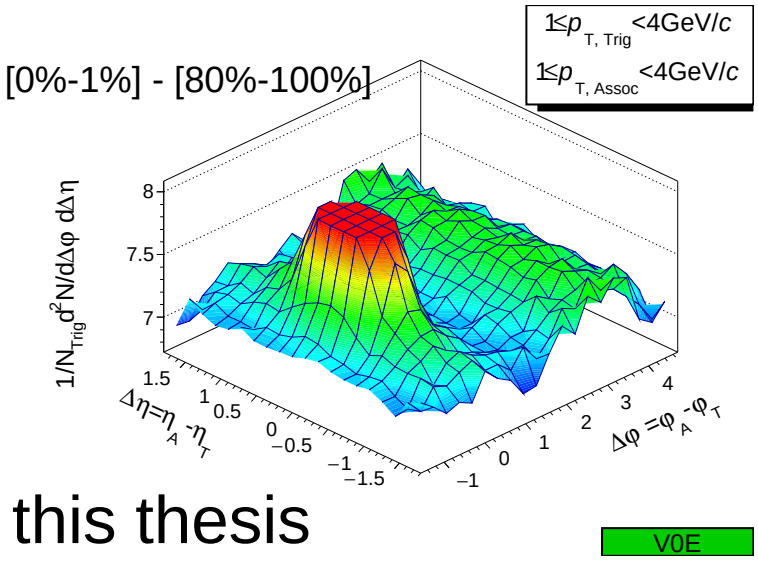

(a) ALICE experimental data, V0E event estimator.

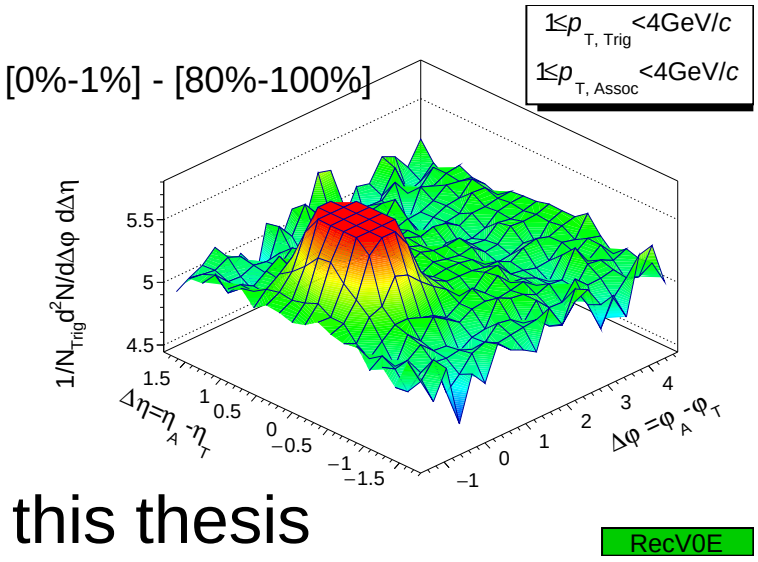

(b) Rec.MC, V0E event estimator.

Figure 5.7: Associated yield per trigger particle in $\Delta\varphi$ and $\Delta\eta$ for charged particles with $1\leq p_T <4$ GeV/c are shown for the $0\% - 1\%$ multiplicity class, after subtraction of the associated yield obtained in the $80\% - 100\%$ event class for (a) ALICE experimental data and (b) Rec.MC Pythia.

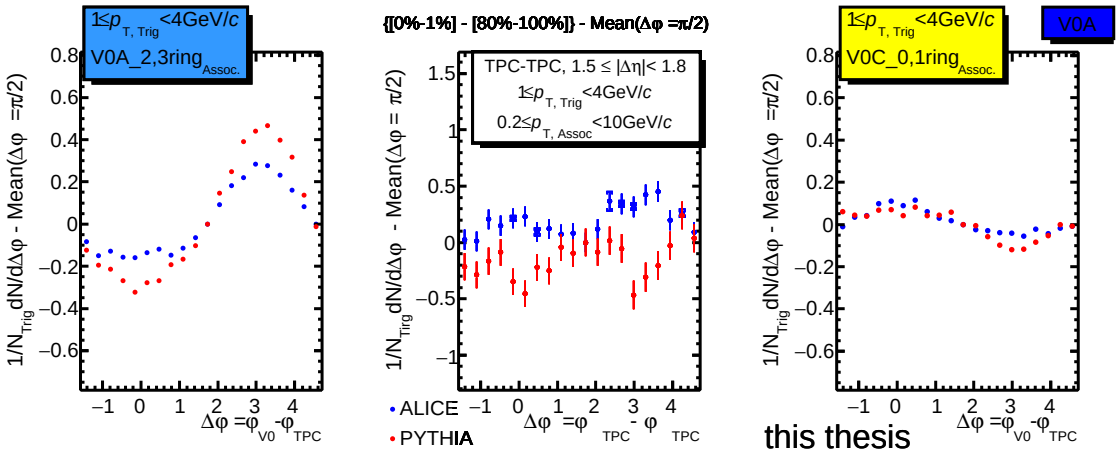

(a) V0A event estimator (V0A: $2.8 < \eta < 5.1$).

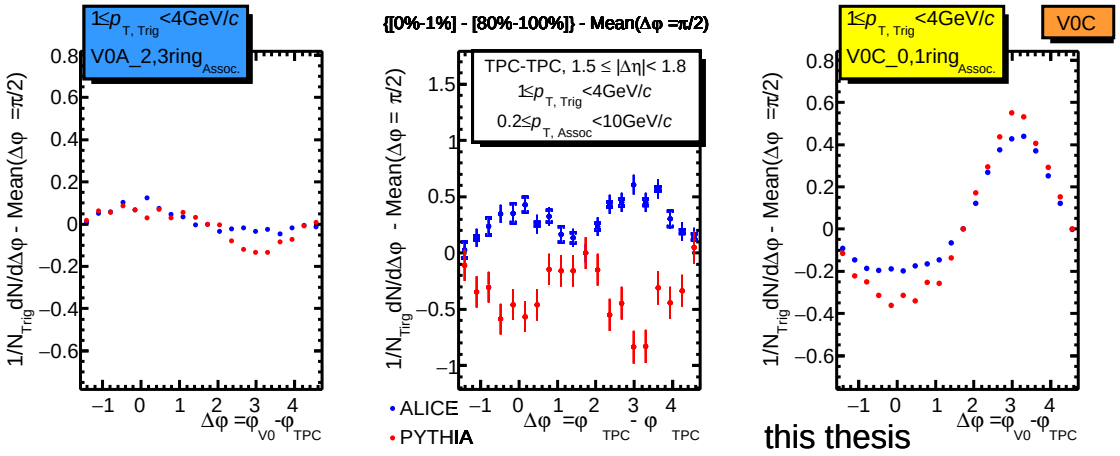

(b) V0C event estimator (V0C: $-3.7 < \eta < -1.7$).

Figure 5.8: Associated yield per trigger particle in $\Delta\varphi$ and $\Delta\eta$ for charged particles with $1 \leq p_T^{Trig} < 4$ GeV/c and mean charged particles of $V0A^{Associ}_{Rings2,3}$ (V0A-TPC, 1.9< $\Delta\eta$ <4.8), $1 \leq p_T^{Trig} < 4$ GeV/c and $0.2 \leq p_T^{Assoc} < 10$ GeV/c (TPC-TPC, 1.5≤ $|\Delta\eta|$ <1.8), and $1 \leq p_T^{Trig} < 4$ GeV/c and mean charged particles of $V0C^{Associ}_{Rings0,1}$ (V0C-TPC, -1.8< $\Delta\eta$ <-4.6) for the $0\% - 1\%$ multiplicity class, after subtraction of the associated yield obtained in the $80\% - 100\%$ event class are measured by the ALICE experiment with blue points, while the red points are from pythia model.

5.4 Interpretation with Elliptic Flow Parameter

The changes of correlation function shape $C(\Delta\varphi)$ are evaluated with $R(\Delta\varphi)$ that are ratio of $C(\Delta\varphi)$ over fitted function $F(\Delta\varphi)$ defined by the correlation shape from the lowest multiplicity. The quality of the fit is successful, see section 4.1.4, section 4.2.2 and section. 4.3.2. The effects of the momentum conservation and the elliptic azimuthal anisotropy correlations can describe most of the azimuthal angular correlation structures observed in two-particle correlations at long range $\Delta\eta$ include the ridge structure. The angular correlation shape variation with respect to the lowest multiplicity ($R(\Delta\varphi)$) in $1.5\leq |\Delta\eta| <1.8$ with $1\leq p_T <4$ GeV/c are shown for TPC-TPC correlation, as shown in Figure 5.9(a). ALICE experimental data show a continuously change to double peaks shapes like elliptic shapes, because of jet-like and ridge-like events with increasing multiplicity selections. Figure 5.9(b) shows the features of elliptic shapes with increasing multiplicity selections for V0-TPC correlation, in up to $1.8< |\Delta\eta| <4.8$ with $1\leq p_T^{Trig} <4$ GeV/c in TPC and all charged particles in $V0^{Assoc}$ (V0-TPC), and Figure 5.9(c) shows up to $5.5< |\Delta\eta| <7.6$ for V0-V0 correlation. Figure 5.10 shows the extracted elliptic parameter coefficients, which corresponds to the product of v_2 parameters, for the 5 multiplicity bins. The new method to extract p_2^{long} parameters, $\frac{c_2^{V0A-TPC}c_2^{V0C-TPC}}{c_2^{V0A-V0C}} \sim p_2^{long}$, $c_2^{TPC-TPC} \sim p_2^{short}$, where the both p_2^{long} and p_2^{short} parameters correspond to the v_2^2 in TPC from two different methods, which are extracted from Figure 5.9(b) and Figure 5.9(c) and as explained in Figure 3.15, has been found to agree with p_2^{short}, which is extracted from Figure 5.9(a).

Error bars indicate statistical uncertainties and small marks in brackets show systematic uncertainties, as Equation 3.14.

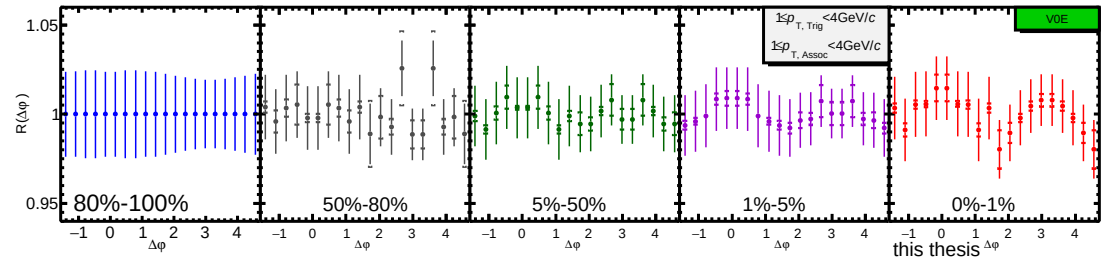

(a) ALICE experimental data, V0E event estimator, TPC-TPC correlation.

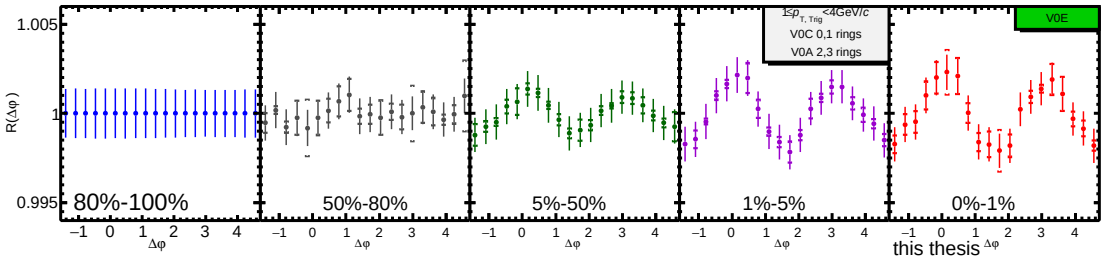

(b) ALICE experimental data, V0E event estimator, V0-TPC correlation.

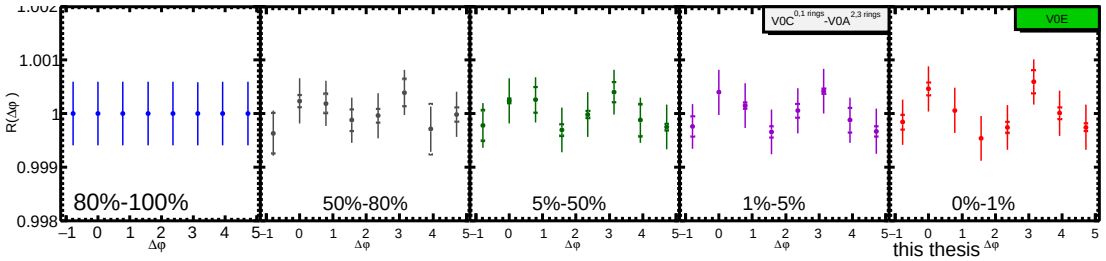

(c) ALICE experimental data, V0E event estimator, V0-V0 correlation.

Figure 5.9: The angular correlation shape variation with respect to the lowest multiplicity ($R(\Delta\varphi)$) in (a) $1.5 \leq |\Delta\eta| < 1.8$, (b) $1.8 < |\Delta\eta| < 4.8$ (c) $5.5 < |\Delta\eta| < 7.6$ are shown for the 5 multiplicity classes.

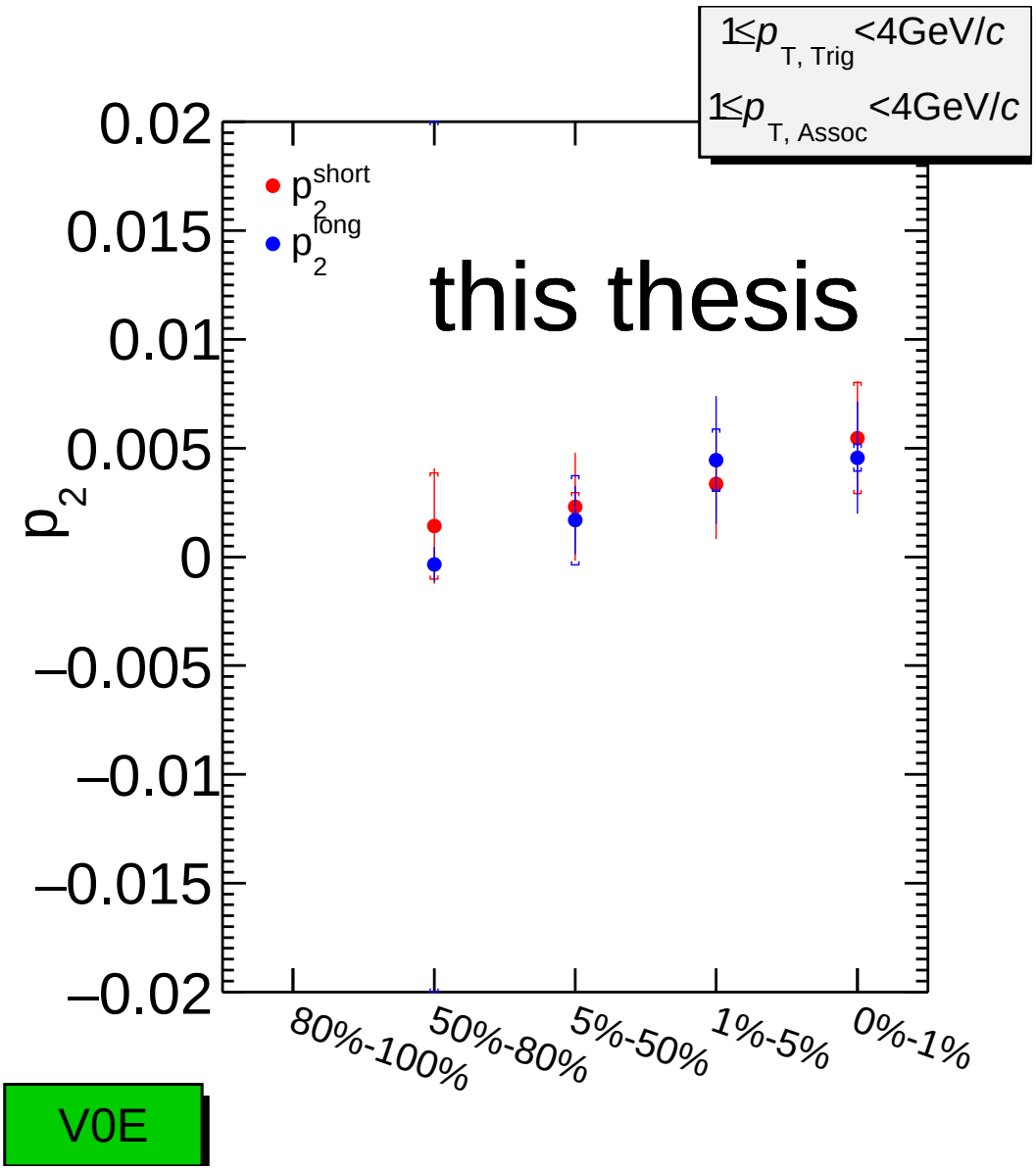

Figure 5.10: Product of two different method of p_2 parameters of two-particle correlation are shown for the 5 multiplicity classes.

5.5 Possible explanations of ridge structure in pp collisions

The ridge phenomena in $\Delta\varphi \approx 0$ in long rang $\Delta\eta$ in heavy ion collisions and p-Pb collisions have been observing over the past several years. It has been described in many different models, some attributing the ridge structure in $\Delta\varphi \approx 0$ in long rang $\Delta\eta$ to the medium response to its interactions with high p_T partons [28] [29] [30] [31], others attribute the ridge structure to multiparton interaction (MPI) in high multiplicity in pp collisions [10], while others attribute the ridge structure to the hydrodynamics medium itself [32], [33], [34], [35], [36].

Pythia simulation cannot explain the ridge structure in high multiplicity in pp collisions in this thesis, especially in Figure 5.5, Figure 5.7. MPI simulation is also not successful to explain multiplicity dependence in pp collisions Figure 5.11 [10]. There is very weak multiplicity dependence, although the ridge structure at large $\Delta\eta$ is seen in this model. Recent theoretical developments, such as EPOS simulation as already pointed out in section 1.2.2 implies that ridge structure in long range $\Delta\eta$ in high multiplicity in pp collisions can be understood by elliptic flow in hydrodynamics model. One of the its evidence is p_T dependence of the extracted v_2^2 like heavy ion collisions [12] [14] [37], as shown in Figure A.5 with an enhanced signal in $1 \leq p_T < 4$ GeV/c.

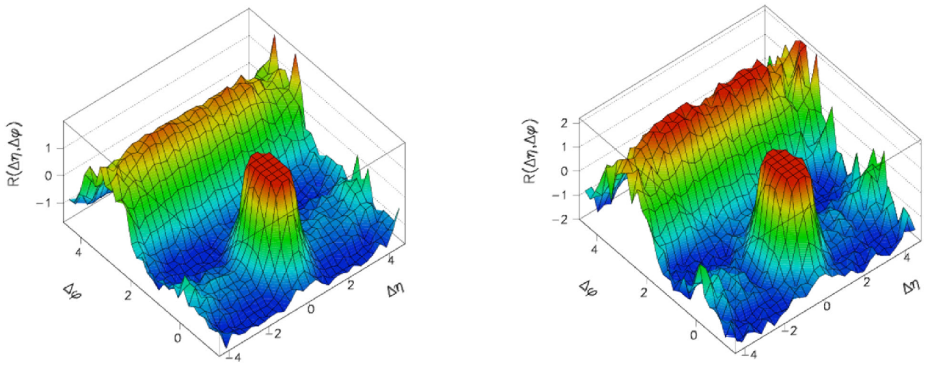

(a) minimum bias events comparing results using Figure 1.16 (b)

(b) high multiplicity events ($N_{ch} > 110$) comparing results using Figure 1.16 (d)

Figure 5.11: Multiparton interaction (MPI) simulation for 2-D charged particle angular correlation functions in pp collisions at $\sqrt{s} = 7$ TeV with $1 < p_T < 3$ GeV/c are shown with (a) minimum bias events and (b) high multiplicity events [10].

Chapter 6

Conclusion

Proton-proton collisions at $\sqrt{s} = 7$ TeV are provided for experiments at CERN-LHC. ALICE experiment as well as the other experiments at LHC have measured as large as 100 tracks in $dN/d\eta$. in one pp event that could mean a small and short-lived but high density system might have been formed.

Measurement of two-particle correlations $C(\Delta\varphi, \Delta\eta)$ has been done in $\sqrt{s} = 7$ TeV pp collisions at ALICE experiment for 5 multiplicity classes in azimuthal angle and pseudo-rapidity. Due to an enhancement of hard collisions, the relative angles in the correlation function of near side jet region become narrower with increasing multiplicity selections. In high multiplicity events near side ridge had been observed in $\Delta\varphi \approx 0$ in $1.5 > |\Delta\eta|$. And extraction of double ridges by subtraction of low multiplicity yield from high multiplicity yield shows a similar magnitude at $\Delta\varphi \approx 0$ and π. Moreover, the shapes of the correlation functions are continuously changing into elliptic shapes with increasing multiplicity selections. The elliptic parameter coefficient v_2 is about $7.4 \pm 1.8\%$ in the highest multiplicity class (top 5% in multiplicity) at $1 \leq p_T < 4$ GeV/c.

The same decomposition procedure had been applied to the pythia simulation and the results showed no ridge as well as negative elliptic parameter coefficient in the highest multiplicity classes.

Multiplicity dependence of small system, such as pp collisions, shows strong correlation with the entire particle productions and biased multiplicity selection. Various event estimators show different shapes of multiplicity dependence, which is event activity dependence in

small system. In order to avoid the auto-correlation from the multiplicity definition as well as various physics biases, such as jet bias, the results suggest V0E (hybrid) event estimators.

Ridge structure had been observed in high multiplicity pp collisions, which imply the formation of hot dense matter like heavy ion collisions and p-Pb collisions. The extraction of elliptic parameter coefficients could serve as an estimate of the amount of collective flow in pp collisions. Therefore, the observed ridge structure in high multiplicity pp collisions could come from collective phenomena like heavy ion collisions, which is called QGP.

Appendix A

Appendix

A.1 Correlation function $C(\Delta\varphi)$ in long range $\Delta\eta$

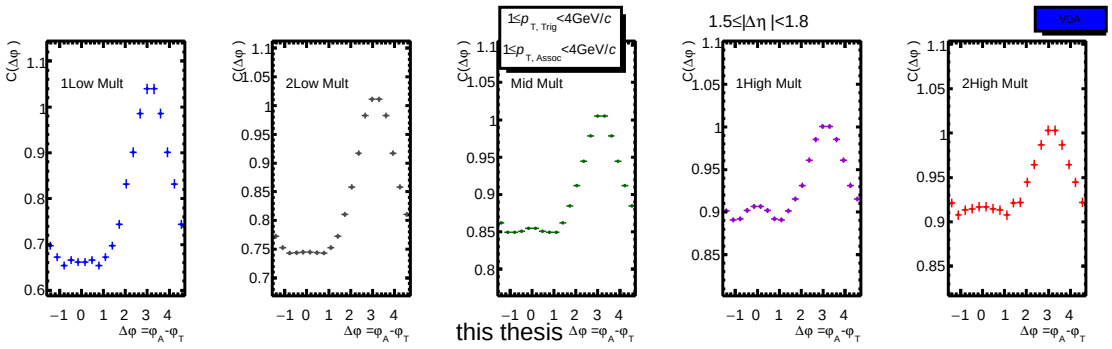

(a) ALICE experimental data, V0A event estimator.

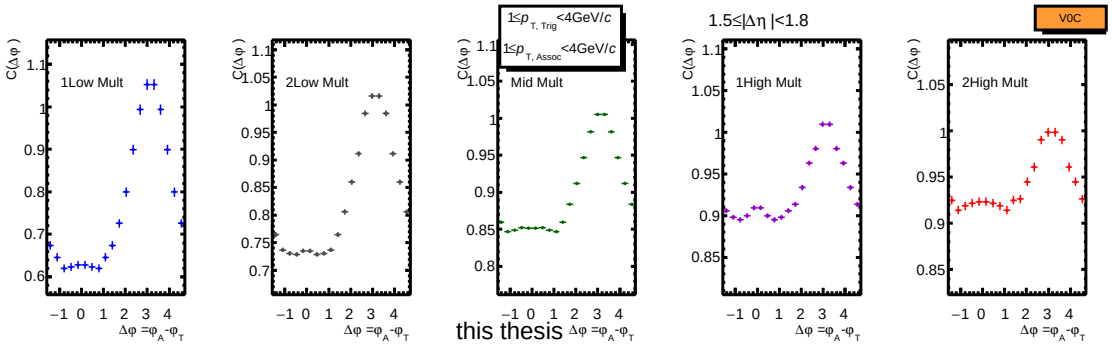

(b) ALICE experimental data, V0C event estimator.

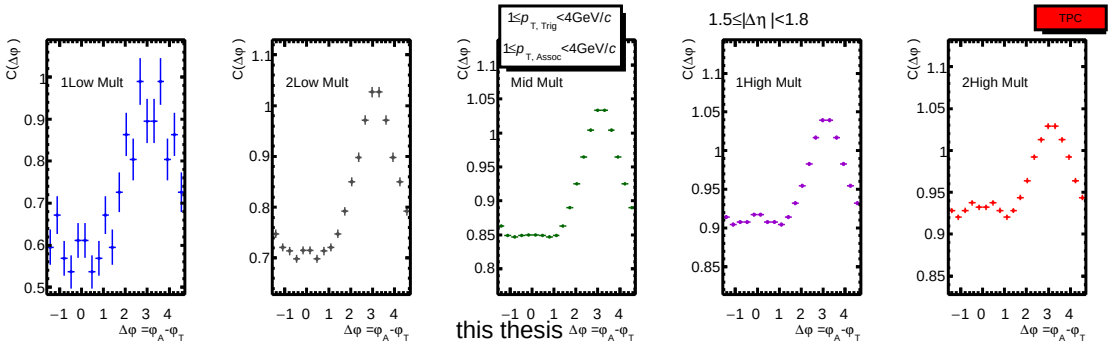

(c) ALICE experimental data, TPC event estimator.

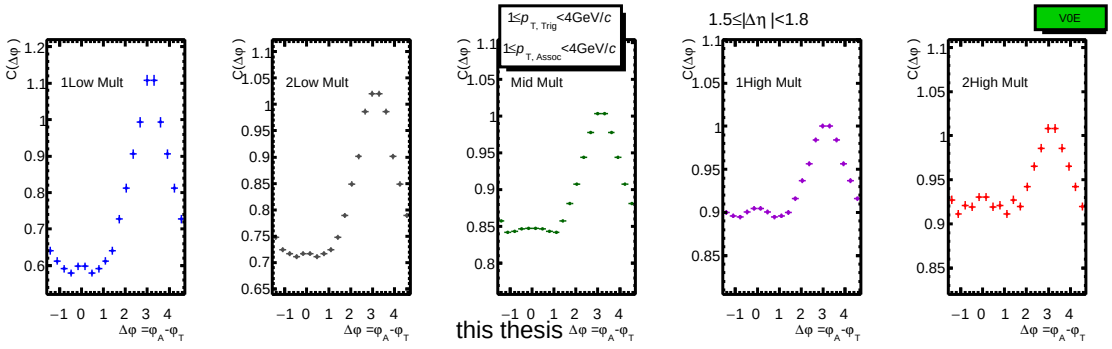

(d) ALICE experimental data, V0E event estimator.

Figure A.1: ALICE experimental data, TPC-TPC correlation, 1-D correlation functions in pp collisions at $\sqrt{s}$ = 7 TeV with 1$\leq p_T^{Trig}$ <4 GeV/c and 1$\leq p_T^{Asso}$ <4 GeV/c for the 5 multiplicity classes by various event estimators are shown in 1.5$\leq |\Delta\eta|$ <1.8.

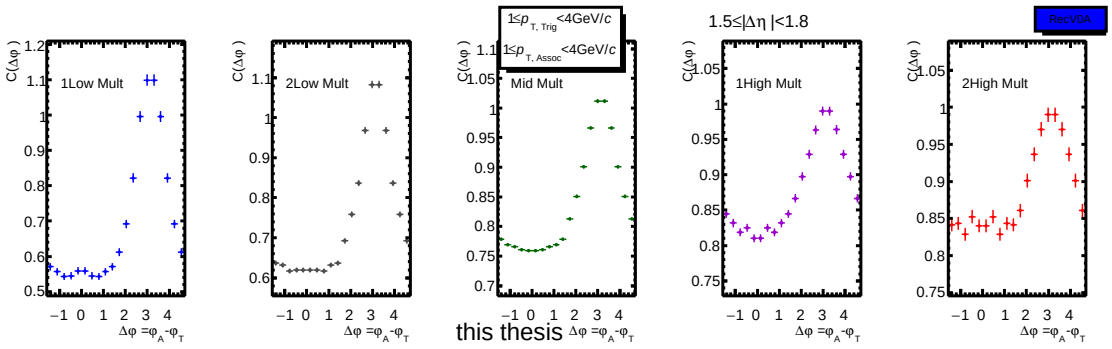

(a) Rec.MC, V0A event estimator.

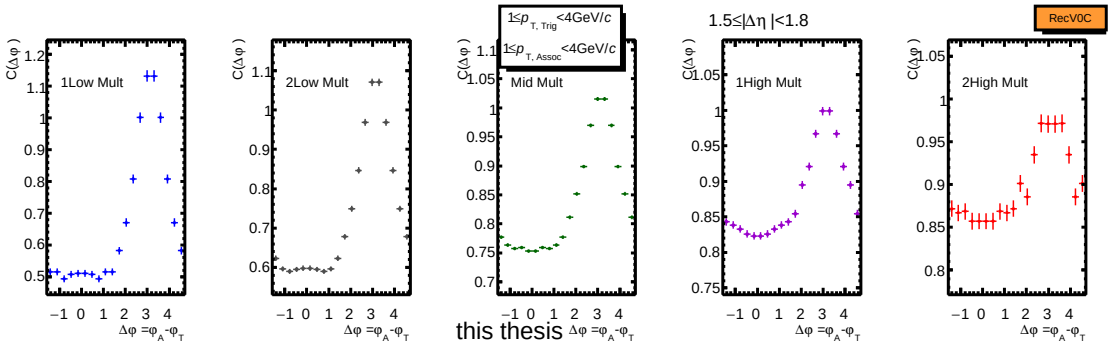

(b) Rec.MC, V0C event estimator.

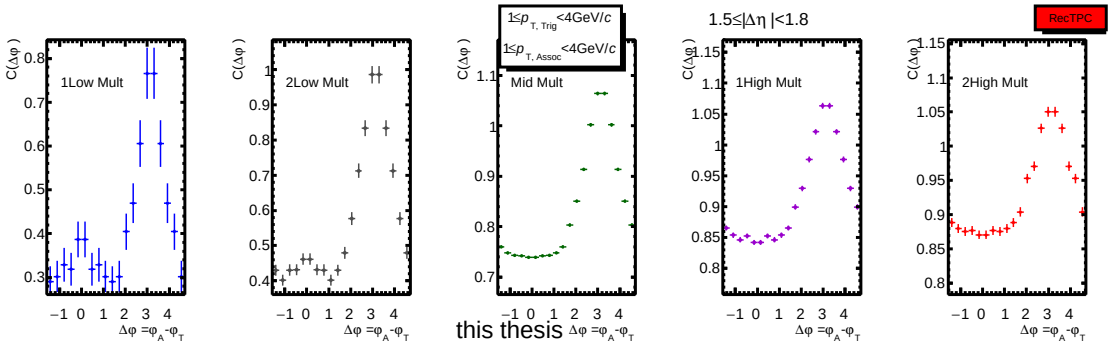

(c) Rec.MC, TPC event estimator.

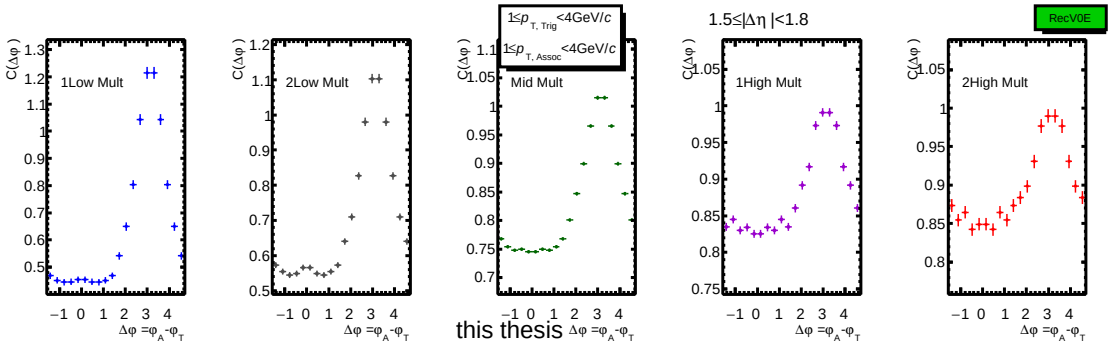

(d) Rec.MC, V0E event estimator.

Figure A.2: Rec.MC, TPC-TPC correlation, 1-D correlation functions in pp collisions at $\sqrt{s} = 7$ TeV with $1 \leq p_T^{Trig} < 4$ GeV/c and $1 \leq p_T^{Asso} < 4$ GeV/c for the 5 multiplicity classes by various event estimators are shown in $1.5 \leq |\Delta\eta| < 1.8$.

A.2 p_T dependence of correlation function $C(\Delta\varphi)$ and $C(\Delta\eta)$

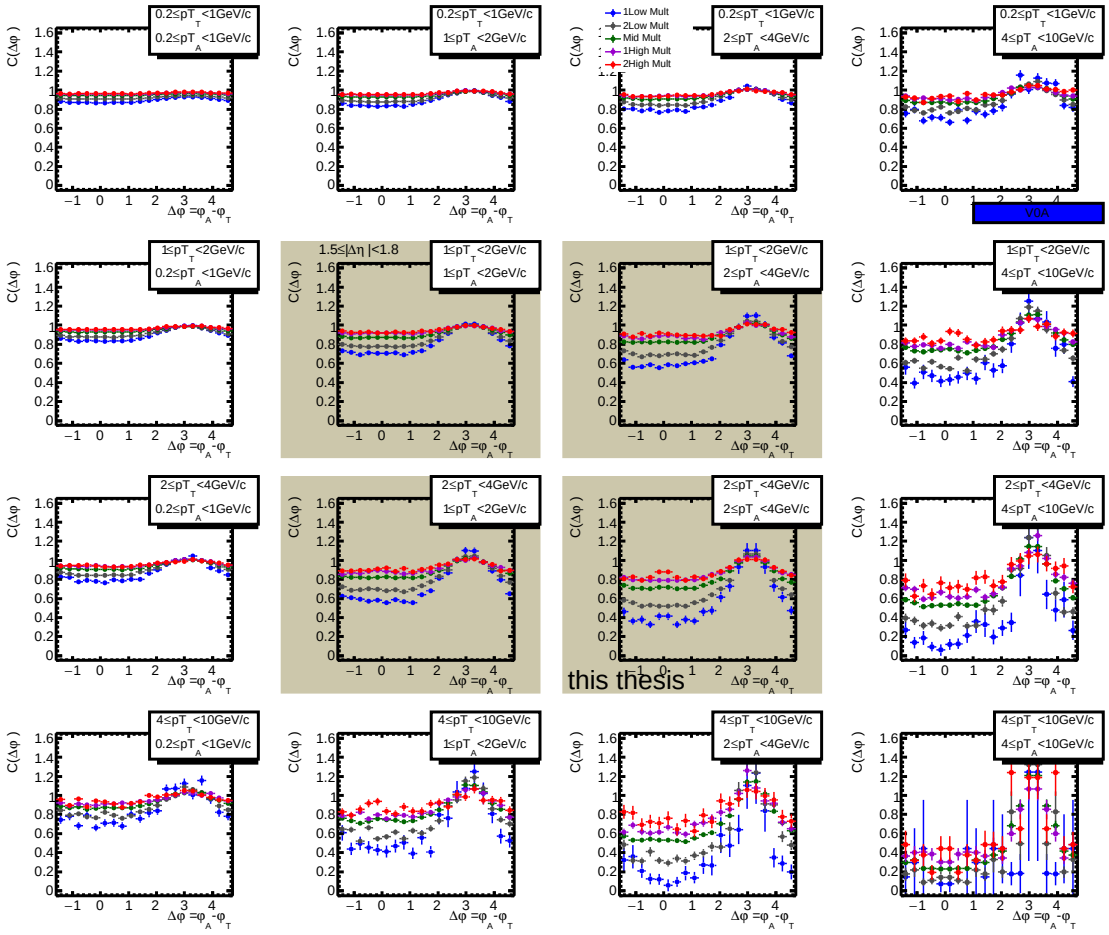

Figure A.3: ALICE experimental data, V0A event estimator, 1-D correlation functions show for p_T dependence in $1.5 \leq \Delta\eta < 1.8$ are shown for the 5 multiplicity classes.

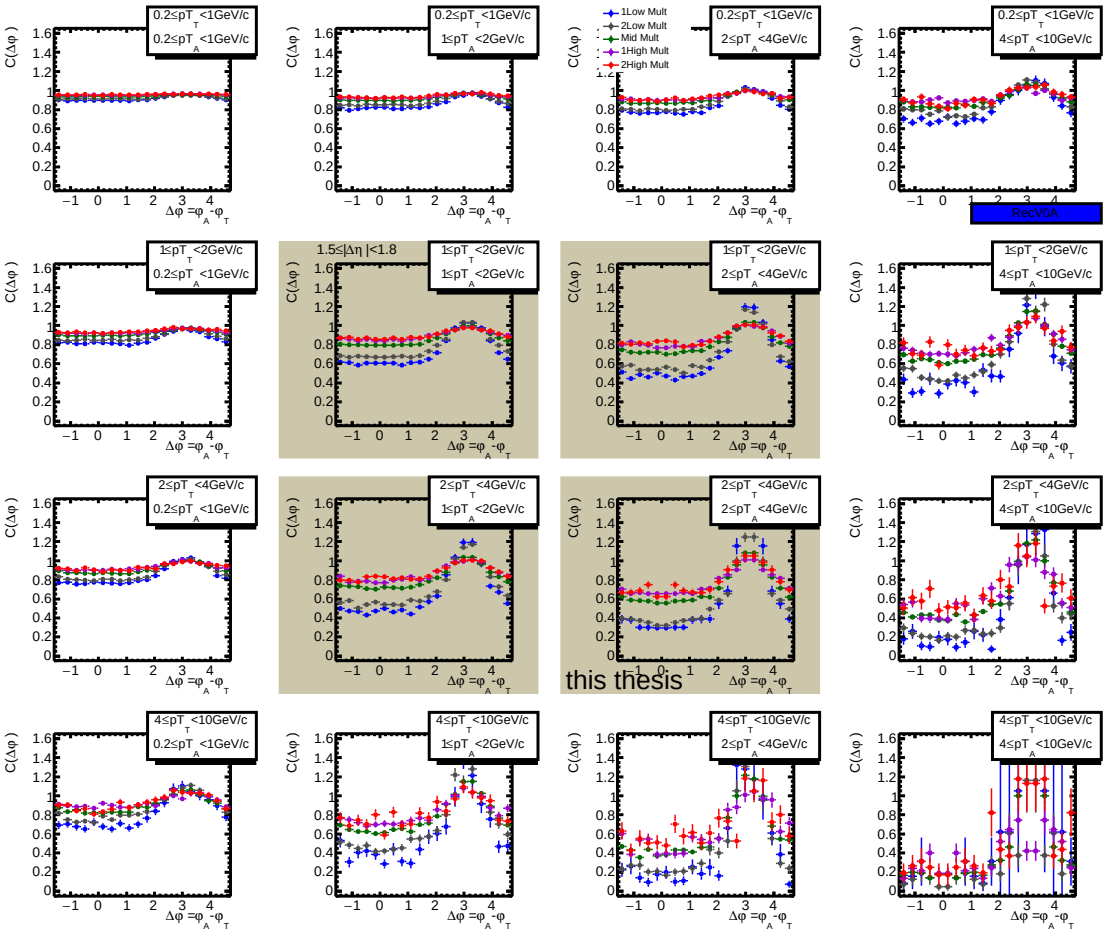

Figure A.4: Rec.MC, V0A event estimator, 1-D correlation functions show for p_T dependence in $1.5 \leq \Delta\eta < 1.8$. are shown for the 5 multiplicity classes.

A.3 p_T dependence of relative correlation shape with respect to multiplicity 50-100%

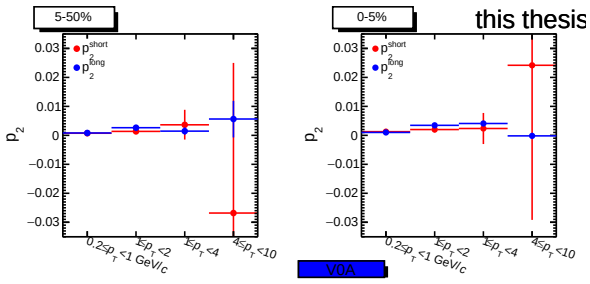

(a) V0A event estimator.

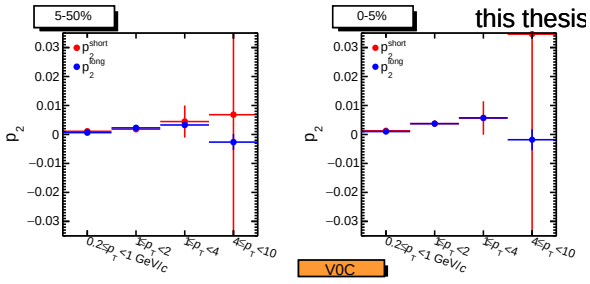

(b) V0C event estimator.

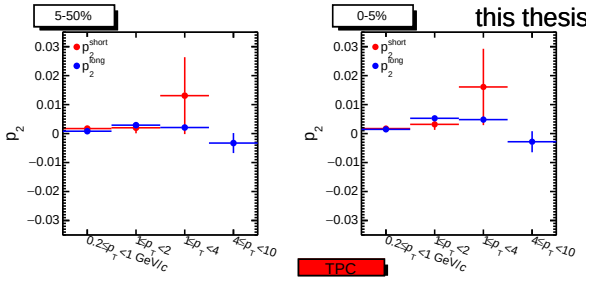

(c) TPC event estimator.

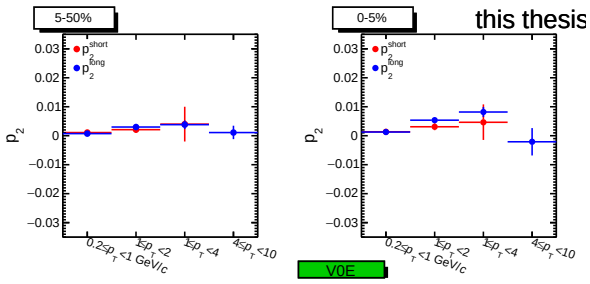

(d) V0E event estimator.

Figure A.5: The extracted $p2^{long}$ parameter and $p2^{short}$ with multiplicity and p_T dependence by various event estimators are shown for the 3 multiplicity classes.

Appendix B

Appendix

B.1 σ values by Gaussian fitting of near side jets

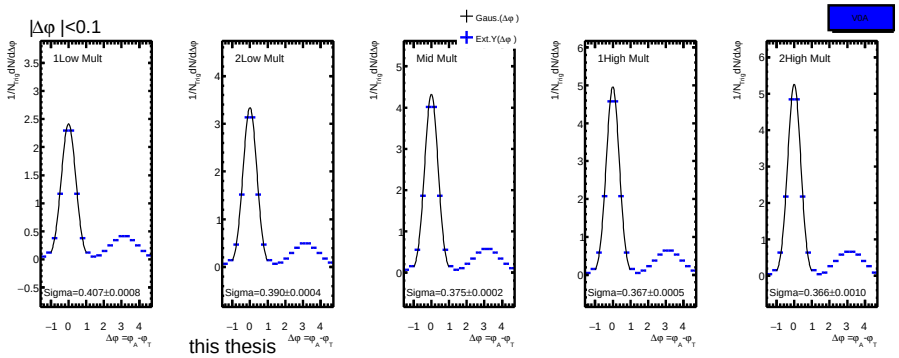

(a) ALICE experimental data, V0A event estimator.

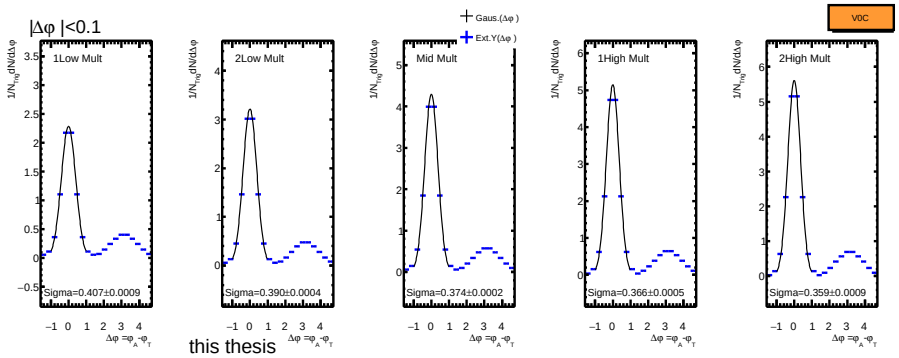

(b) ALICE experimental data, V0C event estimator.

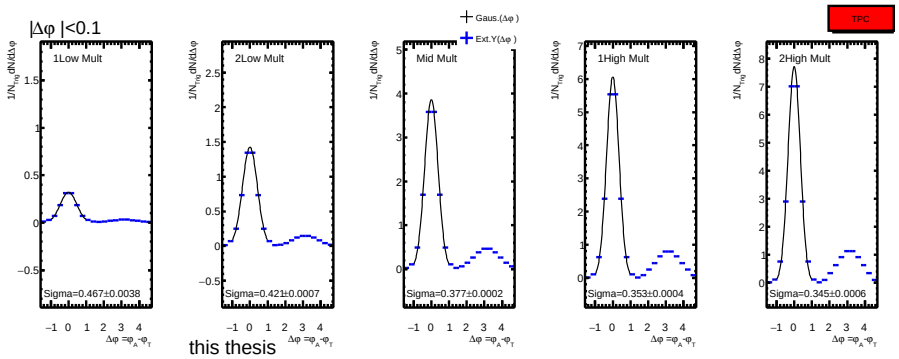

(c) ALICE experimental data, TPC event estimator.

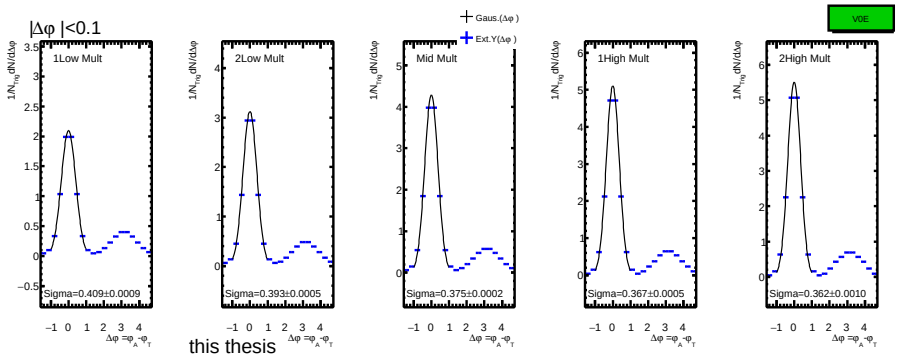

(d) ALICE experimental data, V0E event estimator.

Figure B.1: σ values by Gaussian fitting ($dN/d\Delta\varphi$ in $|\Delta\eta| \leq 0.2$) in pp collisions at $\sqrt{s}$ = 7 TeV with $1 \leq p_T^{Trig}$ <4 GeV/c and $1 \leq p_T^{Asso}$ <4 GeV/c by various event estimators are shown for the 5 multiplicity classes.

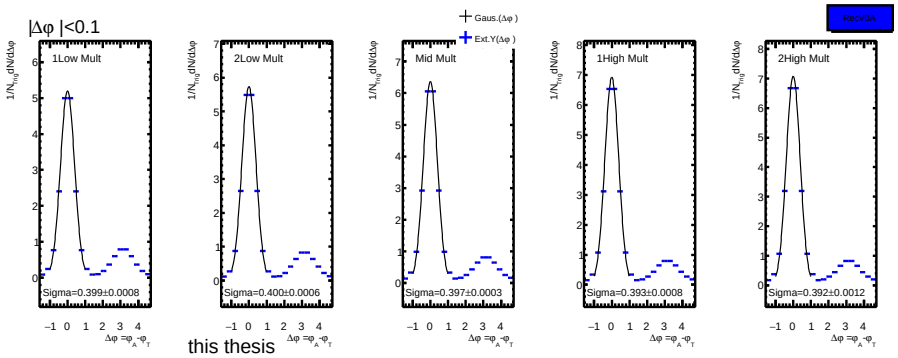

(a) Rec.MC data, V0A event estimator.

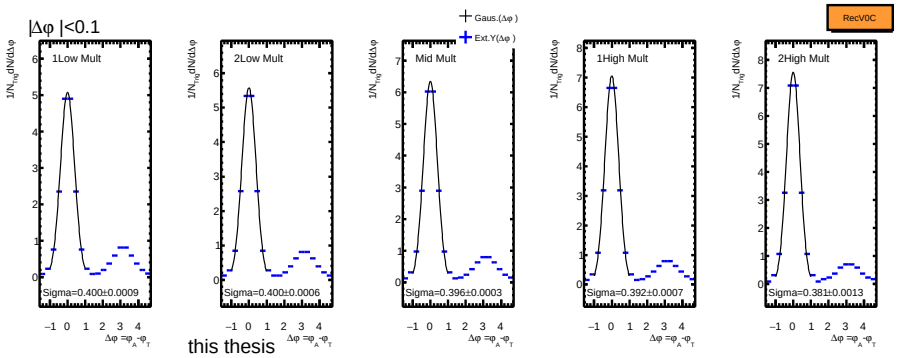

(b) Rec.MC data, V0C event estimator.

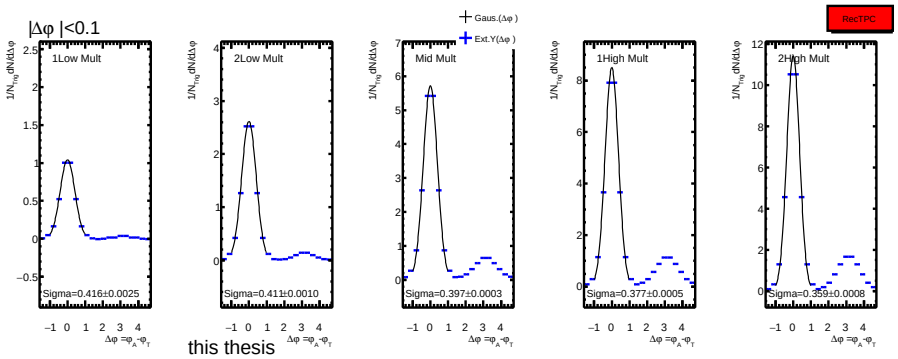

(c) Rec.MC data, TPC event estimator.

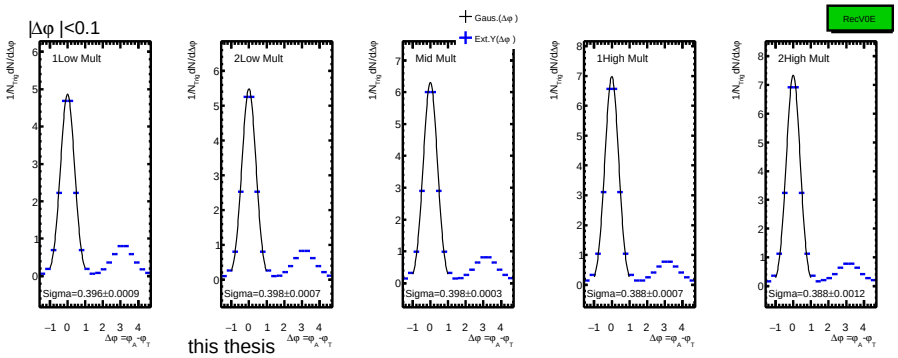

(d) Rec.MC data, V0E event estimator.

Figure B.2: Rec.MC, σ values by Gaussian fitting ($dN/d\Delta\varphi$ in $|\Delta\eta| \leq 0.1$) in pp collisions at $\sqrt{s} = 7$ TeV with $1 \leq p_T^{Trig} < 4$ GeV/c and $1 \leq p_T^{Asso} < 4$ GeV/c by various event estimators are shown for the 5 multiplicity classes.

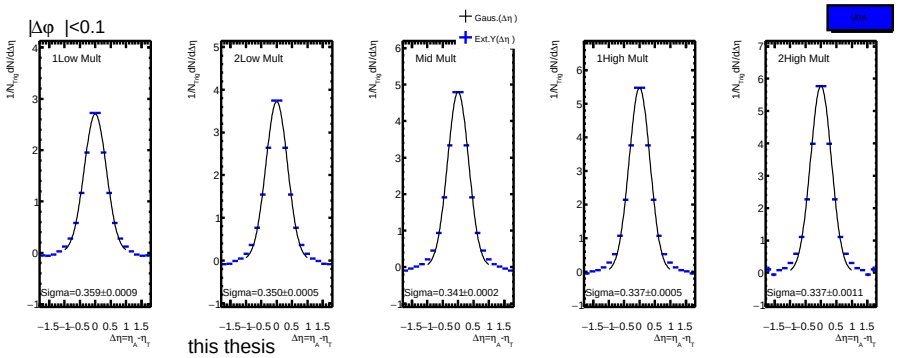

(a) ALICE experimental data, V0A event estimator.

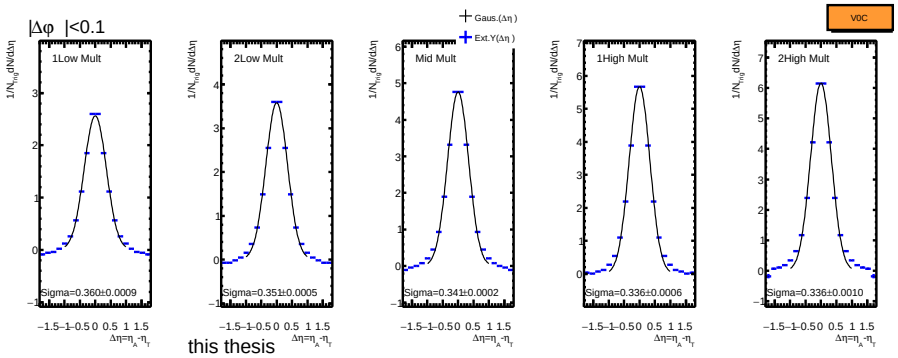

(b) ALICE experimental data, V0C event estimator.

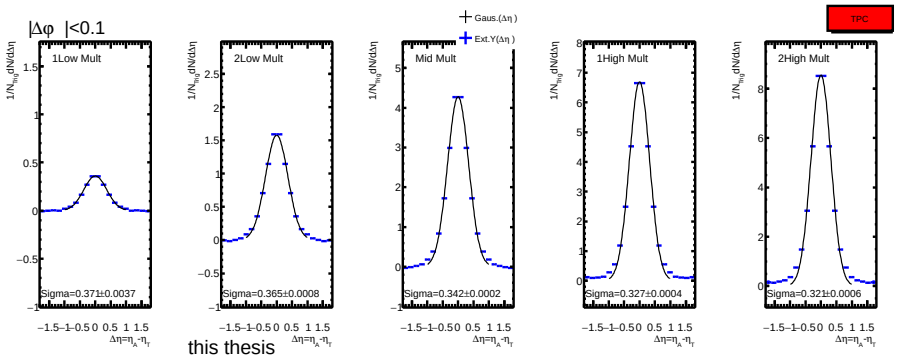

(c) ALICE experimental data, TPC event estimator.

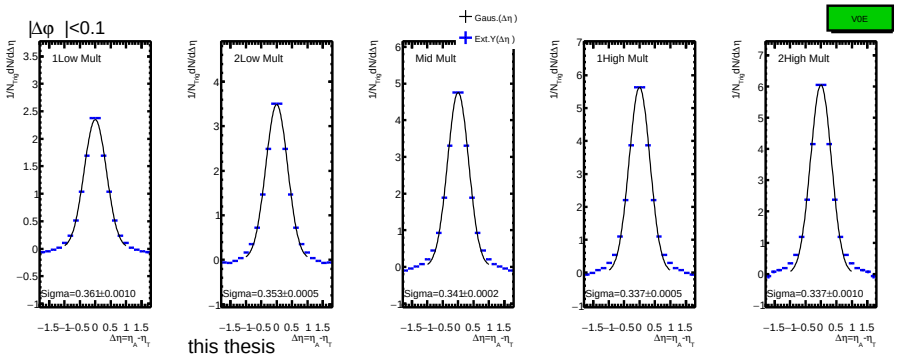

(d) ALICE experimental data, V0E event estimator.

Figure B.3: Rec.MC, σ values by Gaussian fitting ($dN/d\Delta\eta$ in $|\Delta\varphi| \leq 0.1$) in pp collisions at $\sqrt{s} = 7$ TeV with $1 \leq p_T^{Trig} < 4$ GeV/c and $1 \leq p_T^{Asso} < 4$ GeV/c by various event estimators are shown for the 5 multiplicity classes.

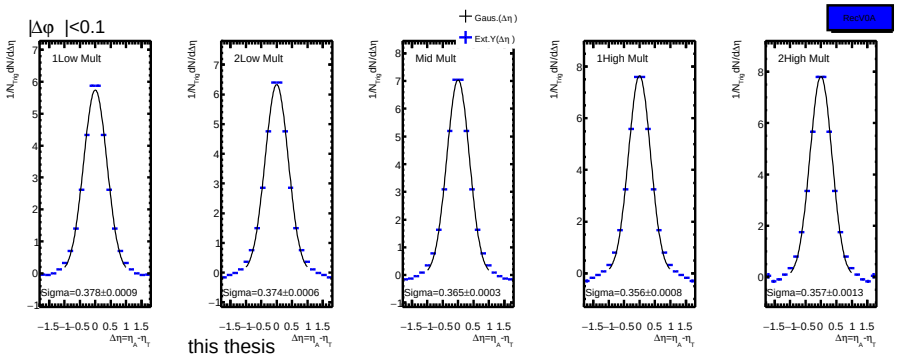

(a) Rec.MC data, V0A event estimator.

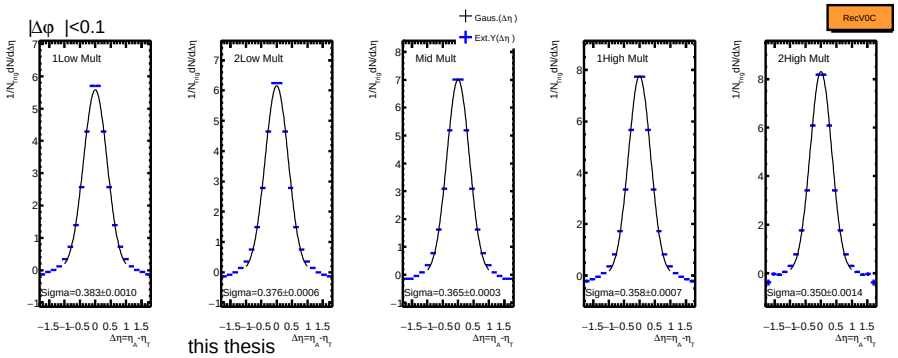

(b) Rec.MC data, V0C event estimator.

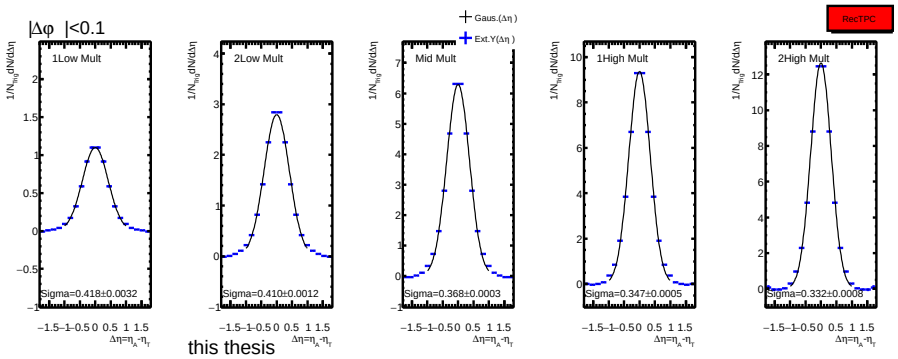

(c) Rec.MC data, TPC event estimator.

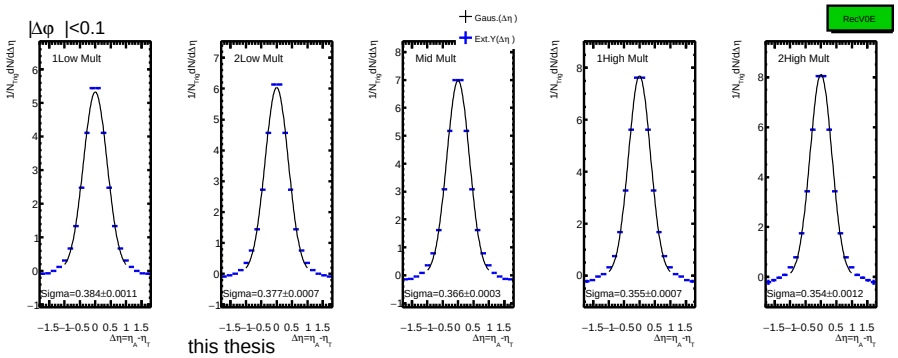

(d) Rec.MC data, V0E event estimator.

Figure B.4: Rec.MC, σ values by Gaussian fitting ($dN/d\Delta\eta$ in $|\Delta\varphi| \leq 0.2$) in pp collisions at $\sqrt{s} = 7$ TeV with $1 \leq p_T^{Trig} < 4$ GeV/c and $1 \leq p_T^{Asso} < 4$ GeV/c by various event estimators are shown for the 5 multiplicity classes.

Appendix C

Appendix

C.1 Relative correlation shape with respect to minimum bias shape

In order to understand the multiplicity dependence of the observed correlation functions with different multiplicity estimators, each of the same event pairs distributions, the mixed event pairs distributions and correlation functions are divided by the average of different multiplicity distributions, as shown in Figure C.1, Figure C.2, Figure C.3 and Figure C.4, for 4 different event estimators, respectively. There is no particular structure in mixed event distributions of V0A, V0C and V0E event estimators. The correlation function shapes are similar for the same event pairs shapes, naturally because of the flat mixed background shapes. However, TPC event estimator shows wing structures in $\Delta\eta$ in mixed event distributions in the lowest and the 2nd lowest multiplicity selections, as shown in Figure C.3, while it shows opposite (negative wing-like) structure in the high multiplicity selections.

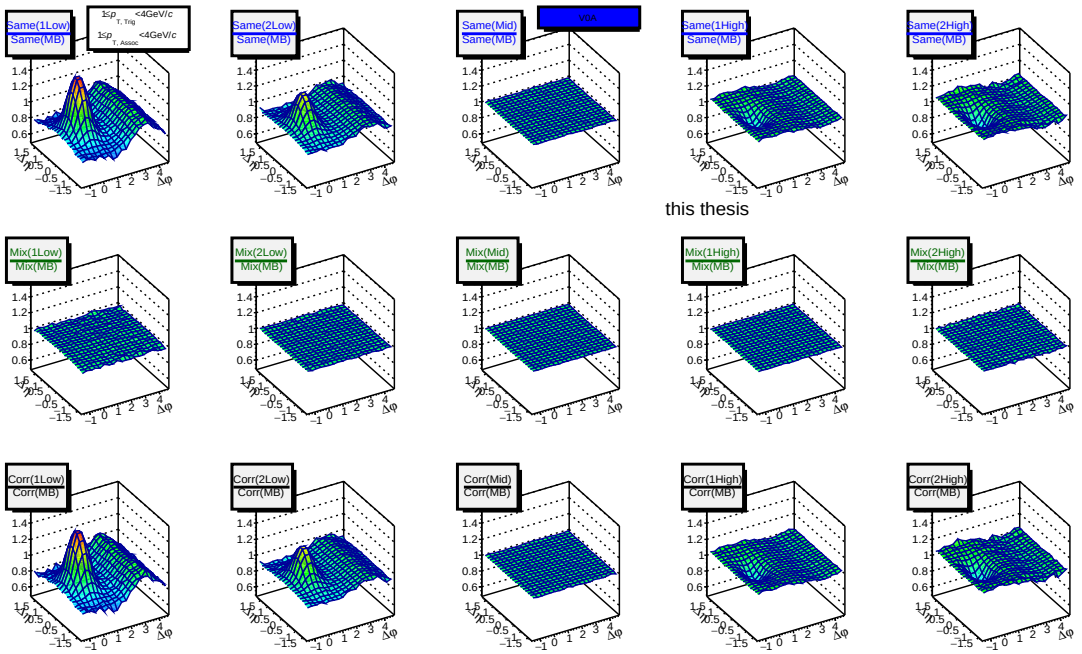

Figure C.1: ALICE experimental data, V0A event estimator, 2-D dihadron correlation functions divided by minimum bais in pp collisions at $\sqrt{s} = 7$ TeV with $1 \leq p_T^{Trig} < 4$ GeV/c and $1 \leq p_T^{Assoc} < 4$ GeV/c are shown for the 5 multiplicity classes.

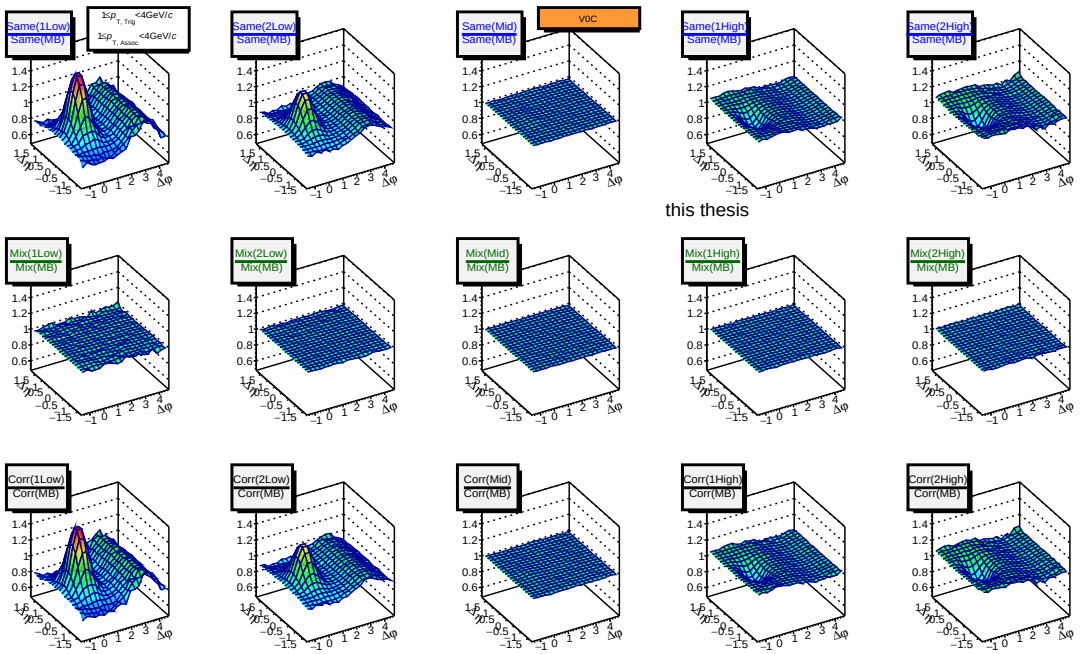

Figure C.2: ALICE experimental data, V0C event estimator, 2-D dihadron correlation functions divided by minimum bais in pp collisions at $\sqrt{s} = 7$ TeV with $1 \leq p_T^{Trig} < 4$ GeV/c and $1 \leq p_T^{Assoc} < 4$ GeV/c are shown for the 5 multiplicity classes.

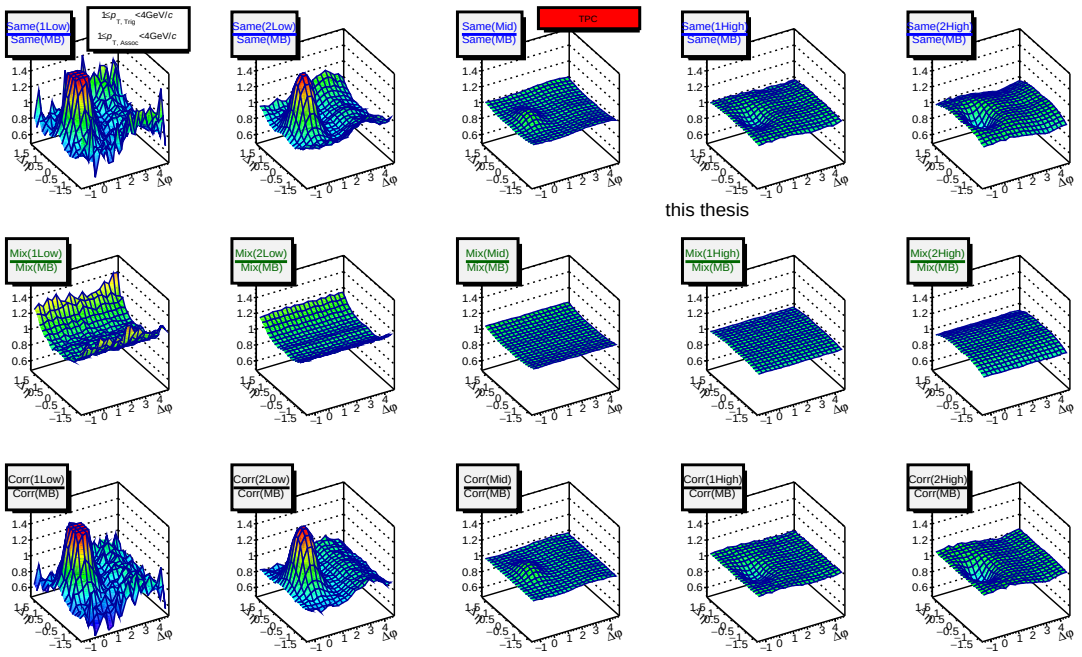

Figure C.3: ALICE experimental data, TPC event estimator, 2-D dihadron correlation functions for the 5 multiplicity classes divided by minimum bais in pp collisions at $\sqrt{s}$ = 7 TeV with 1$\leq p_T^{Trig}$ <4 GeV/c and 1$\leq p_T^{Assoc}$ <4 GeV/c are measured by the ALICE experiment.

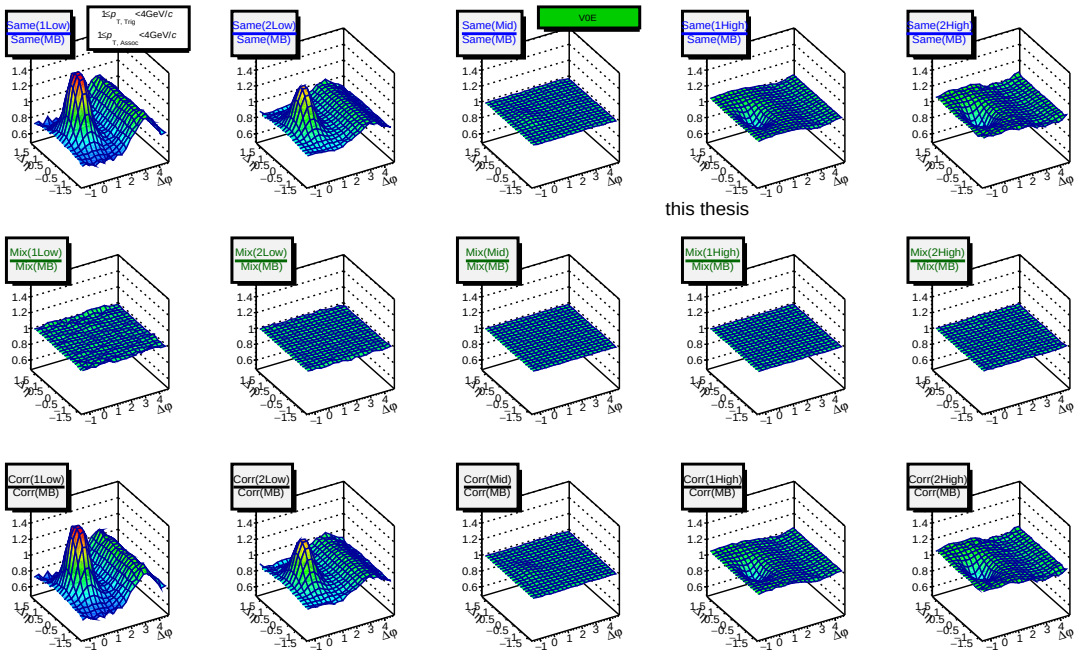

Figure C.4: ALICE experimental data, V0E event estimator, 2-D dihadron correlation functions divided by minimum bais in pp collisions at $\sqrt{s}$ = 7 TeV with 1$\leq p_T^{Trig}$ <4 GeV/c and 1$\leq p_T^{Assoc}$ <4 GeV/c are shown for the 5 multiplicity classes.

Appendix D

Appendix

D.1 Subtraction of flat background (average zyam: zero-yield at minimum)

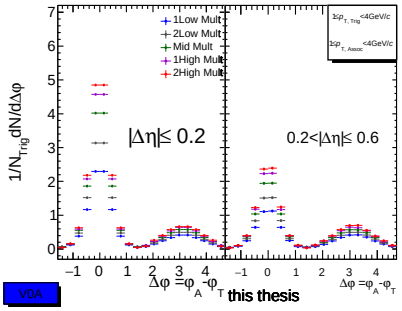

(a) ALICE experimental data, V0A event estimator.

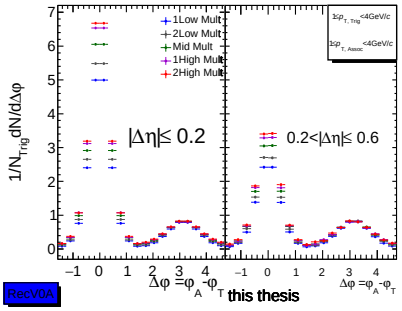

(b) ALICE experimental data, V0A event estimator.

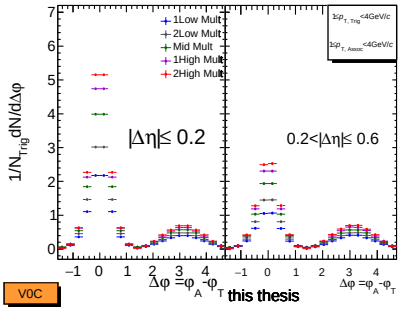

(c) ALICE experimental data, V0C event estimator.

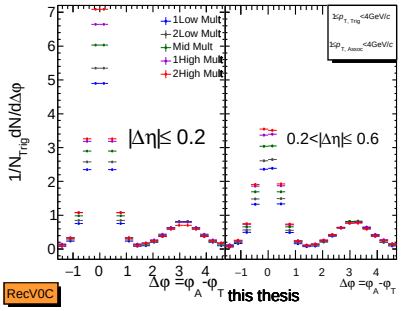

(d) ALICE experimental data, V0C event estimator.

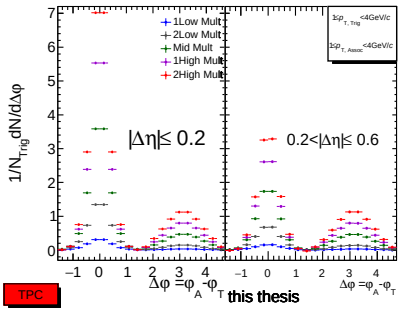

(e) ALICE experimental data, TPC event estimator.

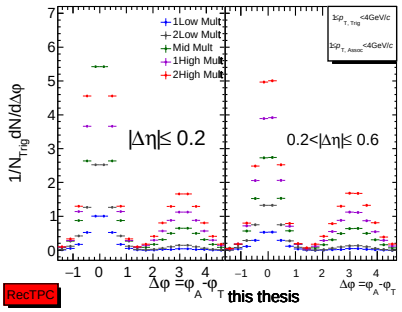

(f) ALICE experimental data, TPC event estimator.

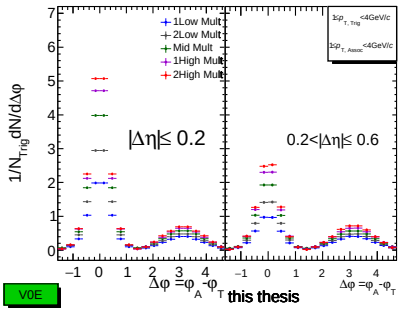

(g) ALICE experimental data, V0E event estimator.

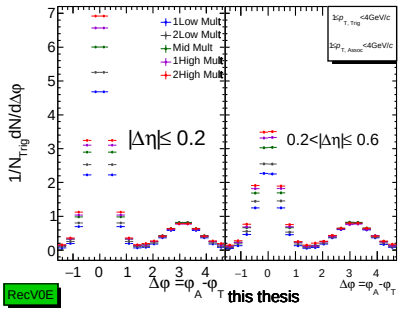

(h) ALICE experimental data, V0E event estimator.

Figure D.1: The subtracted flat background of associated particle yields per trigger in pp collisions at $\sqrt{s} = 7$ TeV with $1 \leq p_T^{Trig} < 4$ GeV/c and $1 \leq p_T^{Assoc} < 4$ GeV/c in $|\Delta\eta| \leq 0.2$ and $0.2 < |\Delta\eta| \leq 0.6$ are shown for the 5 multiplicity classes.

Appendix E

Appendix

E.1 1-D dihadron correlation functions of V0A-TPC, TPC-TPC and V0C-TPC

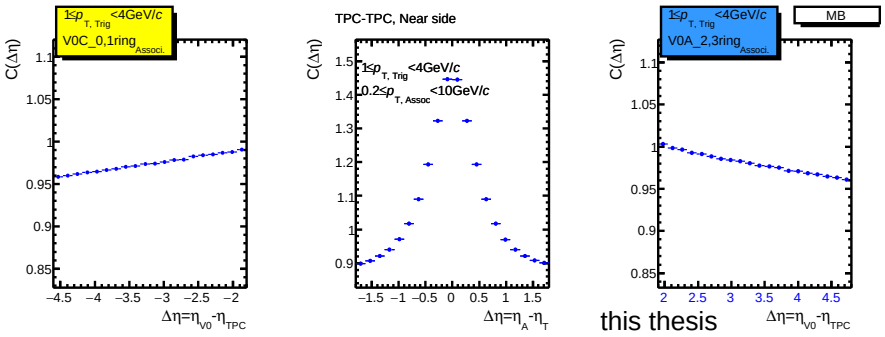

(a) ALICE experimental data, MB, near side.

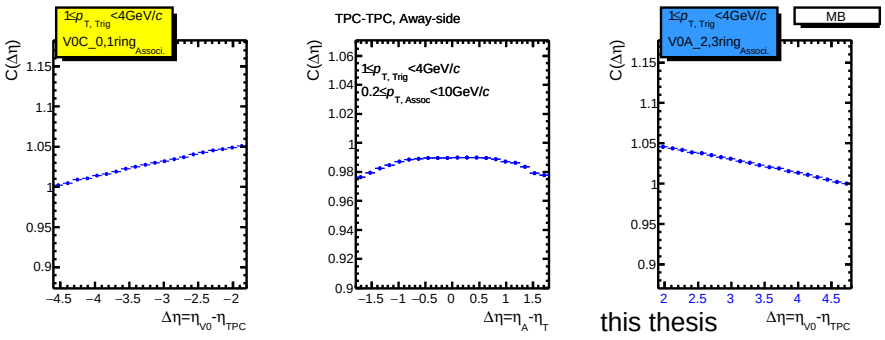

(b) ALICE experimental data, MB, away side.

Figure E.1: ALICE experimental data, 1-D dihadron correlation functions of V0A-TPC, TPC-TPC and V0C-TPC in pp collisions at $\sqrt{s} = 7$ TeV in (a) $|\Delta\varphi| < 0.1$ (near side) and (b) $2.3 < \Delta\varphi < 3.9$ (away side) are shown for the minimum bias (MB).

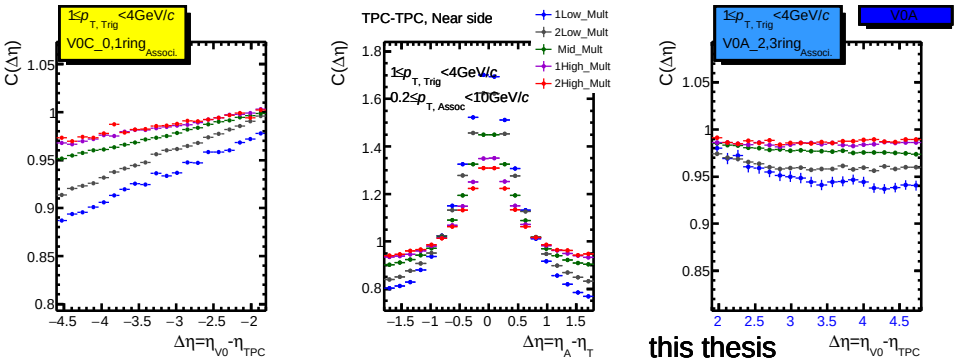

(a) ALICE experimental data, V0A event estimator, near side.

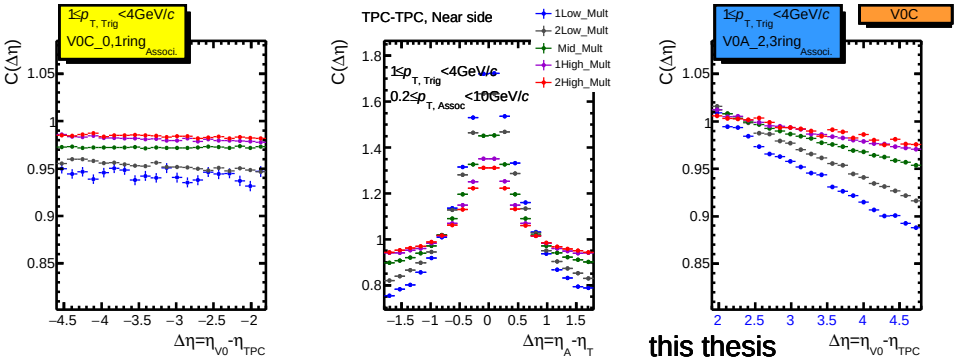

(b) ALICE experimental data, V0C event estimator, near side.

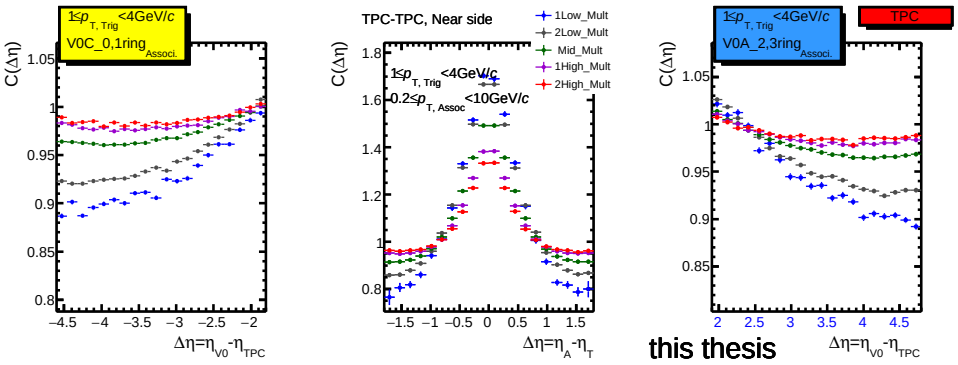

(c) ALICE experimental data, TPC event estimator, near side.

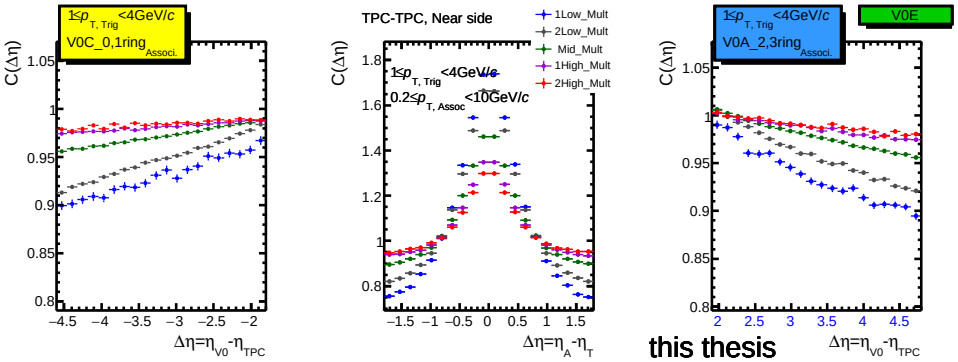

(d) ALICE experimental data, V0E event estimator, near side.

Figure E.2: ALICE experimental data, 1-D correlation functions of V0A-TPC, TPC-TPC and V0C-TPC by various event estimators in pp collisions at $\sqrt{s} = 7$ TeV in $|\Delta\varphi| < 0.1$ (near side) are shown for the 5 multiplicity classes.

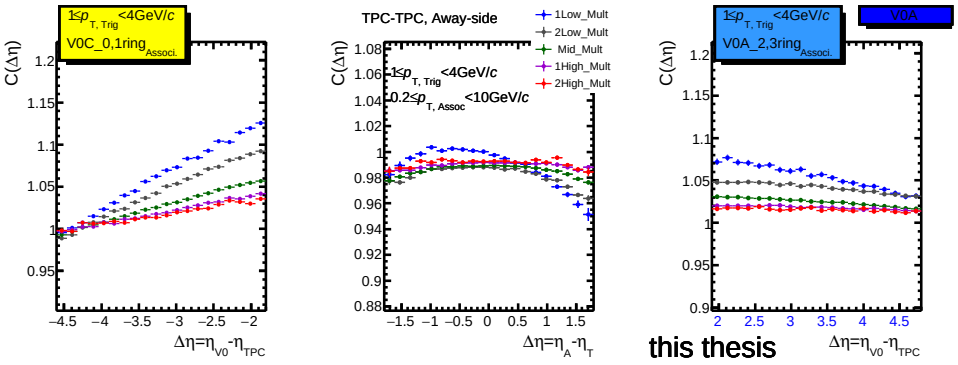

(a) ALICE experimental data, V0A event estimator, away side.

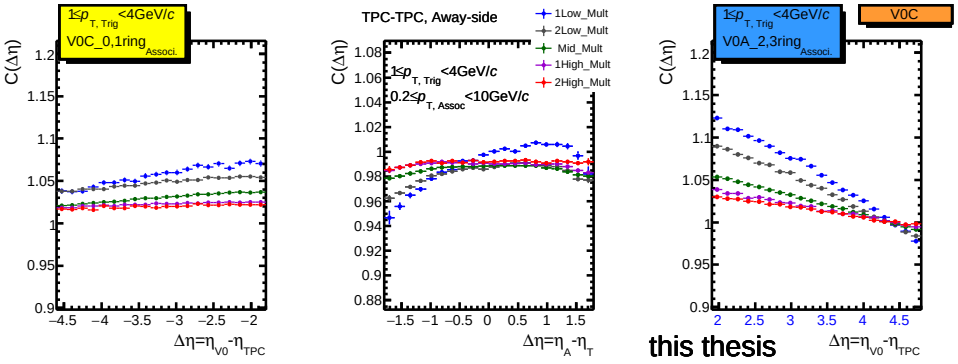

(b) ALICE experimental data, V0C event estimator, away side.

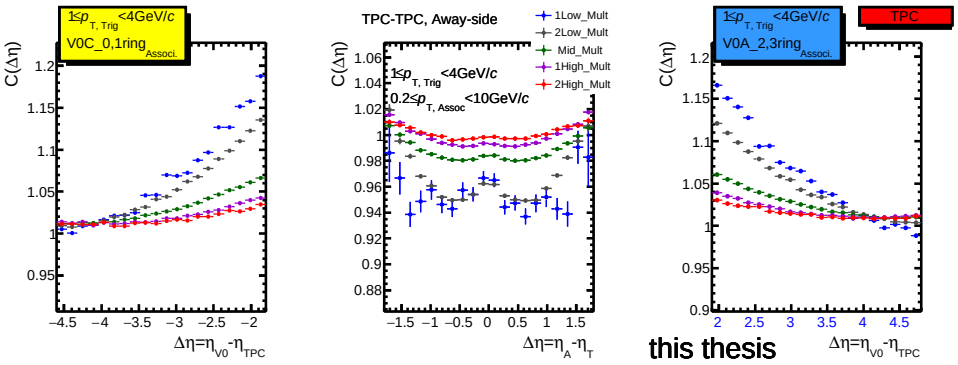

(c) ALICE experimental data, TPC event estimator, away side.

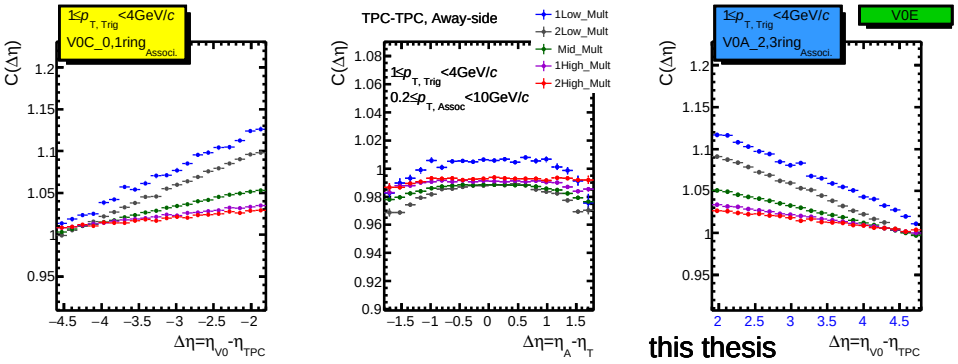

(d) ALICE experimental data, V0E event estimator, away side.

Figure E.3: ALICE experimental data, 1-D correlation functions of V0A-TPC, TPC-TPC and V0C-TPC by various event estimators in pp collisions at $\sqrt{s} = 7$ TeV in $2.3 < \Delta\varphi < 3.9$ (away side) are shown for the 5 multiplicity classes.

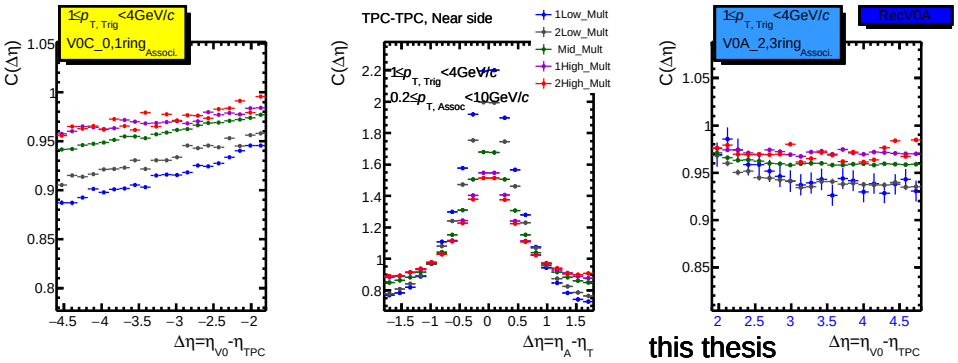

(a) Rec.MC, V0A event estimator, near side.

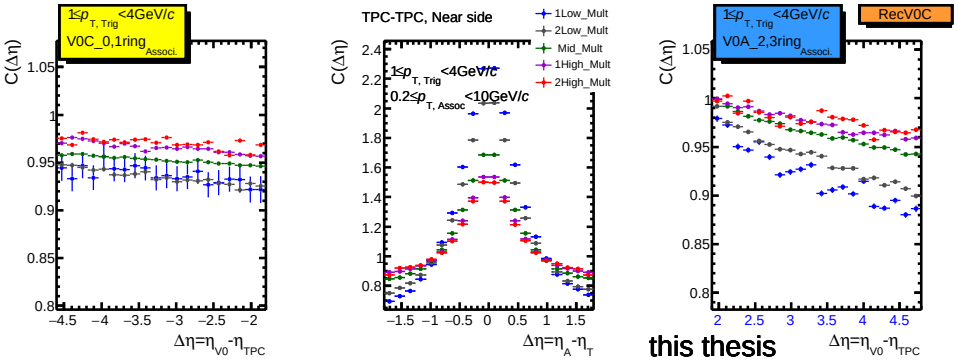

(b) Rec.MC, V0C event estimator, near side.

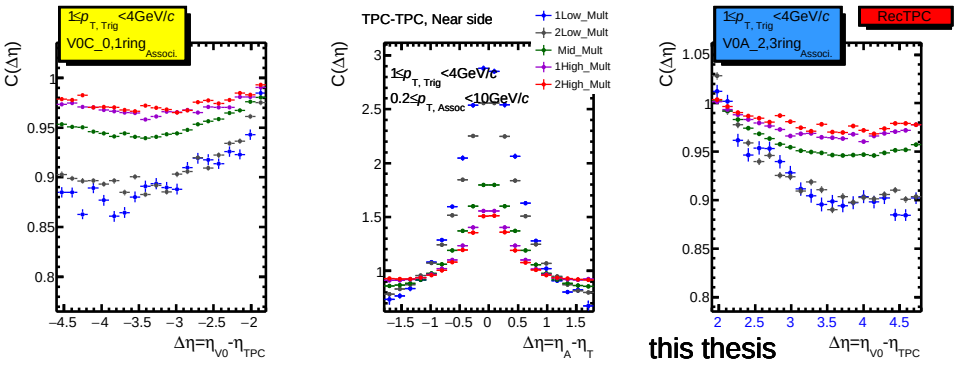

(c) Rec.MC, TPC event estimator, near side.

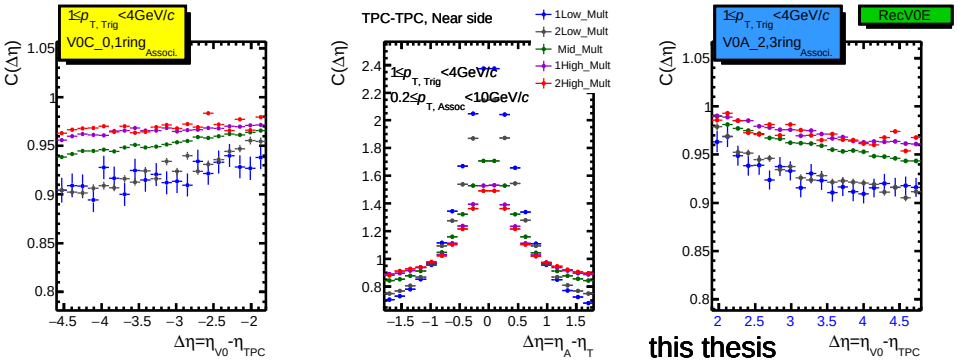

(d) Rec.MC, V0E event estimator, near side.

Figure E.4: Rec.MC, 1-D correlation functions of V0A-TPC, TPC-TPC and V0C-TPC by various event estimators in pp collisions at $\sqrt{s} = 7$ TeV in $|\Delta\varphi| < 0.1$ (near side) are shown for the 5 multiplicity classes.

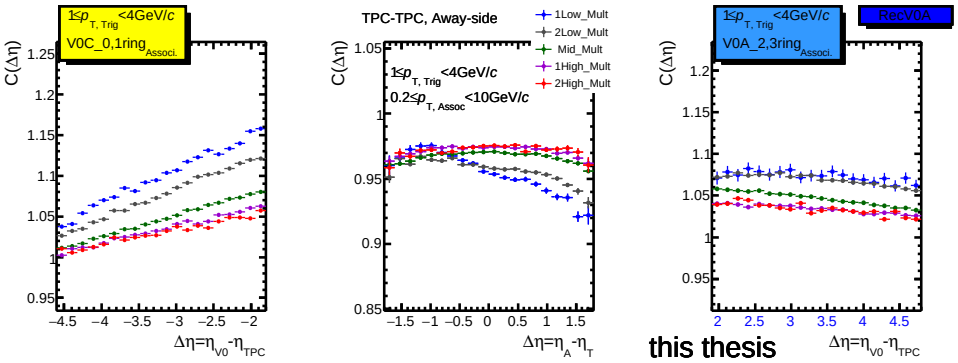

(a) Rec.MC, V0A event estimator, away side.

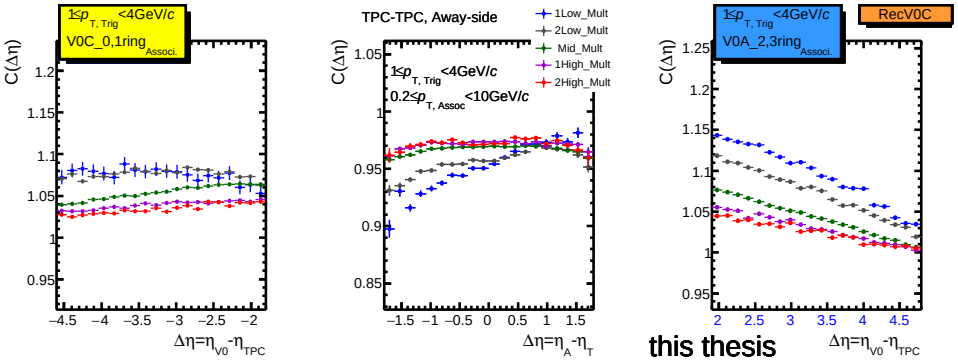

(b) Rec.MC, V0C event estimator, away side.

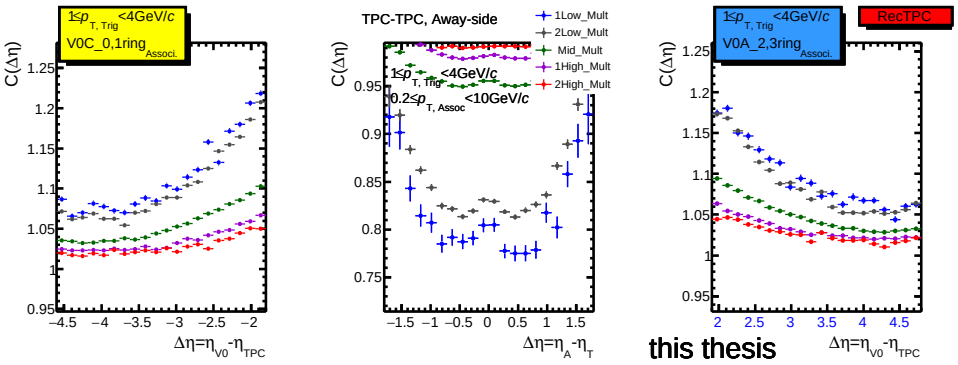

(c) Rec.MC, TPC event estimator, away side.

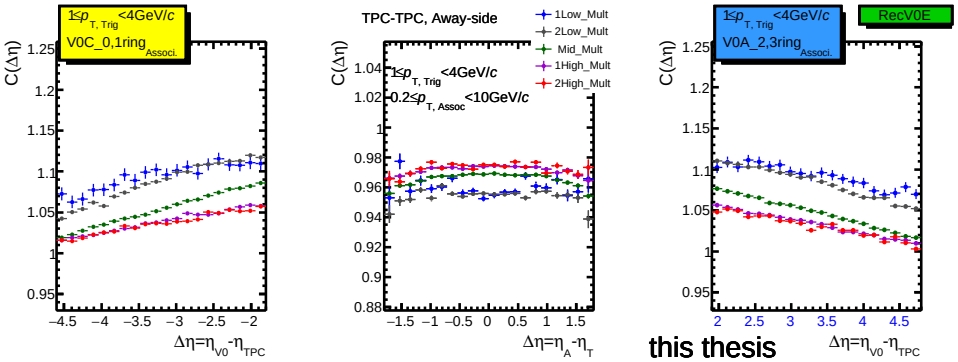

(d) Rec.MC, V0E event estimator, away side.

Figure E.5: Rec.MC, 1-D correlation functions of V0A-TPC, TPC-TPC and V0C-TPC by various event estimators in pp collisions at $\sqrt{s} = 7$ TeV in $2.3 < \Delta\varphi < 3.9$ (away side) are shown for the 5 multiplicity classes.

E.2 $\Delta\varphi$ correlation shape variation as a function of multiplicity

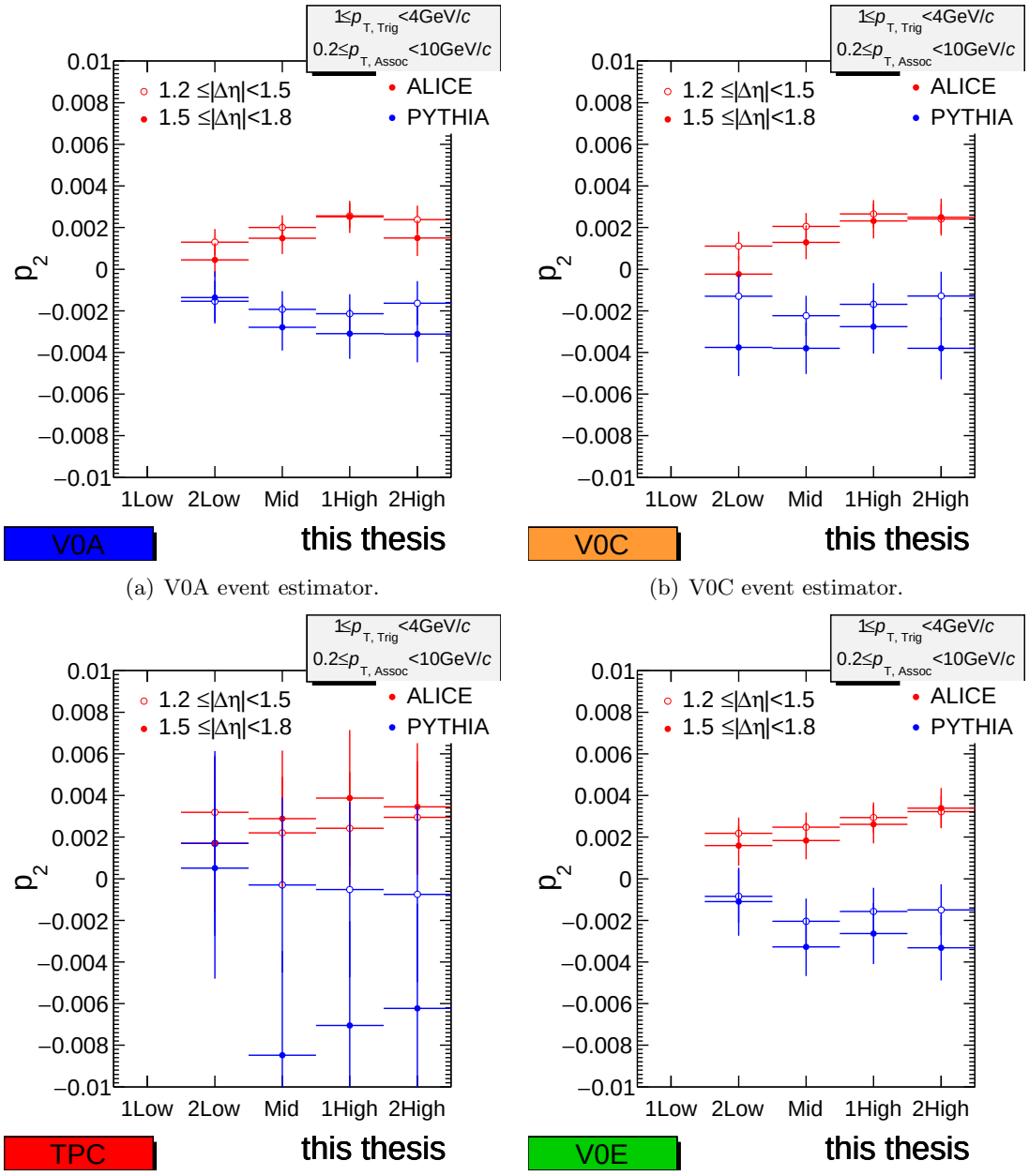

(a) V0A event estimator.

(b) V0C event estimator.

(c) TPC event estimator.

(d) V0E event estimator.

Figure E.6: Product of two p_2 parameters (for trigger and associate particles) of two-particle correlation with respect to the lowest multiplicity are shown for the 5 multiplicity classes.

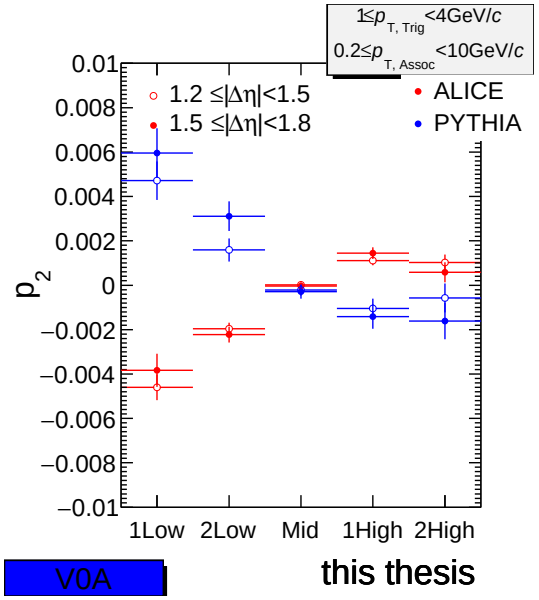

(a) V0A event estimator.

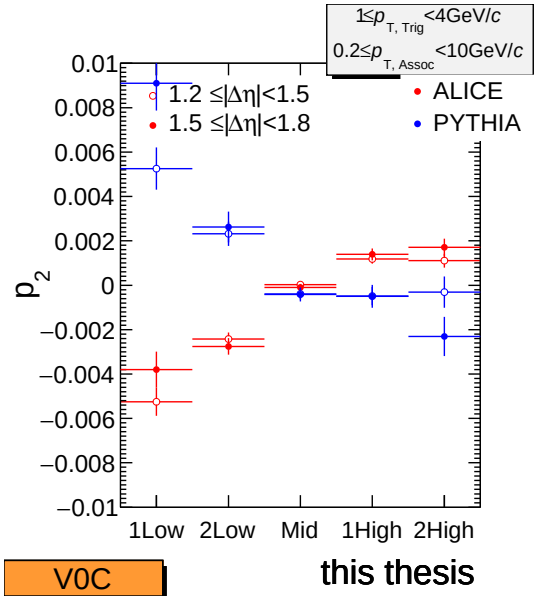

(b) V0C event estimator.

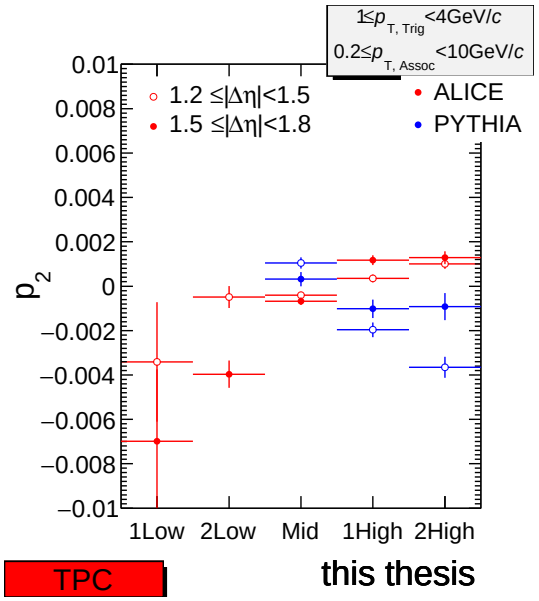

(c) TPC event estimator.

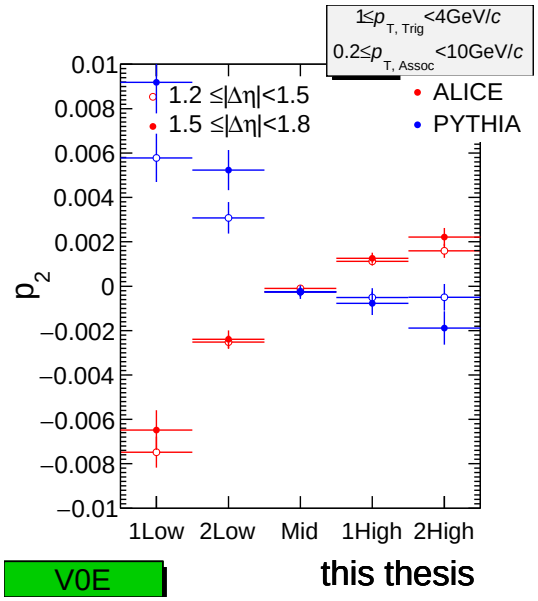

(d) V0E event estimator.

Figure E.7: Product of two p_2 parameters (for trigger and associate particles) of two-particle correlation with respect to MB are shown for the 5 multiplicity classes.

Appendix F

Appendix

F.1 Associate particle yield per trigger of V0A-TPC, V0C-TPC and TPC-TPC correlations

This section show particle yields per trigger $(\Delta\varphi, \Delta\eta)$ of combination of V0 and TPC correlation. Backgrounds rise with increasing multiplicity selections both V0A-TPC, V0C-TPC and TPC-TPC correlations. Most of features of particle yields per trigger $(\Delta\varphi, \Delta\eta)$ are similar with section 4.2.1.

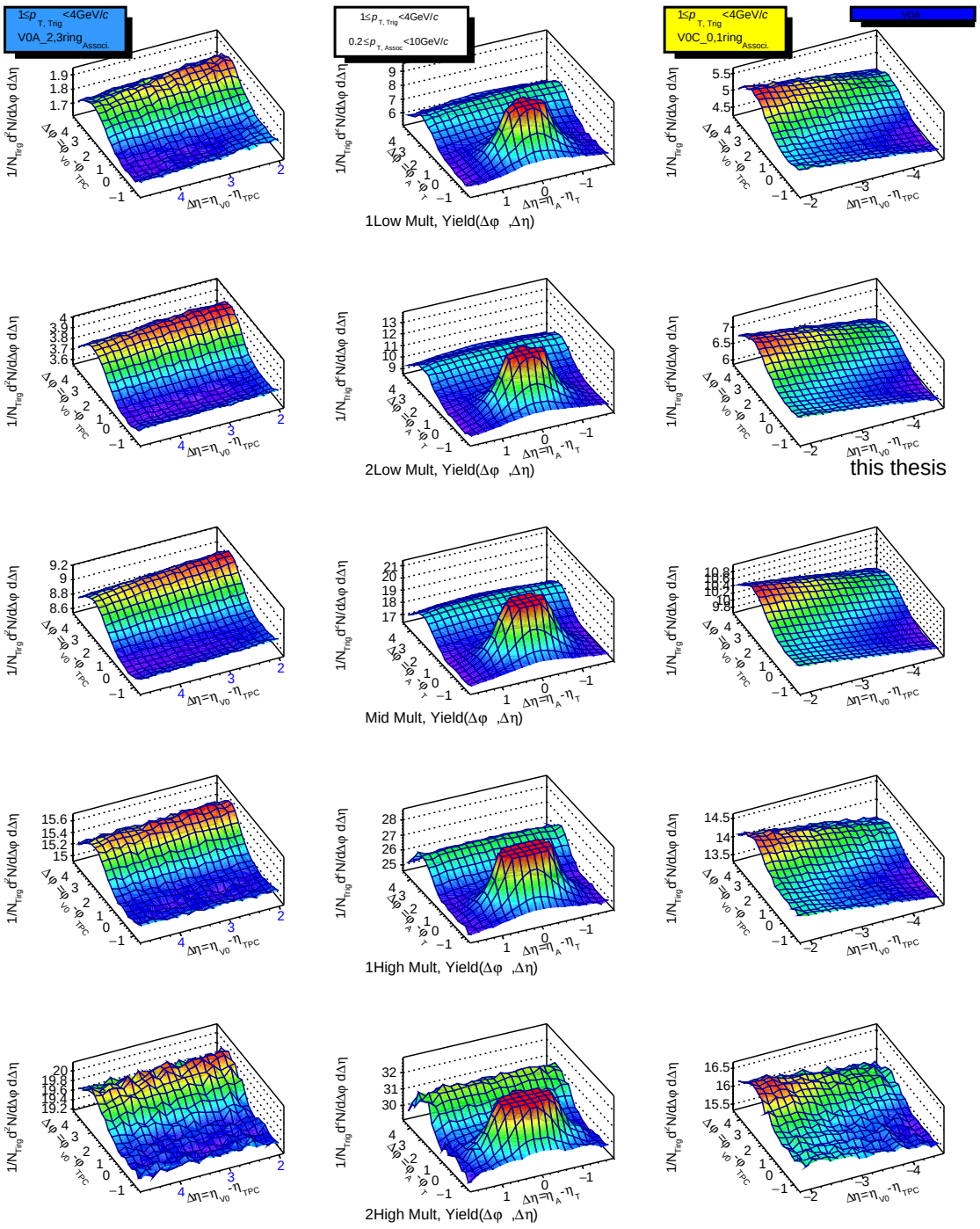

Figure F.1: ALICE experimental data, V0A event estimator, particle yield per trigger particle of V0A-TPC, TPC-TPC and V0C-TPC correlations are shown for the 5 multiplicity classes.

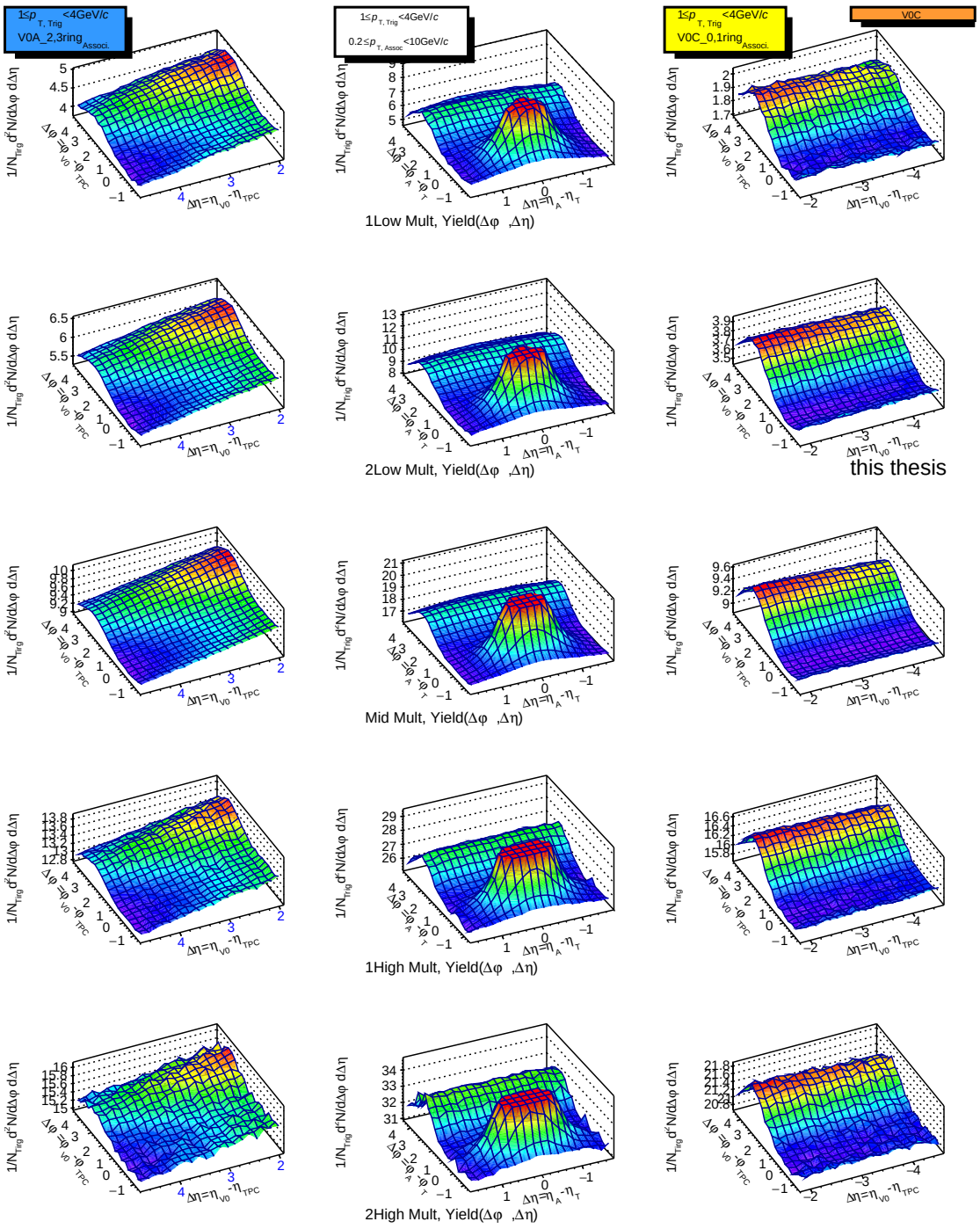

Figure F.2: ALICE experimental data, V0C event estimator, particle yield per trigger particle of V0A-TPC, TPC-TPC and V0C-TPC correlations are shown for the 5 multiplicity classes.

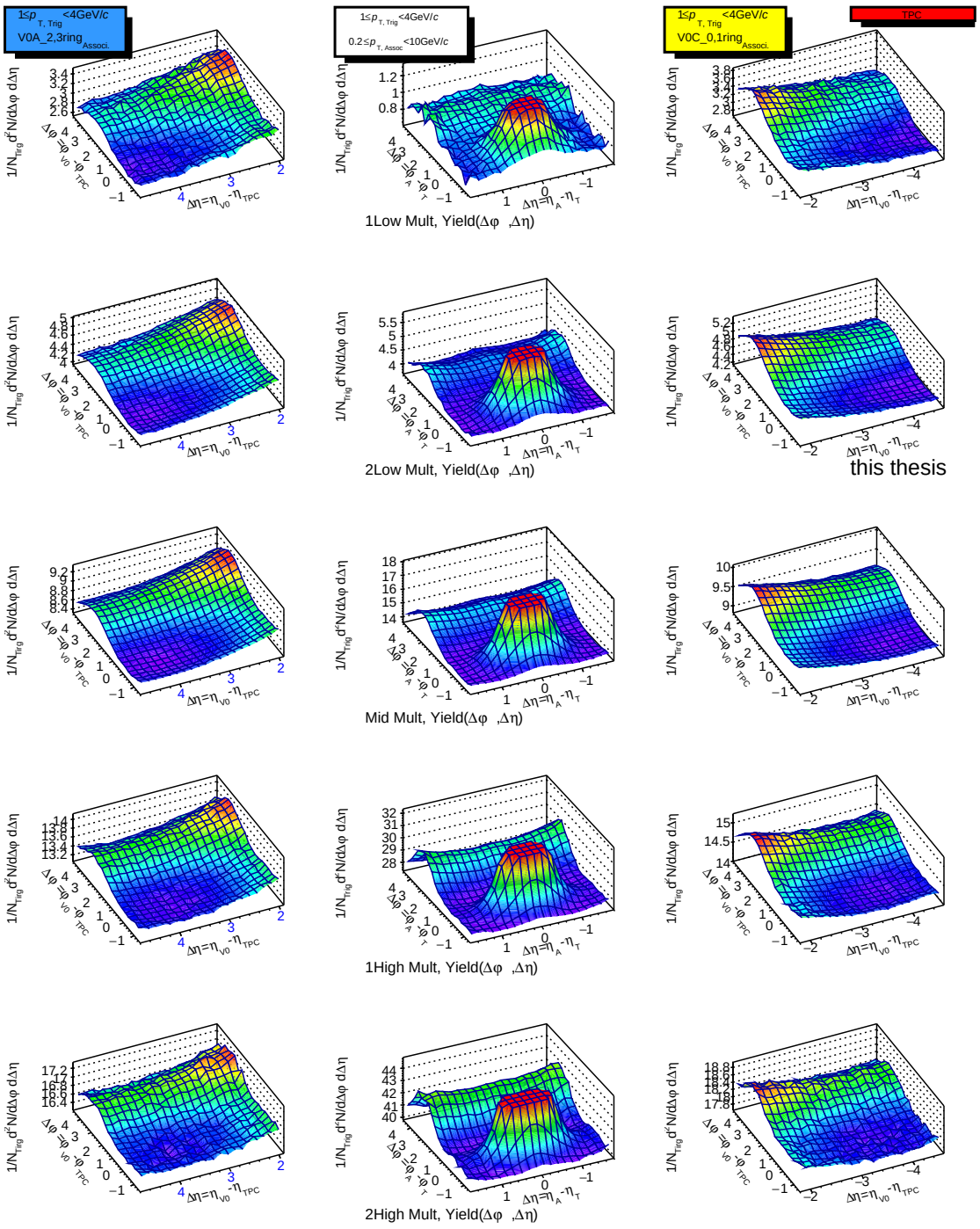

Figure F.3: ALICE experimental data, TPC event estimator, particle yield per trigger particle of V0A-TPC, TPC-TPC and V0C-TPC correlations are shown for the 5 multiplicity classes.

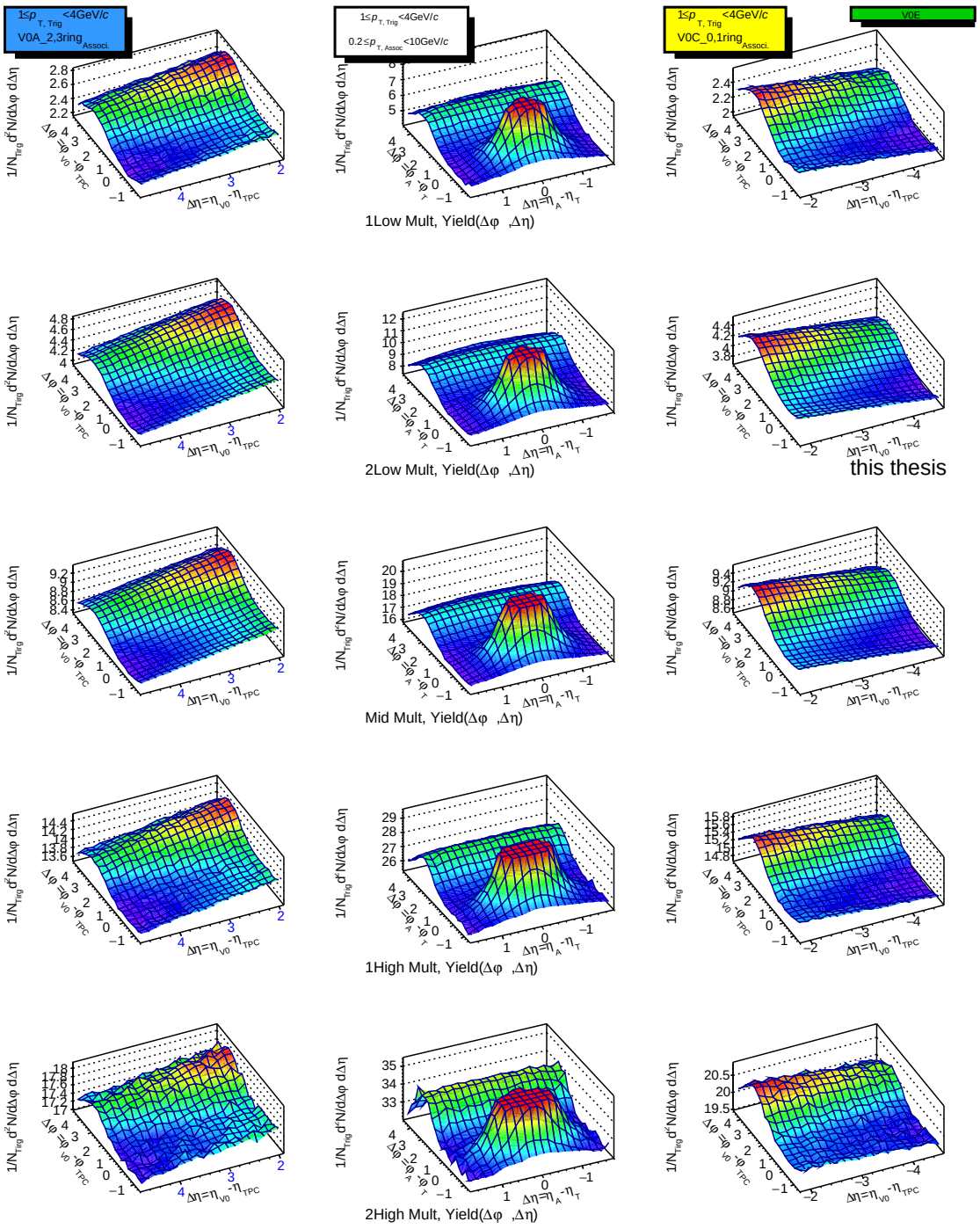

Figure F.4: ALICE experimental data, V0E event estimator, particle yield per trigger particle of V0A-TPC, TPC-TPC and V0C-TPC correlations are shown for the 5 multiplicity classes.

Appendix G

Appendix

G.1 $\Delta\varphi$ correlation shape variation as a function of multiplicity, TPC-V0C 0,1 rings and TPC-V0A 2,3 rings

Figure G.1 and Figure G.2 show the extracted elliptic p_2 parameters of $R(\Delta\varphi)$, which are TPC-V0C 0, 1 rings ($p^{Assoc}_{V0C0,1Rings}$) and TPC-V0A 2, 3 rings ($p^{Assoc}_{V0A2,3Rings}$). The p_2 parameters are increasing with increasing multiplicity in $1.8< |\Delta\eta| <4.8$. However, Rec.MC Pythia shows negative p_2 parameters in all multiplicity.

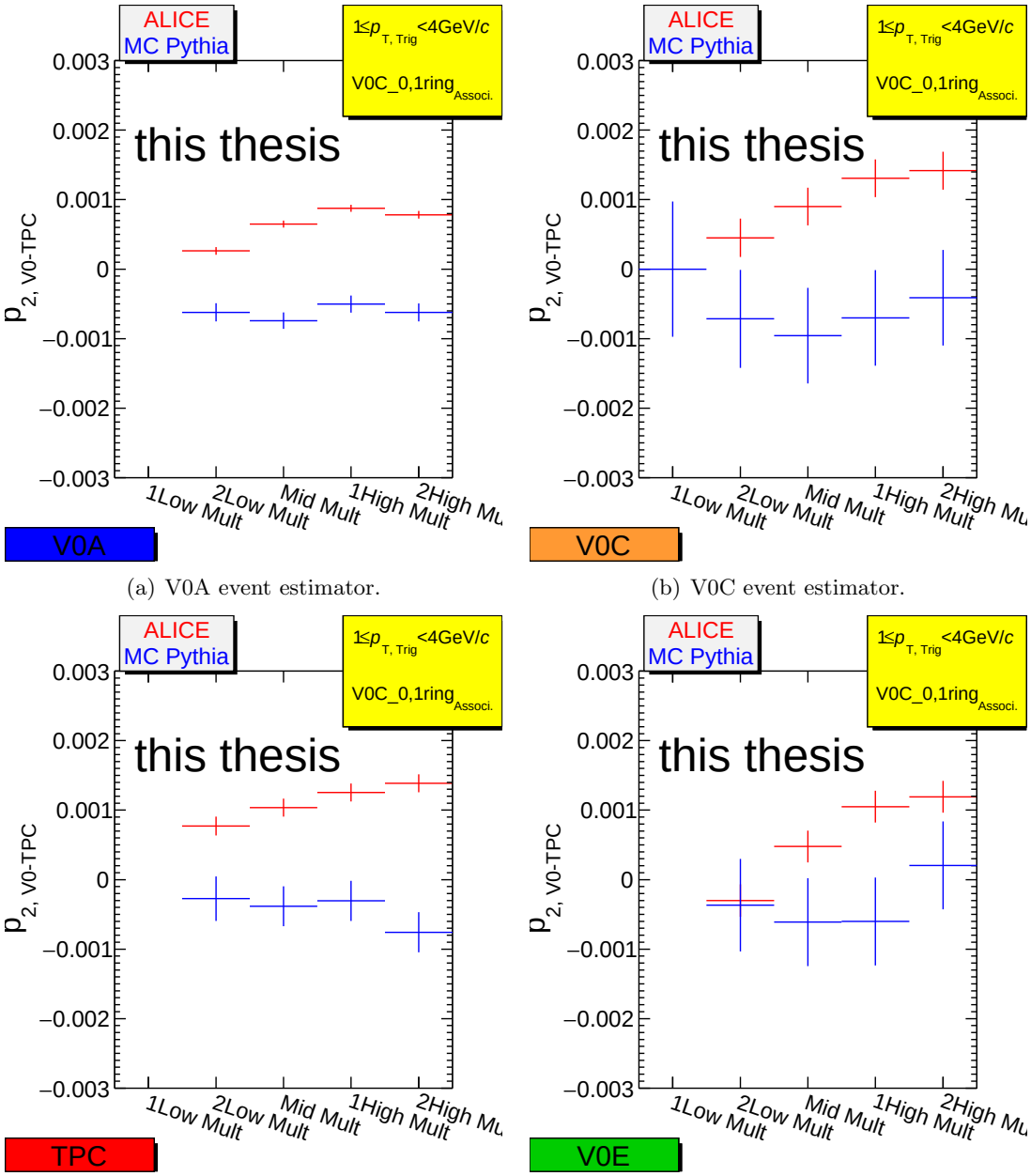

(a) V0A event estimator.

(b) V0C event estimator.

(c) TPC event estimator.

(d) V0E event estimator.

Figure G.1: Product of $p^{Assoc}_{V0C0,1Rings}$ parameters (for trigger and associate particles) of TPC-V0C 0, 1 rings correlation with respect to the lowest multiplicity are shown for the 5 multiplicity classes.

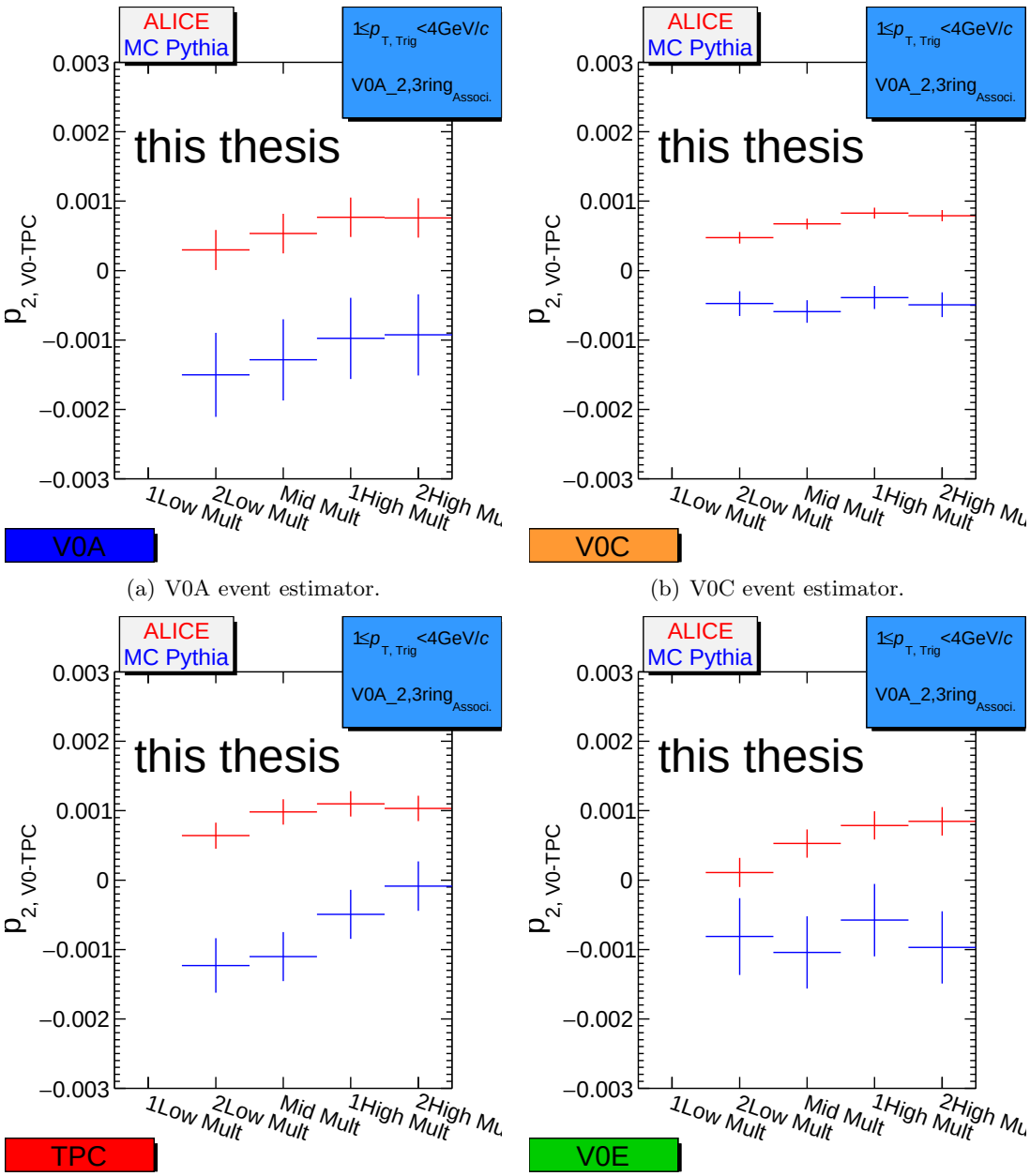

(a) V0A event estimator.

(b) V0C event estimator.

(c) TPC event estimator.

(d) V0E event estimator.

Figure G.2: Product of $p^{Assoc}_{V0A2,3Rings}$ parameters (for trigger and associate particles) of TPC-V0A 2, 3 rings correlation with respect to the lowest multiplicity are shown for the 5 multiplicity classes.

Appendix H

Appendix

H.1 $\Delta\varphi$ correlation shape variation as a function of multiplicity with respect to the minimum bias

Figure H.1 shows p_2^{short} parameters by fitting the correlation shape with another function $F(x) = a + bf(x)$ from the average renormalized correlation shape f(x) from minimum bias for 5 multiplicity classes by various event estimators. In all event estimators, the elliptic p_2^{short} parameters continuously rise with increasing multiplicity selections.

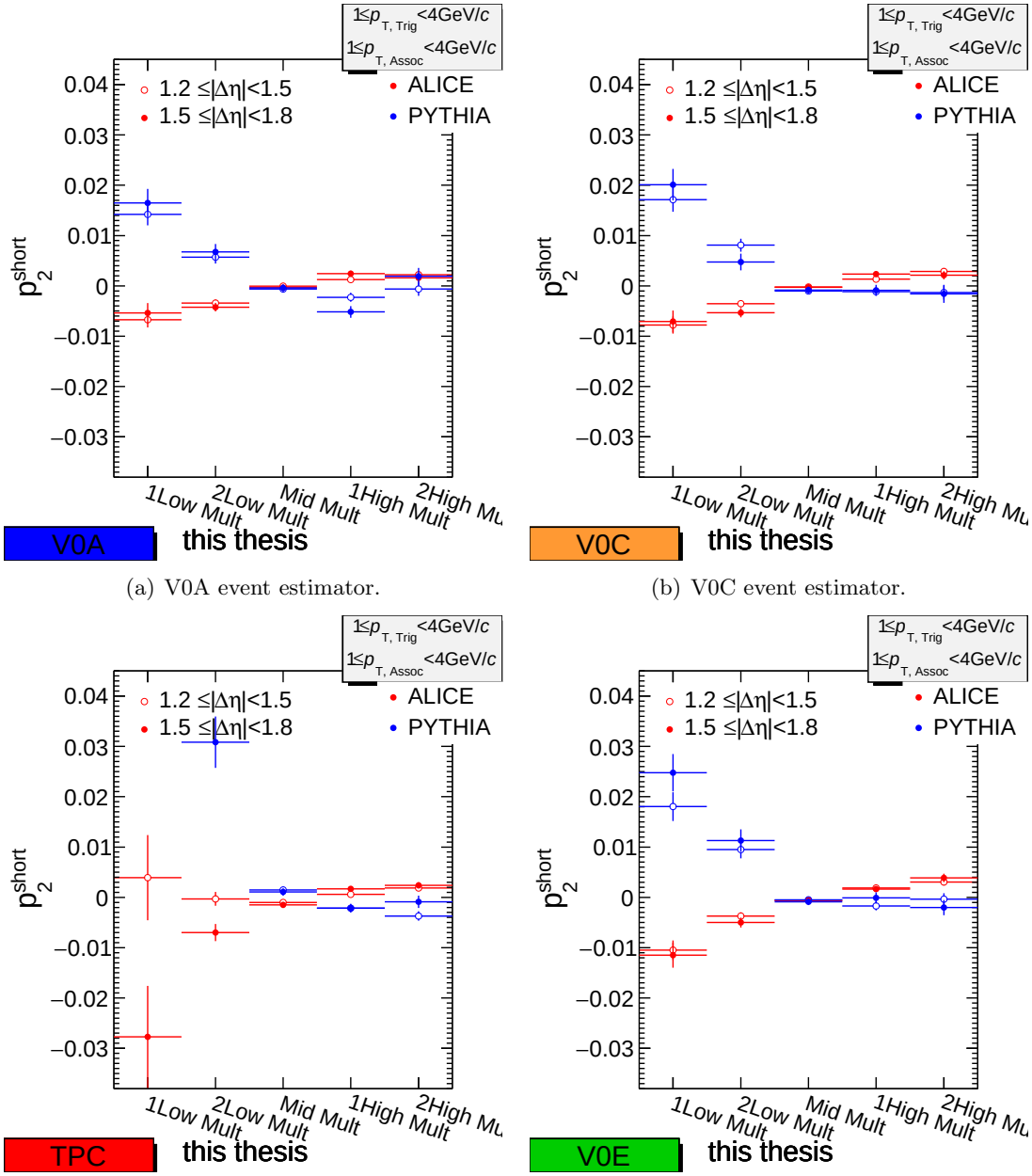

(a) V0A event estimator.

(b) V0C event estimator.

(c) TPC event estimator.

(d) V0E event estimator.

Figure H.1: Product of two p_2 parameters (for trigger and associate particles) of two-particle correlation, TPC-TPC correlation, with respect to the mean of MB are shown for the 5 multiplicity classes.

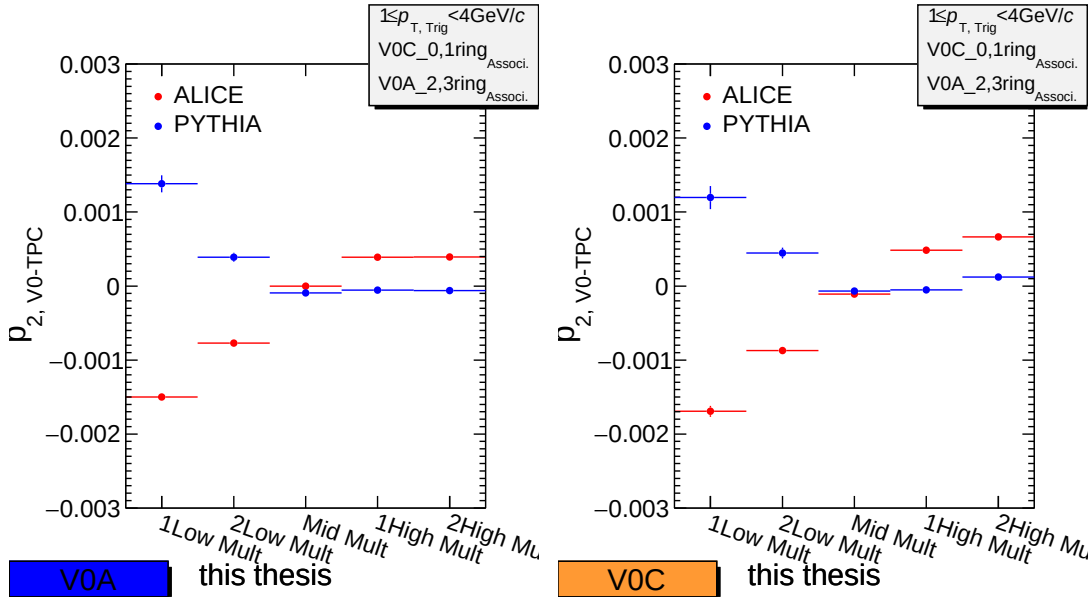

(a) V0A event estimator.

(b) V0C event estimator.

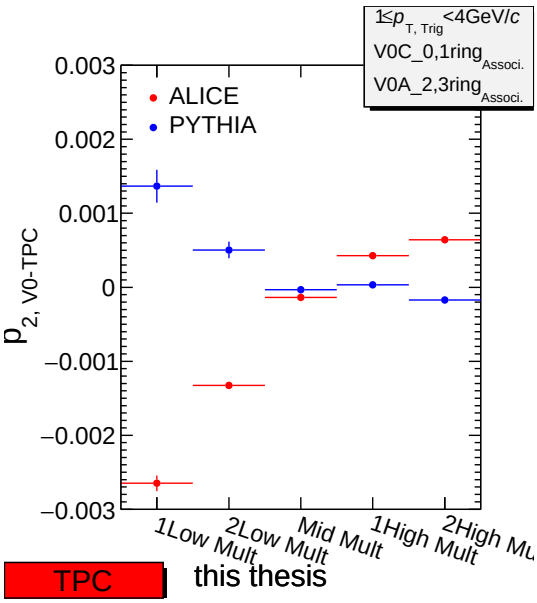

(c) TPC event estimator.

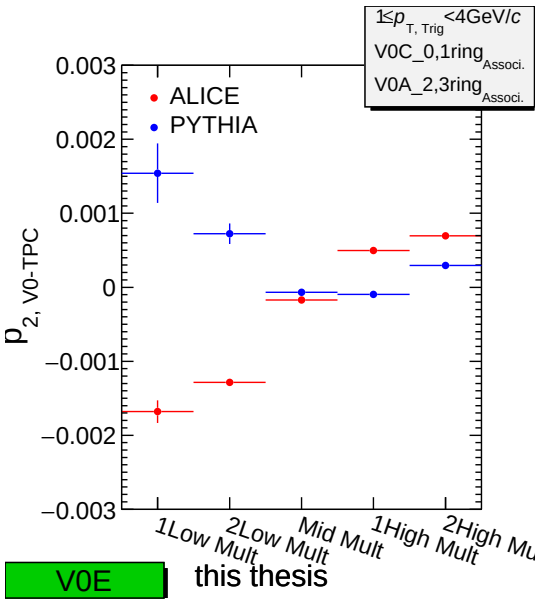

(d) V0E event estimator.

Figure H.2: Product of two p_2 parameters of V0-TPC correlation with respect to the mean of MB are shown for the 5 multiplicity classes.

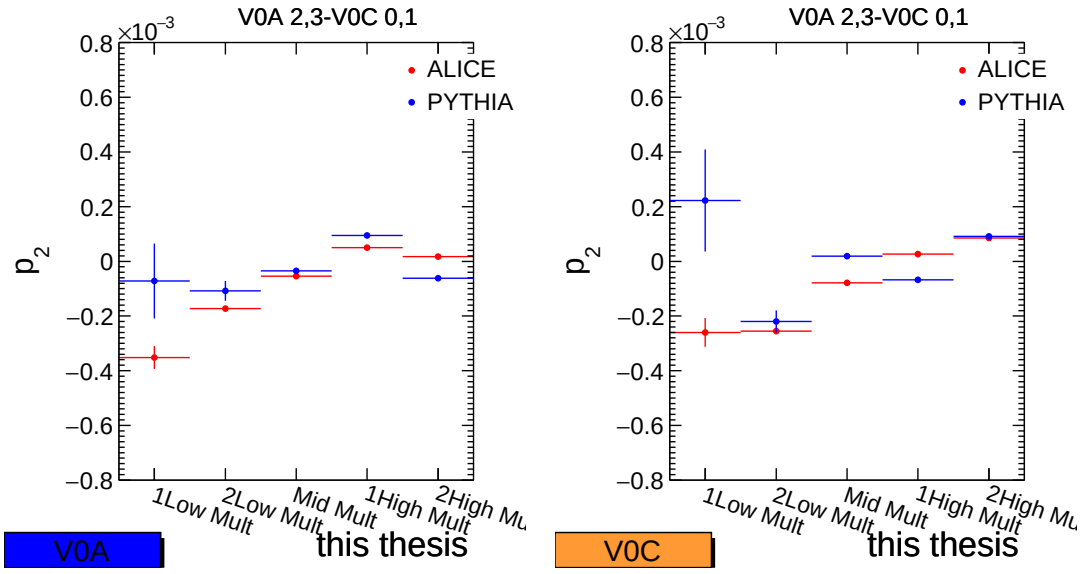

(a) V0A event estimator.

(b) V0C event estimator.

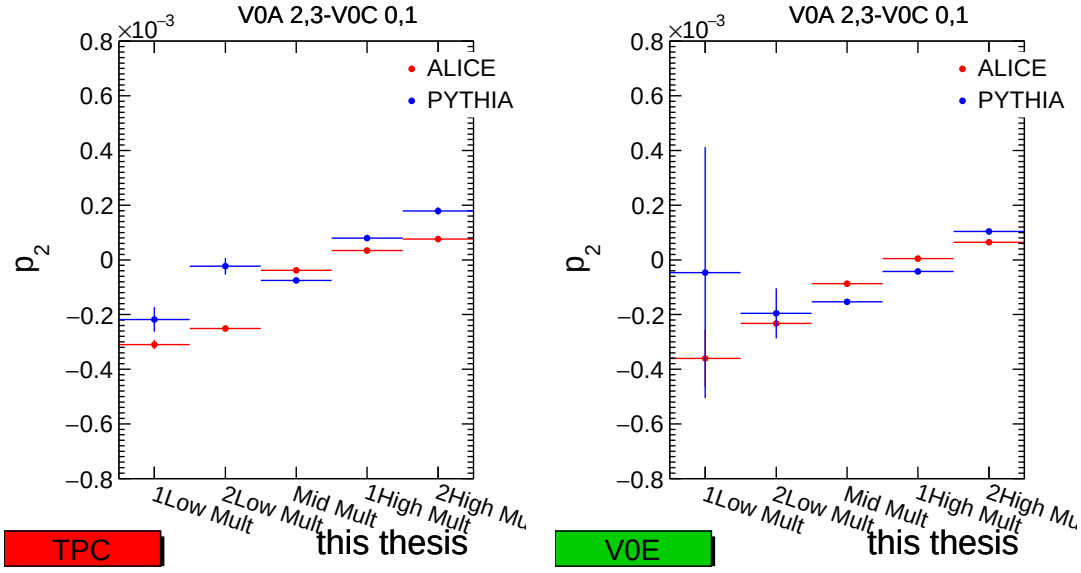

(c) TPC event estimator.

(d) V0E event estimator.

Figure H.3: The extracted p_2 parameter in 5.5< $|\Delta\eta|$ <7.6 with respect to the mean of MB, V0-V0 correlatuin, by various event estimators are shown for the 5 multiplicity classes.

Bibliography

[1] Kohsuke YAGI, Tetsuo HATSUDA and Yasuo MIAKE, Quark-Gluon Plasma from Big Bang to Little Bang.

[2] STAR Collaboration, Experimental and Theoretical Challenges in the Search for the Quark Gluon Plasma: The STAR Collaboration's Critical Assessment of the Evidence from RHIC Collisions, Nucl.Phys.A757:102-183,2005.

[3] Siegfried Bethke, The 2009 World Average of α_s, Eur.Phys.J.C64:689-703,2009.

[4] The TOTEM collaboration, First measurement of the total proton-proton cross section at the LHC energy of $\sqrt{s} = 7$ TeV, EPL, 96, 21002 (2011).

[5] Frithjof Karsch, Lattice QCD at High Temperature and Density, Lect.Notes Phys. 583 (2002) 209-249.

[6] STAR Collaboration, Evidence from d+Au Measurements for Final-State Suppression of High-p_T Hadrons in Au+Au Collisions at RHIC, Phys. Rev. Lett. 91, 072304.

[7] T. Pierog, Iu. Karpenko, J.M. Katzy, E. Yatsenko, K. Werner, EPOS LHC : test of collective hadronization with LHC data, arXiv:1306.0121

[8] ALICE Collaboration, Charged-particle multiplicity measurement in proton-proton collisions at $\sqrt{s} = 7$ TeV with ALICE at LHC, Eur.Phys.J.C68:345-354,2010.

[9] Tanguy Pierog, Sarah Porteboeuf, Iurii Karpenko, Klaus Werner, Collective flow in (anti)proton-proton collision at Tevatron and LHC, arXiv:1005.4526

[10] Sara Alderweireldt, Pierre Van Mechelen, Obtaining the CMS Ridge ect with Multi-parton Interactions, arXiv:1203.2048v2

[11] The ALICE collaboration, Elliptic Flow of Charged Particles in Pb-Pb Collisions at $\sqrt{s_{NN}}$=2.76 TeV, Phys. Rev. Lett. 105, 252302.

[12] The ALICE collaboration, Anisotropic flow of charged hadrons, pions and (anti-)protons measured at high transverse momentum in PbPb collisions at $\sqrt{s_{NN}}$=2.76 TeV, Physics Letters B Volume 719.

[13] The ALICE collaboration, Higher Harmonic Anisotropic Flow Measurements of Charged Particles in Pb-Pb Collisions at $\sqrt{s_{NN}}$=2.76 TeV, Phys. Rev. Lett. 107, 032301.

[14] The ALICE collaboration, Harmonic decomposition of two particle angular correlations in PbPb collisions at $\sqrt{s_{NN}}$=2.76 TeV, Physics Letters B 708 (2012) 249264.

[15] The ALICE collaboration, Transverse Momentum Distribution and Nuclear Modification Factor of Charged Particles in p+Pb Collisions at $\sqrt{s_{NN}}$ = 5.02 TeV, Phys. Rev. Lett. 110, 082302.

[16] B. Alver et al. Charged-particle multiplicity and pseudorapidity distributions measured with the PHOBOS detector in Au+Au, Cu+Cu, d+Au, and p+p collisions at ultrarelativistic energies, Phys. Rev. C 83, 024913.

[17] The ALICE collaboration, Event-by-event mean p_T fluctuations in pp and Pb-Pb collisions at the LHC, Eur. Phys. J. C 74 (2014) 3077.

[18] Huichao Song, QGP viscosity at RHIC and the LHC - a 2012 status report, arXiv:1210.5778

[19] B. Alver et al. System Size, Energy, Pseudorapidity, and Centrality Dependence of Elliptic Flow, Phys. Rev. Lett. 98, 242302.

[20] B. Alver et al. System size dependence of cluster properties from two-particle angular correlations in Cu+Cu and Au+Au collisions at $\sqrt{s_{NN}}$=200 GeV, Phys. Rev. C 81, 024904.

[21] Wei Li, Observation of a "Ridge" correlation structure in high multiplicity proton-proton collisions: A brief review, arXiv:1206.0148

[22] CMS Collaboration, Observation of Long-Range Near-Side Angular Correlations in Proton-Proton Collisions at the LHC, JHEP 1009:091,2010.

[23] ALICE Collaboration, Measuring the Charged Particle Multiplicity with ALICE, Indian J.Phys. 85 (2011) 93-97.

[24] ALICE Collaboration, Alignment of the ALICE Inner Tracking System with cosmic-ray tracks, JINST 5 (2010) P03003.

[25] ALICE Collaboration, The ALICE experiment at the CERN LHC, JINST 3 (2008) S08002.

[26] The ALICE collaboration, Performance of the ALICE VZERO system, JINST 8 (2013) P10016.

[27] The ALICE collaboration, Long-range angular correlations on the near and away side in p-Pb collisions at $\sqrt{s_{NN}} = 5.02$ TeV, Phys.Lett. B719 (2013) 29-41.

[28] C. -Y. Wong, Phys. Rev. C78, 064905 (2008).

[29] S. A. Voloshin, Phys. Lett. B632, 490 (2006).

[30] P. Romatschke, Phys. Rev. C75, 014901 (2007).

[31] E. V. Shuryak, Phys. Rev. C76, 047901 (2007).

[32] A. Dumitru et al., Nucl. Phys. A810, 91 (2008).

[33] S. Gavin, L. McLerran and G. Moschelli, Phys. Rev. C79, 051902 (2009).

[34] K. Dusling, D. Fernandez-Fraile and R. Venugopalan, Nucl. Phys. A828, 161 (2009).

[35] Y. Hama et al., Nonlin. Phenom. Complex Syst. 12, 466 (2009).

[36] B. Alver and G. Roland, Phys. Rev. C81, 054905 (2010).

[37] R. Snellings (STAR and ALICE Collaborations), Eur. Phys. J. C 49, 87 (2007).

[38] http://www.isgtw.org/sites/default/files/Standard_model_infographic.png

[39] http://www.kps.or.kr/storage/webzine_uploadfiles/1325_article.pdf

[40] http://home.web.cern.ch/topics/large-hadron-collider

[41] http://cds.cern.ch/record/841555

[42] http://aliweb.cern.ch/

[43] http://aliceinfo.cern.ch/Public/Welcome.html